2012

A study of surface roughness in the metal forming process

Hejie Li
University of Wollongong

A Study of Surface Roughness in the Metal Forming Process

A thesis submitted to fulfill the requirements

for the award of the degree

Doctor of Philosophy

from

University of Wollongong

by

Hejie Li

BEng, MEng

School of Mechanical, Materials and Mechatronic Engineering

Faculty of Engineering

October 2012

DECLARATION

I, Hejie Li, declare that this thesis, submitted in partial fulfilment of the requirements for the award of Doctor of Philosophy, in the School of Mechanical, Materials and Mechatronic Engineering, Faculty of Engineering, University of Wollongong, is wholly my own work unless otherwise referenced or acknowledged. The document has not been submitted for qualifications at any other academic institution.

_____

Hejie Li

October 2012

ACKNOWLEDGMENTS

I am deeply grateful to my supervisor Professor Zhengyi Jiang for his support, guidance, and continuous encouragement throughout the years of my PhD course. Under his guidance I have studied knowledge and how to obtain knowledge in ways that have helped me contribute more to my area of research.

I also give sincere thanks to Dr. Dongbin Wei, Professor A.K. Tieu, and Professor Jingtao Han for their guidance and close supervision.

I am extremely grateful to Mr. Greg Tillman in the Metrology Laboratory area and AFM for his training and guidance, to Mr. Nick Mackie for SEM training, and to Dr. Buyung Kosasih for 3D profile meter training.

I would also like to thank Mr. Joe Abbot for annealing and heat treating aluminium samples and to Mr. Bob Rowlan and Mr. Cameron Neilson for the experiments on compressing, and to Drs Zhixin Chen and Azidar Gazdiar for the EBSD experiments.

My thanks are also extended to Dr. Xianzhou Zhang, Mr. Ron Marshall, and Mr. Stuart Rodd for designing and manufacturing the compressing equipment and sample holder.

I would also like to thank Mr. Ninan Mathew, Dr. Haibo Xie, Ms Lihong Su, Dr. Hongtao Zhu, Mr. Ahmed Saleh, and Mr. Qiang Zhu, their enthusiastic assistance was an important contribution to complete this thesis.

I am also very grateful to the Australia Government and the University of Wollongong for providing IPRS and UPA scholarships to support my current study.

Finally, I give my heartfelt thanks to my Son Muni Li, my wife Guoying Ni, Mr. Yingjun Ni, and Mrs. Fengyun Zhao for their love, support, and help during my PhD study.

ABSTRACT

Surface roughness affects surface quality and wear and fatigue of metal forming products. The objective of this study is to improve our understanding of the evolution of surface asperity (surface roughness) during cold uniaxial planar compression of aluminium samples. Experimental research and simulation analysis were applied to study the evolution of surface asperity during compression.

Uniaxial planar compression experiments of FCC (Face Centred Cubic) aluminium alloy have been carried out using the designed compressing equipment on an INSTRON 8033 Material Testing Machine to examine the characteristics of surface asperity during compression. These characteristics have been investigated by instruments such as an Atomic Force Microscope (AFM), a 3D profile meter, a Vickers hardness tester, and surface profile meter. The Field Emission Guns-Scanning Electron Microscope (FEG-SEM) with Electron Backscattered Diffraction (EBSD) technique was also used to analyse the surface microstructures of cold, uniaxial planar compressed samples.

The results obtained from these experiments show that compressing parameters such as the reduction (strain), strain rate (deformation velocity), friction (lubrication), and wavelength (a technical term of surface roughness, refers to the length of surface roughness wave because the surface roughness curve is the filtered wave, which has the features of wave) have significant effects on the evolution of surface asperity (surface roughness). In uniaxial planar compression, surface asperity evolves in three stages: when reduction is less than 10 %, plastic deformation takes place in an aggregate of elastic deformation. Elastic deformation plays an important role in the evolution of surface asperity. When reduction exceeds 10 % the influence of plastic deformation on surface asperity becomes obvious, while the influence of elastic deformation is insignificant. When reduction exceeds 40 %, and continues to increase, there is no significant decrease in surface roughness (R_a). The influence of

lubrication on the evolution of surface asperity is also very complicated. For example, when reduction is small (10 %), the layer of lubrication has no obvious influence on surface roughness of the sample. However, when reduction is in a certain range (in this study, it is from 10 to 40 %), lubrication can significantly limit the flattening of surface asperity. When reduction exceeds 40 %, the lubrication is squeezed out and has no obvious effect on the evolution of surface asperity. In cold uniaxial planar compression (CUPC), the relationship between surface roughness R_a and strain is non-linear, which is different from the tensile experiment. The influence of strain rate on surface asperity flattening can be divided into the elastic and plastic deformation stages. During elastic deformation, strain rate has no significant influence on the evolution of surface asperity, but during plastic deformation, an increasing strain rate can lead to a larger surface roughness. At a lower strain, an increasing strain rate can result in a higher hardness, while at a larger strain (60 %) this tendency is reversed, an increasing strain rate leads to a lower hardness. Under the same reduction, an increasing strain rate can lead to a higher flow stress.

Surface roughness shows an obvious sensitivity to the orientation of grains near the surface. In this study the oriented {111} grains are the main source of localised strain. With an increase in reduction, the grain size tends to decrease and the cubic texture {001}<100> is weak, while the brass orientation {110}<112> becomes stronger. At the same time the Schmid factor (also called “orientation hardness”) of the surface area will shift from “hard” (about 0.3) to “soft” (about 0.5). When reduction exceeds 40 %, the in-grain shear band appears in some grains which are 4-5 grains away from the edge and localised strain starts in this area. When reduction exceeds 60 %, most grains have plastic slips, and a few transgranular shear bands that resulted from the deformation twins of brass orientation were observed in the surface area. Under the same reduction, the surface roughness of the sample with a large grain size tended to decrease very slowly, but after compression, the sample with the largest grain size had the maximum surface roughness. The surface roughness R_a is a power exponent function of grain size. Influences of recovery and recrystallisation are not significant in the CUPC process of aluminium.

The initial data of the sample surface roughness, friction, and microstructures

(textures and grain orientations) have been applied in the 2D and 3D crystal finite element models. The simulated results obtained from the experimental results confirmed the influence of deformation parameters (reduction, lubrication, strain rate, and wavelength), and microstructures (textures and grain orientations) on the evolution of surface asperity in uniaxial planar compression.

It is recommended that BCC (Body Centered Cubic) metal and Hexagonal close-packed (hcp) metals such as magnesium (Mg) are used to analyse the evolution of surface asperity in uniaxial compression with different deformation parameters, friction state, and microstructures. The initial surface roughness of compression tool should also be discussed, although there are some difficulties with simulation, and various lubricants should be used to study how they affect the evolution of surface asperity. 3D EBSD mapping by the FIB (Focus Ion Beam) technique is also recommended as a good method to show the practical development of surface microstructure in three dimensions. High temperature deformation processes are also needed to analyse the influence of temperature and oxidation on the evolution of surface asperity, with the revised crystal plasticity constitutive model. The effect of the workpiece size is discussed.

LIST OF CONTENTS

LIST OF FIGIURES

LIST OF TABLES

NOMENCLATURE

a	$a = (K / k_f)^2$ for a three-dimensional junction
a^*	Rate of increase of surface roughness
AFM	Atomic Force Microscope
A_o, A	Cross sectional area before and after compression
A_q	Material constant
A_a	Apparent area of contact between two bodies
A_{HV}	Surface area of the resulting indentation in square millimeters
BCC	Body-centred Cubic
B_1 and B_2	Equation coefficient for roughness
C^*	Coefficient related grain size and surface roughness
C_{11}, C_{12} and C_{44}	Elastic modulus
C_m^*	A non-dimensionalised roughening parameter
CPFEM	Crystal Plasticity Finite Element Method
CUPC	Cold uni-axial planar compression
C'	Parameter depending on the deformation path and kind of metal
d	Average grain size, μm
d_{HV}	Average length of the diagonal left by the indenter in millimeters
d_m	An arbitrary “disturbance” depth
$\boldsymbol{D}$	Tensor of deformation rate
$\boldsymbol{D}^*$	Elastic component of deformation rate tensor
D_m^*	Non-dimensional roughening depth
$\boldsymbol{D}^p$	Plastic component of deformation rate tensor

$\boldsymbol{E}^{(1)}$	Green elastic strain tensor
E_x^*	Non-dimensionalised strain rate
EBSD	Electron Backscattered Diffraction
$f_{\alpha\beta}$	Hardening effect of the slip in the βth slip system on the resolving shear stress in the αth slip system
$\boldsymbol{F}$	Deformation gradient
FCC	Face-centred Cubic
FEG-SEM	Field Emission Guns-Scanning Electron Microscope
F_{HV}	Force applied to the diamond
F_n	Force required to move a body
$\boldsymbol{F}^*$	Deformation gradient of elastic deformation and rigid rotation
$\boldsymbol{F}^p$	Deformation gradient of plastic deformation
$g_{(\alpha)}$	Function of strain hardening
h	Function of self hardening
h_0	Initial hardening rate
h_s	Saturated hardening rate
$\boldsymbol{h}_{\alpha\beta}$	Matrix of hardening tensors
H_o , H	Height of specimen before and after compression
H_m^*	Non-dimensional hardness ratio
H_V	Vickers hardness
K_l	The linear slope
L_0	Length of sample before compression
L	Length of sample after compression
ΔL	Increment of deformation
$\boldsymbol{L}$	Velocity gradient of present configuration
$\boldsymbol{L}^*$	Elastic component of velocity gradient
$\boldsymbol{L}^p$	Plastic component of velocity gradient

l_m	Width of deformation area
m	Sensitive coefficient of strain rate, the power law
m_i	Interface frictional shear factor
$\mathbf{m}_{(\alpha)}$	Unit normal vector in slip plane of α *th* slip system
m_q	Material constant
M	Schmid factor
n	An exponent indicating the effect of grain size
p_n	Normal pressure, kN
P	Load, kN
P_n	Normal force, kN
P^*	Non-dimensional power
q	Ratio of self hardening and patent hardening, as a value of $1 < q < 1.4$
q_l	Latent hardening parameters: 1.0 (co-planar); 1.4 (No co-planar)
R_0	Original surface roughness
$\mathbf{R}^*$	Rotation gradient
R_a	Arithmetic average surface roughness μm
R_q	Root mean squared surface roughness μm
ΔR^*	Maximum increment of roughness
$\mathbf{s}_{(\alpha)}$	Slipping vector of the α *th* slip direction in the initial configuration
$\mathbf{s}^*_{(\alpha)}$	Unit slip vector of the α *th* slip direction in the initial configuration
s_0	Initial value of the deformation resistance
s_s	Value of saturation for deformation resistance
SEM	Scanning Electron Microscope
Δt	Compression time
$\mathbf{T}^{(1)}$	Second $Piola-Kirchhoff$ stress
T	Stress in MPa

$\mathbf{x}$	Position of mass point in present configuration
x	Average grain size,
X_m^*, Y_m^*	Non-dimensional coordinates
$\mathbf{X}$	Position of mass point in initial configuration
$\dot{U}$	Dislocation velocity
$\mathbf{U}^*$	Right stretching gradient
$\mathbf{W}$	Tensor of rotation rate
$\boldsymbol{W}$ *	Elastic component of rotation rate tensor
$\mathbf{W}^p$	Plastic component of rotation rate tensor
W^{p}	The minimum dissipation of energy
$\mathbf{v}$	Velocity of mass point
$\bar{\boldsymbol{\nu}}$	Dislocation velocity
v_x	Velocity component in the x direction
v_y	Velocity component in the y direction
y_1	Regressed average arithmetic surface roughness R_a
$\gamma_{(\alpha)}$	Shearing strain led by the α *th* slip system
$\dot{\gamma}_0$	Reference shearing rate
$\dot{\gamma}_{(\alpha)}$	Shear rate led by the α *th* slip system
Y	Simulated average surface roughness,
τ_{nd}	Shear stress of the slip system
$\tau^{(\alpha)}$	Resolving shear stress in the α *th* slip system
τ_0	Yield stress in MPa
t_1	Exponent
τ_s	Saturated flow stress in MPa
τ_i	Average frictional shear stress
$\overset{\nabla}{\boldsymbol{\tau}}$	Jaumann derivative on the basis of the Kirchoff stress of the tensor of rotation rate $\mathbf{W}$
$\overset{\nabla^*}{\boldsymbol{\tau}}$	Jaumann derivative on the basis of the Kirchoff stress of the tensor of rotation rate $\mathbf{W}$ *

$\mathbf{L}$, $\mathcal{L}$	Fourth order tensors of elastic modulus
$\boldsymbol{\delta}_{\alpha\beta}$	Kronecker sign
δ	Distance from the drawing line to the surface nodes
$\dot{\varepsilon}$	Strain rate
ε	True strain
$\boldsymbol{\sigma}$	Cauchy stress
σ_f	Uniaxial flow stress of the material
μ	Coefficient of friction
ϕ	Angle between the loading axis and normal to slip plane
λ	Angle between the loading axis and direction of slip

LIST OF PUBLICATIONS DURING THE PHD COURSE

1. **H.J. Li**, Z.Y. Jiang, D.B. Wei. Study on effect of strain rate on 3D surface asperity flattening in uniaxial planar compression by CPFEM , Wear, (submitted, under review. Reference number: WOM2013-D-12-00131 E-TP-12-92-A).
2. **H.J. Li**, D.B. Wei, Z.Y. Jiang. Crystal plasticity finite element method analysis of 3D surface asperity flattening in metal forming process, Steel Research International (in press, accepted on 6th May 2012).
3. **H.J. Li**, Z.Y. Jiang, D.B. Wei. Crystal plasticity finite modelling of 3D surface asperity flattening in uniaxial planar compression. Tribology letters, 46(2) (2012) pp.101-112.
4. **H.J. Li,** Z.Y. Jiang, D.B. Wei, J.T. Han, A.K. Tieu. Study on surface asperity flattening during uniaxial planar compression, Wear, 271 (2011) pp.1778-1784.
5. **H.J. Li**, Z.Y. Jiang, D.B. Wei, J.T. Han, Crystal Plasticity Finite Element Modelling of Surface Roughness and Texture of Metals, Proceedings of 10th Anniversary of the International Conference on Technology of Plasticity, Aachen, September 2011, pp.906-911.
6. **H.J. Li**, Z.Y. Jiang, D.B. Wei, J.T. Han and A.K, Tieu. Crystal Plasticity Finite Element Modelling of the Influence of Friction on Surface Roughening during Uniaxial Planar Compression, Materials Science Forum, 654-656 (2010) pp. 1606-1609.
7. **H.J. Li**, Z.Y. Jiang, D.B. Wei, P.J. Yan, A.K. Tieu, J.T. Han, Crystal Plasticity Finite Element Modelling of Surface Asperity Flattening during Uniaxial Planar Compression, International Conference on Tribology in Manufacturing Processes, Nice, June 2010, pp. 397-406.

8. **H.J. Li**, Z.Y. Jiang, D.B. Wei, Y.B. Du, J.T. Han, A.K. Tieu. Surface profile simulation during plain strain compression by crystal plasticity finite element method, Advanced Materials Research, 76-78 (2009) pp. 538-543.
9. **H.J. Li**, J.T. Han, H.C. Pi, H., Z.Y. Jiang, D.B. Wei, D. A.K. Tieu, Modelling texture development during cold rolling of IF steel by crystal plasticity finite element method, Journal of University of Science and Technology Beijing, 15 (6) (2008) pp. 696-701.
10. **H.J. Li**, J.T. Han, Z.Y. Jiang, H.C. Pi, D.B. Wei, A.K. Tieu, Crystal plasticity finite element modelling of BCC deformation texture in cold rolling, Advanced Materials Research, 32 (2008) pp. 251-254.
11. **H.J. Li**, Z.Y. Jiang, J.T. Han, D.B. Wei, H.C. Pi, A.K. Tieu, Crystal plasticity finite element modelling of necking of pure aluminum during uniaxial tensile deformation, Steel Research International, 2 (2008) pp. 655-662.
12. Z.Y. Jiang, **H.J. Li**, J.T. Han, D.B. Wei, H.C. Pi, A.K. Tieu, Crystal Plasticity Finite Element Modelling of Compression of Pure Aluminum, Proceedings of the 6th International Conference on Engineering Computational Technology, Athens, September 2008, pp. 251-265.
13. T.G. Zhou, Z.Y. Jiang, J.L. Wen, **H.J. Li**, and A.K. Tieu: Semi-solid continuous casting-extrusion of AA6201 feed rods. Materials Science and Engineering A 485 (2008), pp. 108-114.

Statement of Contributions to Jointly Authored Works Contained in the Publications

These publications are composed of my research work since the commencement of my PhD candidature, and contain materials previously published or written by the other persons except where due references have been made in the text. In publication No. 12, I was a main researcher for the paper, while in publication No. 13, I was involved in the analysis of stress.

Prof. Z.Y. Jiang, as my principal supervisor at University of Wollongong (UOW), has continuously guided the direction of the research including the experimental

design and data analysis and provided comments and valuable suggestions on all the publications.

My co-supervisor Dr. Wei brought forward me some valuable suggestions to the experimental design and data analysis for publications Nos. 1-12. Prof. A.K. Tieu, as my co-supervisor, provided some helpful advice to publications Nos. 1-12. Prof. J.T. Han gave me some valuable ideas for the experimental design and modelling, and made contributions to publications Nos. 4-12. Dr. P.J. Yan did some data analysis in publication No. 7. Dr. Y.B. Du contributed to the experiments in publication No.8. Dr. H.C. Pi carried out texture analysis for publications Nos. 9-12.

CHAPTER 1

INTRODUCTION

The high surface quality of metal products is a key issue for manufacturing industries. As an important parameter of surface quality, the surface roughness of cold metal manufactured products is an interesting topic in metal manufacturing. The typical surface roughness of metal products is shown in Figure 1.1, and it includes the following parameters: roughness height, roughness width, waviness height, and lay (direction of the finished pattern). The practical surface roughness may be different from the schematic diagram.

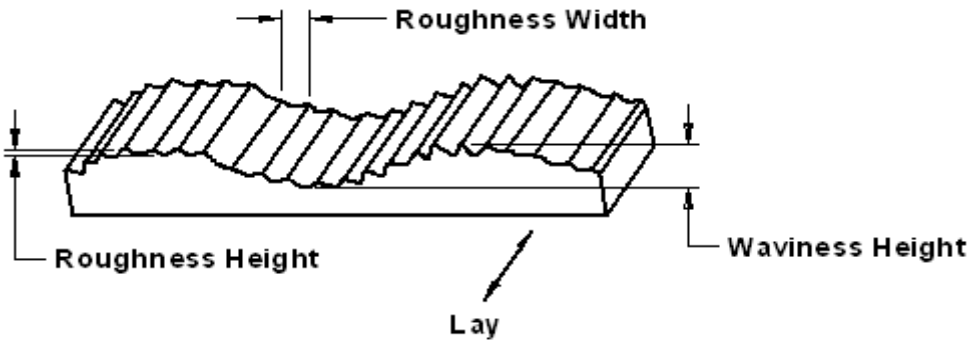

Figure 1.1 Schematic diagram of surface characteristics [1]

1.1 Surface roughness

1.1.1 Definition

Surface roughness, often shortened to roughness, is a measure of the texture of a surface. It is quantified by the vertical deviations of the real surface from its ideal

form. If these deviations are large, the surface is rough; if they are small the surface is smooth. Roughness is typically considered to be the high frequency, short wavelength component of a measured surface [1].

Roughness plays an important role in determining how a real object will interact with its environment. Rough surfaces usually wear more quickly and have higher coefficients of friction than smooth surfaces. Roughness is often a good predictor of the performance of a mechanical component, since irregularities in the surface may form nucleation sites for cracks or corrosion.

Although roughness is usually undesirable, it is difficult and expensive to control during manufacturing. Decreasing the roughness of a surface will usually increase manufacturing costs exponentially, which often results in a trade off between the cost of manufacturing a component and its actual application.

A roughness value can either be calculated on a profile or on a surface. The profile roughness parameter (R_a, R_q …) are more common. The area roughness parameters (S_a, S_q...) give more significant values [1].

1.1.2 Types of surface roughness

1.1.2.1 Profile roughness parameters

Each of the roughness parameters is calculated using a formula to describe the surface. There are many different roughness parameters in use but R_a (Arithmetic average surface roughness) is by far the most common. Other common parameters include R_z (Average distance between the highest peak and lowest valley in each sampling length), R_q (Root mean squared roughness), and R_{sk} (skewness roughness). Some parameters are only used in certain industries or within certain countries. For example the R_k family of parameters is used mainly for the linings of cylinder bores, while the important parameters are primarily used within France.

Since these parameters reduce all of the information in a profile to a single number, great care must be taken in applying and interpreting them. Small changes in how the raw profile data is filtered, how the mean line is calculated, and the physics of the measurement, can significantly affect the calculated parameters.

By convention every 2D roughness parameter is a capital *R* followed by additional characters in the subscript. The subscript identifies the formula that is used and the *R* means that the formula is applied to a 2D roughness profile. Different capital letters imply that the formulas are applied to different profiles. For example, R_a is the arithmetic average of the roughness profile, P_a is the arithmetic average of the unfiltered raw profile, and S_a is the arithmetic average of 3D roughness.

Each of the formulas listed in Tables 1 and 2 assumes that the roughness profile has been filtered from the raw profile data, and the mean line has been calculated. The roughness profile contains *n* ordered, equally spaced points along the trace, and y_i is the vertical distance from the mean line to the *ith* data point. Height is assumed to be positive in the up direction, away from the bulk material.

1.1.2.2 Amplitude parameters

Amplitude parameters characterise surface roughness based on the vertical deviations of the roughness profile from the mean line. Many of them are closely related to the parameters found in statistics for characterising samples of population. For example, R_a is the arithmetic average of the absolute values and R_t is the range of the collected roughness data points.

The average roughness R_a is expressed in units of height. In the English system, R_a is typically expressed in “millionths” of an inch, and is also referred to as "micro-inches" or sometimes just as “micro”.

The amplitude parameters are by far the most common surface roughness parameters found in the United States on mechanical engineering drawings and in the technical literature. Part of the reason for their popularity is that they are straightforward to calculate using a computer.

Table 1.1 Amplitude parameters

Parameter	Description	Formula
R_a [2], R_{aa}, R_{yni}	Arithmetic average of absolute values	$R_a = \frac{1}{n}\sum_{i=1}^{n}\lvert y_i\rvert$ [2]
R_q, R_{RMS} [2]	Root mean squared	$R_q = \sqrt{\frac{1}{n}\sum_{i=1}^{n} y_i^2}$ [2]
R_v	Maximum valley depth	R_v = Mini(y_i)
R_p	Maximum peak height	R_p = Maxi(y_i)
R_t	Maximum Height of the Profile	$R_t = R_p - R_v$
R_{sk}	Skewness	$R_{sk} = \frac{1}{nR_q^3}\sum_{i=1}^{n} y_i^3$
R_{ku}	Kurtosis	$R_{ku} = \frac{1}{nR_q^4}\sum_{i=1}^{n} y_i^4$
R_{zDIN}, R_{tm}	Average distance between the highest peak and lowest valley in each sampling length, ASME Y14.36M-1996 Surface Texture Symbols	$R_{zDIN} = \frac{1}{s}\sum_{i=1}^{s} R_{ti}$, where s is the number of sampling lengths, and R_{ti} is R_t for the *ith* sampling length.
R_{zJIS}	Japanese Industrial Standard for R_z, based on the five highest peaks and lowest valleys over the entire sampling length	$R_{zJIS} = \frac{1}{5}\sum_{i=1}^{5} R_{pi} - R_{vi}$, where R_{pi}, R_{vi} are the *ith* highest peak, and lowest valley respectively.

1.1.2.3 Slope, spacing, and counting parameters

Slope parameters describe the characteristics of the slope of the surface roughness profile. Spacing and counting parameters describe how often the profile crosses certain thresholds. These parameters are often used to describe repetitive roughness profiles, such as those produced by turning on a lathe [3].

Table 1.2 Amplitude parameters

Parameter	Description	Formula
R_{dq}	The RMS slope of the profile within the sampling length	$R_{dq} = \sqrt{\frac{1}{N}\sum_{i=1}^{N}\Delta_i^2}$
R_{da}	The average absolute slope of the profile within the sampling length	$R_{da} = \frac{1}{N}\sum_{i=1}^{N}\lvert\Delta_i\rvert$
Δi	Delta *i* is calculated according to ASME B46.1	$\Delta_i = \frac{1}{60dx}(y_{i+3} - 9y_{i+2} + 45y_{i+1} - 45y_{i-1} + 9y_{i-2} - y_{i-3})$

In this study, only the arithmetic average of absolute values R_a and root mean squared R_q are analysed.

1.2 Significance of this research

In plastically deformed polycrystalline metals, surface roughening is a commonly observed phenomenon. It originates not only from the metal forming process, but also plays an important role in properties such as abrasion, fatigue, magneto-electric property and forming property. As surface roughening is undesirable in practice, and seemingly unavoidable, many researchers and manufacturers seek to understand the factors affecting surface roughening in the metal manufacturing process. In general, there are two reasons why surface roughening appears, one is the internal factor, and

the other is the external factor. The internal factor includes the original surface roughness of the product, grain size, crystal structure and orientation, and the distribution of texture. The external factor refers to the loading path, the stress-strain state (deformation mode) and the surface of the tool [4], so surface roughness after deformation is the superposition of surface roughness resulting from two causes. This is why researchers and manufacturers try to find the relationship between these factors and surface roughness. Most research has focused on reducing surface roughening during deformation by decreasing the original surface roughness and maintaining a uniform heat treatment (uniform grain size). Therefore, there is a strong motivation to understand the mechanisms of surface roughening and the relationship between the two factors and surface roughness in metal manufacturing.

In practical metal forming processes, there are two types of surface roughness evolving, free surface evolution and constrained surface evolution. During plastic deformation, unconstrained metal surfaces tend to become rougher. There are many literatures about the evolution of unconstrained surfaces. Osakada and Oyane [5] found that surface roughness increases with strain, and it is greater for coarser grain materials and for metals with a small number of slip systems. Therefore, CPH (close-packed hexagonal) metals roughen the most, FCC (face-centred cubic) material less, and BCC (body-centred cubic) materials the least. Tokizawa and Yosikawa [6] further included the influence of two material phases on the roughening process. Chen et al. [7] found that grain rotation is the most important factor that determines surface roughening. Becker [8] established a model to address the influence of inhomogeneities in the deformation by suggesting that unconstrained deformation at the surface causes the grains to become displaced in the direction normal to the surface, and thereby increase the overall surface area. Stoudt and Ricker [9] carried out a tensile experiment with AA5052 alloy and demonstrated that the roughening rate ($dR_a/d\varepsilon_{pl}$) depends on the grain size, and pointed out that the surface roughening of a polycrystalline material is a high complex process that results from multiple deformation mechanisms. The evolution of unconstrained metal surfaces is a function of strain, grain size, and loading mode. The friction state and tool have no effect on the evolution of unconstrained metal surfaces.

On the other hand, industrial forming processes are characterised by large area contact between the workpiece and the tool, such as rolling, extrusion and compression. In this case, the surface evolution is called ‘‘contact based’’. Under pure contact loading conditions a reduction in surface roughness will take place. This is also called the “surface asperity flattening process”. Wilson et al. [10, 11] have investigated the effect of bulk plasticity on asperity flattening when the lay of the roughness is parallel to the bulk strain direction (longitudinal roughness). They found that the rate of asperity flattening with bulk strain was related to the spacing and pressure of asperities. Makinouchi et al. [12] used elastic-plastic finite element solutions for the case of transverse roughness. Wilson and Sheu [10] also found out that a large increase in the contact areas with bulk strain required a reduction in the load needed for bulk yielding. Sutcliffe [13] tested and developed Wilson and Sheu’s theories and pointed out that the high pressure between contact asperities and deformation of bulk material affects asperity deformation. Dieter [14] found that the inhomogeneous deformation mechanisms that generate surface roughening also initiate localised strains which induce necking, tearing, or wrinkling in the component during the metal forming process. Wilson [15] also points out that inhomogeneous deformation can accelerate die wear by increasing the friction and abrasion between the metal sheet and the faces of the die. Groche [16, 17] analysed the surface evolution caused by contact loading in a 2D-plane strain finite element (FEA) model, and established a correlation between the surface topology, grain size, and surface evolution.

Today, however, only a little knowledge is gained on the influence of the polycrystalline structure of a workpiece on contact based surface evolution (surface asperity flattening process). Owing to the influences of tool and reduction, friction between the workpiece and the tool is a complicated process. The coefficient of friction is not a constant, and it will vary according to the contact between the workpiece and the tool. This is a challenge for any researcher. Rate-dependent crystal plasticity constitutive theory depicts the quasi-static motion of metal manufacturing. In practice, deformation during the metal forming process is mostly dynamic so when the experiment was designed, some assumptions had to be given to reduce the calculation error. Currently, EBSD (Electron Back-Scattering Diffraction)

maps measured by FEG-SEM (Field Emission Gun Scanning Electron Microscope) are normally two dimensional. In a 2D model it is very convenient to use the experimental orientations in the crystal plasticity finite element model (CPFEM). However, in a 3D simulation, when the 2D EBSD experimental results are put into the model, some assumptions regarding the uniform distribution of grain orientation must be made for the simulation.

This study will focus on the evolution of constrained metal surface (surface asperity flattening). As a common deformation mode, uniaxial planar compression has been selected as the main deformation mode. To understand the relationship between surface roughness and technical parameters (reduction, friction, grain size, texture, grain orientation, original surface roughness and tool), a subroutine of rate-dependent crystal plasticity constitutive model has been generated and then used in the surface asperity flattening model to simulate the constrained surface evolution in the uniaxial planar compression. The methods of research can be classified as experimental and Finite Element Method (FEM) modelling, where a constitutive model has been used in the FEM simulation. Due to the complexity of the process, many assumptions for constitutive equations have been made to obtain the solutions.

1.3 Research objectives

As mentioned above, there have been difficulties with studies concerning surface roughness (surface asperity flattening), with the most problematic ones being in the area of constraint deformation (influence of a tool). The objective of this research is to understand the mechanism of surface roughness in the constraint deformation, and then study the relationship between the surface roughness and technical parameters such as reduction, friction, grain size, texture (grain orientation), and strain rate. On the basis of results, the parameters will be optimised to improve the surface quality of products during cold rolling (uniaxial planar compression is similar to cold rolling). On the other hand, suggestions will be brought forward to help in designing the parameters of the cold rolling process. This overall objective will be realised by pursuing the following objectives:

(1) To determine how the deformation parameters (reduction etc.) affect surface roughness;
(2) To determine how friction affects surface roughness;
(3) To determine how the grain size of the sample affects the development of surface roughness;
(4) To determine how the texture (grain orientation) affects the evolution of surface roughness;
(5) To develop computational models for surface asperity flattening by crystal plasticity finite element models (CPFEM) (2D and 3D);
(6) To simulate the influence of parameters (reduction, friction, texture, grain size, strain rate) on surface roughness during surface asperity flattening by the CPFEM model.
(7) To investigate the mechanism of surface asperity flattening, and
(8) To analyse the mechanics of surface asperity flattening during cold strip rolling.

1.4 Research methodology

The research methods used in this investigation can be described as experimental and numerical modelling where mathematical modelling is an extremely important tool. Owing to the complexity of this process, many mathematical models were needed to simplify the simulation process before solutions could be obtained. With the aid of a digital computer and finite element software (ABAQUS), and rate-dependent crystal plasticity constitutive theory, a complicated simulation of the surface asperity flattening process that considers many factors can be carried out efficiently.

Research of surface roughness faces three challenges, the relationship between the internal factors (strain localised surface texture) and surface roughness, the influence of external factors (reduction, friction and tool), and a suitable roughness model that considers all the internal and external factors. The mechanical parameters are important since they are related to the deformation parameters, microstructures, and strains (plastic slips), and therefore during cold compressing, they must be investigated simultaneously. In this study, the deformation parameters, microstructures, and textures have been analysed, as shown in Figure 1.2. There are

two factors in the cold uniaxial planar compressing process which contribute to the development of surface roughness: the first are external factors such as reduction, friction, tool, and original surface roughness, and the second are internal factors that include texture, grain size, grain orientation, microstructure, and hardness. It is therefore important to develop a predictive rule for the development of surface roughness of aluminium during cold uniaxial planar compression (cold rolling).

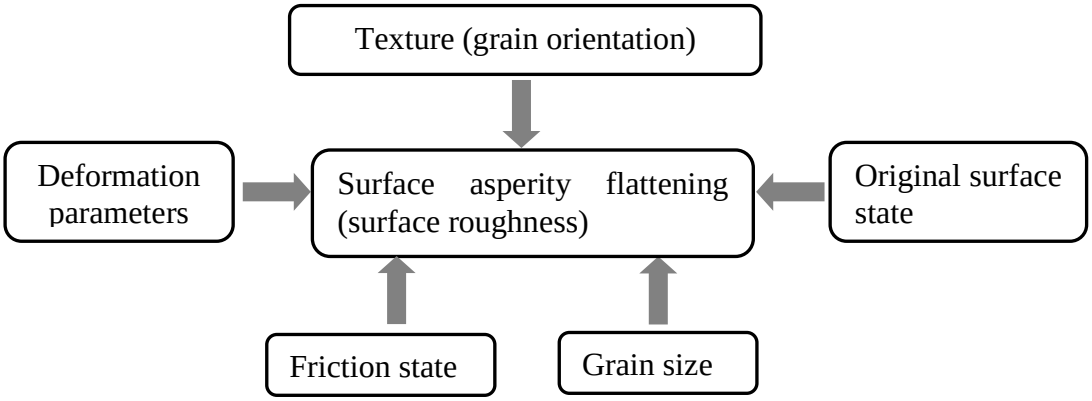

Figure 1.2 Experimental research schedule

In order to develop a predictive model for the development of surface roughness, experiment and crystal plasticity finite element modelling both are used in this study. On the basis of experiments, the relationship between surface roughness (surface asperity flattening), deformation parameters and surface texture are generalised. By using the code from a rated-dependent constitutive model in the commercial finite element software ABAQUS, 2D and 3D models have been established on the basis of the experimental conditions. After the simulation and experiments, the experimental results have been compared with the simulation results, which will verify and validate the proposed model.

1.5 Outline of the thesis

This thesis consists of eight chapters and a bibliography of cited references. The contents of each chapter are as listed below. In this chapter, a background of the surface quality of cold metal manufacturing products and a definition of surface roughness are introduced, and the significance of this study is discussed. The objectives of this thesis are given and the research methodology is also proposed.

Chapter two reviews previous research that is relevant to the current study. It includes common surface defects and reasons. Previous experimental research has focussed on the following factors which contribute to surface roughening, such as deformation parameters (reduction, strain, etc.), grain orientation (texture), grain size, microstructure (different metals), and the original state of the surface. Computer simulation research of surface roughness is also introduced in this chapter. It includes the upper bound method, artificial neural network method and self-affine method.

Chapter three introduces the generation and development of crystal plasticity theory. Two main crystal plasticity theories (rate-independent crystal plasticity constitutive theory and rate-dependent crystal plasticity constitutive theory) are also given in this chapter. The application and methodology of rate-dependent crystal plasticity constitutive theory are also investigated in this study. Some details of this study are included in this chapter, such as the simplification of rate-dependent crystal plasticity constitutive theory, the numerical integration of rate dependent crystal plasticity theory (Updated Lagrange Formulation, Total Lagrange Formulation), the calculation of grain orientation, and the generation and application of UMAT of rate-dependent crystal constitutive in software ABAQUS.

Chapter four introduces the specimen material, experiments, and equipment used in this study. The experiments include uniaxial planar compression, an annealing experiment, hardness testing, surface roughness measuring (two and three dimensions), and a friction and EBSD experiment. The experimental equipment includes the compressing device which has been designed and manufactured, an INSTRON material testing machine, a two dimensional profile meter, AFM (Atomic Force microscope), a three dimensional profile meter, a Vickers hardness tester, a cutting machine, a polishing and grinding machine, an annealing furnace, and an FEG-SEM. In this chapter, some software is used to analyse the experimental results, for example, Channel 5 software which is from the HKL Company, and pole figure drawing software (PFplot).

Chapter five shows the research results of two dimensional crystal plasticity finite element modelling of FCC (aluminium). The surface asperity flattening process has been analysed by the experiment and simulation. The experimental and simulation results showed a good agreement. Some factors (gauged reduction, friction state, wave length, grain size and orientation) which affected the surface asperity flattening process have been analysed. Relationships between the surface asperity flattening (surface roughness) and the parameters have been established. A fully finite element polycrystal model has been used and discussed in this study.

Chapter six introduces the 3D crystal plasticity finite element model which was established on the basis of experimental results. 3D sample surface topology measured with the 3D profile meter was recalculated in the MATLAB and then imported into the 3D crystal plasticity finite element model. The experimental grain orientations have also been used in the 3D model with the assumptions of a uniformly distributed grain orientation. The experimental and simulation results are in good agreement. During the surface asperity flattening process, localised surface strain has been analysed by the experimental and simulation results. The influence of the strain rate on the surface asperity flattening has also been analysed. In the surface asperity flattening process, the surface feature (surface roughness) shows an obvious sensitivity to its orientation. In this study, orientation [111] is the sensitive orientation. The influence of texture on surface roughness is also given.

Chapter seven explains the surface asperity flattening behaviour in uniaxial planar compression on the basis of microtexture evolution. The dependency of the surface asperity feature on the surface (ND) microtexture development is given. Contributions of dislocation accumulation and mobility to the surface asperity are investigated. Recovery and recrystallisation under deformation are taken into account. Influences of in-grain and transgranular shear bands are also analysed.

Chapter eight gives the conclusions and recommendations for future work. This chapter includes conclusions, and the effects of lubrication, reduction, grain size, grain orientation, texture, and strain rate that are recommended for future work. A crystal plasticity analysis of surface asperity flattening of BCC (steel) in the cold

rolling process is also recommended for future study and experimental investigation. High temperature deformation and 3D EBSD mapping with FIB (Focus Ion Beam) technique are also recommended for future work.

CHAPTER 2

LITERATURE REVIEW AND SCOPE OF WORK

In this chapter, a detailed analysis of selected aspects of the extensive literatures concerned with surface roughening in metal manufacturing will be presented to assess the mechanisms involved and important factors which contribute to this process. This chapter begins with the mechanics of surface roughening in metal forming which uses the upper bound method with two models (a velocity field with shear discontinuities and a field with no discontinuities). The second part introduces the friction in metal forming, especially its effect on the coefficient of friction in the real contact area (surface roughness), using models of sliding friction and sticking friction. The third part gives a detailed introduction to the surface defects that are developed in metal forming, including intrinsic surface defects and grain-scale surface defects. The fourth part focuses on the research about surface roughening such as experimental research and simulation. The last part concludes the literature review and research scope in the present study.

2.1 Surface roughening in metal forming

In plastically deformed polycrystalline metals, surface roughening is a commonly observed phenomenon. Surface roughening can be divided into two fundamental types, surface roughening of a free surface and surface roughening of the contact (or lubricated) surface.

2.1.1 Roughening of a free surface

When deformation parts of the surface of a workpiece deform without making contact with a tool or die, the free surface roughens in a mode that is qualitatively and quantitatively similar to that observed on the lubricated surface of a deforming specimen is, therefore, of basic interest. Roughening depends on the mode of deformation (Figure 2.1) [18-20]:

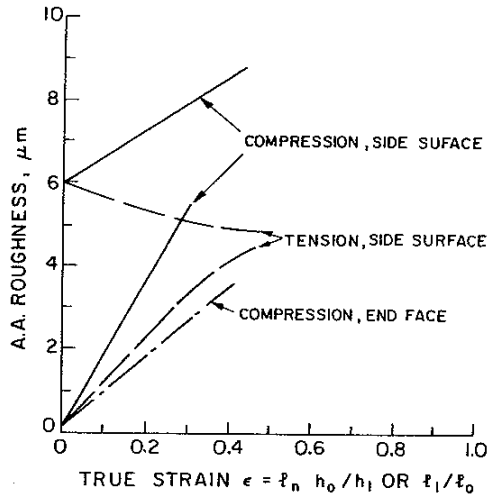

Figure 2.1 Change in roughness of surfaces with deformation [21]

(1) On a workpiece subjected to tension (stretching), initially smooth surfaces (those with R_a=0.1 μm, for example) become rougher, but an initially rough surface (e.g., R_a=0.6 μm) becomes somewhat smoother because the surface features are stretched out [22].

(2) In upsetting a cylinder, the free surface roughens irrespective of its initial roughness because the surface features are pushed closer together and become deeper [20].

(3) In some processes a combination of extension and compression may occur. For instance, during sheet bending the outer surface stretches while the inner surface is

compressed.

2.1.2 Roughening of a constrained surface

In practise, metal forming is a very complicated process since most deformed surfaces are the constrained surfaces which are affected by factors such as the initial roughness of the workpiece or die, the state of lubrication, and so on. The development of workpiece roughness is influenced by a combination of initial roughness, die roughness, and lubrication. This relationship, and the lubrication mechanism, is shown in Figure 2.2.

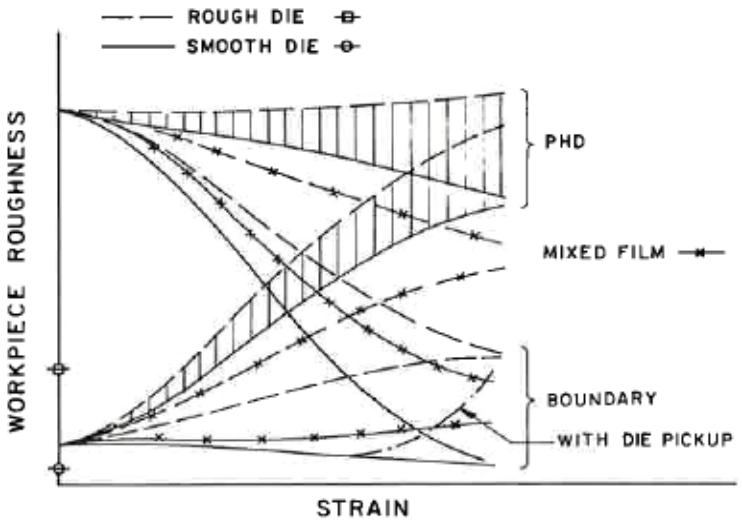

Figure 2.2 Effects of workpiece and die surface roughness on developing roughness with various lubrication mechanisms [22]

With full fluid or solid film lubrication the final finish on a workpiece depends on its roughness and the lubricant used. In a mixed film regime some of the surface features of the die are reproduced on the workpiece, but hydrostatic pockets scattered on the surface make the product rougher than the die. If, however, the valleys in the die become filled with wear products the surface of the workpiece becomes smoother. In a boundary lubricated regime, the surface finish of the die is faithfully reproduced on normal contact and reproduced but modified by sliding during sliding contact.

When the film of lubrication breaks down, the resulting asperity contact, deformation, and smearing, leads to greater roughness, particularly when the surface of the die is rough.

2.2 Mechanics of surface roughening in metal forming

Wilson [11] analysed the mechanics of surface roughening in metal forming. He used some ideas of the mechanics in the upper bound method while considering the interaction between grains with different shear strengths or hardness. He developed two models: one used a velocity field with shear discontinuities, and the other used a field with no discontinuities.

The geometry for the upper bound model is shown in Figure 2.3. Plane strain conditions are assumed with no deformation normal to the plane of the figure. The control volume has a width l_m and a depth b_m. The planes A_m-$A_m{}'$ and B_m-$B_m{}'$ are planes of symmetry which remain plane while the surface is being stretched.

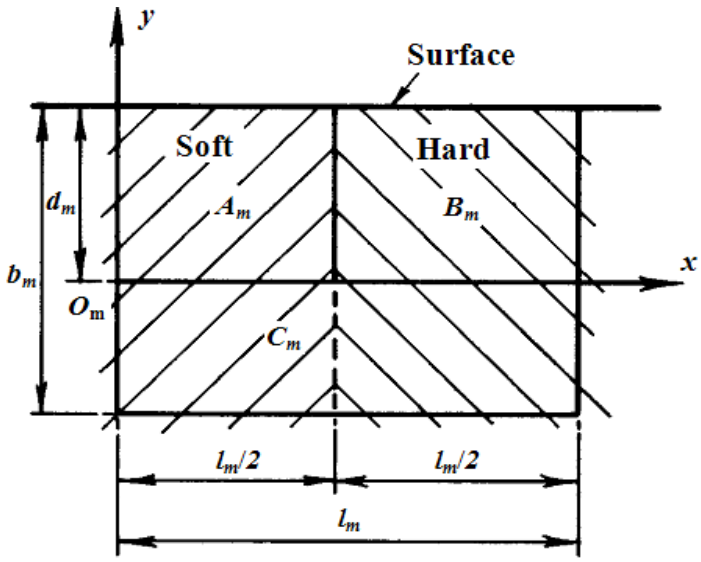

Figure 2.3 Geometry for the upper bound model [11]

The control volume is divided into three regions; regions A_m and B_m each have a width l_m /2 and extend to an arbitrary "disturbance" depth d_m (less than) from the surface. The strains which cause roughening are restricted to A_m and B_m. Below this, in the region C_m, the strain system reverts to uniform plane strain stretching with a strain rate. The material in region A_m, and that part of C_m that is below the region A_m, is assumed to have a shear strength k_m, while that in region B_m, and that part of C_m below region B_m, is assumed to have a shear strength H_{km}. The parameter H_m is called the hardness ratio and is a measure of the inhomogeneity in the material.

The upper bound method uses a kinematically admissible velocity field which must satisfy local incompressibility. Since there is no strain in the z direction, this condition may be written as:

$$\frac{\partial v_x}{\partial x} + \frac{\partial v_y}{\partial y} = 0 \tag{2.1}$$

where v_x and v_x are the velocity components in the x and y directions respectively. To avoid discontinuities, the field in A and B must also satisfy

$$v_x = 0 \text{ along } x = 0 \tag{2.2}$$

$$v_x = \dot{\varepsilon} l_m \quad \text{at } x = l_m \tag{2.3}$$

and

$$v_x = \dot{\varepsilon} x \quad \text{at } y = 0 \tag{2.4}$$

For convenience, it will also be assumed that

$$v_y = 0 \text{ along } y = 0 \tag{2.5}$$

A convenient form for the horizontal velocity component which satisfies Equations (2.2)-(2.4) is

$$v_x = \dot{\varepsilon} x + c(l_m - x)xy \tag{2.6}$$

This is differentiated and substituted into Equation (2.1) and the result is then integrated, subject to Equation (2.5), to obtain the compatible vertical component

$$v_y = c_m(x - l_m/2)y^2 + \dot{\varepsilon} y \tag{2.7}$$

Figure 2.4 shows the distributions of the *x* and *y* velocity components. These are determined from Equations (2.5) and (2.6) in regions *A* and *B*. Uniform strain is assumed in region *C*.

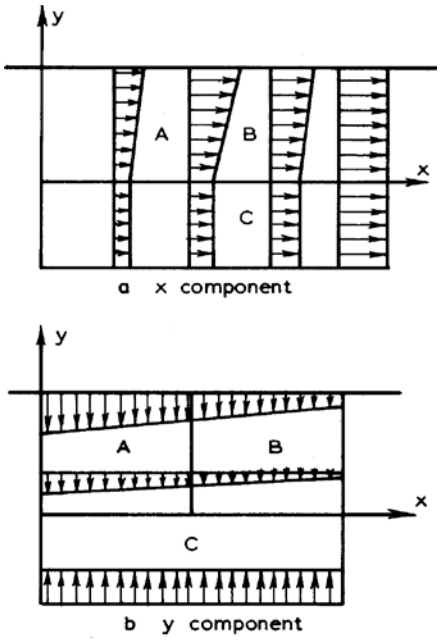

Figure 2.4 Assumed velocity field [11]

The various strain rate components in *A* and *B* may be obtained by differentiation as

$$\dot{\varepsilon}_x = \dot{\varepsilon} + c(1 - 2x)y \tag{2.8}$$

$$\dot{\varepsilon}_x = -\dot{\varepsilon} - c(1 - 2x)y \tag{2.9}$$

and

$$\dot{\varepsilon}_{xy} = c[y^2 + x(l-x)]/2 \tag{2.10}$$

Note that the strain rates depart from the uniform state by an amount that is determined by the arbitrary parameter *c*.

It is convenient to continue the analysis using non-dimensional variables X_m^*, Y_m^*, B_m^*, C_m^* and D_m^* defined by

$$X_m^* = x/l_m,\ Y_m^* = y/l_m,\ B_m^* = b_m/l_m,\ C_m^* = c_m l_m{}^2/\dot{\varepsilon},\ D_m^* = d_m/l_m \tag{2.11}$$

X_m^* and Y_m^* are non-dimensional coordinates, C_m^* is a non-dimensionalised roughening parameter that characterises surface roughening and D_m^* is the non-dimensional roughening depth. The strain rates may be non-dimensionalised by dividing by $\dot{\varepsilon}$, so that

$$E_x^* = \dot{\varepsilon}_x/\dot{\varepsilon} \tag{2.12}$$

Using these non-dimensional variables, Equations (2.8) - (2.10) become

$$E_x^* = 1 + C_m^*(1-2X_m^*)Y_m^* \tag{2.13}$$

$$E_y^* = -1 - C_m^*(1-2X_m^*)Y_m^* \tag{2.14}$$

$$E_{xy}^* = C_m^*[Y_m^{*2} + X_m^*(1-X_m^*)]/2 \tag{2.15}$$

The non-dimensional power P^* is defined by

$$P_m^* = P_m/k_m\dot{\varepsilon}b_m l_m \tag{2.16}$$

where P_m is the power dissipated per unit depth by plastic deformation in the control volume. P_m^* can be obtained from the non-dimensional strain rates by integration as

$$P_m^* = \sqrt{2}\int_{D_m^*-B_m^*}^{D^*}\int_0^{1_m/2}\sqrt{E_{ij}^{*2}}\,dY_m^* dX_m^* + H_m^*\sqrt{2}\int_{D_m^*-B_m^*}^{D_m^*}\int_{1_m/2}^{1_m}\sqrt{E_{ij}^{*2}}\,dY_m^* dX_m^* \qquad (2.17)$$

According to the upper bound method, the values of C_m^* and D_m^* are those which minimise P_m^*. B_m^* must be larger than D_m^*. Thus C_m^* and D_m^* can be obtained as a function of H_m^*. Figure 2.5 shows the non-dimensional roughening parameter C_m^* and disturbance depth D_m^* as functions of the hardness ratio H_m^*. Both C_m^* and D_m^* increase monotonically with H_m^*. The variations of C_m^* and D_m^* with H_m^* can be approximated by

$$C_m^* = -3.981 + 7.533H_m^* - 4.776H_m^{*2} + 1.372H_m^{*3} - 0.149H_m^{*4} \qquad (2.18)$$

and

$$D_m^* = 0.85 + 0.15H_m^* \qquad (2.19)$$

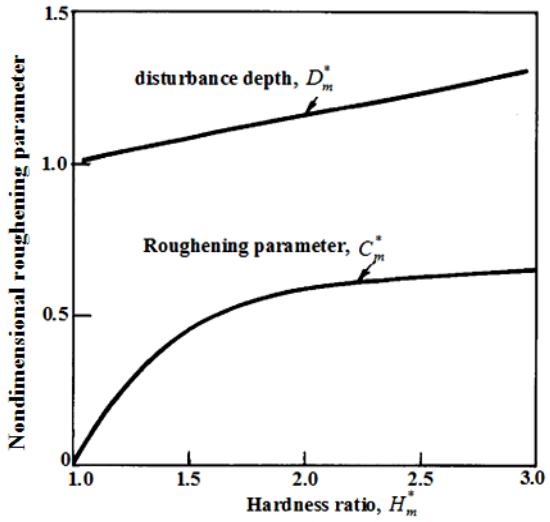

Figure 2.5 Results of upper bound analysis [11]

It is assumed that the roughening is small compared with the length l_m, so the geometry does not change much. Since the variation in velocity is linear, so is the variation in surface height, and a saw toothed profile result. The arithmetic mean roughness value R_a, which will be used for comparison purposes, may be calculated as [11]

$$R_a = (-0.276 + 0.352H_m^* - 0.059H_m^{*2})l_m\varepsilon \tag{2.20}$$

2.3 Friction of metal forming

Friction is the force resisting the relative motion of solid surfaces, fluid layers, and/or material elements sliding against each other. There are several types of friction: dry friction, fluid friction, lubrication friction, skin friction, internal friction, and other types of friction [23]. In this chapter the two most common types are introduced in the work.

2.3.1 Coefficient of friction

In metalworking there are two common types of friction between the die (or tool) and the workpiece. One is sliding friction and the other is the sticking friction [24], as shown in Figure 2.6.

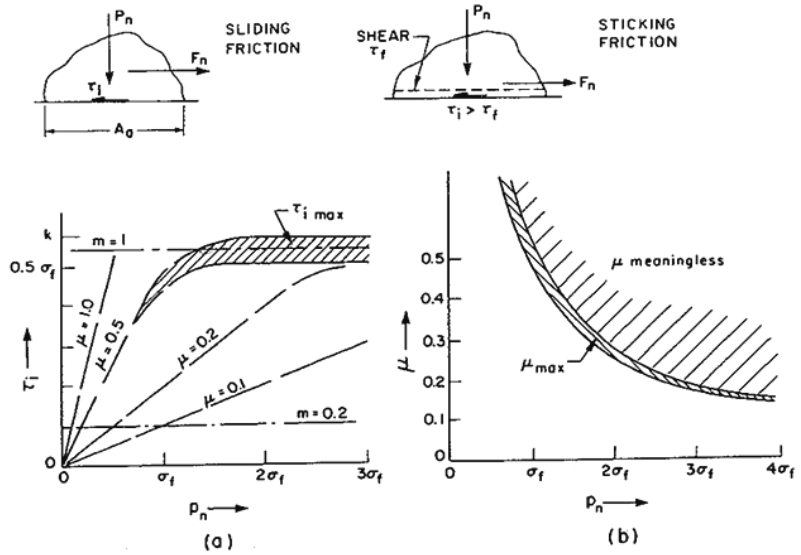

Figure 2.6 Shear stress (a) and maximum coefficient of friction (b) in sliding at various interface pressures [24]

2.3.1.1 Sliding friction

Sliding friction can be defined as

$$\mu = \frac{F_n}{P_n} = \frac{\tau_i}{p_n} \tag{2.21}$$

where F_n is the force required to move the body, P_n is the normal force, τ_i is the average frictional shear stress, and p_n is the normal pressure. Both τ_i and p_n are obtained by dividing the forces by the apparent area of contact A_a between the two bodies (Figure 2.6a). This definition embodies Amonton's two basic laws of friction: the frictional force is proportional to the normal force, and it is independent of the size of the apparent contact area. For the constant μ, the interface shear stress τ_i must increase at the same rate as the interface pressure p_n. It is usual to call Coulomb's friction when this condition is satisfied (broken line in Figure 2.6a).

2.3.1.2 Sticking friction

When τ_i reaches the value of k_f, the material has a further option, instead of sliding against the surface of the die, less energy is required for the material to shear inside the body of the workpiece, while the surface remains immobile (Figure 2.6b). This is described as sticking friction, although no actual sticking to the surface of the die needs to take place. From Equation (2.21), the condition of sticking is

$$\tau_i = \mu p_n > k_f \tag{2.22}$$

Since $k_f = 0.577\sigma_f$ (σ_f is the uniaxial flow stress of the material) according to von Mises stress, it is sometimes called that $\mu_{max} = 0.577$, but this is only true when the full surface conformity reaches at $p_n = \sigma_f$.

2.3.2 Interface shear factor

Owing to the difficulties with μ, Equation (2.22) can be described by

$$\tau_i = m_i k_f \tag{2.23}$$

where m_i is the interface frictional shear factor, which has a value $m_i = 0$ for a frictional interface and $m_i = 1$ for sticking friction. This has a mathematical convenience because τ_i is now defined with the aid of k_f, the value of which is known from the outset. Furthermore, the practice of regarding k_f as a known and well defined property is oversimplified; as pointed out by Shaw [25], severe working associated with interface sliding substantially changes the properties of the near surface layer, making calculations of m on the basis of bulk properties unreliable.

2.3.3 Definition of the coefficient of friction by the real contact area

2.3.3.1 Surface contact

In reality, there are two kinds of surface asperity interactions (as shown in Figure 2.7): asperity may also be encountered during sliding and then plastic deformation of the softer (workpiece) asperity will occur (Figure 2.7a) [26]. A large asperity on the surface of the die (this would develop when cold welding leads to pickup) plows through the workpiece (Figure 2.7b) and contributes to the frictional force [27].

Figure 2.7 Asperity encounters [26, 27]

(a) Coefficient of slide friction

During metal forming the most important thing is where sliding is superimposed onto normal contact [28-34]. The contact between the die and rough workpiece with plastic deformation of the asperities is shown in Figure 2.8. Assuming that the surface of the workpiece consists of identical wedge shaped asperities which are deformed by contact with the surface of a flat tool, based on the slip line field, Wanheim and Bay [28] showed that the real contact area (expressed as a fraction of the apparent contact area $c=A_r/A_a$) depends on both the pressure at the interface and shear strength in the real contact zone m_c. The average frictional stress over the entire apparent area of contact is

$$\tau_i = m_c c k_f \tag{2.24}$$

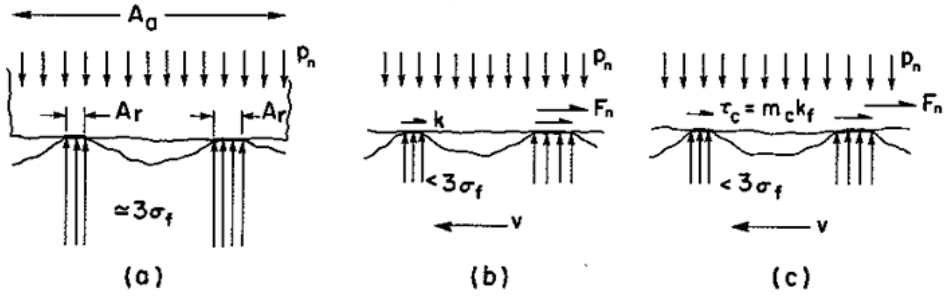

Figure 2.8 Contact between die and rough workpiece with plastic deformation of asperities: (a) with load P_n; (b) with load P_n and shear strength k; (c) with a contaminant layer of shear strength τ_c [28]

So the sliding coefficient of friction can be expressed as

$$\mu = \frac{\tau_i}{p_n} = \frac{m_c c k_f}{p_n} \tag{2.25}$$

where there is a solid film of lubricant, the interface looks similar to that in dry friction except that a film of contaminant is now intentionally introduced. It may act simply as a separating or parting agent, preventing metal-to-metal contact, or it may also possess low shear strength. Sliding is assumed to take place by shear at a stress τ_s. If there is a full conformity between the surfaces of the die and workpiece (Figure 2.9), the interface can be described by the coefficient of friction [35, 36]:

$$\mu = \frac{\tau_s}{p_n} \tag{2.26}$$

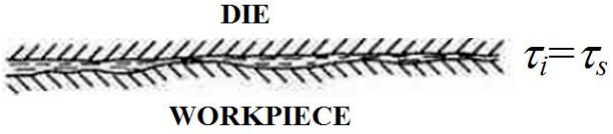

Figure 2.9 Solid lubricated interface [35, 36]

(b) Coefficient of sticking friction

In practical plastic deformation, the surfaces of many dies (before deformation, it is assumed to be flat) are intentionally or through wear, roughened to a point where they can no longer be considered flat. Then asperities of the harder die material encounter and plastically deform the asperities of the workpiece, giving a rise to friction, penetration of the surface contact film, and possibly adhesion and wear. Experimentally it is often found that friction increases with the surface roughness [37], at least under conditions of low adhesion. The probability is very slim indeed that any surface contact film would survive intact to the severe contacts that exist in metalworking. Thus, the surface film is damaged at least in some places (Figure 2.10), and then a higher shear strength (or m_c value) applies locally over a fraction of A_a. If the workpiece tends to adhere to the die, the local shear stress at this "strong junction" reaches k_f. The average shear stress τ_i taken over the whole contact area is then

$$\tau_i = ak_f + cm_c k_f = (a + cm_c)k_f \tag{2.27}$$

where $a = (K / k_f)^2$ for a three dimensional junction and is taken to be around 9 from experimental evidence. Previous research [38] found it ranges from 4 for brass to 20 for mild steel.

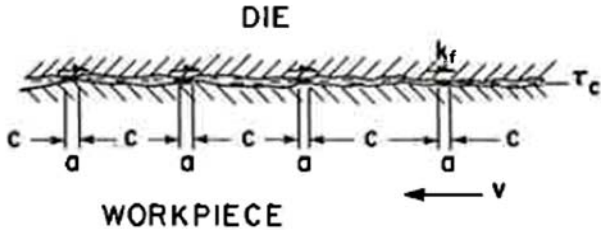

Figure 2.10 Fully conforming dry interface, with metallic contact (a) and contaminant films (c) [38]

2.3.4 Variable friction

Because interface pressures, sliding velocities, temperatures, and other conditions affecting the behaviour of lubricant tend to vary within the contact zone of the die/workpiece, it is to be expected that μ, m_i (m_c) and c should also vary. An exact description of the interface can then be made only with the local value of τ_i although, for convenience the average μ, m_i (m_c) and c are most often assumed in calculations. This is permissible for force calculations, but can lead to errors when calculating the distribution of strain (localised variations of deformation within the body) [39].

2.4 Surface defects during metal forming

Two kinds of surface defects occur during metal forming [4]: one is intrinsic defects and the other is grain-scale defects.

2.4.1 Intrinsic surface defects during plastic straining

Plastic straining of polycrystalline metals is accompanied by the gradual development of microstructural surface defects. It is useful in this context to differentiate between intrinsic and extrinsic defects since with intrinsic ones we denote all changes to the surface that occur in the form of net residual inhomogeneous surface displacement fields result from microstructure dynamics during plastic straining. It is typical of such surface defects that they occur likewise in the bulk material. In other words any microstructure phenomenon which gives a rise to a heterogeneous displacement inside the bulk material upon plastic straining can find its equivalent in a surface defect (e.g. glide steps, shear bands, hard and soft grains). With extrinsic surface defects we denote all changes to the surface that occur through mechanical contact (forming tools, friction, non-homogeneity of forces and material flows) or by corrosion. These latter effects are not necessarily connected to

characteristic microstructure mechanisms which appear likewise in the bulk material.

Intrinsic surface defects occur at different spatial scales and can have different origins, similar to the corresponding hierarchy of heterogeneous displacement fields caused by lattice defects in the bulk material during plastic straining. Figure 2.11 and Table 2.1 show some examples of surface displacements in hierarchical order, including surface defects generated by elastic distortions, (a) point defects, (b) atomic slip steps caused by single dislocations leaving the bulk, (c) larger crystallographic slip steps created by sets of collectively gliding dislocations on parallel or identical glide planes, (d) surface twins or athermal stress-induced transformation phenomena such as martensite, (e) non-crystallographic glide traces caused by dislocation bands which contain localised and collective slip activity on parallel and non-parallel glide systems, (f) surface cracks, (g) orange peel phenomena where crystals at the surface undergo individual out-of-plane displacements, (h) individual surface deformation by hard and soft phases (e.g. hard precipitates in a soft matrix), (i) as well as ridging and roping phenomena characterised by the collective deformation of larger sets of similarly oriented grains typically resulting in a banded surface topology. Orange peel and ridging phenomena will be addressed in detail. Depending on the material and boundary conditions, various types of surface defects can occur at the same time during plastic straining, but elasticity is involved in all cases. From a microstructural standpoint it makes sense to sort the different mechanisms and effects listed above, into three basic groups of intrinsic surface defects according to whether they are predominantly governed by point effects, dislocations, or interfaces, similar to plastically strained bulk material.

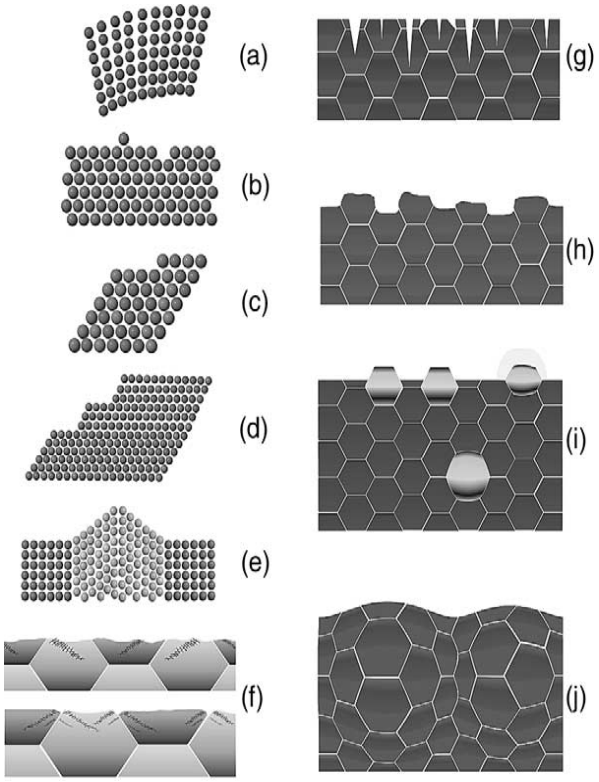

Figure 2.11 Some examples of surface defects in hierarchical spatial order (also see Table 2.1). (a) Elastic distortion; (b) point defects; (c) atomic surface steps caused by single dislocations; (d) larger crystallographic slip steps created by sets of collectively gliding dislocations on parallel or identical glide planes; (e) surface twins or athermal stress induced transformation phenomena such as martensite; (f) non-crystallographic glide traces caused by dislocation bands which contain localised and collective slip activity on parallel and non-parallel glide systems; (g) surface cracks; (h) orange peel phenomena where crystals at the surface undergo individual out-of-plane displacements; (i) individual surface deformation by hard and soft phases (e.g. hard precipitates in a soft matrix); (j) ridging and roping phenomena, which are characterised by the collective deformation of larger sets of grains typically resulting in a banded surface topology [4].

Table 2.1 Hierarchy of surface defects generated during elastic-plastic deformation [4]

Surface phenomenon	Underlying mechanisms
Elastic distortions	Local stress state and Hooke's law
Point defects	Diffusion, mechanics
Creep pores and hills	Diffusion, mechanics, creep
Atomic slip steps	Dislocation penetrating the surface
Larger crystallographic slip steps	Dislocation bands consisting of sets of collectively gliding dislocations on parallel or identical glide planes
Surface twins	Stress-induced orientation dependent twin formation
Athermal transformation phenomena	Stress-induced orientation dependent phase transformations (e.g. martensite)
Non-crystallographic glide traces	Dislocation bands which contain localized and collectively slip activity on parallel and non-parallel glide systems; often related to macroscopic strains
Cracks	Fracture mechanics
Orange peel	Different crystals produce individual out-of-plane grain-scale surface displacements due to their different orientation factors and resulting shape changes
Surface co-deformation of hard and soft phases	Hard and soft matter assembled in one microstructure
Ridging and roping	Collective deformation of larger sets of grains typically resulting in a banded surface topology

2.4.2 Grain-scale surface defects during plastic straining

Grain-scale roughening in homophase alloys can be grouped into orange peel and banding phenomena. The former is characterised by out-of-plane displacement fields

(negative or positive), which roughly map the grain shape of the material. The latter is commonly referred to as ridging or roping phenomena. They occur in the form of banded surface undulations which typically extend along the rolling direction of the material, and have a transverse extension above the grain size (Figure 2.12).

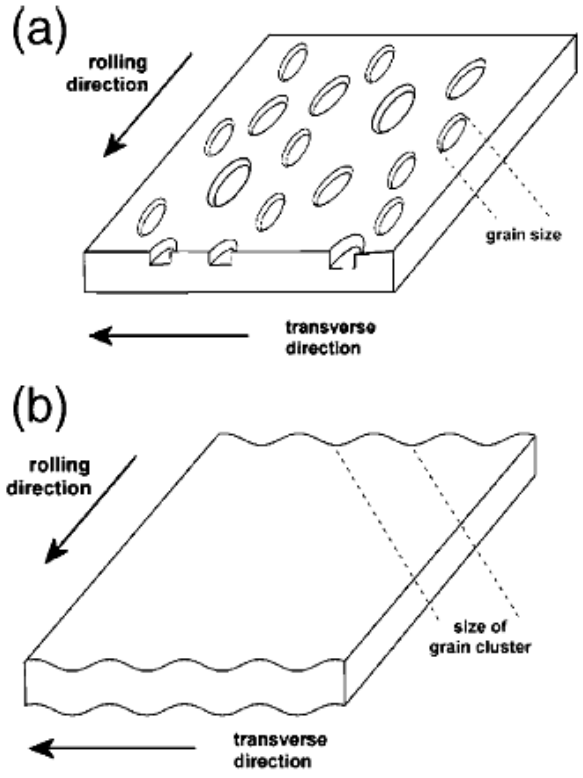

Figure 2.12 Grain-scale roughening in homophase alloys occurs in the form of orange peel and banding phenomena [4]

Typical macro surface roughening phenomena are shown in Figure 2.13, and can be divided into three types. The first is riding which often occurs along the transverse direction during tensile deformation in the rolling direction. The second is ribbing which occurs along the direction of thickness. The top and bottom are symmetric along the thickness plane. It can appear during the tensile deformation of aluminium (AA3002) along the transverse direction [40]. The third one is grooving or directional roughening. Baczynski et al. [41] observed this kind of surface roughening during the tensile deformation of 6111 Al plate. They found that both

ridges and valleys on the upper and lower surfaces are irregularly distributed in the rolling direction (RD) and that ribbed profiles and corrugations are rare.

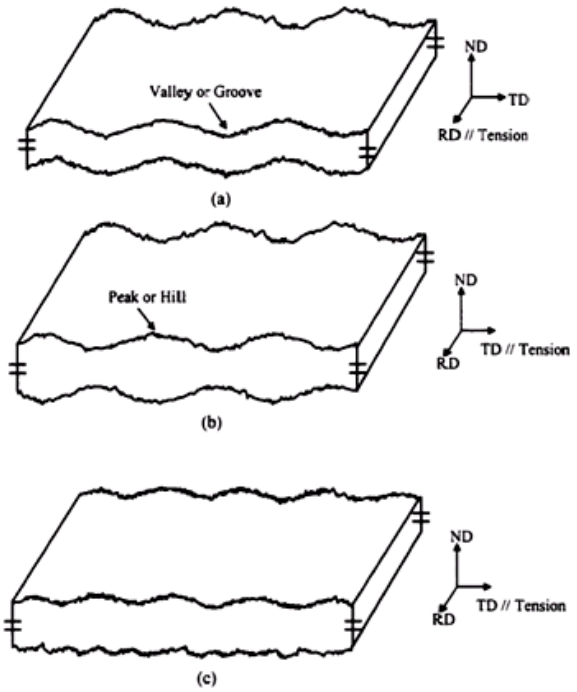

Figure 2.13 Three types of grain scale surface roughening phenomena [40, 41]

2.5 Experimental research on surface roughness

There are lots of studies on surface roughness in grain scale. Most of them focused on the relationships between the surface roughness and grain structure, plastic strain, grain size, and grain texture.

2.5.1 Effect of crystal structure on surface roughness

Osakada and Oyane [19] did a compression with the following metal (HCP Zn and Mg, FCC Cu and Al-5%Mg, 70-30 brass and 18-8 stainless steel) and BCC (Fe-0.03%C and 13Cr stainless steel). They compared the surface roughness from the roughness-strain curve and found a descending arrangement as follows

$$R_{HCP} > R_{FCC} > R_{BCC} \tag{2.28}$$

They reported that the difference of the movable slip systems in the different crystal structures is the cause of this trend. In general, there are three movable slip systems in HCP, 12 movable slip systems in FCC, and 48 movable slip systems in BCC. With the less movable slip systems, the volume deformation constraints cannot be met, and then the interactions between the deformation grains easily lead to severe surface roughening.

There are some literatures about influence of phase on surface roughness. C. Messner et al. [42] studied the Forged duplex steels and found that the surface roughness amplitude highly depends on the characteristic length scale of the microstructure: the larger the mean intercept phase domain size the higher is the amplitude of the surface profile. J. Grum and Kisin [43] found the direct relationship between the size of the soft phase and the roughness of the surface formed after fine turning of aluminium-silicon alloys. Morosov et al. [44] investigated the magnetic structure inhomogeneites induced by an external magnetic field near a rough surface of a collinear uniaxial antiferromagnet. They found the relationship between magnetic structure inhomogeneites and rough surface. Raabe et al. [4] also pointed out that inhomogeneity of surface deformation by hard and soft phases can generate the surface defect to change the surface roughness of sample

2.5.2 Effect of plastic strain on surface roughness

It has been demonstrated from the research that surface roughness is linearly dependent on the plastic strain [41, 45, 46]. The equation is as follows:

$$R = K_l \cdot \varepsilon + R_0 \tag{2.29}$$

where K_l is the linear slope (surface roughness rate) and R_0 is the original surface roughness. It is an empirical equation of the relationship between the surface

roughness and plastic strain ε .

Kawai et al. [47] and Dai et al. [48] obtained the relationship between the strains and the different wavelengths of surface cambers. Kawai et al. calculated the dominant wave length obtained from the power spectrum of surface cambers in an equiaxial stretching experiment of 1050 aluminium plate. The results show there is a linear increment relationship between the dominant wavelength and the strain. On the other hand, Dai et al. [48] obtained different results. In a stretching experiment with 2024-T3 aluminium plate, they determined the dominant wavelength component with two dimensional self correlation functions. At the same time a functional image of the dominant wavelength and true strain were drawn up: when the strain is less than 4 %, the dominant wavelength decreases rapidly, but when the strain is between 4-8 %, the dominant wavelength tends to saturation and the saturating wavelength is nearly twice the size of an average grain. They considered that grain rotation was the main reason for changes in the wavelength of the main surface roughness. With a small strain, the sample altered from an original mirror face to a rough surface, but when the strain exceeded 18 %, the change of dominant wavelength was only based on the mesoscopic surface camber. So the trend has changed.

Thomson and Nayak [49] pointed out that there was no good correlation between the surface roughness of deformed steel plate and the equivalent strain since the surface roughness alternation on rolling and transverse directions relates to a change in directions of the anisotropic parameters. By tracing the surface topography of stretched samples with the multi-stress and original polished states, they studied the forming mechanism of surface roughness in the free surface of a metal plate, and pointed out that the surface camber increases with an increase in the plastic strain.

Mahmudi and Mehdizadeh [50] have done a uniaxial and equiaxial direction stretching experiment with 70-30 brass plate and studied its surface roughness. The results show that there is a good relationship between the grain size and surface

roughness. They found that the increment of surface roughness is a direct ratio to the strain and grain size of the plate. Mahmudi and Mehdizadeh also reported that the transverse surface roughness is more obvious than the longitudinal surface roughness, mainly because of inhomogeneity in the grain structure, and the material.

2.5.3 Relationship between texture and surface roughness

Previous researchers studied the relationship between the surface roughness and grain texture. Wilson et al. [51, 52] did the research on copper plate with a strong cubic texture. The result shows that surface roughening decreases with an increase of specific textures, mainly because the intergranular incompatibility of deformation was small. However, under a finite strain the cubic orientation is instable. Meanwhile, a copper plate with a strong cubic texture can generate a much larger local strain than a plate without the texture under less strain.

Baczynski [41] analysed the waving phenomenon in an auto metal alloy. The EBSD result shows that the distribution of the grains with Gauss orientation plays a main role in the waving phenomenon. Huh and Engler [53] investigated the intermediate annealing effect of a Cr 17 % ferritic stainless steel sheet on the texture and ridging. They found that if the gradient of texture in the thickness of the plate, and the recrystallisation texture are weak, ridging cannot be formed easily.

Engler et al. [54] analysed the relationship between ridging and texture in an Al-Mg-Si (6xxx) plate used for automobile body panels. They reported that the density of cubic orientation has a strong correlation to the height of the ridging. Raabe et al. [4] did research on the grain-scale micromechanics of polycrystal surfaces of Al-Mg-Si (alloy AA6022) plate to analyse the relationship between the polycrystal microstrain and surface roughness, and established a relationship between the microstrain and banded microtexture components (Cube, Goss, {111} [*uvw*]). Ji and Was [55] found that when Nb films were deposited onto Si substrates

using ion beam assisted deposition (IBAD), both the surface roughness and texture increased linearly with film thickness, up to a critical value. A linear relationship was obtained between the surface roughness and alignment of the grain orientation (Figure 2.14).

2.5.4. Relationship between grain size and surface roughness

Grain size is one of the main factors which lead to surface roughness. It has been shown from experimental results that the larger the grain, the rougher the surface. From the research results, Osakada and Oyane [19] pointed out that the surface roughness R_a is proportional to the applied strain ε and the averaged grain size d and is expressed as follows.

$$R_\alpha = c^* \cdot d \cdot \varepsilon \tag{2.30}$$

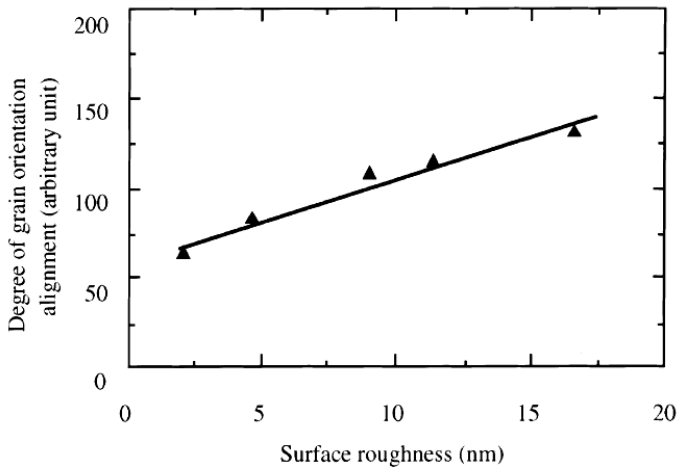

Figure 2.14 Relationship between the degree of grain alignment and surface roughness before bridge over with the least squares linear fit [19]

Stoudt and Ricker [56] confirmed the equation by their experimental results. They carried out a uniaxial tension with three different grain size samples of aluminium alloy AA 5052 (Figure 2.15). The different size grains were developed by three separate heat treatments [57]: the first was 96 hours at 540 °C (referred to as the HT

condition), the second was 2 hours at 350 °C (referred to as the O condition), and the third was H32, or the as-received condition. The H3x condition refers to a stabilised condition produced through a low temperature thermal treatment designed to retain a small amount of residual strain in order to stabilise the mechanical properties and ductility [58, 59]. The H32 condition contains the lowest amount of residual strain and a fine grain structure. They found the roughening rate ($dR_\alpha/d\varepsilon_{pl}$) depended on the grain size in this alloy. With the grain sizes (average grain size) included in their experiment, the relationship between the roughening rate and grain size also appears to be linear (Figure 2.16).

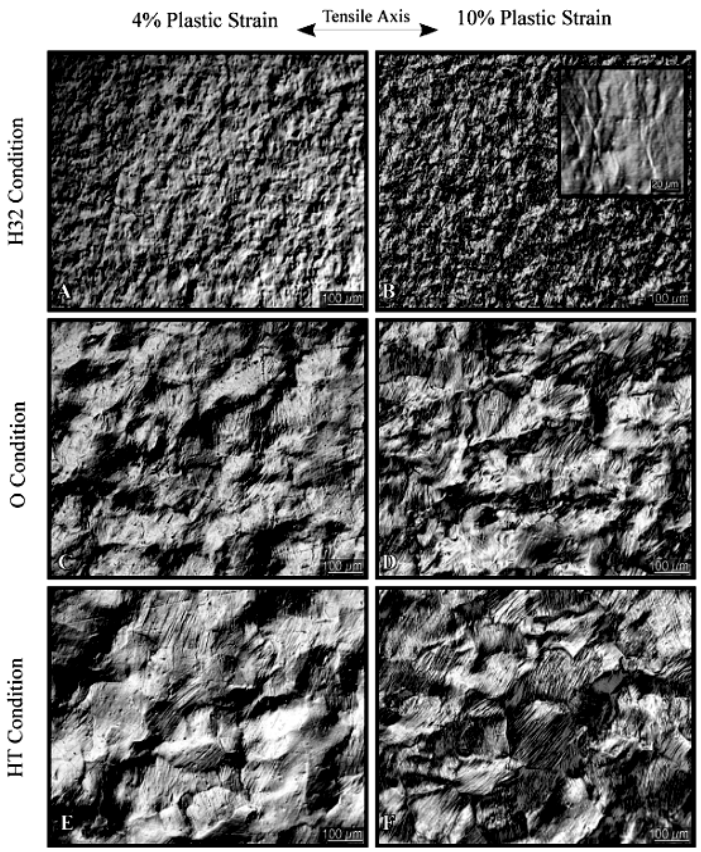

Figure 2.15 Optical micrographs depicting the relationship between the surface roughness induced by deformation, grain size, and plastic strain in AA5052. The inset image in B is a higher magnified view of the surface morphology. Note that the R_a values for B and C are the same, yet the morphologies differ dramatically [56]

In order to obtain a more accurate correlation between the surface roughness and averaged grain size, Wang et al. [60] proposed a revised equation for the surface roughness $R_{\alpha 3}$. They expressed the relationship between the surface roughness and average grain boundary with a power exponent function. It is shown as

$$R_a = C^{'} \cdot d^n \cdot \varepsilon = a^* \cdot \varepsilon \tag{2.31}$$

$$C^{'} = R_{a3} /(\varepsilon \cdot d^n) \tag{2.32}$$

where $C^{'}$ is a parameter depending on the deformation path and the kind of metal, a^* is the rate of increase of surface roughness, and *n* is an exponent indicating the effect of grain size.

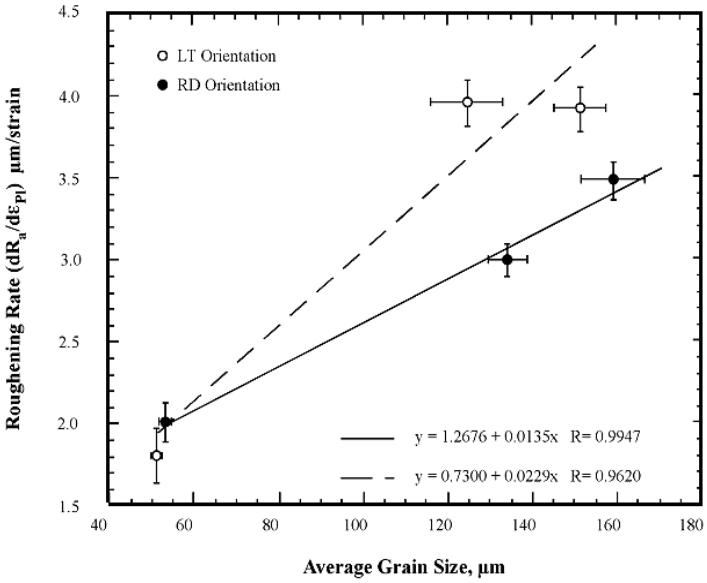

Figure 2.16 The roughening rate behaviour of AA5052 shown as a function of grain size and orientation with respect to rolling direction. A regression analysis performed on the arithmetic mean roughness (Ra) values is the basis of the data shown in this figure [58, 59].

They carried out uniaxial tensile tests on specimens of pure annealed aluminium

sheet with various averaged grain sizes. They found that the surface roughness increases as plastic strain is applied, and the increase is high in the specimen with a large grain size, and their results showed a good agreement with those of Osakada and Oyane [19].

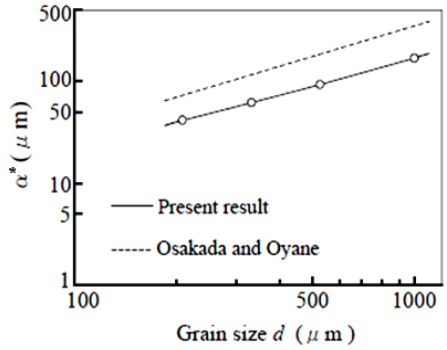

Figure 2.17 Relationship between factor α^* ($\alpha^* = R_{a3}/\varepsilon$) and grain size [57]

On a consideration of the influence of initial surface roughness R_0 on the surface roughness, the equation of surface roughness can be defined [19, 48] as

$$R = a' \cdot d \cdot \varepsilon + R_0 \tag{2.33}$$

where a' is a constant and d is the average grain size. Oskada et al. [19] calculated the α from the stretch and compression experiments of Al-5% Mg alloy with different size grains: a'=0.35. Dai et al. [48] not only observed a linear relationship between R and d, they also obtained a linear relationship between the dominant wavelength λ and d. The larger the grain, the more important its influence on surface roughness. If the thickness of a plate is only two or three grain sizes thick, the grain deformation will determine its volumetric deformation.

2.5.5 Effect of R_0 on the roughening rate

Chen et al. [61] carried out a stretch forming of aluminium alloy sheet. They defined the relationship between the surface roughness R and strain ε_c along the tensile

direction as:

$$R = R_0 \qquad \varepsilon_c < \alpha_s$$

$$R = R_0 + K_1(\varepsilon_c - \alpha_s) \qquad \varepsilon_c \geq \alpha_s \qquad (2.34)$$

where α_s is the strain after which the roughness rises linearly.

They carried out tensile testing of steel S with different initial roughness to examine the effect of initial roughness on the rate of roughening. The results show that a change in R_0 does not affect the value of the maximum roughness increment ΔR^* of the material at the onset of strain instability but does influence K and α (Figure 2.18). When the initial roughness is changed from 0 to 5 μm, α_s varies from 0 to 0.1 and K from 12.7 to 15.2 μm. For general commercial deep drawing cold rolled steel, the original surface roughness is usually from 3 to 5 μm, so that the variations in K and α are not great, amounting to 1 μm and 0.05 respectively.

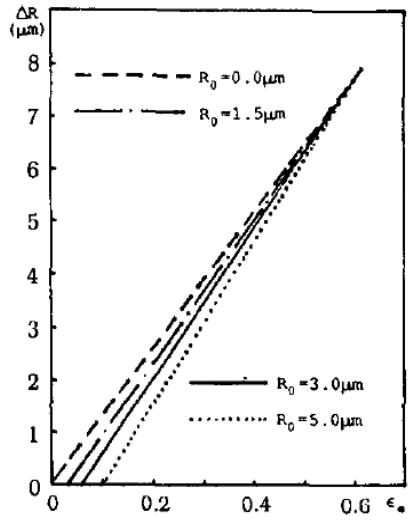

Figure 2.18 Effect of initial surface roughness R_0 on roughening rate K of steel S [61]

2.5.6 Effect of tool roughness

During metal forming, the roughness of the tool affects the roughness of the workpiece. Contact between the tool and the workpiece is either direct or indirect. During direct contact, no lubricant is used when metal forming so the tool makes direct contact with the workpiece. Here the surface finish of the workpiece mainly depends on the surface of the tool. In most current metal forming processes, lubricants are used to decrease friction and improve the surface finish. In this situation the tool does not make direct contact with the workpiece. Indeed the layer of lubrication is a most important aspect in the surface development of the workpiece. As mentioned in Section 2.1.2, it is a very complicated process. There are lots of literatures that describe this process [62-66]. Normally, a combination of the tool, lubricant and the workpiece itself contributes to the surface finish.

2.5.7 Other research on surface roughness

A mis-phasing optical interference method was used to measure the three dimensional surface roughness. In the 1990s, auto-orientation imaging was developed, which allowed the relationship between the orientation of the surface grains and surface roughness to be studied further. Lee et al. [67] studied the development of orange peel of an auto 6022-T4 aluminium plate using an inference microscope and EBSD (Electron Back Scatter Diffraction). However, there was no report on the relationship between the development of orange peel and orientation of the surface grains. Wittridge and Knutsen [68] studied the development of grain-scale surface roughness during uniaxial stretching deformation.

2.6 Computer simulation of surface roughness

2.6.1 Upper bound method

With the development of computer simulation techniques, many researchers have

done numerical simulations of surface roughness. Wilson and Sheu [69, 70] used the upper bound technique to simulate the development of surface asperities during the metal forming process. They generated a new concept of “effective hardness” which concerns the flattening of surface asperities during plastic volumetric deformation. They also gave a correlation between the volumetric strain rate and the contact area. Sheu et al [69] incorporated the modified surface roughness into the empirical model of surface roughness flattening, and thought that an increase in the slope rate and decrease in the strain growth rate of the contact surface were the main reasons for surface roughening.

2.6.2 Crystal plasticity finite element method

Becker [8] used the Crystal Plasticity Finite Element Method (CPFEM) to simulate the effects of strain localisation on surface roughening during sheet forming. This first used a concrete method to describe the generation of grain-scale surface roughness induced by inhomogeneity in the material. They selected 6111-T4 aluminium plate and measured 77 different grain orientations as the input elements to simulate strain location during metal forming. It is shown that the strain only occurs within a surface area of 2-3 grains in length, whereas valleys form in the free area affected by the strain location band. Peaks will be formed at an area of low strain which intersects the surface of two strain location bands, as shown in Figure 2.19. Becker’s results emphasised that the incompatible deformation of adjacent grains in or near the surface area is the main cause of surface roughening. Surface roughness can be decreased by generating a strong, stable texture.

Beaudoin et al. [71] also did a simulation of surface roughness. They input the surface grain orientations of 6111-T4 aluminium plate as hexagonal meshes and simulated the surface roughening process of biaxial tension and planar strain tension, and found that the interaction between the surface cubic grains and adjacent grains is the main reason for irregular deformation. They also did a hydraulic bulging

experiment of metal materials with and without textures and discovered that there was no ride generated in the metal without textures. Recently, some researchers simulated surface roughening by CPFEM [72, 73].

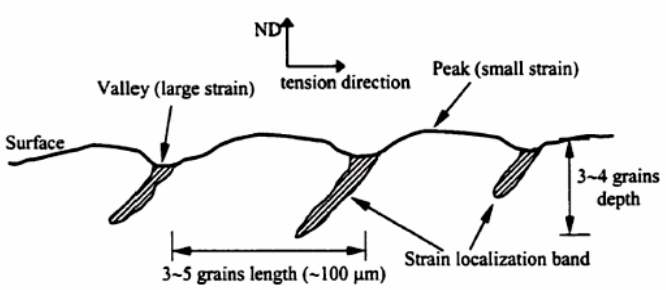

Figure 2.19 Peak and valley of the tensile deformation area based on the Becker plane strain deformation [8]

Shin et al. [72] studied how the texture affected ridging while 430 and 409L stainless steels were under tension. All the samples used are from the column grain and equiaxed grain areas of stainless steels. The X-Ray diffraction and EBSD (Electron Back Scatter Diffraction) were used to test the texture of the specimens and then this data was input into the CPFEM model. The results show that the ridging under tension was very severe in the stainless steel with column grains and the surface of the 409L stainless was very poor. The results of this simulation shows that the ridging was generated by a low plastic strain rate of the {001}<110> grain cluster and different shear deformation of the {111}<110> or {112}<110> clusters, as shown in Figures 2.20 and 2.21. It can be seen from Figure 2.20 that the grains are randomly distributed so that the specimen can have a matrix texture (MT) without any riding, and the strain has been distributed in a regular pattern after 20 % tensile strain. Figure 2.21 shows the initial mesh of the specimen with colonies in different orientations and strain distributions after a tensile strain of 0.2. This result indicates that the CPFEDM simulated the ridging quite well. The low plastic-strain ratio of {001}<110> colonies and different shear deformation of the {111}<110> or

{112}<110> gives rise to ridging. The height of the ridging simulated here is lower than the other simulated results.

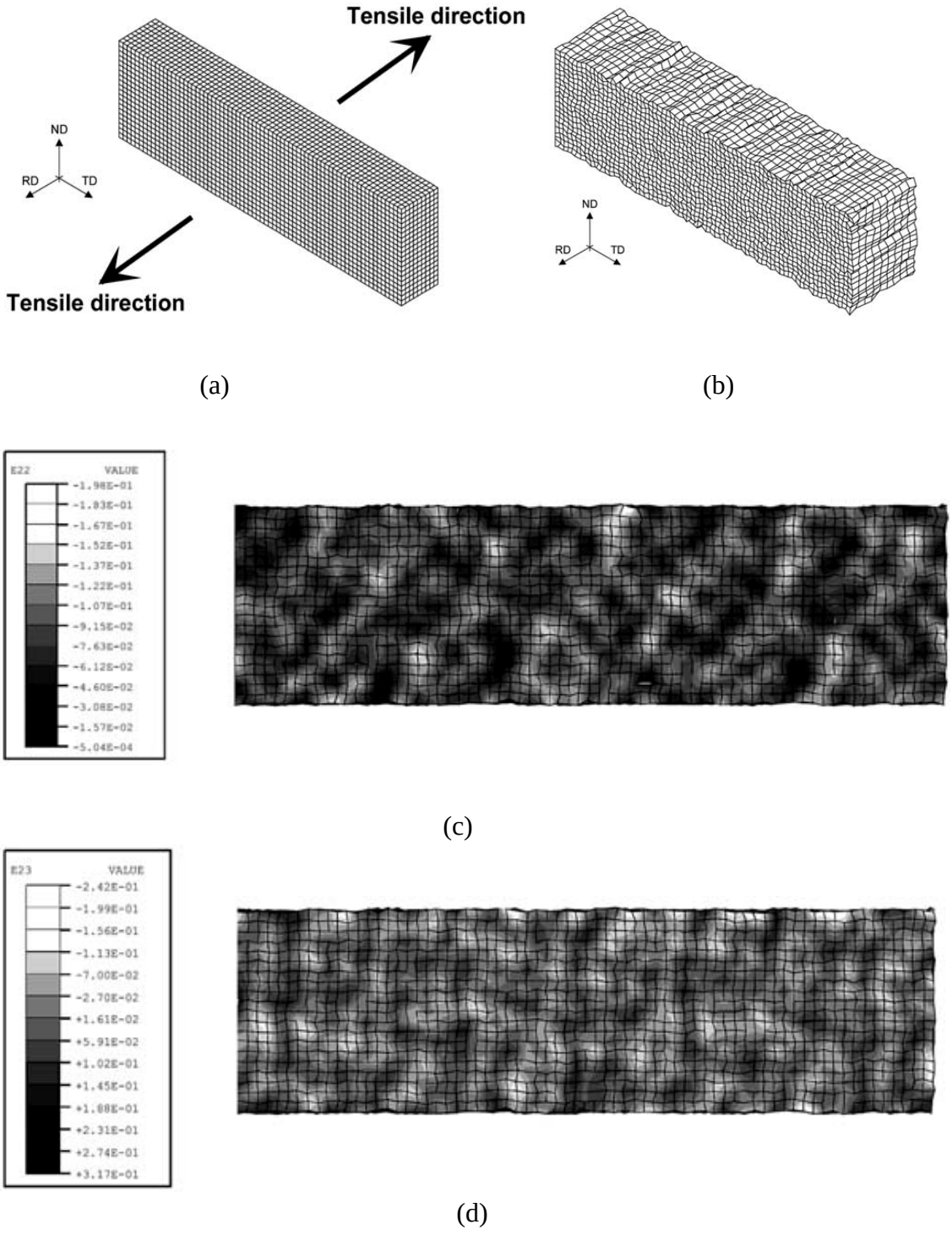

Figure 2.20 Calculated shape and distributed strain of a textured specimen after 20 % of tensile strain. (Left upper, (a) original mesh, left lower, (b) deformed mesh

(two times), right upper, (c) distribution of tensile strain, right lower, (d) distribution of shear strain) [72]

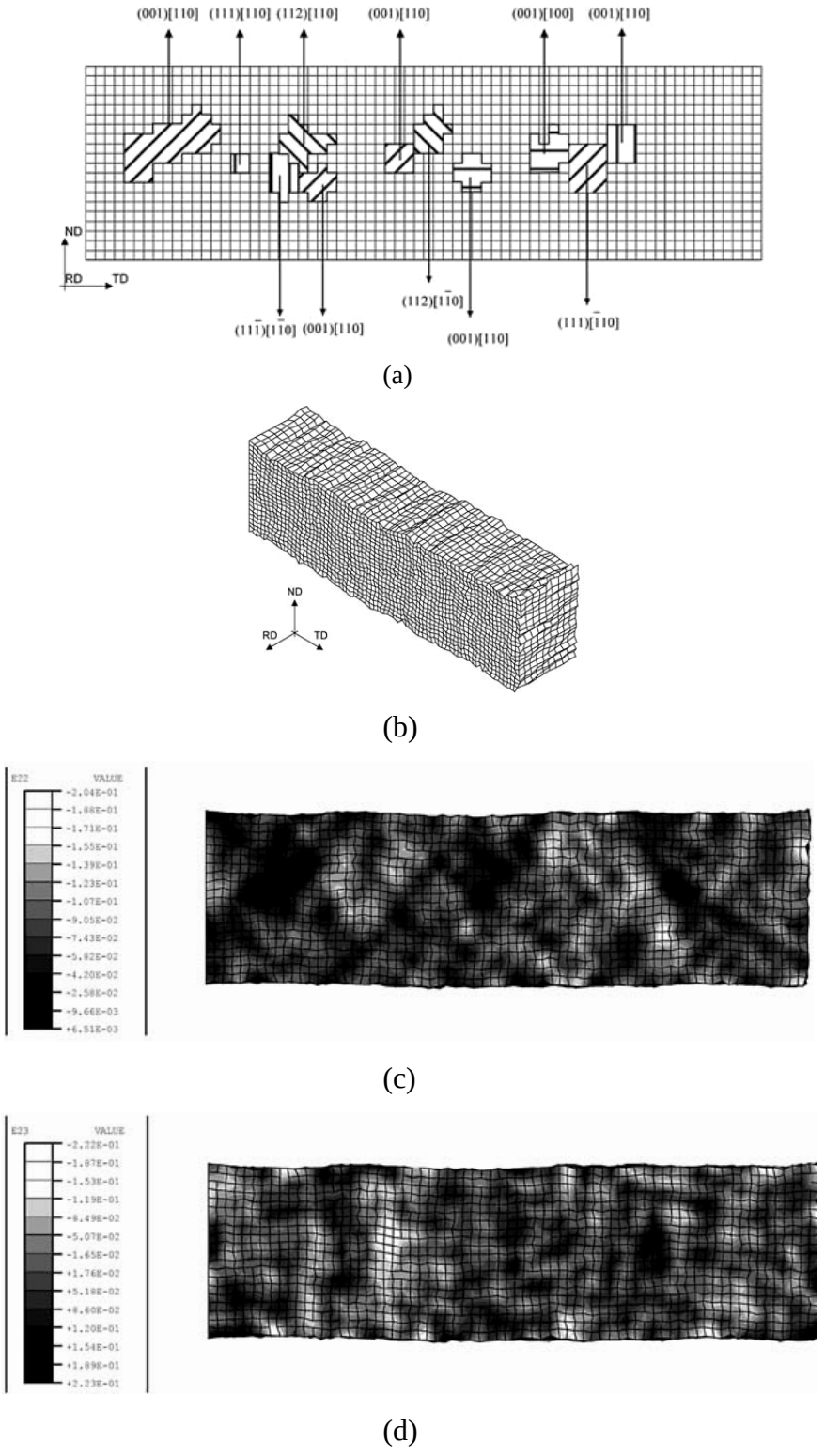

Figure 2.21 Calculated shape and distribution of strain of the textured specimen

includes different grain colonies after 20 % of tensile strain(left upper, (a) original mesh, left lower, (b) deformed mesh (two times), right upper, (c) distribution of tensile strain, right lower, (d) distribution of shear strain) [72]

Wu and Lloyd [74] simulated development of the surface asperity of an AA6111 aluminium plate during the tensile process. They incorporated the EBSD experimental data directly into the finite element models. The constitutive equations at each integrated point were described by single crystal plasticity theory. They analysed the effect of some parameters on surface roughening, such as the specimen size, sensitivity of the strain rate, workhardening, loading path, step size of EBSD, the distribution of space orientation and intergranular deforming inhomogeneity, and obtained from those results that the surface roughening was controlled by the space distribution of grain orientation along the thickness direction. The effect of the space distribution of orientation on surface roughening is shown in Figure 2.22 (Experimental and 5 cases results). It can be seen that in the first two cases, the surface layers and central layers have the same volume, i.e., $2N_s$=$2N_c$=34. The predicted R_b in both cases is found to be significantly lower than the one based on the measured EBSD. Since the number of grains in the central and surface layers is exactly the same, it appears that the interior grains contribute more to surface roughening than the grains on or near the free surface. These results, together with those for Cases 3 and 4 with $2N_s$=10 ($2N_c$ = 58), strongly suggest that the surface roughening could be very significantly underestimated if the interior grains are only considered as a supporting layer for the surface grains. If all the grain orientations are randomly assigned into the finite element mesh (Case 5), the calculated surface roughening tendency is reduced significantly.

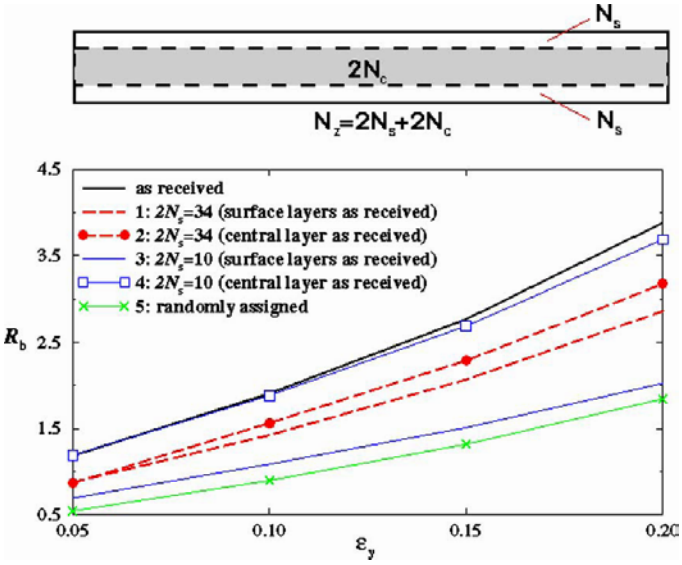

Figure 2.22 Orientation influence of the surface roughening [74]

2.6.3 Neural network method

Oktem et al. [75] coupled a genetic algorithm with a neural network when end milling mold parts to find the optimum cutting parameters leading to minimum surface roughness without any constraints. A good agreement was observed between the predicted values and experimental measurements.

Zain et al. [76] presented an ANN (Artificial Neural Network) model for predicting the surface roughness in the machining process by considering the Artificial Neural Network (ANN) as the essential technique for measuring surface roughness. El-Sonbaty et al. [77] developed ANN models to analyse and predict the relationship between the cutting conditions and corresponding fractal parameters of machined surfaces in a face milling operation. The predicted profiles were found statistically similar to the actual measured profiles of test specimens.

Susic et al. [78] presented a newly developed system for an online estimation of the roughness and hardness parameters of surfaces involved in sliding friction. The

system's performance was tested in an online pin-in-disk experiment, and for most of these experiments the ability to reliably recognise and place given cases in correct classes was greater than 94 %.

Durmus et al. [79] used the neural networks to predict the wear and surface roughness of an AA 6351 aluminium alloy. It was observed that the experimental results coincided with ANN results. The ANN architecture used was a 4:9:9:2 multilayer type, as shown in Figure 2.23. The results show that the maximum wear strength was found in a specimen aged naturally for a week at room temperature, and minimum surface roughness was found in a specimen artificially aged at 180 °C. Both the experimental results and ANN results have confirmed it

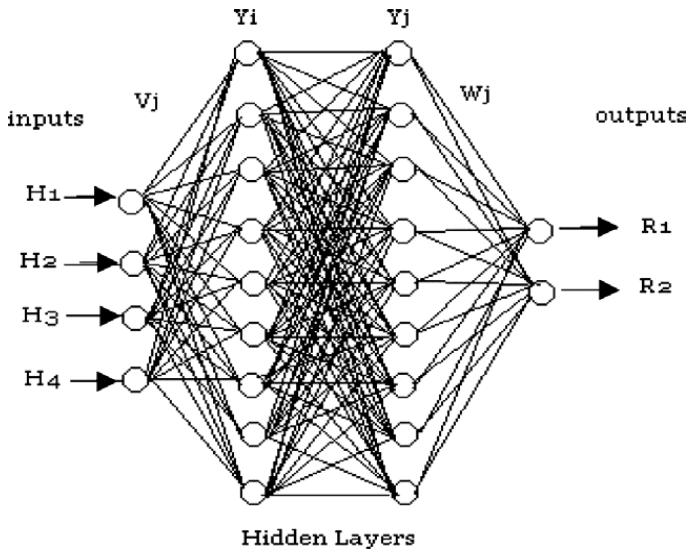

Fig. 2.23 The ANN's architecture [79]

2.7 Problems and findings from the literature review

There are many literatures about surface roughening in metal forming processes. Research has been carried out to analyse the friction mechanism of metal forming. The influence of factors on surface roughening, such as plastic strain, friction, microstructure, texture, grain size, and the initial surface roughness of the workpiece

and die, are also mentioned by some researchers in their results.

However, little research has been done on the surface development of constraint surfaces (surface asperity flattening process) with CPFEM (crystal plasticity finite element method). Most current CPFEM research focuses on the development of free surface (surface roughening) by uniaxial and biaxial tensile deformation. Some researchers focus on the constraint surface to analyse the relationship between friction and surface roughness, but few have used the crystal plasticity constitutive theories to explain how parameters influence surface roughness. In particular, there are almost no reports that mention the relationship between the orientation of surface grains and surface roughness. The texture development of the constraint surface is also a very interesting topic. It seems that the influence of friction on the development of texture is still not known very well. In metal forming, the strain rate contributes significantly to the workpiece workhardening, but there is little research on how the strain influences surface roughness.

2.8 Research scope in the present study

In this study the development of surface roughness of the constraint surface will be investigated. A physical simulation will be conducted on an INSTRON servo-hydraulic testing machine using a channel die specifically designed for this study. Because cold uniaxial planar compression is similar to cold rolling, a uniaxial planar channel die was designed in this study. The relationship between the surface roughness and related parameters such as gauged reduction, friction, texture (grain orientation), and grain size and strain rate will be identified, as mentioned above, although a CPFEM model will also be established on the basis of the experimental results of compression, AFM, and EBSD. The objective of this study is to understand the mechanism of surface roughening of the constraint surface in metal forming by crystal plasticity theories, and build up the relationship between the deterministic parameters and probabilistic parameters, and then suggest corrective changes during

cold uniaxial planar compression. This research also seeks to solve the simulation problems that resulted from different dimensions of models. The detailed crystal plasticity constitutive theories and methodology will be introduced in Chapter 3.

CHAPTER 3

THE CONSTITUTIVE THEORY AND METHODOLOGY OF CRYSTAL PLASTICITY

3.1 Historical view

3.1.1 Historical view of finite element simulation

The first finite element simulation was performed by Courant in 1943 [80]. It is an effective tool to solve the complicated equation of metal forming. The breakthrough with this method came with the publication of "The Finite Element Method in Structural and Continuum Mechanics" by Zienkiewicz in 1967 [81]. In the 1980s, most finite element simulations related to metal and plastic deformation were based on the isotropy and a rate independent model of the material. With the appearance of new problems in large strain and complicated loading paths the necessity to establish more accurate models to express the properties of metal materials became urgent. Of these existing models, the internal variable model was the typical model used to explain plasticity rheological dynamics by the yielding criterion and the workhardening theories. Since the 1990s, finite element simulation has made significant progress as the structure of the material has been directly incorporated into the finite element model. This structure is the geometric structure observed by all kinds of microscopes, for example, polycrystal, grain, dislocation, precipitated phase and all kinds of defects [82]. So with the appearance of parallel computation and the acquisition of automatic data and visualised facilities, computer finite element simulation of the material has been changed from macro modelling to multiscale simulation of the materials. This tendency is shown in Figure 3.1.

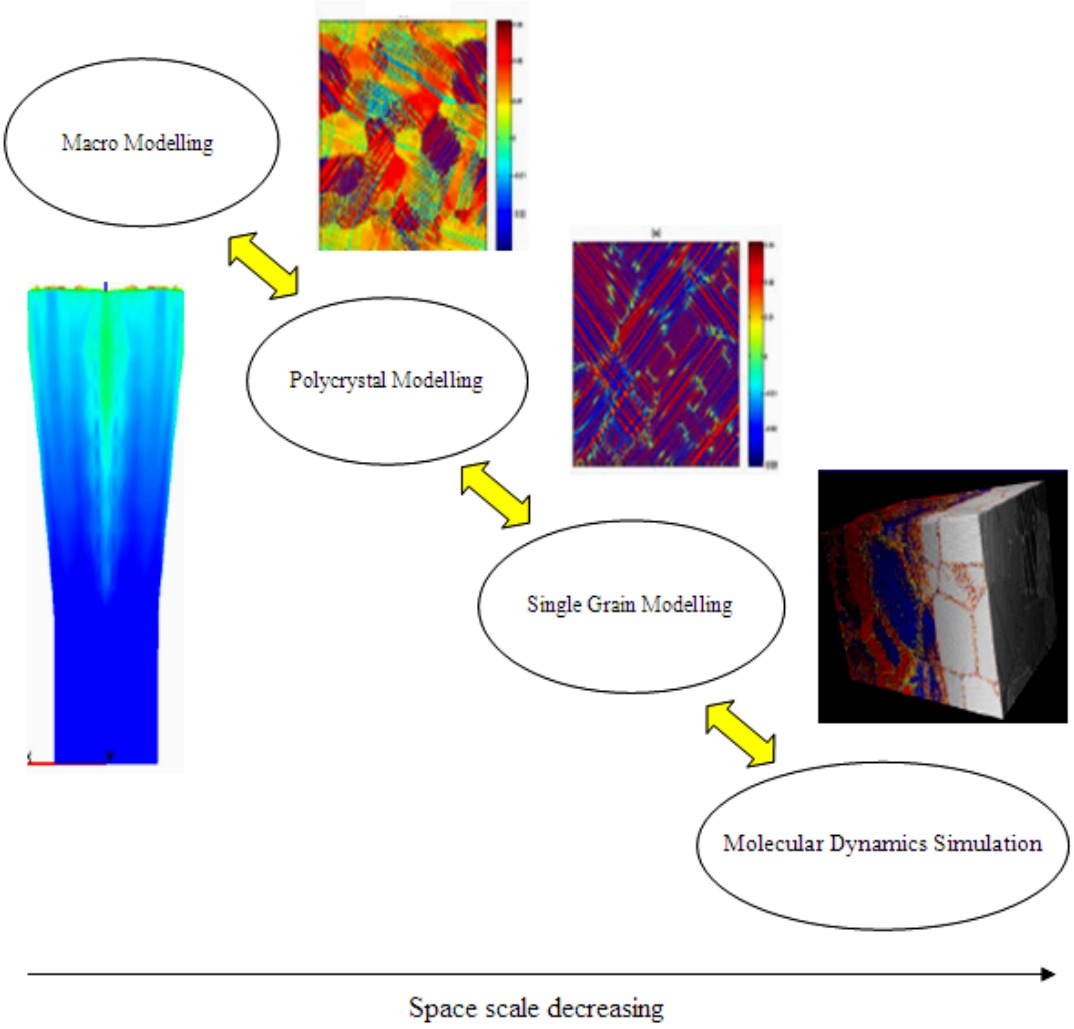

Figure 3.1 Multiscale simulation of material

3.1.2 Historical view of crystal plasticity theories

Researchers have studied the behaviour of crystal plastic deformation from 1930 to 1960 [83-86]. These early research achievements were related to features such as the geometry and crystallography of plastic deformation. Based on the theories of plastic deformation and strength, the concept of dislocation has been presented, and from which current dislocation theories have developed. On the other hand, these modified dislocation theories can promote the development of crystal plasticity theory. In essence, compared with the constitutive relationship used several decades ago, the present constitutive relationship has improved significantly. The research work of crystal plasticity can be dated back to the pioneering work of Sachs [87], Taylor [88],

Bishop-Hill [89, 90], Kroner [91], Orowan [92], Schimid [93] and Polanyi [94-96]. These forerunners were conscious of the tightly relationship between plastic deformation and grain structure. Their work reminded latecomers that research into crystal plastic deformation must start with the crystal microstructure, and it should not be studied at the macroscopic level. The large strain inherent in the crystal is often accompanied by the phenomenon of strain localising and plastic damage where the material experiencing this large strain has strongly inhomogeneous stress and strain fields. These kinds of problems could not be solved analytically, but could be handled by employing the finite element method. The crystal plasticity finite element method refers to the method which directly uses the crystal plasticity constitutive equation.

The rapid development of computer techniques has provided important conditions for the use of the crystal plasticity finite element method. Over the past twenty to thirty years, the crystal plasticity finite element method has become a hot topic in the research field of mechanics and materials. The fundamentals of the crystal plasticity finite element method were first brought forward by Hill and Rice [97]. Their theory is based on the Schmid rule of the crystal plastic deformation process. In 1982, Pierce et al. [98] established a simulation method and successfully used it to simulate the formation of a shear band in soft grain metal. In 1985, Asaro and Needleman [99] developed a rate-dependent constitutive equation of crystal plasticity and related numerical method, but since then the CPFEM has become more popular in the field of materials and mechanics. The general method for using CPFEM is to establish a relationship between the micro polycrystal and the material, or its continuous points. At first, each grain is expressed by the constitutive equation of single grain parameters, but then the whole deformation process is averaged and it is assumed that the single grain micro response relates to the polycrystal averaging responses.

3.2 Crystal plasticity theory

3.2.1 Geometrics and kinematics of crystal plasticity deformation

There are mechanisms such as plastic slip and grain deformation during the metal forming process, but the grains can slip by becoming dislocated or deformed

elastically by grain lattice rotating. The geometrics and kinematics of crystal plasticity deformation were developed by Hill and Rice [97], and Pierce et al. [98], Asaro, and Needleman [99] have also described this.

During the process of single grain deformation, the gross deformation gradient can be expressed as [91, 100-103]

$$F = \frac{\partial x}{\partial X} = F^* \cdot F^p \tag{3.1}$$

where F is the gross deformation gradient, x is the position of the material point in the present configuration, X is the position of material point in the initial configuration, F^* is the gross deformation gradient combined by the elastic deformation (lattice distortion) and rigid rotation, and F^p is the displacement gradient caused by the slip. The whole deformation process of a single grain can be divided into two processes: first, the un-deformed lattices move with a gradient of F^p, and then the material and lattice deform and result in the gross deforming gradient F^*, after the elastic deformation is unloaded, the F^p is the residual deformation. The whole process is shown in Figure 3.2.

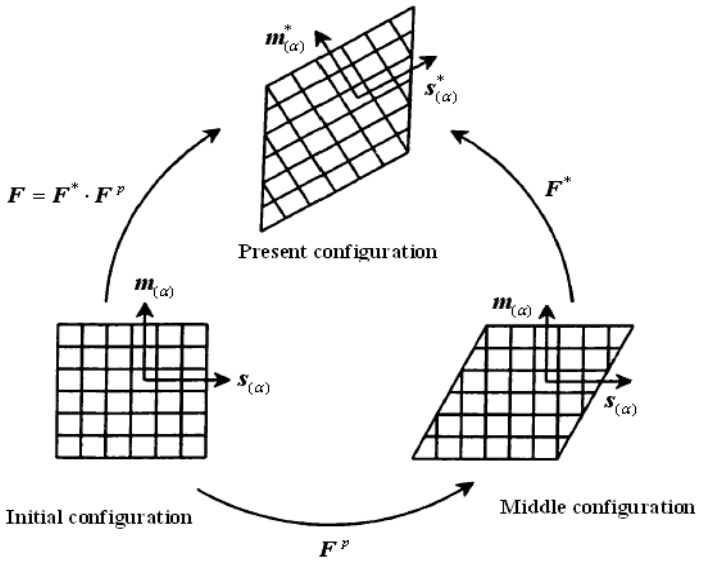

Figure 3.2 Kinematics of crystal elastic-plastic deformation generated by slip [91]

When the grain deforms and rotates, so the grain lattice vectors do. The $s^{(\alpha)}$ is the slip vector in the $\alpha\, th$ slip direction. After deformation it can be expressed as

$$s^{*(\alpha)} = F^* \cdot s^{(\alpha)} \tag{3.2}$$

Other vectors in the slip plane have similar transformations. After deformation, the un-deformed normal vector $m^{(\alpha)}$ in the slip plane is as follows:

$$m^{*(\alpha)} = m^{(\alpha)} \cdot F^{*-1} \tag{3.3}$$

In the reference configuration $s^{(\alpha)}$ and $m^{(\alpha)}$ are the unit vectors in $\alpha\, th$ slip system. In general, $s^{*(\alpha)}$ and $m^{*(\alpha)}$ are not the unit vectors, but they still have orthogonal relationship $s^{*(\alpha)} \cdot m^{*(\alpha)} = s^{(\alpha)} \cdot m^{(\alpha)} = 0$. The current velocity gradient L can be expressed as

$$\boldsymbol{L} = \frac{\partial \boldsymbol{v}}{\partial \boldsymbol{x}} = \frac{\partial \boldsymbol{v}}{\partial \boldsymbol{X}} \frac{\partial \boldsymbol{X}}{\partial \boldsymbol{x}} = \dot{\boldsymbol{F}} \cdot \boldsymbol{F}^{-1} = \boldsymbol{L}^* + \boldsymbol{L}^p \tag{3.4}$$

$$\boldsymbol{L}^* + \boldsymbol{L}^p = \dot{\boldsymbol{F}}^* \cdot \boldsymbol{F}^{*-1} + \boldsymbol{F}^* \cdot \dot{\boldsymbol{F}}^p \cdot \boldsymbol{F}^{p-1} \cdot \boldsymbol{F}^{*-1} \tag{3.5}$$

where v is the velocity of the material point, $\boldsymbol{L}^*$ is the elastic part of the deformation gradient, and $\boldsymbol{L}^p$ is the plastic part of the deformation gradient.

Plastic deformation of a single crystal can be expressed as

$$\boldsymbol{F}^p = \boldsymbol{I} + \boldsymbol{\gamma}_{(\boldsymbol{\alpha})} \boldsymbol{s}_{(\boldsymbol{\alpha})} \otimes \boldsymbol{m}_{(\boldsymbol{\alpha})} \tag{3.6}$$

Therefore, the polycrystal plastic deformation can be expressed as

$$\dot{\boldsymbol{F}}^p = \sum_{\boldsymbol{\alpha}=1}^{n} \dot{\boldsymbol{\gamma}}_{(\boldsymbol{\alpha})} \boldsymbol{s}_{(\boldsymbol{\alpha})} \otimes \boldsymbol{m}_{(\boldsymbol{\alpha})} \tag{3.7}$$

$$\boldsymbol{F}^{p^{-1}} = \boldsymbol{I} - \sum_{\boldsymbol{\alpha}=1}^{n} \boldsymbol{\gamma}_{(\boldsymbol{\alpha})} \boldsymbol{s}_{(\boldsymbol{\alpha})} \otimes \boldsymbol{m}_{(\boldsymbol{\alpha})} \tag{3.8}$$

From Equations (3.7) and (3.8), it can be drawn as

$$\dot{\boldsymbol{F}}^p \cdot \boldsymbol{F}^{p^{-1}} = \sum_{\boldsymbol{\alpha}=1}^{n} \dot{\boldsymbol{\gamma}}_{(\boldsymbol{\alpha})} \boldsymbol{s}_{(\boldsymbol{\alpha})} \otimes \boldsymbol{m}_{(\boldsymbol{\alpha})} \tag{3.9}$$

So $\boldsymbol{L}^*$ and $\boldsymbol{L}^p$ of Equations (3.4) and (3.5) can be expressed as

$$\boldsymbol{L}^* = \dot{\boldsymbol{F}}^* \cdot \boldsymbol{F}^{*-1} \tag{3.10}$$

$$\boldsymbol{L}^p = \boldsymbol{F}^* \cdot \dot{\boldsymbol{F}}^p \cdot \boldsymbol{F}^{p-1} \cdot \boldsymbol{F}^{*-1} = \sum_{\boldsymbol{\alpha}=1}^{n} \dot{\boldsymbol{\gamma}}_{(\boldsymbol{\alpha})} \boldsymbol{s}^*_{(\boldsymbol{\alpha})} \otimes \boldsymbol{m}^*_{(\boldsymbol{\alpha})} \tag{3.11}$$

The $\boldsymbol{L}^*$ and $\boldsymbol{L}^p$ can be expressed separately as

$$\boldsymbol{L}^* = \dot{\boldsymbol{F}}^* \cdot \boldsymbol{F}^{*-1} \tag{3.11}$$

$$\boldsymbol{L}^p = \boldsymbol{F}^* \cdot \dot{\boldsymbol{F}}^p \cdot \boldsymbol{F}^{p-1} \cdot \boldsymbol{F}^{*-1} \tag{3.12}$$

where $\gamma_{(\alpha)}$ is the shear strain of the α *th* slip system, $\dot{\gamma}_{(\alpha)}$ is the shear rate of the α *th* slip system. Alternatively, L can be divided into two parts according to the deformation and rotating velocities, and may be written as follows:

$$L = D + \Omega \tag{3.13}$$

where D, Ω are the symmetric tensors of deforming velocity and rotating velocity respectively. Their components can be described by the velocity v and coordinate x as:

$$D_{ij} = 1/2(\partial v_i / \partial x_j + \partial v_j / \partial x_i) \tag{3.14}$$

$$\Omega_{ij} = 1/2(\partial v_i / \partial x_j - \partial v_j / \partial x_i) \tag{3.15}$$

D and Ω can be divided into the elastic part (D^*, Ω^*) and plastic part (D^p, Ω^p):

$$D = D^* + D^p \ , \ \Omega = \Omega^* + \Omega^p \tag{3.16}$$

From Equations (3.4) and (3.5), it can be obtained as

$$D^p + \Omega^p = F^* \cdot \dot{F}^p \cdot F^{p-1} \cdot F^{*-1} \tag{3.17}$$

Because the plastic deformation is caused by grain slip, Equation (3.17) can be changed as

$$\boldsymbol{D}^{p}+\boldsymbol{\Omega}^{p}=\sum_{\boldsymbol{\alpha}=1}^{n}\dot{\boldsymbol{\gamma}}^{(\boldsymbol{\alpha})}\boldsymbol{s}^{*(\boldsymbol{\alpha})}\boldsymbol{m}^{*(\boldsymbol{\alpha})} \tag{3.18}$$

Equation (3.18) sums all the activated slip systems, $\dot{\boldsymbol{\gamma}}^{(\boldsymbol{\alpha})}$ is the slip rate in the α *th* slip system, and $\dot{\boldsymbol{\gamma}}^{(\boldsymbol{\alpha})}$ can be defined as

$$\dot{F}^{p}F^{p^{-1}}=\sum_{\alpha=1}^{n}\dot{\gamma}^{(\alpha)}s^{(\alpha)}m^{(\alpha)} \tag{3.19}$$

For convenience, the tensors P^{α}, W^{α} of the α *th* slip system can be defined as

$$P^{(\alpha)}=1/2\left(s^{*(\alpha)}m^{*(\alpha)T}+m^{*(\alpha)}s^{*(\alpha)T}\right) \tag{3.20}$$

$$W^{(\alpha)}=1/2\left(s^{*(\alpha)}m^{*(\alpha)T}-m^{*(\alpha)}s^{*(\alpha)T}\right) \tag{3.21}$$

Hence, the deformation and rotation tensors of Equation (3.16) can be expressed as

$$D^{p}=\sum_{\alpha=1}^{n}P^{(\alpha)}\dot{\gamma}^{(\alpha)} \tag{3.22}$$

$$\Omega^{p}=\sum_{\alpha=1}^{n}W^{(\alpha)}\dot{\gamma}^{(\alpha)} \tag{3.23}$$

Equations (3.1) to (3.23) are the basic equations of crystal plasticity kinematics. These equations show the relationship between the shear rate and rate of macroscopic deformation.

3.2.2 Rate independent crystal plasticity constitutive equation

It is assumed that grain slip has no effect on the elastic property. According to the description of Hill and Rice [97], the elastic constitutive equation can be expressed as

$$\overset{\nabla^{*}}{\tau}=L:D^{*} \tag{3.24}$$

where L is the fourth order tensor of elastic modulus, $\overset{\nabla^{*}}{\tau}$ the Jumann rate of the Kirchhoff stress, the component of L can be taken as the partial derivative of some

free energy. The superscript * is expressed as the partial derivative for the axial stress which rotates with the lattice. $\overset{\nabla^*}{\tau}$ can be defined as

$$\overset{\nabla^*}{\tau} = \dot{\tau} - \Omega^* \cdot \tau + \tau \cdot \Omega^* \tag{3.25}$$

where $\dot{\tau}$ is the material rate of the Kirchhoff stress, it can be defined as $\rho_0 / \rho\sigma$, σ is the Cauchy stress, ρ_0 and ρ are the reference and currently mass densities respectively. In order to describe the constitutive equation of the material, the Jaumann stress rate can be defined as

$$\overset{\nabla}{\tau} = \dot{\tau} - \Omega \cdot \tau + \tau \cdot \Omega \tag{3.26}$$

The difference between Equations (3.25) and (3.26) can be defined as

$$\overset{\nabla^*}{\tau} - \overset{\nabla}{\tau} = \sum_{\alpha=1}^{n} \beta^{(\alpha)} \dot{\gamma}^{(\alpha)} \tag{3.27}$$

where

$$\beta^{(\alpha)} = W^{(\alpha)} \cdot \tau - \tau \cdot W^{(\alpha)} \tag{3.28}$$

Hence, it can be obtained as

$$\overset{\nabla}{\tau} = \overset{\nabla^*}{\tau} - \left(\overset{\nabla^*}{\tau} - \overset{\nabla}{\tau} \right) = L : D^* - \sum_{\alpha=1}^{n} \beta^{(\alpha)} \dot{\gamma}^{(\alpha)} \text{ (From Equation (3.24))} \tag{3.29}$$

$$= L : (D - D^p) - \sum_{\alpha=1}^{n} \beta^{(\alpha)} \dot{\gamma}^{(\alpha)} \tag{3.30}$$

Equation (3.22) is employed in Equation (3.30), and then

$$\overset{\nabla}{\tau} = L : D - \sum_{\alpha=1}^{n} \left[L : P^{(\alpha)} + \beta^{(\alpha)} \right] \dot{\gamma}^{(\alpha)} \tag{3.31}$$

where $\dot{\gamma}^{(\alpha)}$ in Equation (3.31) is not determined. It can be described by the stress and strain tensors. In order to obtain the value of $\dot{\gamma}^{(\alpha)}$, the resolving shear stress in the α *th* slip system can be expressed as

$$\tau^{(\alpha)} = m^{*(\alpha)} \cdot \tau \cdot s^{*(\alpha)} = P^{(\alpha)} : \tau \tag{3.32}$$

Equation (3.32) is differentiated, it can be expressed as

$$\dot{\tau}^{(\alpha)} = \dot{P}^{(\alpha)} : \tau - P^{(\alpha)} : \dot{\tau} \tag{3.33}$$

where

$$\dot{P} = \frac{1}{2}\left(s^* m^{*T} + m^* s^{*T}\right)^* = \frac{1}{2}\left(\dot{s}^* m^{*T} + s^* \dot{m}^{*T} + \dot{m}^* s^{*T} + m^* \dot{s}^{*T}\right) \tag{3.34}$$

Firstly, $\dot{s}*$ and $\dot{m}^*$ must be obtained. So Equations (3.2) and (3.3) can be differentiated as

$$\begin{aligned} \dot{s}^* &= \left(F^* s^*\right)^* = \dot{F}^* s^* \\ &= \dot{F}^* F^{*-1} F^* s \\ &= \left(\dot{F}^* F^{*-1}\right) s^* \end{aligned} \tag{3.35}$$

$$\dot{m}^* = \left[\left(F^{*-1}\right)^T m\right]^* = \left(F^{*-1}\right)^T m \tag{3.36}$$

For

$$\left(F^* F^{*-1}\right)^* = 0$$

$$\Rightarrow \dot{F}^* F^{*-1} + F^* \dot{F}^{*-1} = 0$$

$$\Rightarrow \dot{F}^{*-1} = -F^{*-1} \dot{F}^* F^{*-1}$$

$$\Rightarrow \left(\dot{F}^{*-1}\right)^T = -F^{*-1} \dot{F}^* F^{*-1}$$

So

$$\dot{m}^* = \left(F^{*-1}\right)^T m$$

$$= \left(- F^{*-1}\dot{F}^* F^{*-1}\right)m$$

$$= \left(\dot{F}^* F^{*-1}\right)^T m^* \tag{3.37}$$

Equations (3.35) and (3.37) can be used in Equation (3.34), and the result is

$$\dot{P} = \frac{1}{2}\left[\left(\dot{F}^* F^{*-1}\right)s^* m^{*T} - s^* m^{*T}\left(\dot{F}^* F^{*-1}\right) - \left(\dot{F}^* F^{*-1}\right)^T m^* s^{*T} + m^* s^{*T}\left(\dot{F}^* F^{*-1}\right)^T\right]$$

$$= \frac{1}{2}\left[\left(\dot{F}^* F^{*-1}\right)s^* m^{*T} - \left(\dot{F}^* F^{*-1}\right)m^* s^{*T}\right] + \frac{1}{2}\left[- m^* s^{*T}\left(F^* F^{*-1}\right) + m^* s^{*T}\left(F^* F^{*-1}\right)^T\right]$$

$$= \frac{1}{2}\left[\left(L^* s^* m^{*T} - L^{*T} m^* s^{*T}\right) + \left(- s^* m^{*T} L^* + m^* s^{*T} L^{*T}\right)\right]$$

$$= \frac{1}{4}\left[\left(L^* - L^{*T}\right)\left(s^* m^{*T} + m^* s^{*T}\right) + \left(L^* + L^{*T}\right)\left(s^* m^{*T} - m^* s^{*T}\right)\right]$$

$$- \frac{1}{4}\left[\left(s^* m^{*T} + m^* s^{*T}\right)\left(L^* - L^{*T}\right) + \left(s^* m^{*T} - m^* s^{*T}\right)\left(L^* + L^{*T}\right)\right]$$

$$\Rightarrow \dot{P}^{(\alpha)} = \Omega^* P^{(\alpha)} + D^* W^{(\alpha)} - P^{(\alpha)}\Omega^* - W^{(\alpha)} D^* \tag{3.38}$$

Equation (3.38) is used in Equation (3.33), so,

$$\dot{\tau}^{(\alpha)} = \dot{P}^{(\alpha)} : \tau + P^{(\alpha)} : \dot{\tau}$$

$$= \left(\Omega^* P^{(\alpha)} + D^* W^{(\alpha)} - P^{(\alpha)}\Omega^* - W^{(\alpha)} D^*\right) : \tau + P^{(\alpha)} : \dot{\tau} \tag{3.39}$$

If Equation (3.24) is used in Equation (3.39), it can be written as ($\dot{F}^* F^{*-1} = D^* + \Omega^*$)

$$\dot{\tau}^{(\alpha)} = \Omega^* P^{(\alpha)} : \tau - P^{(\alpha)}\Omega^* : \tau + D^* W^{*(\alpha)} : \tau - W^{*(\alpha)} D^* : \tau + P^{(\alpha)} : \left(\overset{\nabla^*}{\tau} - \Omega^*\tau + \tau\Omega^*\right)$$

$$= D^* W^{(\alpha)} : \tau - W^{(\alpha)} D^* : \tau + P : \overset{\nabla^*}{\tau}$$

($AB : C = A : CB^T = B : A^T C$, τ is symmetric tensor)

$$= D^* : W^{(\alpha)} \tau - D^* : \tau W^{(\alpha)} + P^{(\alpha)} : \overset{\nabla^*}{\tau}$$

$$= D^* : \beta + P^{(\alpha)} : L : D^*$$

$$= \left(P^{(\alpha)} : L + \beta\right) : D^* \tag{3.40}$$

$$= m^* \cdot \left(\overset{\nabla^*}{\tau} - D^* \cdot \tau + \tau \cdot D^* \right) \cdot s^{*T} \tag{3.41}$$

According to the theory of dislocation, dislocation is determined by the value of the shearing stress where, after $\tau^{(\alpha)}$ equals the critical value τ_0, dislocation in the $\alpha\, th$ slip system is activated and the slip direction of dislocation is up to the direction of τ_0.

After the grain yields, the resolving shearing stress increases as the grains harden. The increment of stress is determined by the increment of the slipping strain and the coefficient of hardening. It can be expressed as

$$\sum_{\beta=1}^{n} h_{\alpha\beta} \dot{\gamma}^{(\beta)} \tag{3.42}$$

where $h_{\alpha\beta}$ expresses the effect of slip in the $\beta\, th$ slip system on the resolved shear stress in the $\alpha\, th$ slip system. So in the activated slip system it can be obtained as

$$\dot{\tau}^{(\alpha)} = \sum_{\beta=1}^{n} h_{\alpha\beta} \dot{\gamma}^{(\beta)} \tag{3.43}$$

It can also be obtained from Equation (3.40)

$$\tau^{(\alpha)} = \left(P^{(\alpha)} : L + \beta\right) : D^*$$

$$= \left(P^{(\alpha)} : L + \beta\right)\left(D - D^p\right) \tag{3.44}$$

If Equation (3.41) is used in Equation (3.43), it can be obtained as

$$\dot{\tau}^{(\alpha)} = \left(P^{(\alpha)} : L + \beta\right) : D - \sum_{\beta} \left(P^{(\alpha)} : L : P^{(\beta)} + \beta^{(\alpha)} : P^{(\beta)}\right)\dot{\gamma}^{(\beta)} \tag{3.45}$$

For the mobile slip system, if this equation is used in the previous equation, the result is as

$$\left(P^{(\alpha)} : L + \beta^{(\alpha)}\right) : D = \sum_{\beta=1}^{n} N_{\alpha\beta}\dot{\gamma}^{(\beta)} \tag{3.46}$$

The matrix $N_{\alpha\beta}$ in the previous equation can be expressed as

$$N_{\alpha\beta} = h_{\alpha\beta} + P^{(\alpha)} : L : P^{(\beta)} + \beta : P^{(\beta)} \tag{3.47}$$

From Equation (3.47), if the matrix $N_{\alpha\beta}$ is reversible, the slip strain rate $\dot{\gamma}^{(\beta)}$ can be obtained. If the hardening coefficients are mutually independent, this condition can always be met. Therefore, the slip rate can be obtained from Equation (3.46) as

$$\dot{\gamma}^{(\alpha)} = \left(N^{-1}\right)_{\alpha\beta}\left(P^{(\beta)} : L + \beta^{(\beta)}\right) : D \tag{3.48}$$

If Equation (3.48) is used in Equation (3.33), the constitutive equation of material can be obtained as

$$\overset{\nabla}{\tau} = C : D \tag{3.49}$$

where *C* is the rigid matrix, it can be written as

$$C = L - \sum_{\alpha}\sum_{\beta}\left(P^{(\alpha)} : L + \beta^{(\alpha)}\right)\left(N^{-1}\right)_{\alpha\beta}\left(P^{(\beta)} : L + \beta^{(\beta)}\right) \tag{3.50}$$

3.2.3 Rate dependent crystal plasticity constitutive equation

The obvious defect in the rate independent crystal plasticity constitutive equation is that it cannot make the shear rate unique and its hardening coefficient is too complicated. In order to overcome these defects, Pierce [104] and Asaro et al. [105] developed a rate dependent crystal plasticity constitutive theory.

This theory considers that deformation has no effect on the elastic property of grain, and therefore the Jaumann rate of the Kirchhoff stress based on the intermediate state can be expressed as

$$\overset{\nabla^*}{\tau} = L : D^* \tag{3.51}$$

It can be obtained from a similar deduction in Section 3.2.2

$$\overset{\nabla}{\tau} = L : D - \sum_{\alpha} R^{(\alpha)} \dot{\gamma}^{(\alpha)} \tag{3.52}$$

where $R^{(\alpha)}$ is

$$R^{(\alpha)} = L : P^{(\alpha)} + \beta^{(\alpha)} \tag{3.53}$$

A feature of this rate dependent constitutive equation is that the shearing rate is determined by the current state and stress since it is independent of the stress rate and deformation path. This is the fundamental difference between the rate independent constitutive equation and rate dependent constitutive equation. There is an exponential function relationship between the slip rate and resolving shear stress which is shown in the following equation

$$\dot{\gamma}^{(\alpha)} = \dot{a}^{(\alpha)} \left[\frac{\tau^{(\alpha)}}{g^{(\alpha)}} \right] \left[\frac{\tau^{(\alpha)}}{g^{(\alpha)}} \right]^{(1/m)-1} \tag{3.54}$$

where *m* is the stress sensitive parameter of the slip system. If the slip rate is always $\dot{a}$, the resolving shearing stress $\tau^{(\alpha)}$ equals $g^{(\alpha)}$. In fact, equation $\tau^{(\alpha)} = g^{(\alpha)}$ can be taken as a reference state and $\dot{a}$ is the slip rate in the reference state. $g^{(\alpha)}$ represents the ability of the grain to harden. However, a practical expression of $g^{(\alpha)}$ is probably complicated, so in order to simplify the simulation, a simplified function of $g^{(\alpha)}$ is used where it is only a function of the gross slip deformation.

$$g^{(\alpha)} = g^{(\alpha)}(\gamma) \tag{3.55}$$

where γ is the gross slip deformation

$$\gamma = \sum_{\alpha} \left| \gamma^{(\alpha)} \right| \tag{3.56}$$

The hardening feature of the material can be embodied by the function $g^{(\alpha)}$, when $\gamma = 0$, the initial value of $g^{(\alpha)}$ is τ_0. The variation of $g^{(\alpha)}$ can be expressed as

$$\dot{g}^{(\alpha)} = \sum_{\beta} h_{\alpha\beta} \left| \dot{\gamma}^{(\beta)} \right| \tag{3.57}$$

where $h_{\alpha\beta}$ is the function of γ.

In the rate dependent constitutive equation, there is no obvious yield point in the metal, but if the resolving stress in the slip system is not zero, plastic shearing continues. However, because the stress sensitive parameter *m* is small ($m < 0.02$), the shear rate is minimal when the resolving shear stress is less than τ_0. Therefore, the τ_0 can be taken as the yield resolving shear stress.

The hardening modulus matrix $h_{\alpha\beta}$ includes not only the effect of self hardening (hardening caused by slip in the self-slip system), but also the effect of latent hardening (hardening caused by slip of the else slip systems). It can be expressed as

$$h_{\alpha\beta} = qh + (1-q)h\delta_{\alpha\beta} \tag{3.58}$$

where q is the ratio of self hardening and latent hardening. In general $1 < q < 1.4$, but in order to make the $h_{\alpha\beta}$ symmetric, it can also be expressed as

$$h_{\alpha\beta} = qh + (1-q)h\delta_{\alpha\beta} + \frac{1}{2}\left(\beta^{(\alpha)} : P^{(\beta)} - \beta^{(\beta)} : P^{(\alpha)}\right) \tag{3.59}$$

The hardening of the slip system can be fitted by the hyperbolic curve. It is shown in the following equation

$$h(\gamma) = h_0 \sec h^2 \left(\frac{h_0 \gamma}{\tau_s - \tau_0} \right) \tag{3.60}$$

3.3 Development of polycrystal constitutive theories

In polycrystal constitutive theory, plastic behaviour is taken as an average response of all the single grains. Several types of polycrystal models have been used in the simulation of polycrystal plastic behaviour.

The earliest polycrystal model had been brought forward by Sachs [87] in 1928, and it described the simplest grain deformation. It assumed that each grain in the polycrystal has the same stress state as the whole polycrystal aggregate. This assumption only meets the stress balance of boundaries of the grains, but could not maintain the intergranular strain compatibility. Moreover this model assumed that during deformation each grain is taken as a single grain without any constraints, and therefore plastic deformation of the grains can be generated by a single slip system. In practical polycrystal aggregates, the stress state of each grain is not the uniaxial stress state and their deformation is not the same. Furthermore, the surrounding grains can influence deformation by the constraint of the grain boundaries. For the above reasons, the original Sachs model can only describe the plastic behaviour of single grain, could not deal with polycrystal deformation [106]. But after making modification, Sachs model can successfully depict polycrystal deformation.

In 1938, Taylor [88] developed the Taylor full constraint model based on the assumption of homogeneous strain in polycrystals. Taylor assumed each grain in the aggregate experiences the same stain as the polycrystal $\varepsilon_y = \varepsilon_z = -1/2\varepsilon_x$, and ignored the elastic strain. This assumption can only meet the compatibility of the grain boundary, but ignores the stress equilibrium. Under this condition, the five slip systems of the grain will be activated, this is the Taylor rule. If the volume of specimen is assumed as a constant under the condition of plastic strain, then there are five independent strain tensors in the specimen need to be activated and produce any change in shape. Taylor set up a multiple slip model with the assumption of the same slip systems, and considered that every combination of the five cubic <110> {111} slip systems can lead to deformation. The slippage $\sum \left| d\gamma_i \right|$ needed by the strain

increment $d\varepsilon_x$ was calculated, and the external stress can be obtained by the following equation.

$$\sigma_x = \tau\left(\left|d\gamma_i\right| \Big/ d\varepsilon_x\right) = M\tau \tag{3.61}$$

where τ is the shear stress, M is the Taylor factor of grain orientation.

Bishop and Hill [107] expanded the Taylor theory with a multiple strain condition. Taylor defined the slip system with minimum shear stress, but Bishop and Hill determined the slip systems by the principle of maximum work. The two methods are theoretically equivalent. Lin [108] modified the Taylor model by the addition of elasticity. It was considered that the grain deformation (elastic deformation and plastic deformation) equals the applied deformation (elastic deformation and plastic deformation) of polycrystal aggregate. For large strains the TBH (Taylor-Bishop-Hill) model has strict conditions and could not predict the situation without an equiaxed grain. The relaxed Taylor model [109] solved the former problems because it allowed for the difference between the transgranular strain and an average of the large strain. In the relaxed Taylor model the applied shear rate should not be met as it released the constraint conditions. According to this assumption, intergranular local incompatibility is permitted. The key point of the relaxed Taylor models is that the strain compatibility can improve the stress homogeneity.

In the 1960s, a new, internally consistent polycrystal model had been developed that meets the need of the stress equilibrium and strain compatibility [91, 110]. It can deal with the problems of internal stress while polycrystals are being deformed. This internally consistent model explains the interaction between the grain and the external environment by taking the grain as an elasto-plastic ball or an ellipsoid inclusion embedded in an infinitely homogeneous medium. The Eshelby method is applied to solve this kind of problem and obtain the relationship between the stress and strain of polycrystal aggregate in the grain scale. The final aim of this model is to establish how the polycrystals respond by linking the intergranular stress and strain with the stress and strain in a homogeneous medium. Many kinds of internally consistent models have been set up by including the features and properties of

different microstructures in the constitutive rules. The first internally consistent model has been developed by Kroner [91]. He assumed that the base is an isotropic elastic infinite medium. The following internally consistent models were all based on this model and modified the description of the mechanical properties of the base. Hill [111] put an elastic base in his model. Berveiller and Zaoui [112] simplified the Hill model by the assumption of isotropic plasticity and the introduction of a new scalar plastic function. Iwakuma and Nemat-Nasser [113] generalised the application of Hill's model in finite deformation by an explanation of grain deformation and revolution. When the grain shape turns from an initial ball into a prolate and oblate ball, a modified Eshelby tensor will be used in the grain deformation.

3.4 Application of crystal plasticity finite element simulation

The CPFEM has already been applied to simulate polycrystal deformation. It includes bulk and sheet forming. There are at present, two applications of CPFEM: one is to predict how the microstructure will develop and the other is the prediction of properties. Some simulations only focus on one case, while others focus on the development of microstructure and prediction of properties.

3.4.1 Texture simulation

Texture is the main reason for material anisotropy. CPFEM has already successfully simulated texture and its development. Asaro and Needman [99] first used a rate dependent elasto-plastic polycrystal model to predict deformed texture under different stress-strain paths in single phase FCC metal. The rate dependent model successfully solved the problem that the movable slip system in the rate independent model is not unique. In rate dependent theories, because the slip rates of all slip systems are the same, the rotation and textures of the lattice are all the same.

Mathur et al. [114] simulated the development of rolling texture, and compared it to the measured texture data and modelling texture [115]. In their simulation, the relaxed polycrystal model has been applied to explain the development of grain shape and texture induced by the deformation. It is shown in Figure 3.3.

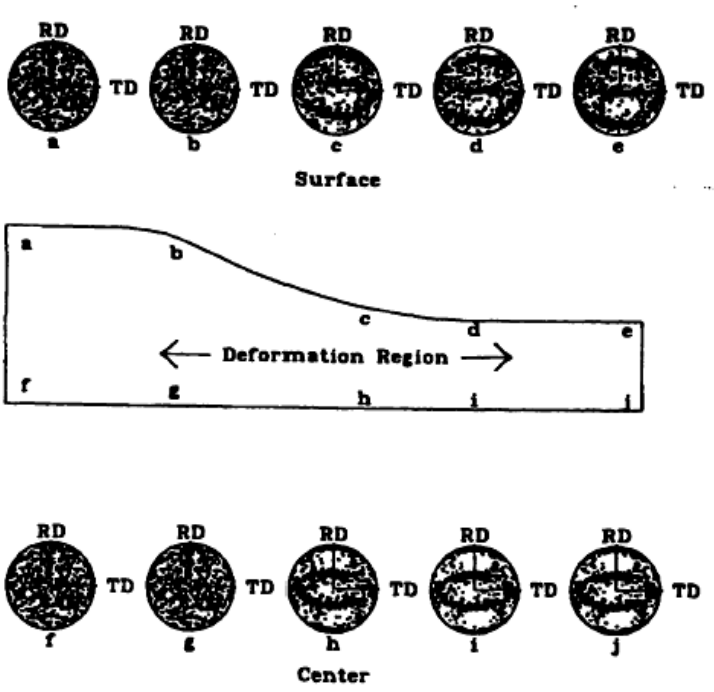

Figure 3.3 The development of {111} pole figures of aluminium surface and centre during the first pass of the rolling process [114]

In 1992 Kalidindi et al. [116, 117] developed a fully implicit procedure of time integration and used it to simulate the texture development of FCC metal. The results showed that this model has the ability to make good predictions. Sarma and Dawson [118] developed a polycrystal model which included interaction of the adjacent grains and used it to simulate the development of texture. They compared their modelling results with the results obtained from the Taylor model and finite element model. When the results were compared, the polycrystal model concluded that interaction between the adjacent grains can improve the prediction of the strength and position of the special texture, as shown in Figure 3.4. The experimental data showed a peak near the {112} <111> copper orientation, seen as regions of high intensity along the *y*-axis, on the circumference and near the centre of the pole figure. The prediction by the Taylor model showed a shift in this component towards the {4411}<11118> Dillamore orientation or Taylor orientation. This component has shifted inwards from the circumference and outwards from the centre along the *y*-axis. Both the finite element simulation and neighbourhood compliance model predicted that this component would be close to the copper orientation. Another

deficiency of the Taylor model is its failure to predict the {110}<211> brass orientation, which appears at the extreme left and right positions along the *x*-axis, and rotated away from the *y*-axis along the circumference at the top and bottom. The neighbourhood compliance model predicts a strong brass orientation, even more than the finite element simulation.

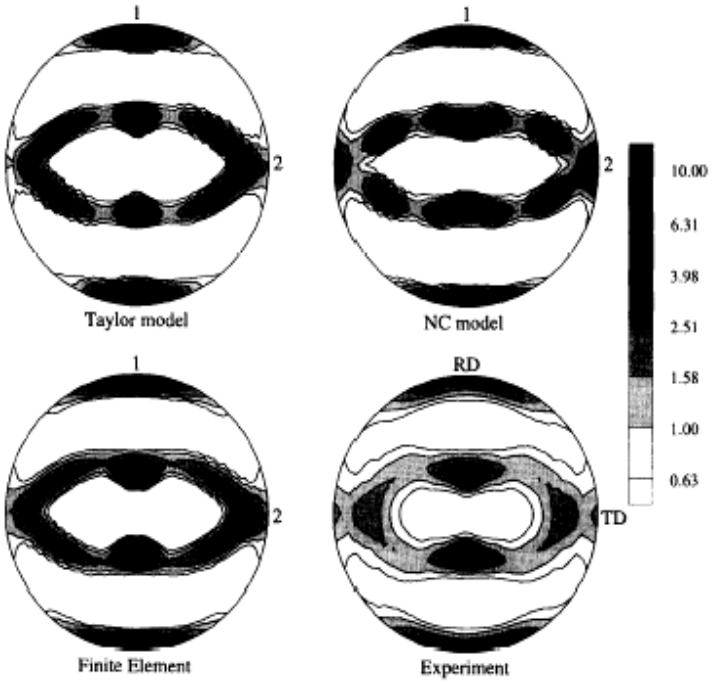

Figure 3.4 Homolographic projection of <111> pole figure during the planar compression [118]

Some researchers have already tried to use the ODF (Orientation Distributing Function) to describe the distribution of three dimensional oriental grains [119-122]. In 1996, Kumar and Dawson [119, 120] first applied the oriental space to finite element simulation of texture development. In 2000, Kumar and Dawson [120] used the new tool of texture analysis to simulate the deforming texture of FCC in Rodriguez Space. Bachu and Kalidindi [123] studied the accuracy of the finite element method application in FCC texture development. They analysed the oriental densities of α and β textures using modelling from the Taylor and finite element models. Their results showed that the simulation results from the finite element model are much close to the experimental results than the Taylor model, as shown in Figure 3.5.

In 2000, Choi et al. [124] studied the oriental stabilisation and texture development during the deep drawing process of FCC metal. Delannay et al. [125] predicted the texture of cold rolling aluminium plate under medium deformation. Recently, Rabbe and Roters [126] discussed the drawing method of a texture map in finite element simulation. They also considered the Gauss global texture is more suitable in the FEM simulation.

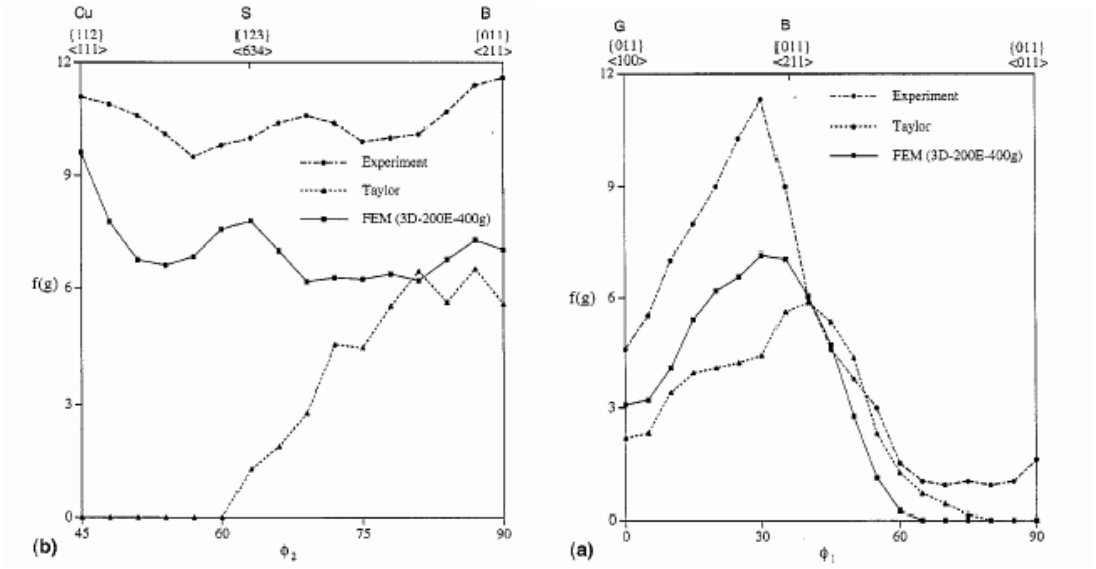

(a) α texture (b) β texture

Figure 3.5 Comparison of the modelling textures (α and β textures) with the experimental results [123]

3.4.2 Other applications of CPFEM

The CPFEM not only successfully simulated the texture development, but has also been widely applied in simulating the responses of material properties, yielding surface [127-129], earring [130-134], forming limit diagram [88, 135-139], surface roughness [8, 71-74], residual stress [140], necking [141, 142], and fatigue wear [143-153] etc.

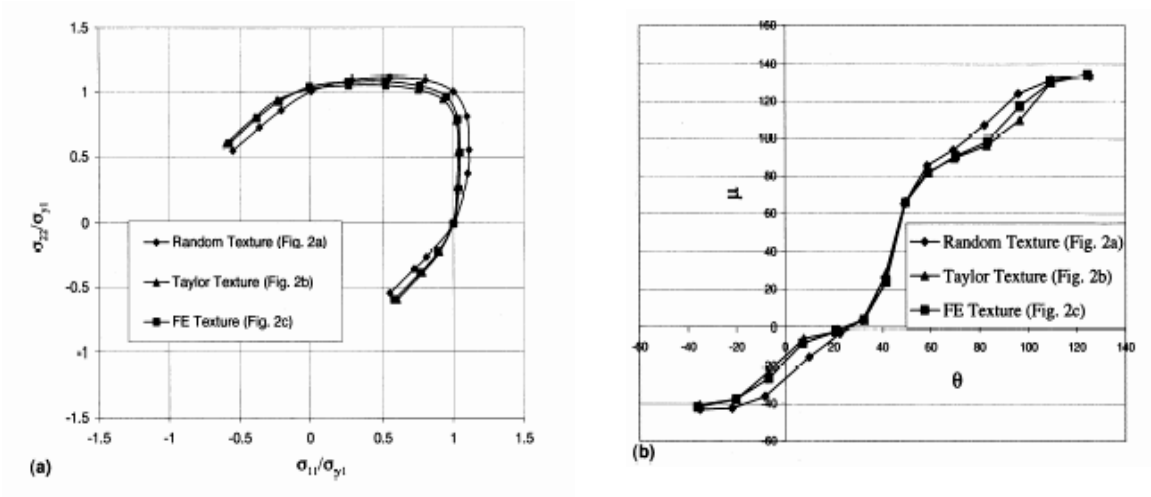

Figure 3.6 (a) Finite element prediction of polycrystal yield surface of three textures, (b) Finite element prediction of polycrystal yield surface normal line of three textures [128]

Beaudoin et al. [127] obtained the yield surface by weighing the orientation of the aggregate. Kalidindi and Schoenfeld [128] calculated the yield surface of FCC metal by the number uniform predictions of texture, as shown in Figure 3.6. Kowalczyk and Gambin [129] set up a plastic anisotropic model based on the yield surface related to the textures. It was a combination of the phenomenological and physical models. Based on the Schmid rule, the unique strain velocity direction can be determined. This model is more effective than the other physical models.

Earring is the main problem that occurs during deep drawing. Not only does it produce extra waste, it can also lead to anisotropy along the cup wall. Many researchers applied CPFEM to study deep drawing and the development of earring. Balasubramanian and Anand [130] found that the crystal plasticity theory can be used to analyse and optimise deep drawing technology. Zhou et al. [131] simulated the effect of texture on the earring of FCC metal. Inal et al. [132] applied a polycrystal and phenomenological models to simulate the earring process. The results of this modelling were that the ear was formed at the beginning of the deep drawing process. The ear is mainly led by the original texture of the metal material. The texture development has no influence on the shape of the ear.

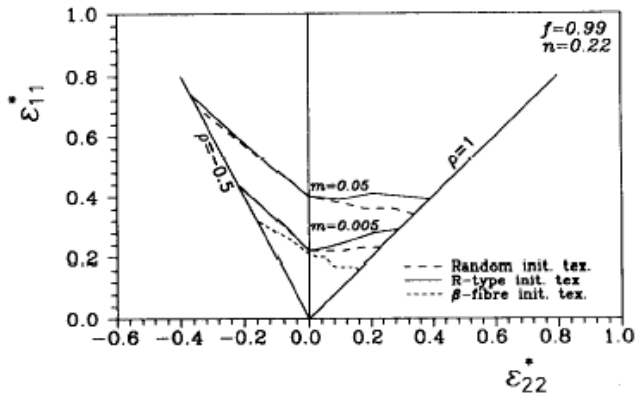

Figure 3.7 Prediction of FLD of annealing aluminium plate (m=0.005, 0.05) [135]

The forming property is often assessed by the forming limit diagram (FLD). The FLD had first been developed by Keeler in 1961, who took the forming limit as a function of the deformation path. Asaro and Needleman [99] carried out the first research on this. Zhou et al. [135], Wu et al. [136] and Savoie et al. [137] solved the influence of assumption of original texture and constitutive theories on the FLD. Zhou et al. [135] applied the rate dependent model and M-K method to predict the FLD of annealing FCC metal with different original textures, as shown in Figures 3.7 and 3.8. Recently, Nakamachi et al. [138] and Xie et al. [139] used the CPFEM to study the effect of texture on the forming properties of FCC and BCC metals.

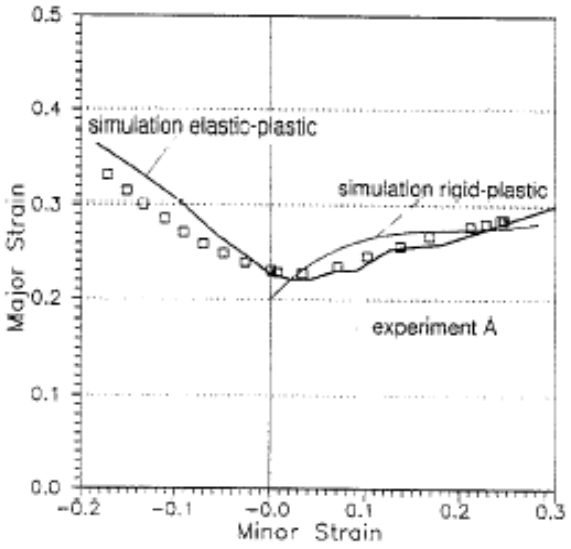

Figure 3.8 Comparison of the experimental FLD and the simulated FLDS [137]

During the metal forming process, the development of surface roughness has an enormous influence on the friction and surface quality of the product. It also plays an important role in material properties such as wear, fatigue, magneto-electric property, and forming properties. Many researchers have studied the phenomenon of surface roughening for several decades. The CPFEM applied in the research of surface roughness started from Becker and Beaudoin et al's research work [8, 71]. Becker [8] studied the effect of local strain on surface roughening during sheet forming.

However, most of the former researchers' work only focused on surface roughening of the free surface, for example the uniaxial and biaxial stretch and compression. Few researchers carried out studies of the surfaces with constraints such as the contact surface and friction surface. Furthermore, some reports only gave a qualitative analysis of the relationship between surface roughening and the other parameters. During metal forming the process of constraint deformation is more popular. The relationships between surface roughening and other technical parameters under that condition need to be studied further. This is the aim of this study.

3.5 Simplification of rate dependent crystal plasticity theory

In this study the rate dependent crystal plasticity constitutive equation has been used in the finite element model to simulate surface asperity flattening under different technical parameters (reduction, friction, annealing heat treatment, strain rate, different wave lengths and grain orientations). Crystal plasticity constitutive model is the base for crystal plasticity finite element modelling. Different crystal models have different applications in finite element modelling. As described in Sections 3.3 and 3.4, classical crystal constitutive equations are expressed by the objective stress rate (Jaumann stress rate) and deformation rate. It is very complicated to use constitutive equations in numerical simulations. In order to reduce the calculation time, Kalidindi's crystal plasticity model [116, 117] has been used to simplify the simulation of rate dependent crystal plasticity finite element modelling.

3.5.1 Decomposition of the crystal plastic deformation gradient

The kinematics of crystal plastic deformation is described in Section 3.2. According to the decomposition of the deformation gradient, it is very difficult to obtain a rotation matrix of the present configuration. Therefore, a polar decomposition of the elastic deformation gradient (right polar decomposition) shall be carried out to solve the rotation matrix. A schematic of the polar decomposition of the deformation gradient is shown in Figure 3.9.

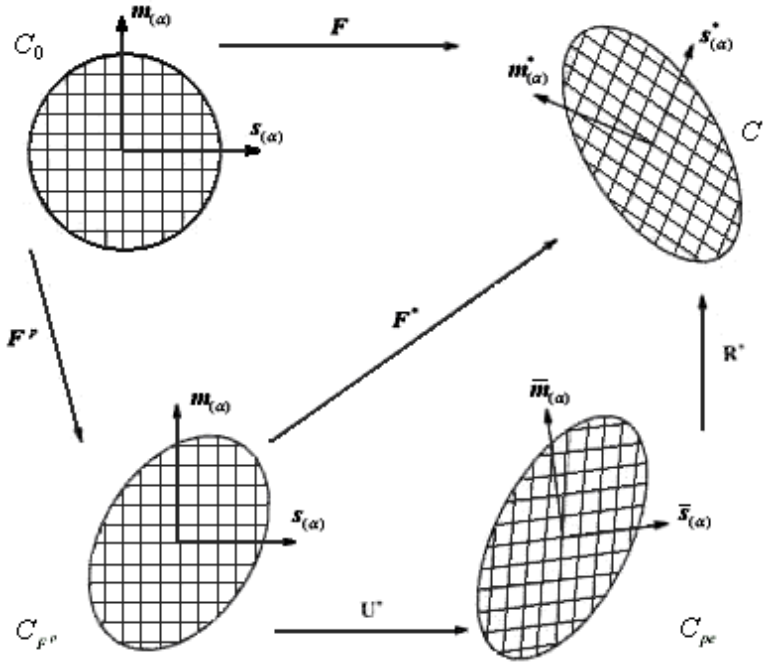

Figure 3.9 Schematic of the polar decomposition of the deformation gradient [154]

After two middle configurations C_{F^p} (pure plastic deformation) and C_{p^e} (pure elastic stretching), the initial configuration will turn to the present configuration C. During this process the elastic deformation gradient F^* is polarised and decomposed to the right stretching gradient U^* and rotation gradient R^* which is shown as [155, 156]

$$F^* = U^* R^* \tag{3.62}$$

3.5.2 Elastic constitutive equation

The crystal elastic constitutive equation can be expressed as

$$T^{(1)} = \mathcal{L} : E^{(1)} \quad . \tag{3.63}$$

where $T^{(1)}$ is the second $Piola-Kirchhoff$ stress tensor, $\mathcal{L}$ is the fourth order tensor, $E^{(1)}$ is the $Green$ elastic strain tensor. The $T^{(1)}$ can be expressed as follows

$$T^{(1)} = F^{*-1}\left(\det\left(F^{*}\right)\sigma\right)\left(F^{*}\right)^{-T} \tag{3.64}$$

where σ is the $Cauchy$ stress.

The $E^{(1)}$ can be expressed as

$$E^{(1)} = \frac{1}{2}\left(F^{*T}\cdot F^{*} - I\right) \tag{3.65}$$

3.5.3 Flow rule of plastic deformation

Flow rule of plastic deformation gradient F^{p} is shown as

$$\dot{F}^{p}F^{p^{-1}} = \sum_{\alpha=1}^{n}\dot{\gamma}_{(\alpha)}s_{(\alpha)}\otimes m_{(\alpha)} \tag{3.66}$$

where $\dot{\gamma}_{(\alpha)}$ is the plastic shear rate of the $\alpha\ th$ slip system.

3.5.4 Equation of kinematics

The relationship between the shear rate $\dot{\gamma}_{(\alpha)}$ and the resolving shear stress $\tau_{(\alpha)}$ of the $\alpha\ th$ slip system can be expressed by a power exponent equation [98, 104, 116, 157-159]. The power exponent equation is shown as

$$\dot{\gamma}_{(\alpha)} = \dot{\gamma}_{0}\,\mathrm{sgn}(\tau_{(\alpha)})\left|\frac{\tau_{(\alpha)}}{s_{(\alpha)}}\right|^{1/m} \tag{3.67}$$

where $s_{(\alpha)}$ is the slip resistance of the αth slip system.

$$\tau_{(\alpha)} \approx T^{(1)} \cdot s_{(\alpha)} \otimes m_{(\alpha)} \tag{3.68}$$

3.5.5 Hardening law

For cubic metal the hardening equation of the slip system can be simplified as [160]

$$\dot{s}_{(\alpha)} = \sum_{\beta=1}^{n} h_{\alpha\beta} \left| \dot{\gamma}_{(\beta)} \right| \tag{3.69}$$

The hardening matrix of the slip system α led by the slip system β is shown as [161-163]

$$h_{\alpha\beta} = h_0 [q_l + (1 - q_l)\delta_{\alpha\beta}] \left\{ 1 - \frac{s_{(\beta)}}{s_s} \right\}^a \tag{3.70}$$

where q_l is the latent hardening parameter, $\delta_{\alpha\beta}$ is the *Kronec*ker symbol. h_0, a and s_s are the material parameters.

3.5.6 Models of polycrystal homogenisation

(1) Taylor averaging procedure

The essential assumptions in the Taylor type polycrystal model are that all the grains have an equal volume and the local deformation gradient in each grain is homogeneous and identical to the macroscopic deformation gradient at the continuum material point level. The local deformation gradient can be expressed [116, 123] as

$$F = \overline{F} \tag{3.71}$$

where F is the local deformation gradient in each grain, $\overline{F}$ is the macroscopic deformation gradient at the continuum material point level.

The stress response at each macroscopic continuum material point is given by the average volume of the multitude of microscopic single crystalline grains comprising the material point. Then, with $\sigma^{(k)}$ denoting the Cauchy stress in the *kth* crystal, these assumptions lead to:

$$\bar{\sigma} = \frac{1}{N}\sum_{k=1}^{N}\sigma^{(k)} \tag{3.72}$$

where $\bar{\sigma}$ is the volume averaged stress, and N is the total number of grains comprising the material point. The influences of grain shape, size, and distribution are not considered in this equation.

(2) Finite element averaging procedure

In this approach the finite element calculations have been used to make a transition from the response of a single grain (or a region within a grain) to the response of a polycrystalline aggregate. It is assumed that [116, 123, and 160] each element represents one grain, and is assigned an orientation as the initial texture. So each grain is modelled to allow for non-uniform deformation between and within the grains, and both the equilibrium and compatibility are satisfied in the weak finite element sense. In this study the number of elements and number of grains in each element and the distributions of grain orientations in the mesh are varied.

3.6 Numerical integration of rate dependent crystal plasticity theory

The numerical integration of the crystal elastic-plastic constitutive equation will be carried out for the application of crystal plasticity theory in finite element modelling. Currently, researchers have already brought forward many methods of explicit and implicit integration. The above mentioned methods mainly include the rate dependent constitutive equation and rate independent constitutive equation. In this study, the Total Lagrangian implicit integration procedure has been used to integrate the crystal plasticity constitutive model.

3.6.1 Total Lagrangian Formulation

There are two choices to solve the crystal elastic-plastic constitutive equation. One is the Total Lagrange Formulation (T.L. Formulation); the other is the updated Lagrange Formulation (U.L. Formulation). In the Total Lagrange Formulation all the initial variables (*t=0*) will be taken as the reference configuration, but in the Updated Lagrange Formulation, all the variables of time *t* will be taken as a reference configuration. Both the Lagrange Formulations are shown as [164]

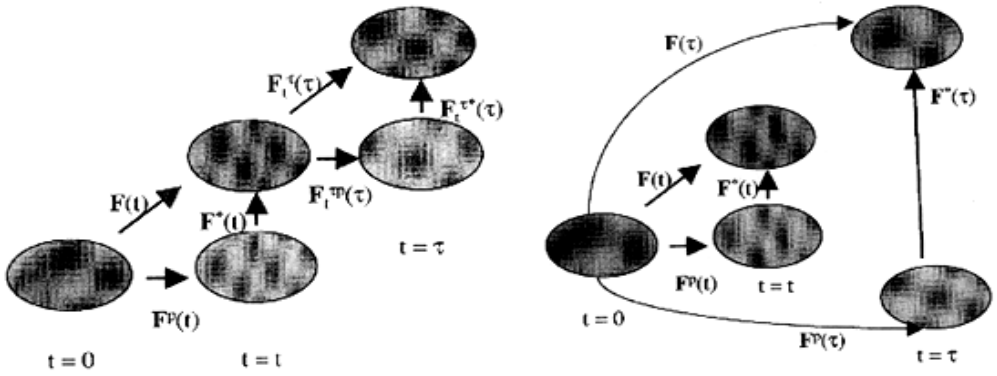

(a) Updated Lagrange Formulation (b) Total Lagrange Formulation

Figure 3.10 Numerical integrating procedures of constitutive equations [164]

The advantages of using the Lagrange Formulation in the crystal plasticity model are as follows: 1) optional solution can be applied to solve the grain orientation of special time step, but not the orientations of each time step. The time for calculation will be significantly shortened, 2) application of fully implicit integration is available and, 3) interfaces can be supplied for the application of other deformation mechanisms (such as twin etc.) in the crystal plasticity model.

3.6.2 Fully implicit integration procedure

In order to reduce the consumption of time, Kalidindi brought forward a fully implicit numerical procedure for crystal plasticity constitutive equations. The assumptions are as

1) Initial configurations ($s_{(a)}$, $m_{(a)}$) are given, 2) values of ${}^{t}F$, ${}^{t}F^{p}$ and ${}^{t}s_{(\alpha)}$ are also given, 3) ${}^{\tau}F$ of time $\tau = t + \Delta t$ can be estimated.

According to the flow rule of Equation (3.66), F^{p} of time $t + \Delta t$ can be obtained as

$$ {}^{\tau}F^{p} \doteq \left\{ I + \sum_{\alpha=1}^{n} {}^{\tau}\Delta\gamma_{(\alpha)} s_{(\alpha)} \otimes m_{(\alpha)} \right\} {}^{t}F^{p} \tag{3.73} $$

where ${}^{\tau}\Delta\gamma_{(\alpha)}$ is as

$$ {}^{\tau}\Delta\gamma_{(\alpha)} = \dot{\gamma}_{(\alpha)}({}^{\tau}\tau_{(\alpha)}, {}^{\tau}s_{(\alpha)})\Delta t \tag{3.74} $$

${}^{\tau}\Delta\gamma_{(\alpha)}$ can be expressed as

$$ {}^{\tau}\Delta\gamma_{(\alpha)} = \dot{\gamma}_{(\alpha)}(\tau_{(\alpha)}({}^{\tau}T^{(1)}), {}^{\tau}s_{(\alpha)})\Delta t \tag{3.75} $$

Simultaneously,

$$ {}^{\tau}F^{p^{-1}} = {}^{t}F^{p^{-1}} \left\{ I - \sum_{\alpha=1}^{n} {}^{\tau}\Delta\gamma_{(\alpha)} s_{(\alpha)} \otimes m_{(\alpha)} \right\} \tag{3.76} $$

At the time $t + \Delta t$, the stress can be obtained as

$$ {}^{\tau}T^{(1)} = \mathcal{L} : \left[\frac{1}{2} \left\{ {}^{\tau}F^{p^{-T}} {}^{\tau}F^{T} {}^{\tau}F {}^{\tau}F^{p^{-1}} - I \right\} \right] \tag{3.77} $$

If

$$ X = {}^{\tau}F^{p^{-T}} {}^{\tau}F^{T} {}^{\tau}F {}^{\tau}F^{p^{-1}} \tag{3.78} $$

If Equation (3.76) is used in Equation (3.78), it can be obtained as

$$ \begin{aligned} X = {}& {}^{t}F^{p^{-T}} {}^{\tau}F^{T} {}^{\tau}F {}^{t}F^{p^{-1}} - \\ & \sum_{\alpha=1}^{n} {}^{\tau}\Delta\gamma \left(s_{(\alpha)} \otimes m_{(\alpha)} \right)^{T} {}^{t}F^{p^{-T}} {}^{\tau}F^{T} {}^{t}F^{p^{-1}} - \\ & {}^{t}F^{p^{-T}} {}^{\tau}F^{T} {}^{\tau}F {}^{t}F^{p^{-1}} \sum_{\alpha=1}^{n} {}^{\tau}\Delta\gamma \left(s_{(\alpha)} \otimes m_{(\alpha)} \right) + O\left(\Delta\gamma^{\alpha^{2}} \right) \end{aligned} \tag{3.79} $$

If $O\left(\Delta\gamma^{\alpha^2}\right)$ is omitted then Equation (3.79) can be expressed as

$$ {}^{\tau}F^{p^{-T}}\,{}^{\tau}F^{T}\,{}^{\tau}F\,{}^{\tau}F^{p^{-1}} \doteq A-\sum_{\alpha=1}^{n}{}^{\tau}\Delta\gamma B_{(\alpha)} \tag{3.80} $$

$$ A={}^{t}F^{p^{-T}}\,{}^{\tau}F^{T}\,{}^{\tau}F\,{}^{t}F^{p^{-1}} \tag{3.81} $$

$$ B_{(\alpha)} = A\left(s_{(\alpha)}\otimes m_{(\alpha)}\right)+\left(s_{(\alpha)}\otimes m_{(\alpha)}\right)^{T}A \tag{3.82} $$

Finally, Equation (3.80) is used in Equation (3.77) as

$$ {}^{\tau}T^{(1)} \doteq T^{(1)tr}-\sum_{\alpha=1}^{n}\Delta\gamma\left(\tau_{(\alpha)}({}^{\tau}T^{(1)},{}^{\tau}s_{(\alpha)})\right)C_{(\alpha)} \tag{3.83} $$

Among the equations,

$$ \boldsymbol{T}^{(1)tr} = \mathcal{L}:\left[(1/2)\{\boldsymbol{A}-\boldsymbol{I}\}\right] \tag{3.84} $$

$$ \boldsymbol{C}_{(\alpha)} = \mathcal{L}:\left[(1/2)\boldsymbol{B}_{(\alpha)}\right] \tag{3.85} $$

where $\boldsymbol{T}^{(1)tr}$, $\boldsymbol{A}$, $\boldsymbol{B}_{(\alpha)}$ and $C_{(\alpha)}$ can be obtained by the given tensors, and $\Delta\gamma_{(\alpha)}$ is the function of unknown tensors ${}^{\tau}T^{(1)}$ and ${}^{\tau}s_{(\alpha)}$.

Further, fully implicit integration is used in the equation of slip resistance $s_{(\alpha)}$ as

$$ {}^{\tau}s_{(\alpha)}={}^{t}s_{(\alpha)}+\sum_{\beta=1}^{n}h_{\alpha\beta}({}^{\tau}s_{(\beta)})\left|\Delta\gamma_{(\beta)}\left(\tau_{(\alpha)}({}^{\tau}\boldsymbol{T}^{(1)},{}^{\tau}s_{(\beta)})\right)\right| \tag{3.86} $$

where Equations (3.83) and (3.86) are the non-linear equations of ${}^{\tau}\boldsymbol{T}^{(1)}$ and ${}^{\tau}s_{(\alpha)}$. Equation (3.85) can be solved by two step iterations. In the first step iteration ${}^{\tau}s_{(\alpha)}$ can be estimated and ${}^{\tau}\boldsymbol{T}^{(1)}$ will be solved by Equation (3.83). The Newton iterative method has been used in the calculation. The equation is shown as

$$ {}^{\tau}\boldsymbol{T}^{(1)}_{n+1}={}^{\tau}\boldsymbol{T}^{(1)}_{n}-\mathcal{J}_{n}^{-1}\left[\boldsymbol{G}_{n}\right] \tag{3.87} $$

where

$$\mathcal{J}_n = \boldsymbol{I} + \sum_{\alpha=1}^{n} \left\{ \frac{\partial}{\partial \tau_{(\alpha)}} \Delta\gamma_{(\alpha)} \left(\boldsymbol{\tau}_{(\alpha)} ({}^{\tau}\boldsymbol{T}_n^{(1)}, {}^{\tau}s_{(\alpha)k}) \right) \right\} \boldsymbol{C}_{(\alpha)} \otimes \left(\boldsymbol{s}_{(\alpha)} \otimes \boldsymbol{m}_{(\alpha)} \right) \tag{3.88}$$

where tensors with subscripts of n and n+1 refer to the estimated tensors after n and n+1 step iterations, tensor $s_{(\alpha)k}$ means the value of ${}^{\tau}s_{(\alpha)}$ after k times' updating.

The increment of iteration can be expressed as

$$\Delta\boldsymbol{T}^{(1)} = {}^{\tau}\boldsymbol{T}_{n+1}^{(1)} - {}^{\tau}\boldsymbol{T}_n^{(1)} \tag{3.89}$$

If

$$\left| \Delta\boldsymbol{T}_{ij}^{(1)} \right| < \eta s_0 \tag{3.90}$$

The first step iteration will be finished, otherwise

$${}^{\tau}\boldsymbol{T}_{n+1}^{(1)} = {}^{\tau}\boldsymbol{T}_n^{(1)} + \eta s_0 \operatorname{sgn}\left\{ \Delta\boldsymbol{T}^{(1)} \right\} \tag{3.91}$$

where η is a constant.

After the convergence of ${}^{\tau}\boldsymbol{T}^{(1)}$, the second step iteration of ${}^{\tau}s_{(\alpha)}$ will start as

$${}^{\tau}s_{(\alpha)k+1} = {}^{t}s_{(\alpha)} + \sum_{\beta=1}^{n} h_{\alpha\beta} ({}^{\tau}s_{(\beta)k}) \left| \Delta\gamma_{(\beta)} \left(\tau_{(\alpha)} ({}^{\tau}\boldsymbol{T}_{n+1}^{(1)}, {}^{\tau}s_{(\beta)k}) \right) \right| \tag{3.92}$$

The initial values of ${}^{\tau}\boldsymbol{T}^{(1)}$ and ${}^{\tau}s_{(\alpha)}$ are ${}^{t}\boldsymbol{T}^{(1)}$ and ${}^{t}s_{(\alpha)}$ at time t, respectively Criteria of convergence is as

$$Max\left\{ {}^{\tau}\boldsymbol{T}^{(1)} \right\} < 10^{-4}, \; Max\left\{ {}^{\tau}s_{(\alpha)} \right\} < 10^{-3} \tag{3.93}$$

${}^{\tau}\Delta\gamma_{(\alpha)}$ can be obtained by a combination of Equations (3.67), (3.69) and (3.75). Then ${}^{\tau}\boldsymbol{F}^{p}$ and ${}^{\tau}\boldsymbol{F}^{p^{-1}}$ can be obtained by Equation (3.73). ${}^{\tau}\boldsymbol{F}^{*}$ can be obtained from

Equation (3.1), ${}^{\tau}\mathbf{E}^{(1)}$ can be obtained by Equation (3.65), and ${}^{\tau}\boldsymbol{\sigma}$ can be updated by Equation (3.64).

3.7 Calculation of grain orientation

If the initial grain orientation can be expressed by a matrix $\boldsymbol{g}$, the grain orientation in the specimen coordinate can be expressed as [165-171]

$$\mathbf{b}^{g} = \mathbf{g}\mathbf{b}^{c} \tag{3.94}$$

where $\mathbf{b}^{c}$ is the grain orientation in grain coordinates, $\mathbf{b}^{g}$ is the same vector of specimen coordinates. At time τ, the vector of the specimen can be expressed as

$${}^{\tau}\mathbf{b}^{g} = \mathbf{R}^{*}\mathbf{b}^{g} = \mathbf{R}^{*}\mathbf{g}\mathbf{b}^{c} \tag{3.95}$$

Therefore, the grain orientation matrix is $\mathbf{R}^{*}\mathbf{g}$, by the new grain orientation matrix, and three Euler angles can be obtained.

3.8 UMAT of crystal plasticity constitutive model employed in ABAQUS

ABAQUS is software used for engineering modelling which is widely applied as advanced general finite element software. It can solve problems, ranging from simplified linear analysis to complicated non-linear simulations. ABAQUS provides a lot of sub-routines which allow users to define their own models with special functions. The user subroutine UMAT is an interface for the FORTRAN programming by which a user can define a material model that is different from the ABAQUS program library [172, 173]. ABAQUS does not provide a crystal plasticity constitutive model, so a crystal plasticity constitutive model can be used by programming the ABAQUS/Standard UMAT.

3.8.1 UMAT of ABAQUS

User-defined Material Mechanical Behaviour (UMAT) exchanges the data with ABAQUS by an interface with the main ABAQUS solving program. In the input file,

properties of materials can be defined in the module of “USER MATERIAL”. Owing to data exchange and some shared variables, UMAT has a certain rule that is shown as [174, 175]

```
SUBROUTINE UMAT (STRESS, STATEV, DDSDDE, SSE, SPD, SCD,
1 RPL, DDSDDT, DRPLDE, DRPLDT,
2 TRAN, DSTRAN, TIME, DTIME, TEMP, DTEMP, PREDEF, DPRED, CMNAME,
3 NDI, NSHR, NTENS, NSTATV, PROPS, NPROPS, COORDS, DROT, PNEWDT,
4 CELENT, DFGRD0, DFGRD1, NOEL, NPT, LAYER, KSPT, KSTEP, KINC)
C
      INCLUDE’ABA_PARAM.INC’
C
      CHARACTER*80 CMNAME
      DIMENSION STRESS (NTENS), STATEV (NSTATV),
1 DDSDDE (NTENS, NTENS), DDSDDT (NTENS), DRPLDE (NTENS),
2 STRAN (NTENS), DSTRAN (NTENS), TIME (2), PREDEF (1), DPRED (1),
3 PROPS (NPROPS), COORDS (3), DROT (3, 3), DFGRD0 (3, 3), DFGRD1 (3, 3)

user coding to define DDSDDE, STRESS, STATEV, SSE, SPD, SCD
and, if necessary, RPL, DDSDDT, DRPLDE, DRPLDT, PNEWDT

RETURN
END
```

This interface has two functions, one is to make sure the stress state of the material is at the current increment, and calculate all kinds of variables of the material state. The other is to calculate the Jacobian matrix $\partial\Delta\sigma/\partial\Delta\varepsilon$ of current material configuration. UMAT has no special requirements for the material constitutive model so it is quite suitable for theoretical study. The stability and rate of convergence depends on the material constitutive model.

In the UMAT, there are many matrices such as DDSDDE, DDSDDT, DRPLDE etc. which express the stress and strain state, etc. Different tensors have elements with different freedoms so when the UMAT code is compiled, the sorts of element should be considered. Some explanations of variables are given as

DDSDDE (NTENS, NTENS) is the Jacobian matrix ($\partial\Delta\sigma / \partial\Delta\varepsilon$) of constitutive equations, $\Delta\sigma$ is the stress increment at the current step incremental step, $\Delta\varepsilon$ is the strain increment. DDSDDE (*I*, *J*) expresses the variance ratio of the *I*th stress component interacted by the *J th* strain component. It is a symmetric matrix.

STRESS (NTENS) is an array of the stress tensors which includes NDI normal stress components and NSHR shear stress components. At the beginning of the incremental step calculation, the matrix of the stress tensors is transferred to the UMAT by an interface between UMAT and the main program. When the calculation of the incremental steps has been finished, the matrix of stress tensors will be updated by UMAT. In the finite-strain problem of rigid rotation, the stress tensors will be rotated before calling the incremental step. In the UMAT, the stress tensors are the Cauchy stresses (true stress).

STATEV (NSTATEV) is used to store the array of state variables related to the solution. They are also transferred to the UMAT at the beginning of the incremental step calculation. The data can be updated in the subroutine USDFLD or UEXPAN, and then transferred to UMAT. The dimension of state variables can be defined by the "*DEPVAR".

PROPS (NPROPS) are the array of material constants. NPROPS is the number of materials. It is the same as the definition of "CONSTRANTS" in the subroutine "*USER MATERIAL". The data of PROPS (NPROPS) is the same as the data of the subroutine "*USER MATERIAL". At each incremental step, SSE, SPD, SCD can separately define the elastic strain energy, the plastic dissipative energy, and the creep dissipative energy.

PNEWDT is the ratio of the suggested time increment and current time increment. The step increment can be controlled by this variable. If the value of PNEWDT is less than 1, the current iteration will stop and select a smaller step size for the solution. The new step is the value of PNEWDT×DTIME. If the value of PNEWDT is larger than 1, the iteration of the current incremental step will converge. The size of the next loading step will increase, and the new step size is the value of PNEWDT×DTIME. The value of PNEWDT will be the minimal in all the iterations of the automatic step mode. If the mode is not activated, there will be no response when the value of PNEWDT exceeds 1, and the calculation will stop when the value of PNEWDT is less than 1.

STRAN (NTENS) is the array of total strain tensors at the beginning of the iteration of the incremental step. The rigid rotation has been taken into consideration.

DSTRAN (NTENS) is the array of strain increments. It only includes the mechanical strain increment, but no thermal strain increment.

TIME (2) is the total time when the iteration of incremental step starts.

DTIME is the time increment of incremental step.

NDI is the number of normal stress or strain components.

NSHR is the number of shear stress or shear strain components.

NTENS is the number of the total stress or strain components, NTENS=NDI+NSHR.

NSTATV is the number of variables of material definition.

NPROPS is the number of material constants.

COORDS is the array of current material configuration.

DROT (3, 3) is the matrix of rotation increments.

DFGRD0 (3, 3) is the deformation gradient tensor when the iteration of incremental step starts.

DFGRD1 (3, 3) is the deformation gradient when the iteration of incremental step finishes.

NOEL is the number of elements.

NPT is the number of integration points.

KSTEP is the number of loading steps.

KINC is the number of incremental steps.

3.8.2 Flowchart of the UMAT subroutine employed in ABAQUS

On the basis of a numerical integration algorithm, the crystal plasticity constitutive model has been written into UMAT and used in the finite element software ABAQUS. The flowchart of the UMAT code used in ABAQUS is shown in Figure 3.11.

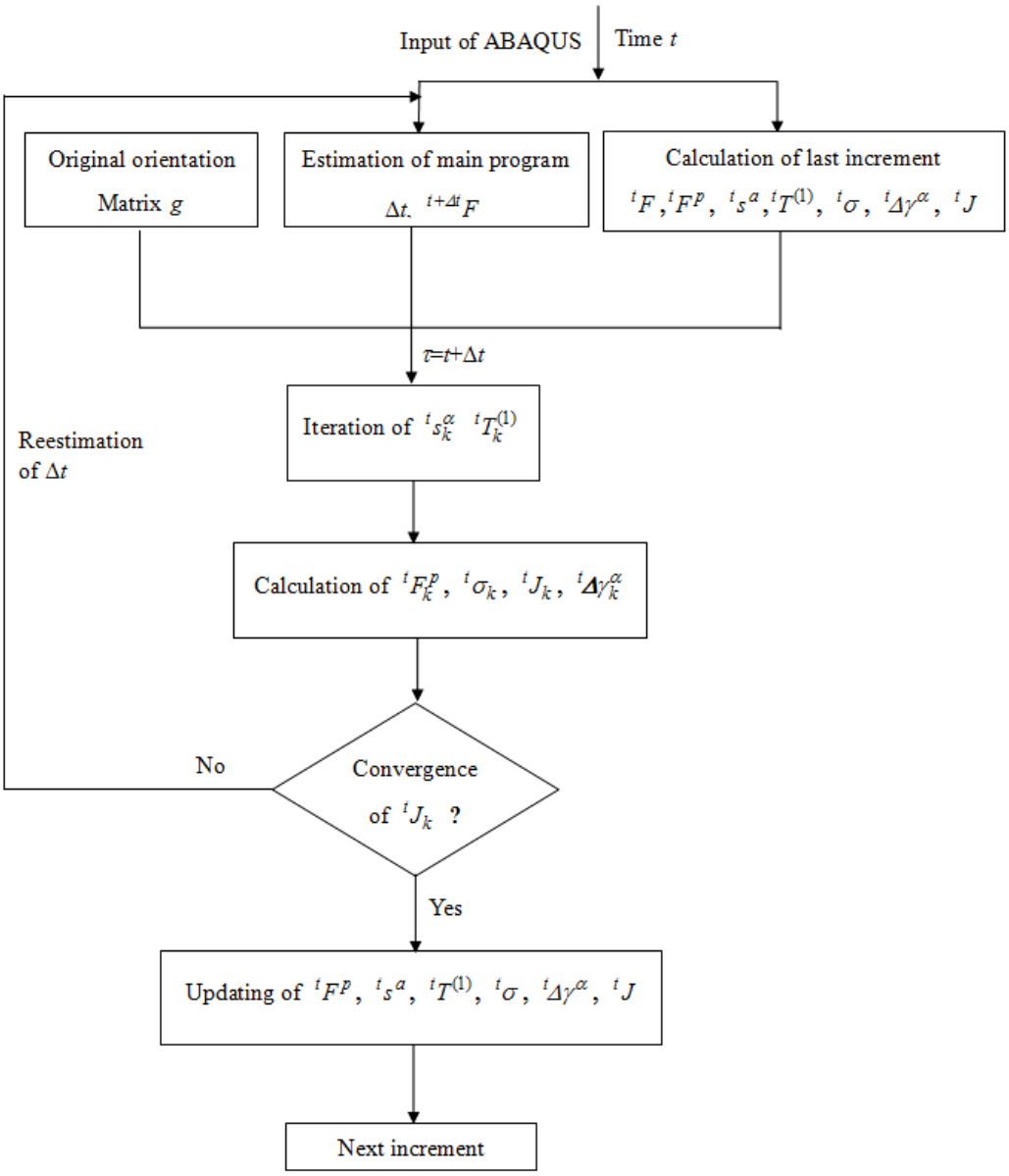

Figure 3.11 Flowchart of the UMAT code used in ABAQUS

When the UMAT is first used, the increment step will be initialised and the data of grain orientation and slip system will be input. At the starting time *t* of incremental step, the ABAQUS main program will include UMAT with the initial grain orientation matrices, time increments, and all the updating variables calculated from the last step. Then the variables ${}^{\tau}s_k{}^{\alpha}$ and ${}^{\tau}\boldsymbol{T}_k{}^{(1)}$ of time τ will be iterated and solved. The values of variables ${}^{\tau}\boldsymbol{F}_k{}^{p}$, ${}^{\tau}\boldsymbol{\sigma}_k$, ${}^{\tau}\Delta\gamma_k{}^{\alpha}$ and Jacobian matrix ${}^{\tau}\boldsymbol{J}_k$ can be obtained by the related equations. If the Jacobian matrix converges, the values of ${}^{\tau}s^{\alpha}$,

${}^{\tau}\boldsymbol{T}^{(1)}$, ${}^{\tau}\boldsymbol{F}^{p}$, ${}^{\tau}\boldsymbol{\sigma}$, ${}^{\tau}\Delta\gamma^{\alpha}$ and ${}^{\tau}\boldsymbol{J}$ will be updated, and then the iteration of the next increment will be calculated. If the Jacobian matrix does not converge, the time increment will be estimated and iterated. The Newton-Raphson iteration method is used in ABAQUS to solve the non-linear finite element equilibrium equation. It is as

$$\sum\left(\int \boldsymbol{B}^{T}\boldsymbol{J}\boldsymbol{B}dV\right)\boldsymbol{C}^{k} = \boldsymbol{P}(t+\Delta t) - \sum\int \boldsymbol{B}^{T}\left[\boldsymbol{\sigma}(t) + \Delta\boldsymbol{\sigma}(\Delta u^{k})\right]dV \tag{3.96}$$

$$\Delta u^{k+1} = \Delta u^{k} + C^{k} \tag{3.97}$$

where *B* is the transfer matrix from the dislocation increment to the strain increment, $\Delta\varepsilon = \boldsymbol{B}\Delta u$. The stress increment is a function of the strain increment and also a function of the dislocation increment. After the K times' iterations, the corrected displacement is given in the first equation. When the Newton-Raphson iteration method is used to solve the finite element equations, the Jacobian matrix ${}^{t+\Delta t}J = {}^{t+\Delta t}\left(\partial\Delta\sigma/\partial\Delta\varepsilon\right)$ (Matrix DDSDDE) will be updated. If the Jacobian matrix cannot be expressed explicitly, the rigid matrix can replace it. In the solving process, the time increment and deformation gradient of time *t* is input into the UMAT by the ABAQUS program and the increment of stress tensors will be updated, and the stress tensor at time $t+\Delta t$ will be obtained. If the Jacobian matrix can be expressed implicitly, the matrix DDSDDE needs to be updated to improve the rate of convergence.

3.9 Methodology of crystal plasticity finite element modelling

In this study, the methodology of crystal plasticity finite element modelling (Figure 3.12) follows the rules as:

Rate-dependent crystal plasticity constitutive models have been written into the UMAT and then used in the ABAQUS main program (geometric model). The geometric model of this study is established on the basis of experimental conditions (reduction, strain rate, friction, original surface roughness and original texture information). The modelling results will be compared with the experimental results. Furthermore, the relationship between the surface asperity flattening process (surface

roughness) and the above mentioned parameters will be investigated. The mechanism of surface asperity flattening will be analysed.

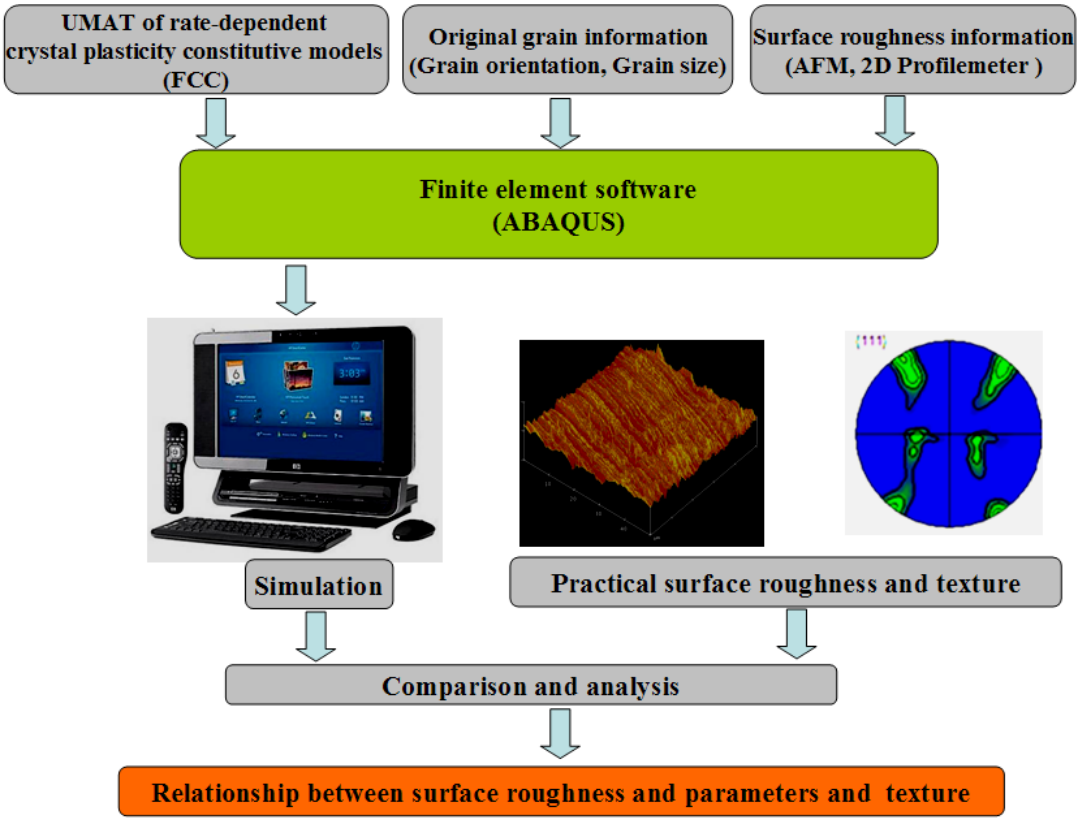

Figure 3.12 Methodology of crystal plasticity finite element modelling

3.10 Summary

In this chapter, the development of crystal plasticity finite element modelling has been introduced. The two current popular crystal plasticity theories (rate dependent and rate independent theories) and the primary applications of CPFEM have been described. In this study, the rate dependent crystal plasticity constitutive model has been used in the simulation. Some simplifications of the rate dependent constitutive equations have been shown in this chapter. The numerical integration algorithms for the simulation have also been detailed. A calculation of the grain orientation matrix can be obtained by matrix rotation and tensor calculation. The compiling rule of the UMAT in ABAQUS is introduced in detail. The flowchart of UMAT in ABAQUS and the methodology for this study are also described.

CHAPTER 4

EXPERIMENTAL INSTRUMENTS AND APPLIED METHODOLOGY

4.1 Introduction

Purpose designed compressing equipment was used in the INSTRON 8033 material testing machine to obtain information on the evolution of surface asperity of aluminium samples under cold uniaxial planar compression. Several experimental facilities were used to investigate the evolution of surface asperity of these samples. An atomic force microscope (AFM) from Digital Instruments was used to trace the evolution of 3D surface topology of the samples before and after compression. A 2D surface profile meter (Hommel Tester T1000) was used to analyse the surface roughness of samples before and after cold planar compression. A 3D profile meter was also used to analyse the development of 3D surface topology and surface roughness in a relatively large area (Maximal range is $500\times500\times500\ \mu m^3$). A JOEL 7100F FEG-SEM was used to obtain information on the surface microstructure and texture (grain orientations and slip). An M-400-H1 Vickers Hardness tester was applied to investigate the development of the sample's hardness. All the samples were cut by a Precision Cut-Off Machine Accutom-50 with a certain configuration of cutting parameters. Annealing heat treatment was carried out in the vacuum tube annealing stove.

4.2 Material

Cubic metal includes FCC and BCC metals. They are all research objects of material scholars and researchers. Belong to heat-treatment-strengthened alloy, 6061 Al alloy

has some good properties such as formability, weldability, machining performance and corrosion resistance. With the moderate intensity, it can still maintain a better operability. Due to its excellent properties, it is widely used in a range of industry, for example decoration, packaging, construction, transportation, electronics, aviation, aerospace, weapons and other industries. It is also a typically simple FCC metal. Therefore, we choose 6061 T5 as the experimental material in this study. Main components of 6061 Al alloy are magnesium and silicon, which form phase called Mg2Si. Its melting temperature is 660 °C. The typically microstructure of 6061 is shown as in Figure 4.1, and all parameters of 6061T5 alloy are shown in Tables 4.1-4.3. The supplier of Al 6061 plate is the NSW branch of Bohler-Uddeholm. Australia.

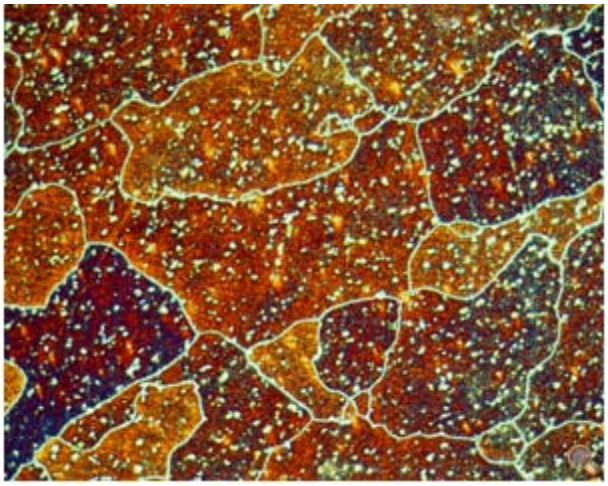

Figure 4.1 microstructure revealed using Weck's reagent (magnifications: 200) [176]

Table 4.1 Chemical compositions of 6061T5 Al plate (wt %)

Element	Cu	Mn	Mg	Zn	Cr	Ti	Si	Fe	Al and else
Contents	0.15-0.4	0.15	0.18-0.12	0.25	0.04-0.35	0.15	0.4-0.8	0.7	------

Table 4.2 Physical parameters of 6061T5 Al plate

Melting point	Solution temperature	Recrystal temperature	Burning temperature	Uniform temperature	Hardness
Contents	582-652 °C	529 °C	582 °C	550 °C	28.00 (HV)

Table 4.3 Mechanical parameters of 6061T5 Al plate

Parameters	Tensile/Bearing yield strength (MPa)	Poisson ratio	Young's modulus of elasticity (GPa)	Plastic strain %
Value	276 /386	0.33	68.9	12/17

According to the requirement that the metal compression and EBSD (Electron Back Scatter Diffraction) experiments be conducted at room temperature, the specimens were manufactured as: 10mm×10mm×6mm. A sketch of the sample is shown in Figure 4.2.

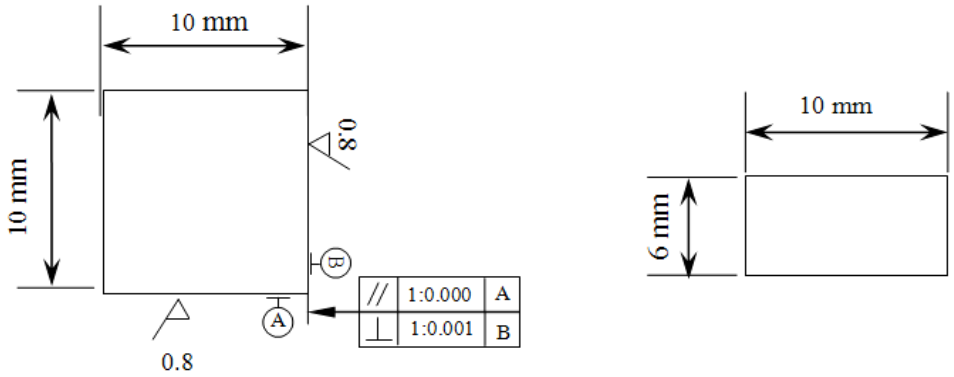

Figure 4.2 The specimen's dimension

4.3 Compressing equipment

In order to carry out uniaxial planar compression, a set of compressing equipment was designed, built and installed into an INSTRON 8033 material testing machine. The details are shown in the following.

4.3.1 Material of compressing equipment

The compressing experiments were carried out on the compressing tools. It includes the compression mould and tool. The material for the experimental equipment is a high tensile steel EN25. Its compositions are shown in Table 4.4.

Table 4.4 Compositions of EN25 (High tensile steel) (wt %)

Element	C	Si	Mn	Cr	Mo	Ni
Contents	0.30	0.25	0.60	0.50	0.50	2.50

4.3.2 Compressing equipment

The experimental equipment was manufactured by the workshop. In order to load and unload it easily and conveniently, the compression mould consists of two separate parts connected with a screw at the centre. The dimensions of the compression mould and tool are shown in Figures 4.3-4.7.

a) Compression mould

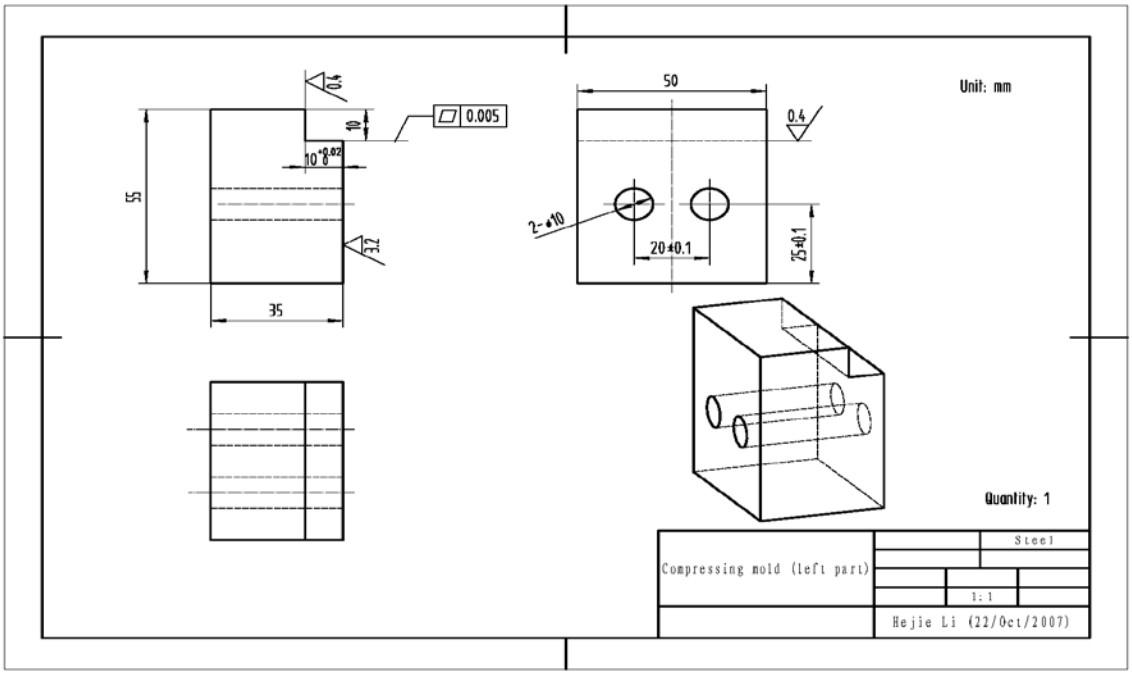

Figure 4.3 Left part of the compression mould

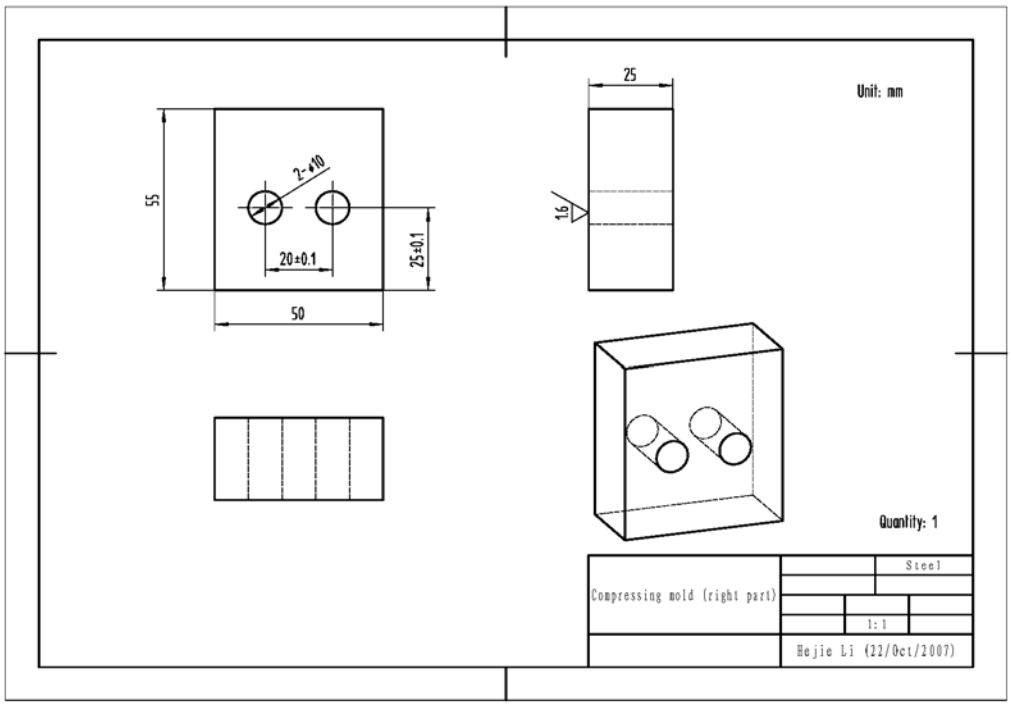

Figure 4.4 Right part of compression mould

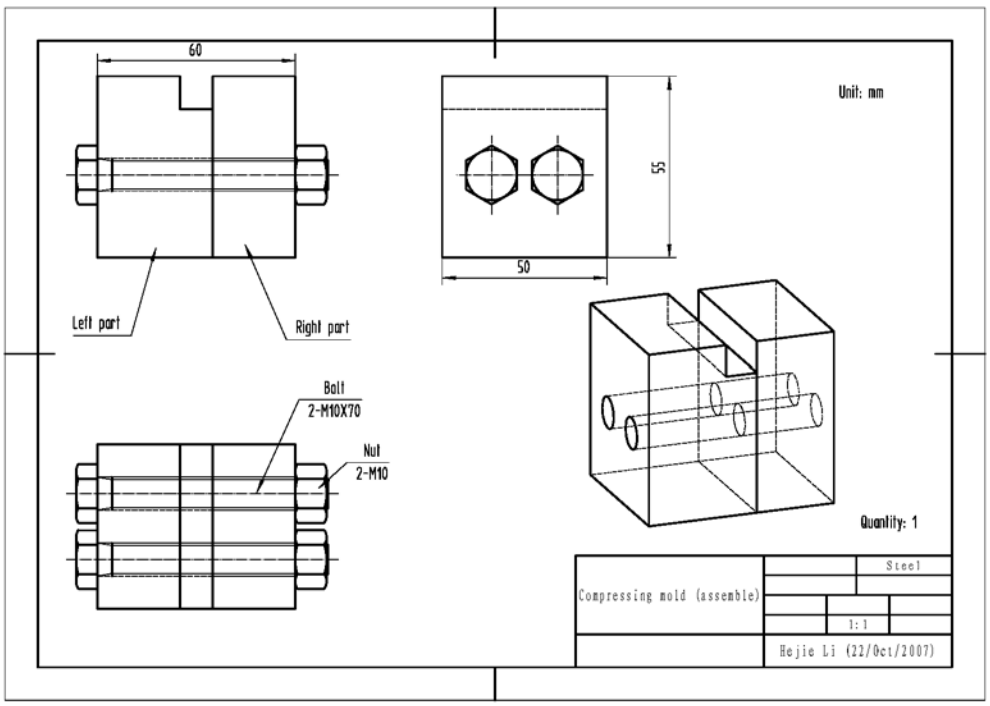

Figure 4.5 Combination of compression mould

b) Compression tool

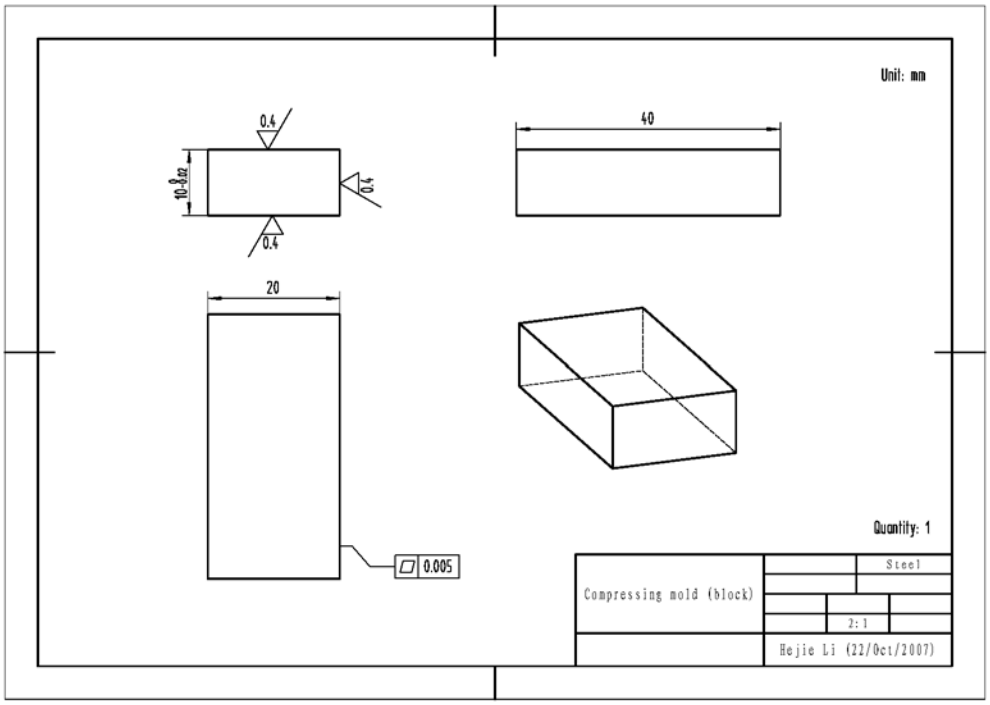

Figure 4.6 Compression tool

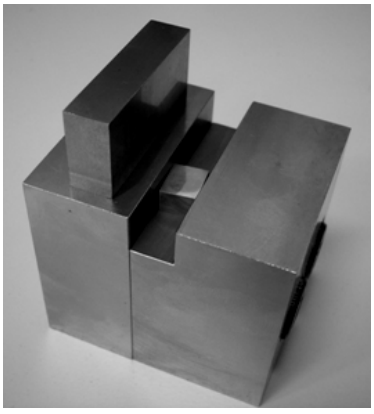

Figure 4.7 Photo of the compression mould, tool and sample

4.3.3 Compressing procedure

The compressing experiments were carried out on the INSTRON 8033 Material Testing Machine (Figure 4.8). The designed compressing equipment was used in this machine.

Figure 4.8 INSTRON 8033 Material Testing Machine

In order to comply with the compression process, the strain rate of compression is the same as the simulation. In practice the strain rate could not be controlled by the machine during the compression, so velocity has been selected to replace the strain rate. Therefore, the practical strain rate needs to be transformed to a practical compression velocity. It is assumed that the length of sample before compression is L_0, and after compression its length is L, the increment of deformation is ΔL, the practical strain rate is $\dot{\varepsilon}$, the true strain is ε, the compression time is Δt, the velocity is $\dot{U}$. The transfer equations are shown as follows

$$L = L_0 + \Delta L \tag{4.1}$$

$$\varepsilon = \ln \frac{L}{L_0} \tag{4.2}$$

$$\Delta t = \varepsilon / \dot{\varepsilon} \tag{4.3}$$

$$\dot{U} = \Delta L / \Delta t \tag{4.4}$$

It is assumed that the deformation is $0.4\,L_0$. In the experiment the compression strain rates are 0.0001 and 0.001 s^{-1}. The corresponding velocities are 0.33 and 3.3 mm/s. On the other hand, the experimental results obtained are load (kN) and displacement (mm), so the true stress and strain can be obtained by the isometric method. The equations are shown as

$$\sigma = P / A \tag{4.5}$$

$$HA = H_o A_o \Rightarrow A = \frac{H_o A_o}{H} \tag{4.6}$$

From Equations (4.5) and (4.6), it can be obtained as

$$\sigma = \frac{PH}{H_o A_o} = P(1 - \frac{\Delta H}{H_o}) / A_o \tag{4.7}$$

where P is the load, kN, σ the true stress, MP_a, A_o, A the cross section area before and after compression, mm^2, respectively, H_o, H the height of specimen before and after compression respectively, mm. According to the experimental results (load P, displacement ΔH and original cross section area A_o), the true stress and strain can be obtained by the equations. The experimental schedule is shown in Table 4.5.

Table 4.5 Experimental schedule of compression

Number	Original height (mm)	Reduction (%)	Height after deformation (mm)	Lubrication	Strain rate (s^{-1})
1	6.3	5	4.9	With/No	0.001/0.01
2	6.3	10	4.8	With/No	0.001/0.01
3	6.3	20	4.5	With/No	0.001/0.01
5	6.3	40	4.25	With/No	0.001/0.01
5	6.3	60	4	With/No	0.001/0.01
6	6.3	80	3.75	With/No	0.001/0.01

In the current study, the reduction can make sense to describe the different behavior with the same size samples. In other study, the strain has been used as a parameter to depict the deformation behavior of samples.

4.4 Heat treatment experiment

In order to obtain the ideal uniform grains, a special annealing heat treatment with an annealing temperature of 100°C lower than uniform temperature of Al 6061T5 alloy is selected. All the samples were heat treated in the vacuum tube annealing stove. The heat treatment schedule is shown in Table 4.6

Table 4.6 Annealing schedule

Sample	Temperature (°C)	Holding time (hours)
1	400	2
2	400	4
3	450	2
4	450	4
5	500	2
6	500	4

4.5 2D profile meter

The Hommel Tester T1000 is used to measure the surface profile of samples before and after compression. The instrument is a modern, easy to handle and portable instrument that can characterise the periphery of the compressed sample surface with a resolution of 0.01 µm. A number of standard surface roughness parameters (R_a, R_z, R_t, R_{max}, t_{pi}, t_{pa}) are available for determining the magnitude of surface flaws and characterising the surface profile. These can be calculated from the unfiltered measured profile, the filtered roughness profile, or the filtered waviness profile, depending on the type of parameter measured. This instrument is shown in Figures 4.9 and 4.10.

Figure 4.9 Hommel Tester T1000 surface profile meter

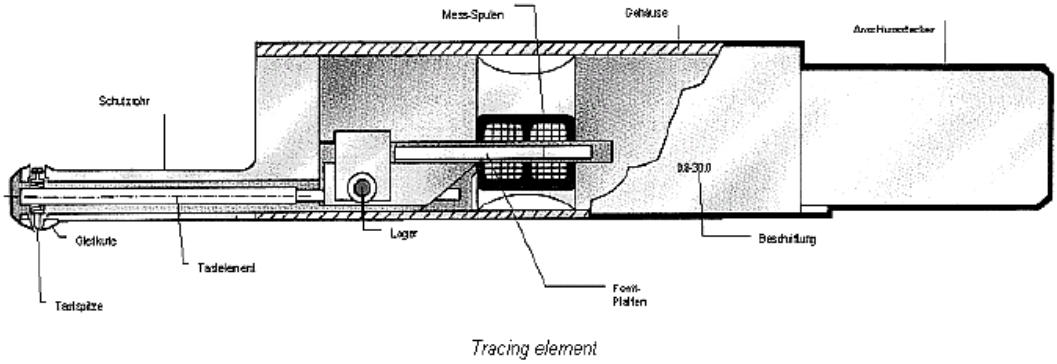

Figure 4.10 Schematic diagram of Hommel Tester T1000 surface profile meter

The Hommel Tester T1000 can carry out profile measurement from 8.0 to 320 μm. Its tip radius is 5 μm at an angle of 90°. In the measurements the engaging force is 0.8 mN. 6 points were measured on each sample with the tip kept vertical to the rolling direction (RD). All the two dimensional measurements are carried out in the central areas of the sample top surface. For one point, the measurement result is the average of six measured results in this area.

4.6 AFM (Atomic Force Microscope) measurement

A Multi-Mode Scanning Probe Microscope (SPM) from Digital Instrument operating in control AFM mode (Nanoscope IIIA AFM) has been employed to obtain topographic images for the surfaces of samples. Contact mode AFM operates by scanning a tip attached to the end of a cantilever across the sample surface while

monitoring the change in the cantilever's deflection with a split photodiode tip. The tip contacts the surface through the absorbed layer of fluid on the surface of the sample. Force constants usually range from 0.01 to 1.0 N/m, resulting in forces ranging from nN to μN in an ambient atmosphere [177].

Characteristics of the standard silicon nitride probes are listed in Table 4.7.

Table 4.7 Characteristics of the standard silicon nitride scanning tips

Items	Parameter values
Nominal tip radius of curvature	20-60 nm
Cantilever lengths	100 & 200 μm
Cantilever configuration	V-shaped
Sidewall angles	35°

Figure 4.11 shows the design of the scanning tip and its four silicon nitride cantilevers. AFM is a probe microscopy of multiple scanning types. The probe has 4 cantilevers with different geometries attached to each substrate. In the measurement of surface profile, the lateral resolution is 1-5 nm, vertical resolution is 0.08 nm.

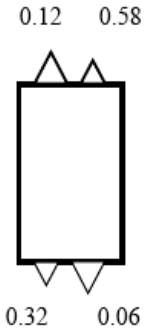

Figure 4.11 Diagrammatic sketch of AFM scanning tip and cantilever spring

All the surface roughness data of samples before compression will be used in the models. All the surface roughness data of samples after compression will be compared with the modelling results of surface roughness.

4.7 3D profile meter

3D profile meter was used to analyse the evolution of surface asperity in a relatively large area (Figure 4.12). Measuring area of the 3D profile meter is about 500×500×500 μm^3 with the minimal data resolution of 0.5 nm.

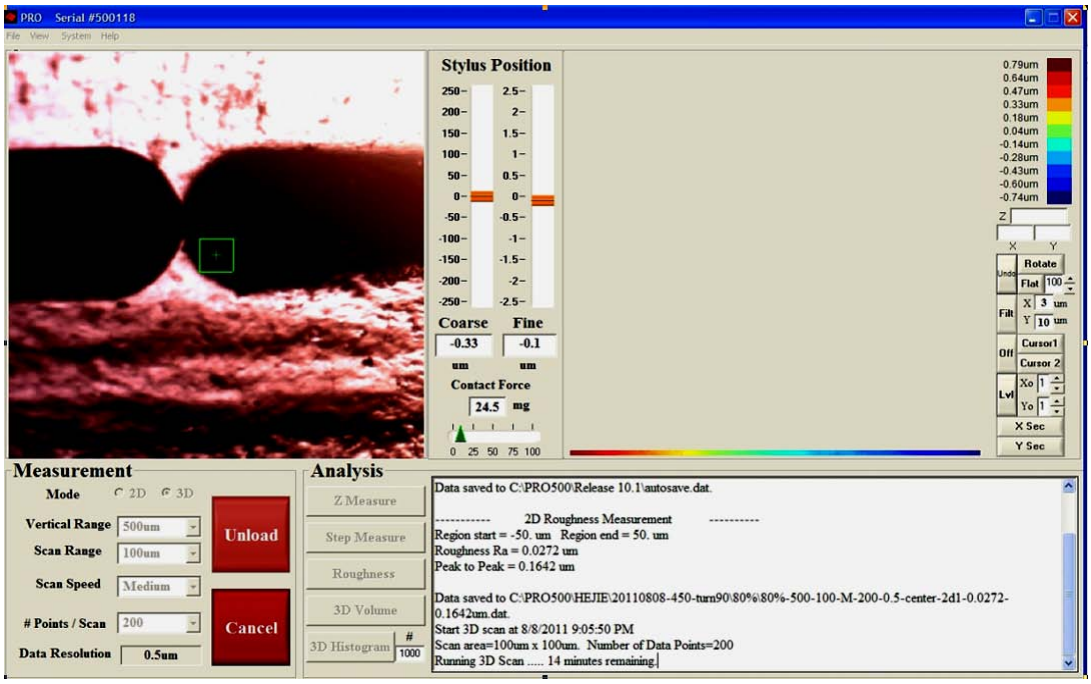

Figure 4.12 Measuring interface of 3D profile meter

4.8 Hardness tester

The Vickers hardness test was developed in 1921 by Robert L. Smith and George E. Sandland at Vickers Ltd as an alternative of the Brinell method to measure the hardness of materials [178]. The basic principle, as with all common measures of hardness, is to observe the material's ability to resist plastic deformation from a standard source. The unit of hardness given by the test is known as the Vickers Pyramid Number (HV) or Diamond Pyramid Hardness (DPH). The hardness number is determined by the load over the surface area of the indentation and not the area normal to the force, and is therefore not a pressure. The hardness number is not really a true property of the material and is an empirical value that should be seen in conjunction with the experimental methods and hardness scale used. The HV number is then determined by the ratio F_{HV}/A_{HV} where F_{HV} is the force applied to the

diamond in kilograms-force, and A_{HV} is the surface area of the resulting indentation in square millimetres. A_{HV} can be determined by the following formula [179]:

$$A_{HV} = \frac{{d_{HV}}^2}{2\sin(136^\circ / 2)} \tag{4.8}$$

It can be approximated by evaluating the sine term to give,

$$A_{HV} \approx \frac{{d_{HV}}^2}{1.8544} \tag{4.9}$$

where d_{HV} is the average length of the diagonal left by the indenter in millimetres. Hence [180],

$$HV = \frac{F_{HV}}{A_{HV}} \approx \frac{1.8544 F_{HV}}{{d_{HV}}^2} \tag{4.10}$$

where F_{HV} is in kgf and d_{HV} is in millimetres. If the load F_{HV} is in Newtons, the above equation can be expressed [181]:

$$HV = \frac{F_{HV}}{A_{HV}} \approx \frac{0.1891 F_{HV}}{{d_{HV}}^2} \tag{4.11}$$

where F_{HV} is in Newtons and d_{HV} is in millimetres.

Vickers hardness numbers are reported as: 440HV30, or if the duration of the force differs from 10 to 15s, e.g. 440Hv30/20, where: 440 is the hardness number, HV gives the hardness scale (Vickers), 30 indicates the load used in kg, and 20 indicates the loading time if it differs from 10 to 15s.

The Vickers hardness tester, test scheme, and indentation are shown in Figures 4.13-4.15 respectively.

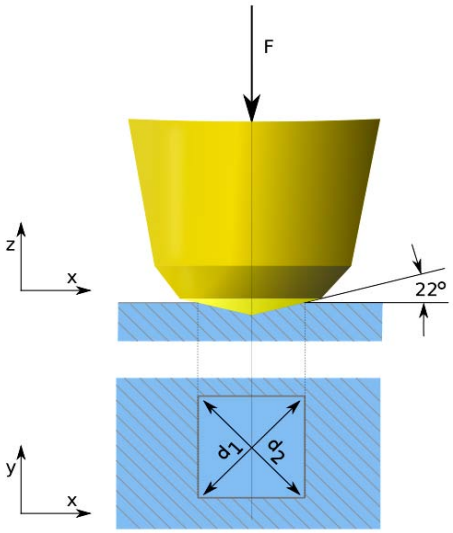

Figure 4.13 Vickers test scheme

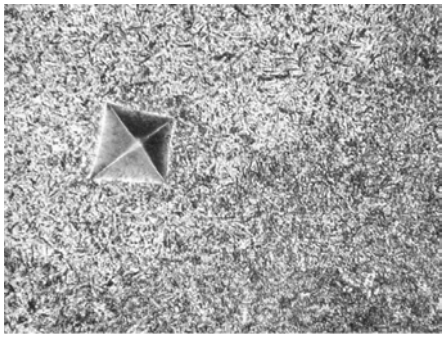

Figure 4.14 An indentation left in case-hardened steel

Figure 4.15 Vickers hardness tester

4.9 EBSD experiment

4.9.1 Introduction

The term “electron backscatter diffraction” (EBSD) is now synonymous with both the scanning electron microscope (SEM) technique and the accessory system that can be attached to an SEM. Accelerated electron in the primary beam of a scanning electron microscope (SEM) can be diffracted by atomic layers in crystalline materials. These diffracted electrons can be detected when they impinge on a phosphor screen and generate visible lines, called Kikuchi bands, or "EBSP's" (electron backscatter patterns). These patterns are effectively projections of the geometry of the lattice planes in the crystal, and they give direct information about the crystalline structure and crystallographic orientation of the grains from which they originate. When used in conjunction with a data base that includes crystallographic structure information for phases of interest and with software for processing the EPSP's and indexing the lines, the data can be used to identify phases based on crystal structure and also to perform fabric analyses on polycrystalline aggregates.

EBSD provides quantitative microstructural information about the crystallographic nature of metals, minerals, semi-conductors, and ceramics-in fact most inorganic crystalline materials. It reveals the grain size, grain boundary character, grain orientation, texture, and phase identity of the sample under the beam. Centimetre - sized samples with millimetre-sized grains, to thin metal films with nanograins may be analysed. The nominal angular resolution limit is ≈0.5° and the spatial resolution is related to the resolution of the SEM, but for modern field emission SEMs (FE-SEMs), 20 nm grains can be measured with reasonable accuracy [182]. The macroscopic sample size depends on the ability of the SEM’s stage and chamber to orient a sample at 70° tilt at an appropriate working distance, usually in the range 5 to 30 mm.

4.9.2 Working principle

EBSD operates by arranging a flat, highly polished (or as-deposited thin film) sample at a shallow angle, usually 20°, to the incident electron beam (Figure 4.16) (since the

SEM stage is often used to tilt the plane of the sample to this shallow angle, the value of stage tilt is often referred to and is typically 70°). With an accelerating voltage of 10-30 kV, and incident beam currents of 1–50 nA, electron diffraction occurs from the incident beam point on the sample surface. With the beam stationary, an EBSD pattern (EBSDP) emanates spherically from this point.

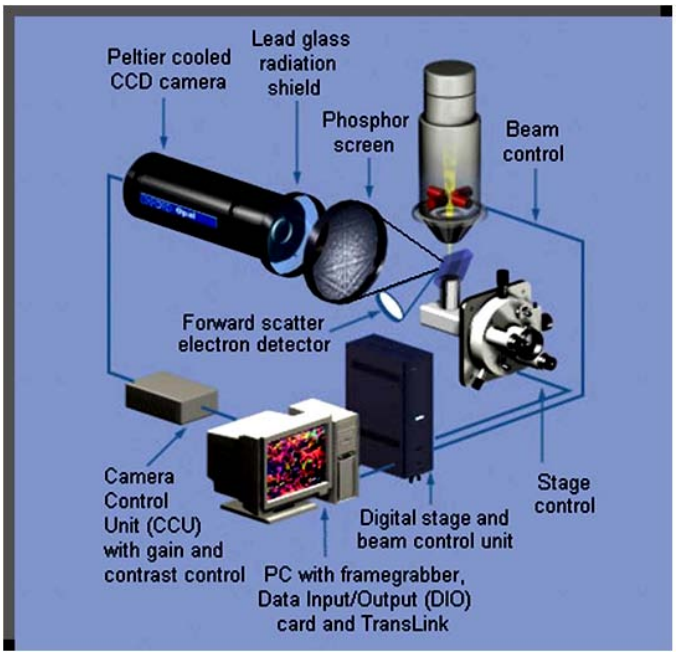

(a)

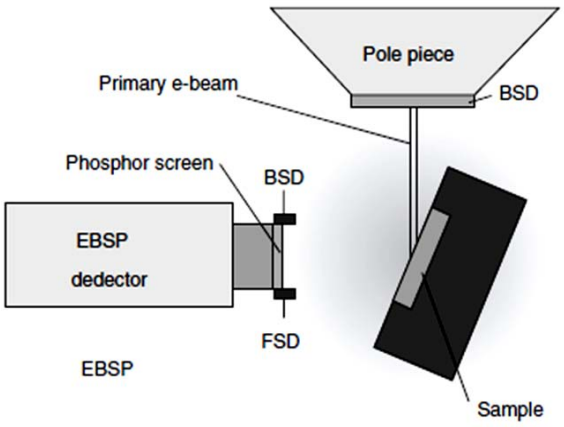

(b)

Figure 4.16 Schematic arrangement of sample orientation in the SEM [183]

When the primary beam interacts with the crystal lattice (Figure 4.17), low energy loss backscattered electrons are channelled and then subjected to path differences

that lead to constructive and destructive interferences. If a phosphor screen is placed a short distance from the tilted sample, in the path of the diffracted electrons, a diffractive pattern can be seen. There is discussion of the electron interactions involved, in particular Wells, “Comparison of Different Models for the Generation of Electron Backscattering Patterns in the SEM,” gives a good description of the competing theories.

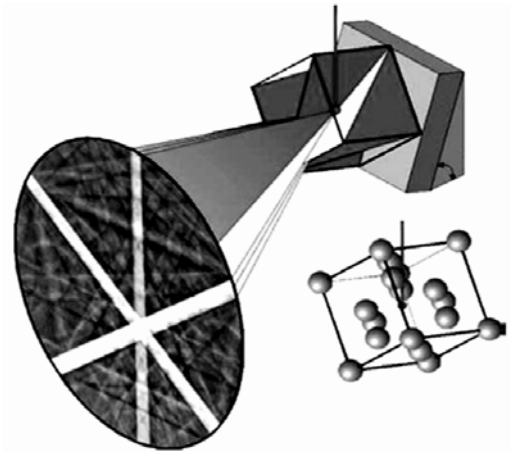

Figure 4.17 Electron interactions with crystalline material [183]

The spatial resolution of the technique is governed by the SEM electron optics as in conventional backscattered electron imaging. For high resolution imaging on nanograins, high-performance FE-SEMs are required, along with small samples and short working distances. The EBSP detector attaches to a free port on the SEM chamber. Ideally, the port will be orthogonal to the stage tilt axis so that the sample may easily be tilted toward the detector at 70°, although other orientations are possible. Typically, the port allows the detector to have a nominal working distance of ~20 mm, since a highly tilted sample necessitates moderate working distances. For small samples, shorter WDs may be attained if the EBSP detector and SEM port allows close proximity to the objective lens.

In our study the JEOL 7001F FEG-SEM was used to measure the orientation data of samples before and after deformation. All the orientation data before compression will be analysed and then employed in the crystal plasticity finite element model. All the orientation data after compression will be analysed to compare with the modelling results. Software Channel 5 is used to acquire the online texture

information, and analyse the offline scanning map. The software interface is shown in Figure 4.18.

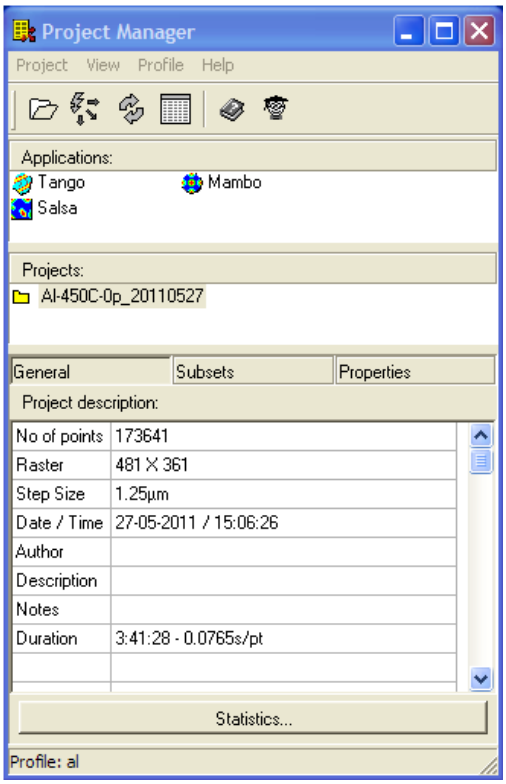

Figure 4.18 Interface of software Channel 5

4.10 Sample's preparation for EBSD experiment

4.10.1 Cutting

After compression, the sample is cut by the Precision Cut-Off Machine Accutom-50 (Struers Company). The Precision Cut-Off Machine is shown in Figure 4.19.

Figure 4.19 Precision Cut-Off Machine Accutom-50

All samples have been cut according to the following parameters:

Blade: 459CA

Preset feed speed: 0.100 mm/s

Actual feed speed: 0.100 mm/s

Rotation speed: 3000 rpm

Cut number: Single

Cooling system: Recirculation contents

Contents: 4l

Cooling unit flow: 800 ml/min

The sample of EBSD experiment is cut to a 2 mm thick slice. The cutting position is shown in Figure 4.20.

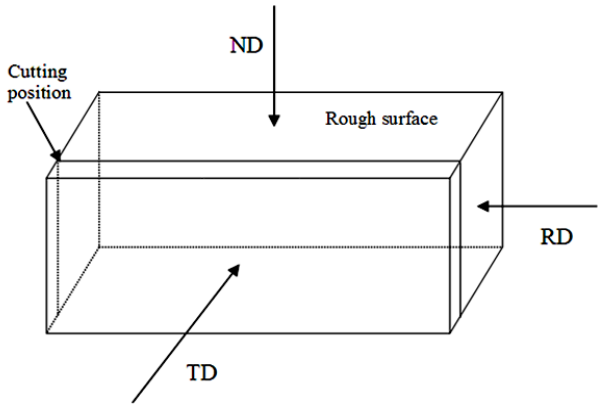

Figure 4.20 Schematic of EBSD sample's cutting

4.10.2 Grinding and polishing

(a) Coarse grinding process

The Al 6061 sample polishing procedure includes two processes. After cutting, the sample is first ground by the LECO GP20 Grinder/Polisher with No P800 polishing paper (Figure 4.21) to make the surface flat. This is the coarse grinding process.

Figure 4.21 LECO GP20 Grinder/Polisher

(b) Fine grinding process

Then the sample will be polished by the Struers DAP-7 Struers DAP-7 Wet Polisher (Figure 4.22). This is the fine polishing process. The polisher is shown in Figure 4.22. The fine polishing process includes the following steps: (1) 9 μm Largo polishing cloth with 9 μm lubricant; (2) 3 μm Mol (MD) polishing cloth with 3 μm lubricant; (3) 0.025 μm chemical pan with the OPS liquid.

Figure 4.22 Struers DAP-7 Wet Polisher

4.10.3 Etching

After fine polishing, all the samples were etched in a solution for about 30 s. The etching solution includes 10 % Nitric acid, 1 % Hydrofluoric acid, and 89 % distilled

water. The microstructures were observed by the optical microscope. The aim of etching is to remove the oxide layer of aluminium and disclose the microstructure of the sample.

4.10.4 Electrolytic polishing

Electrolytic polishing is a good method for removing the stressed surface layer of the sample which has been affected by the stress of polishing and grinding. The electrolytic polishing was carried out in the Struers Lectroopol-5 with the A3 electrolyte at room temperature (about 18 °C). The schematic figure of electrolytic polishing is shown in Figure 2.23.

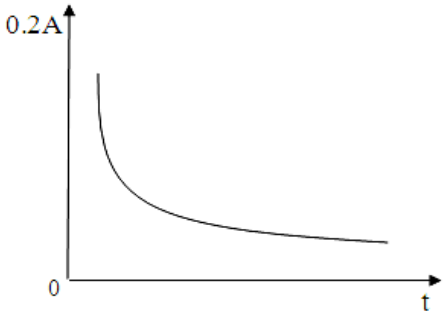

Figure 4.23 Relationship between electronic current and time

4. 11 Pole figure plotting

All the results from the simulation will be plotted by the software Pole figure plotting.

4.11.1 Principle of pole figure plotting

The pole figure can be plotted by two kinds of projection: stereoscopic projection, equal area projection. They are shown in Figures 4.24 and 4.25. The principle of Stereoscopic projection is as follows:

(1) Ortho-normality of crystallographic plane indices

In a crystal coordinate system, the crystallographic plane indices will be ortho-normalised to a new vector $o^{'} = (o_i^{'})$ (i=1, 2, 3), for example, $(111) = 1/\sqrt{3}(1,1,1) = \mathbf{o}^{'}$.

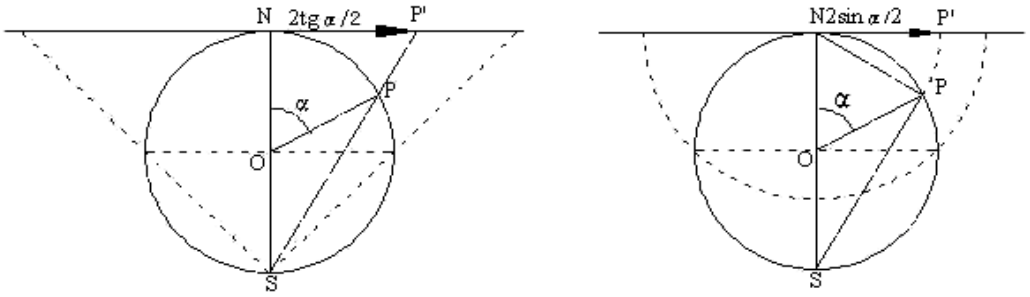

(a) Stereoscopic projection (b) equal area projection

Figure 4.24 Principles of two kinds of projection

(2) Coordinate transformation

The vector $o^{'}$ will be transformed to the specimen coordinate system by applying the orientation matrix g, as mentioned in Chapter 3.

$$\mathbf{o} = \mathbf{g}^{-1}\mathbf{o}^{'} \tag{4.12}$$

(3) Assumption of unit ball

It is assumed that it is a unit ball. Then the vector *o* can be expressed as

$$o_1 = \sin\alpha\cos\beta \ , \ o_2 = \sin\alpha\sin\beta \ , \ o_3 = \cos\alpha \tag{4.13}$$

The coordinate in the pole figure can be obtained as

$$X = \frac{o_1}{1+o_3} \ , \ Y = \frac{o_2}{1+o_3} \tag{4.14}$$

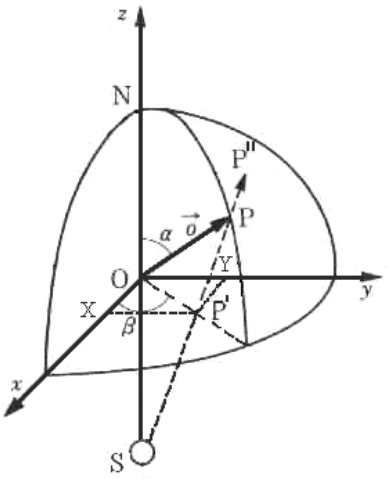

Figure 4.25 Principle of stereoscopic projection

4.11.2 Introduction of the Pole Figure plot (PF plot)

All the information about the texture (grain orientations) will be plotted by the software Pole Figure plot. This software has been generated on the basis of Mat lab. The interface is shown in Figure 4.26.

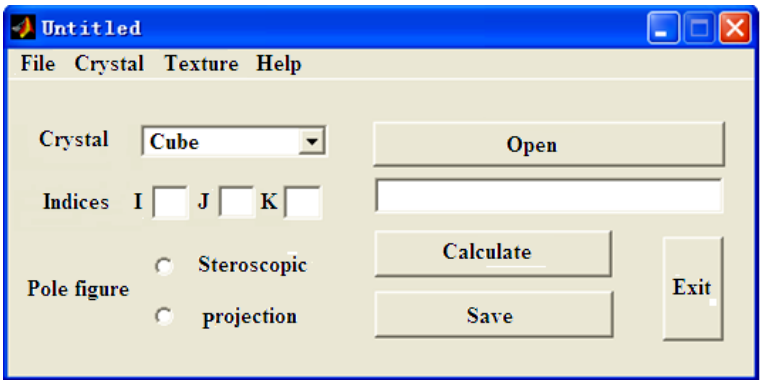

Figure 4.26 Interface of Pole figure plot

This software can simply generate the pole figure (Figure 4.27) by the grain orientation data file. Its procedure can be operated as

(1) Selection of the crystal types: cubic or others
(2) Input of crystallographic plane indices
(3) Selection of Pole Figure types
(4) Input of Euler angle data files

(5) Calculation

(6) Save

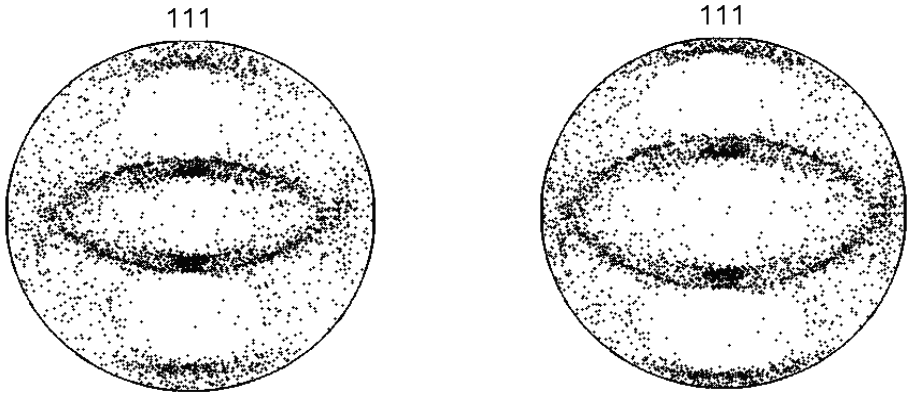

(a) Pole Figure of stereoscopic projection (b) Pole Figure of equal area projection

Figure 4.27 Two kinds of pole figures

This software can only express information of the texture by the format of point aggregates. All the pole figures only include the information of grain orientation intensity, but not cover any information such as isoline, volume weight and so on. Currently, only black-white figure can be drawn from the data, which show the same information as the color figure.

4. 12 Experimental methodology

A series of cold uniaxial planar compression tests were carried out under different deformation conditions to examine the influences of deformation parameters such as reduction, lubrication, strain rate, microstructure and texture on the evolution of surface asperity.

i) Before compression all the samples were cut into the sizes required in the experimental design;

ii) All the cutting samples were carried out the annealing heat treatment;

iii) All the samples were measured by 2D and 3D profile meters (AFM);

iv) Hardness tests were carried out before compression;

v) Samples were compressed by the designed channel die used in the INSTRON 8033 Material Testing Machine under different deformation

conditions: reduction ranges between 0-80 %, lubrication, and different strain rates and different annealed states;

vi) After compression, the evolution of surface asperity of the sample was measured by the 2D and 3D profile meters;

vii) Hardness tests were carried out on the samples after compression;

viii) After compression, the compressed samples were cut to the suitable size for EBSD experiment and then ground, polished, and electrolytically polished or etched.

viiii) EBSD experiments were carried out on the samples before and after compression.

4. 13 Experimental results

4.13.1 Microstructures

After annealing, all the samples were electrolytically polished and anodised, and then the TD and ND directions were measured. The microstructures were obtained as follows.

(a) Microstructures in normal direction of samples

The parameters of annealing heat treatment of the three samples are shown in Table 4.8.

Table 4.8 Parameters of annealing heat treatment

Sample	Temperature (°C)	Time (hour)
1	400	2
2	450	2
3	500	2

The microstructures of Normal Direction with different annealing temperatures are shown in Figures 4.28-4.30, here all the three microstructures are homogeneous in a normal direction, and after annealing the grains in the three samples are all uniform and equiaxed. Table 4.9 shows that all the grain sizes with different annealing temperatures are close to 100 μm, and with an increase in annealing temperature, grains in a normal direction tend to be slightly finer. The reason for this is that when

the temperature reaches 500 °C (the recrystallising temperature of 6061T5 Al is 529 °C), recrystallisation will take place in some areas of the samples.

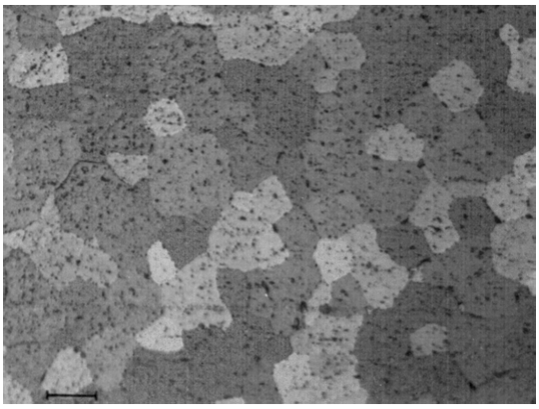

Figure 4.28 Microscope of sample 1 in normal direction (400 °C, 2 h, 100 μm)

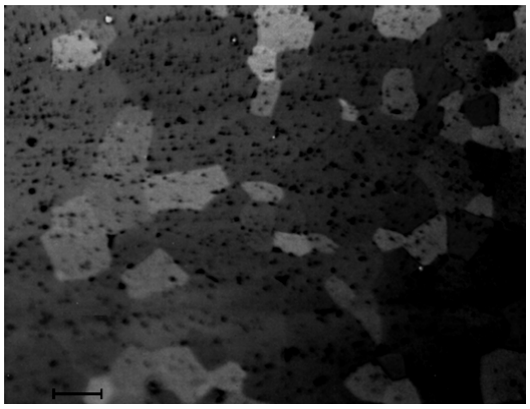

Figure 4.29 Microstructure of sample 2 in normal direction (450 °C, 2 h, 100 μm)

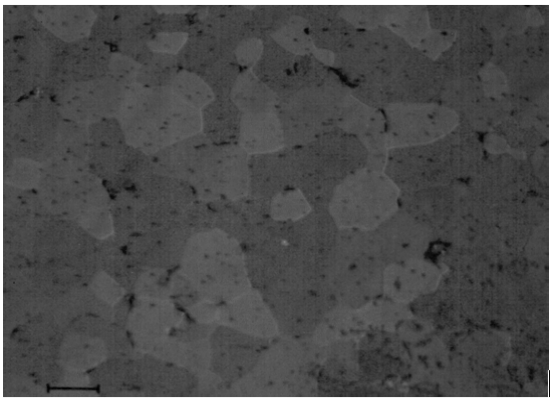

Figure 4.30 Microstructure of sample 3 in normal direction (500 °C, 2 h, 100 μm)

Table 4.9 Average grains size in ND direction

Sample number	Sample 1	Sample 2	Sample 3
Grain size (μm)	100.68	105.48	98.40

(b) Microstructures in transverse direction of samples

The microstructures in a transverse direction with different annealing temperatures are shown in Figures.4.31-4.33. In a transverse direction the microstructures are all homogeneous, and all grains tend to be uniform and equiaxed. From Table 4.10, it can be concluded that with an increase in annealing temperature, the grains in TD have the same tendency as those in the normal ND, i.e., the grains tend to be much finer.

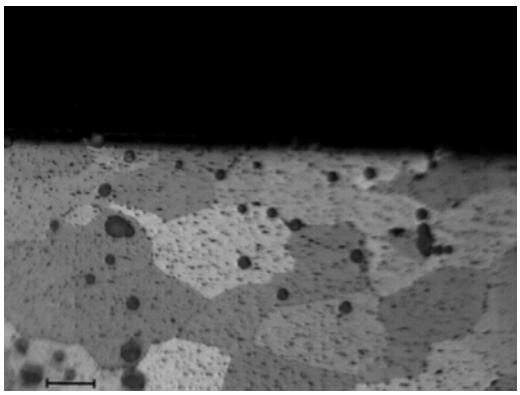

Figure 4.31 Microstructure of sample 1 in transverse direction (400 °C, 2 h, 50 μm)

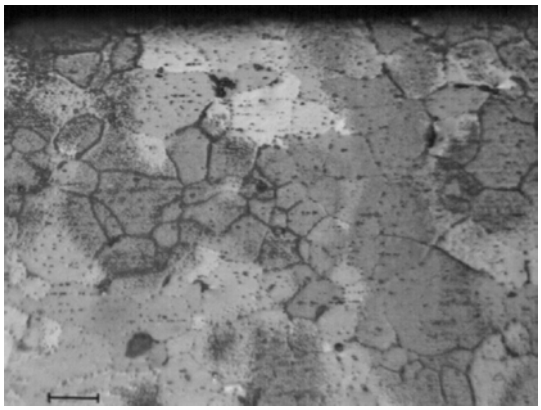

Figure 4.32 Microstructure of sample 2 in transverse direction (450 °C, 2 h, 50 μm)

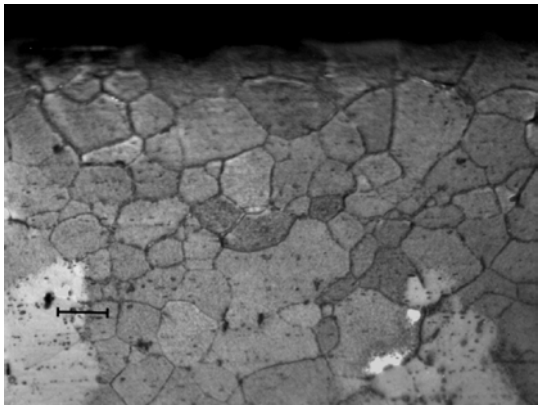

Figure 4.33 Microstructure of sample 3 in transverse direction (500 °C, 2 h, 50 μm)

Table 4.10 Average grains size in TD direction

Sample number	Sample 1	Sample 2	Sample 3
Grain size (μm)	61.88	49.13	40.35

4.13.2 Experimental results of AFM (compression tool)

According to the standard of ISO4287-1997 (Geometrical Product Specifications of Surface Texture: Profile Method-Terms, Definitions, and Surface Parameters), 6 areas with a specified location (it is central area in this study, the measuring range is 90 μm×90 μm) were measured and averaged for each sample. The parameters of the surface of the compression tool obtained from the AFM are shown in Table 4.11.

Table 4.11 Parameters of compression tool surface

Name	Z (nm)	R_{ms} (R_q) (nm)	R_a(nm)	R_{max} (nm)	Srf.area (μm)	Srf.area diff (%)
Value	125.18	7.524	5.718	125.18	402.84	0.710

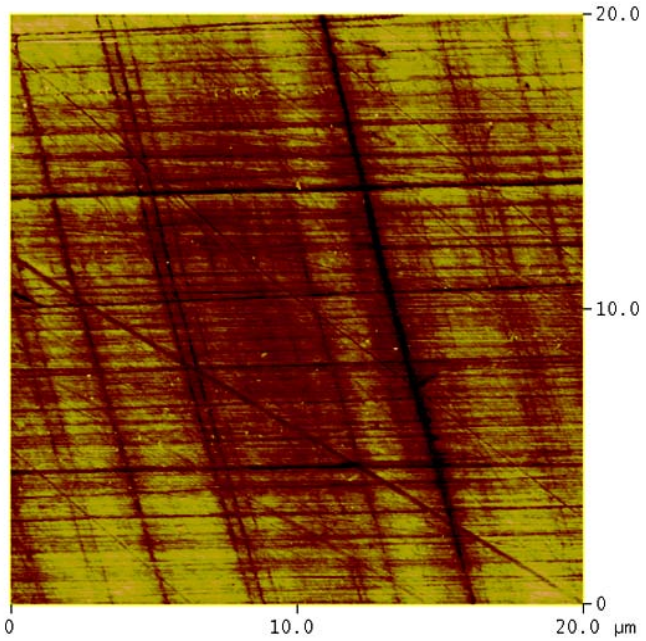

Figure 4.34 Two dimensional surface roughness of tool measured by AFM

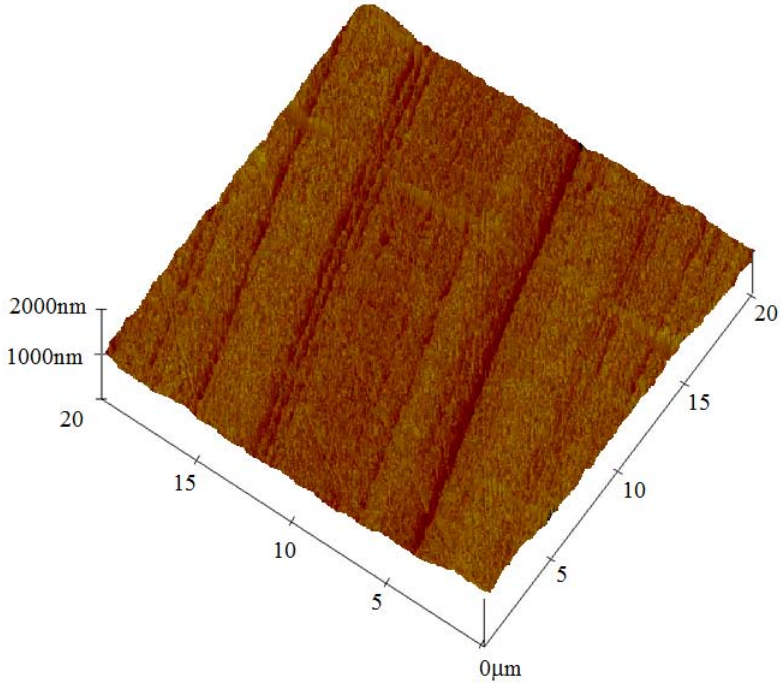

Figure 4.35 Three dimensional surface roughness of tool measured by AFM

From Figures 4.34 and 4.35, it can be seen that the surface roughness of the compression tool is only 5.718 nm. EN25 is the high tensile steel with (2.5 % nickel-chromium-molybdenum) high hardenability, generally supplied hardened and tempered in the tensile range of 930-1080 MPa (condition U). The mechanical

parameters of EN25 steel are shown in Table 4.12. For 6061T5 Al plate, it is a soft aluminium alloy. The parameter of Al is shown in Tables 4.2 and 4.3.

Table 4.12 Mechanical parameters of high tensile steel EN25

Parameters	Tensile strength (MPa)	$\sigma_{0.2}$ (MPa)	Elongation (%)	Hardness (HV)
EN25	930/1080	725	12	269/331

It can be seen that the hardness of steel EN25 is nearly ten times of that of the 6061T5 Al alloy. So compared to the Al alloy, the EN25 steel compression tool can be taken as rigid without any deformation during compression. Practically, the compression tool has little deformation in uniaxial compression. However, compared to the sample, the deformation of the compression tool is negligible. Therefore, it is assumed that the surface of the compression tool keeps intact before and after the compression.

4. 14 Summary

In this chapter the instruments and methodologies used for the experiments have been introduced. Materials of samples and tool have also been detailed respectively. Software used for the analysis of experimental results has also been described. The results of these experiments and simulations will be discussed further in the following chapters.

CHAPTER 5

CRYSTAL PLASTICTY FINITE ELEMENT MODELLING OF 2D SURFACE ASPERITY FLATTENING

5.1 Introduction

In this chapter, three cases studies are introduced. Firstly, the general material parameters of FCC crystal are given, and the 12 typical slip systems of FCC metal are also mentioned. Then the evolution of the surface profile is simulated by a 2D crystal plasticity finite element model (CPFEM), and the grain orientation is mentioned. Thirdly, the influences of the grain size and orientation on the surface roughness (surface asperity) are investigated using the 2D crystal plasticity finite element method. Finally, effects of friction and wave length on surface asperity flattening (surface roughness) are also analysed by applying 2D crystal plasticity finite element modelling. The experimental results are also employed in the 2D CPFEM model and compared to the simulation results.

5.2 Simulation parameters

5.2.1 Material parameters

In Section 3.5.2, the crystal elastic constitutive equation is indicated in Equation (3.63). In the face centred cubic (FCC) crystal, this tensor only includes three non zero and unrelated components, as shown in the following equations.

$$\mathcal{L}_{iiii} = C_{11} \tag{5.1}$$

$$\mathcal{L}_{iijj} = C_{12}(i \neq j) \tag{5.2}$$

$$\mathcal{L}_{ijji} = C_{44}(i \neq j) \tag{5.3}$$

where C_{11}, C_{12} and C_{44} are the elastic modulus. In the FCC metal (aluminium), values of the three parameters can be obtained as [184]: C_{11} = 1067500 MPa, C_{12} = 60410 MPa, and C_{44} = 28340 MPa.

It is assumed that the hardening states of all the slip systems are homogeneous, q can be referred to reference [99], and other parameters are the same as reference [184]. All parameters for Equations (3.65) and (3.68) are listed in Table 5.1.

Table 5.1 Material parameters of aluminium [99, 185]

Parameter	Value	Parameter	Value
C_{11}	106750 MPa	s_0	12.5 MPa
C_{22}	60410 MPa	h_0	60 MPa
C_{44}	28340 MPa	s_s	75 MPa
$\dot{\gamma}_0$	0.001	a	2.25
m	0.02	q_l	1.0 (coplanar) 1.4 (No coplanar)

where $\dot{\gamma}_0$ is the reference shearing rate (s^{-1}), m is the power law, s_0 is the initial value of the deformation resistance, h_0 is the value of initial hardening rate, s_s is the saturation value of the deformation resistance, a is the exponent in the hardening equation, q_l is the latent hardening parameters.

5.2.2 Slip systems

In a single FCC aluminium crystal there are 12 slip systems {111}<110>: 4 slip planes A, B, C and D, and three slip directions in each slip plane. The slip systems are shown in Table 5.2. In the simulation it is assumed that all the slip systems have the same shear rate.

Table 5.2 Slip planes and directions of FCC aluminium [164]

Slip plane	Slip direction		
A(1 1 1)	[0 1 -1]	[1 0 -1]	[1 -1 0]
B(-1 1 1)	[1 0 1]	[1 1 0]	[0 1 -1]
C(1 -1 1)	[1 0 -1]	[0 1 1]	[1 1 0]
D(1 1 -1)	[1 -1 0]	[1 0 1]	[0 1 1]

5.3 Simulation of surface asperity flattening in uniaxial planar compression

5.3.1 Undeformed model and mesh

Due to the symmetry, half of the sample is selected as the two dimensional model. All the nodes in the left side of the model have no displacement in direction 1, and at the bottom of the sample are constrained by the rigid mould, and the tool is rigid (Figure 5.1). Three displacements have been applied in the simulation (0.0005, 0.001 and 0.0015 mm), and a fully finite element polycrystal model has been used in the study. There are 259 CPE4R continuum solid elements, each grain (orientation sets) is described by several finite elements: grain 1 includes 67 elements, grain 2 includes 72 elements, grains 3 and 4 both include 45 elements, and grain 5 includes 22 elements, grain 6 only includes 8 elements.

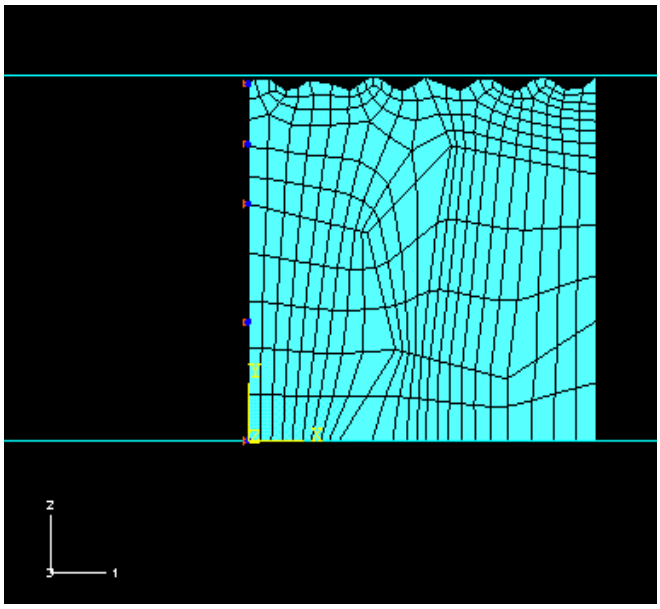

Figure 5.1 Two dimensional undeformed model and mesh

5.3.2 Marked grain and surface roughness

In the simulation, random grain shapes and surface roughness are used in the two dimensional model. In total, there are three layers (surface layer, central layer and bottom layer) in the two dimensional model: grains 1 and 2 are in the surface layer, grains 3 and 4 are in the central layer, and grains 5 and 6 in the bottom layer. The surface roughness and grains are shown in Figure 5.2.

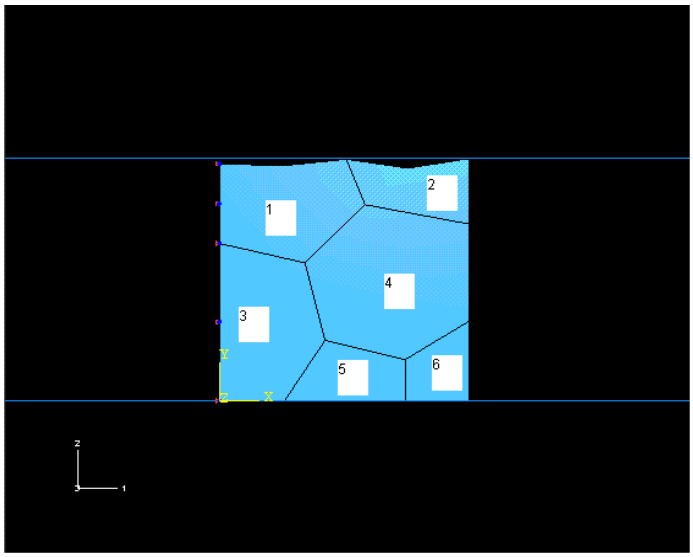

Figure 5.2 Marked grains in undeformed model

5.3.3 Deformation contours under different reductions

(a) Deformation contour with a reduction of 10 %

The deformation contour with a reduction of 10 % is shown in Figure 5.3. From Figure 5.3 it can be seen that under a reduction of 0.5 mm, the surface profile of the sample changed significantly and the mesh deforms obviously. The contour map of this deformation also shows that the maximum stress appears at the area of grains 2, 4 and 5.

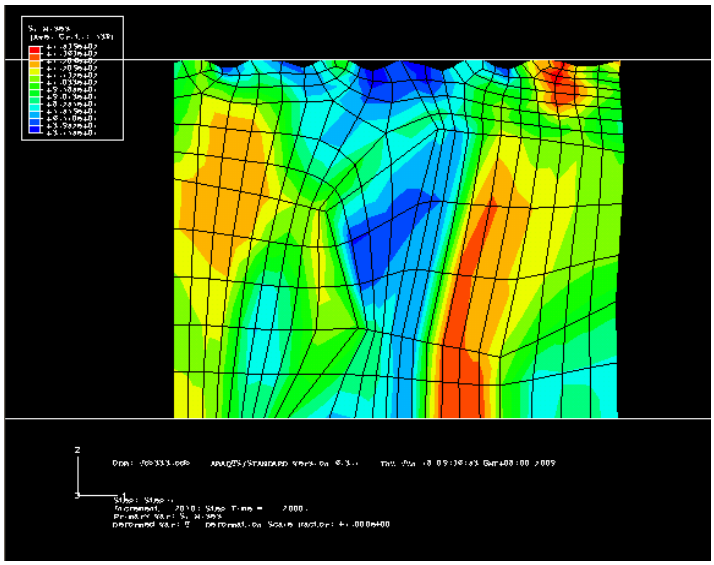

Figure 5.3 Deformation contour with a reduction of 10 %

(b) Deformation contour with a reduction of 20 %

The deformation contour with a reduction of 20 % is shown in Figure 5.4. It can be seen that with an increase in reduction, the surface profile of the sample is much flatter than that in Figure 5.3 and the mesh becomes more distorted. This deformation contour also shows the maximum stress shifts from the original area of grains 2, 4, and 5 to the area of grains 1, 3, and 5, and the right edge of grain 2.

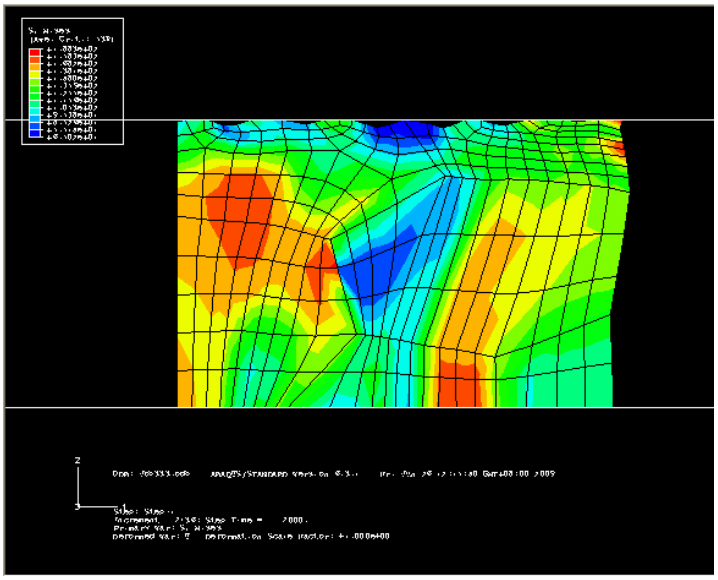

Figure 5.4 Deformation contour with a reduction of 20 %

(c) Deformation contour with a reduction of 30 %

Compared to Figures 5.3 and 5.4, the model in Figure 5.5 experiences the largest deformation, and the mesh becomes increasingly distorted. Meanwhile, it is shown from the contour that the maximum stress appears in grains 3 and 5.

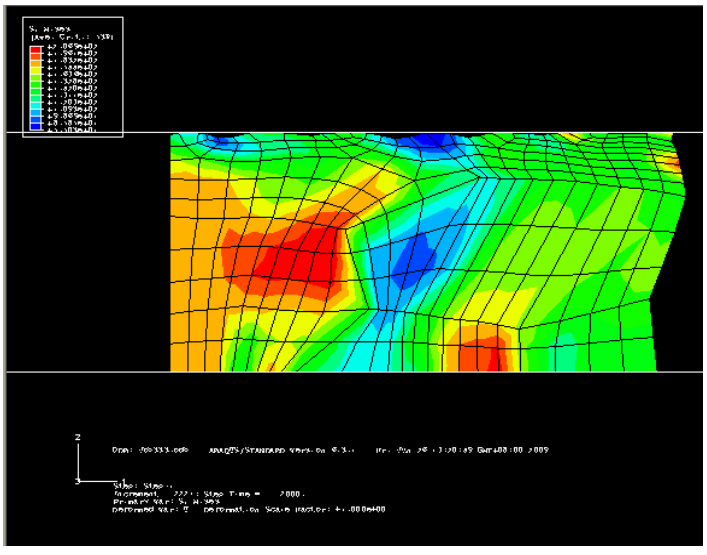

Figure 5.5 Deformation contour with a reduction of 30 %

5.3.4 Grain rotation from the simulation results

All the grain rotation angles during compression are shown in Tables 5.3-5.5. Under a reduction of 10 %, grains 1 and 4 and 5 rotate with the maximum angles. Because this simulation is based on two dimensional models, we only focussed on grain rotations in the transverse direction (angle OMEGA) in this study. During compression, the variation of surface roughness is mainly led by the three grains rotations. Grains in the three layers (surface layer, central layer and bottom layer) all contributed to the change of surface roughness of the sample.

Table 5.3 Euler angles for grain rotation under a reduction of 10 %

Grain number	THETA	PHI	OMEGA
1	-53.35	120.972	218.3452
2	-0.8929	128.994	125.3891
3	-48.6992	111.774	164.0696
4	105.7984	-109.58	-235.148
5	436.4864	95.8106	208.9282
6	270.0523	44.1304	175.7532

Table 5.4 Euler angles for grain rotation under a reduction of 20 %

Grain number	THETA	PHI	OMEGA
1	2.6683	-0.2465	-0.2817
2	1.7957	0.0921	-1.5013
3	-2.1521	0.1002	2.1807
4	1.1332	-0.3341	0.4979
5	-2.5985	-0.1308	2.3693
6	0.3471	0.0318	-0.2611

Table 5.5 Euler angles for grain rotation under a reduction of 30 %

Grain number	THETA	PHI	OMEGA
1	1.9819	-0.2996	-0.1096
2	0.5656	-0.061	-0.3358
3	-2.9933	0.107	2.9892
4	9.7716	-3.1002	2.2071
5	-20.7164	-6.4652	1.2813
6	0.1634	0.014	-0.1017

It can also be seen from Table 5.3 that the largest rotation takes place in grains 3 and 5. So rotations in grains 3 and 5 are the main reason for the variation in surface roughness. In this stage, only the central and bottom layers give a rise to the change of surface roughness. It is very difficult to test these results by practical experiments.

For a reduction of 30 % (Table 5.5), grains 3 and 4 rotated with the largest angle, and the variation in surface roughness resulted mainly from the rotation of grains 3 and 4.

In general, at the beginning of compression, variation in surface roughness is led by the three layers of grains. With an increase in reduction, the influence of the surface grain rotation on surface roughness becomes smaller. When reduction reaches a certain value, only grain rotations in the central layer play an important role on surface roughness.

5.3.5 Comparison of surface profiles before and after compression

In the simulation, three reductions (10, 20 and 30 %) are employed in the model. The surface profiles before and after planar compression are shown in Figures 5.6-5.8. It can be seen that with an increase in reduction, the top surface profile tends to be smoother and flatter.

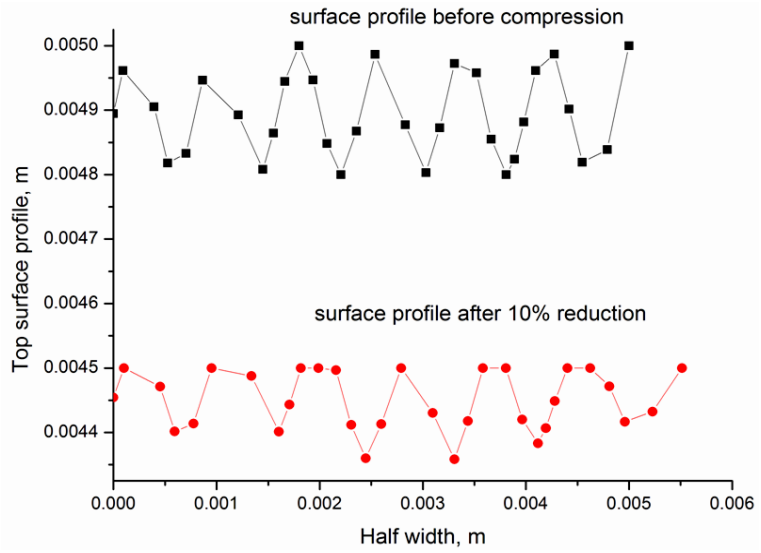

Figure 5.6 Surface roughness after planar compression (10 % reduction)

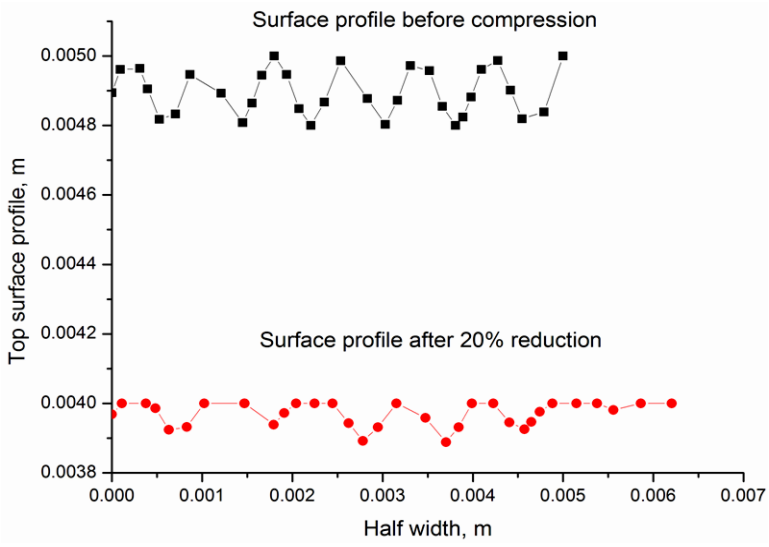

Figure 5.7 Surface roughness after planar compression (20 % reduction)

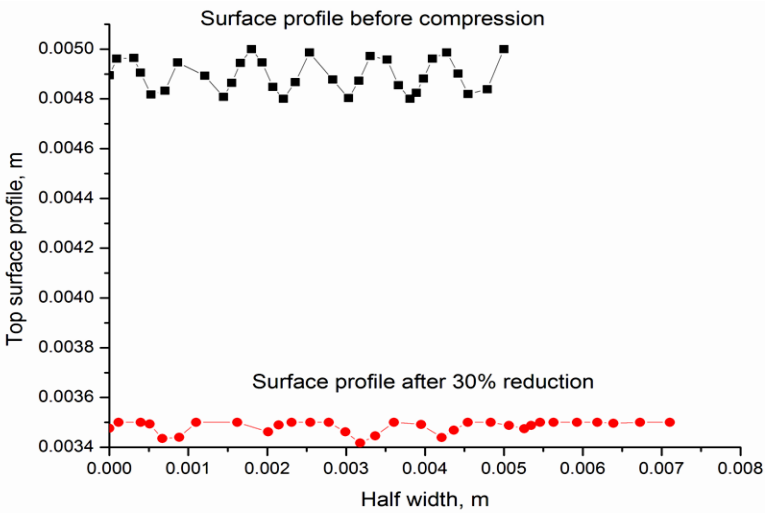

Figure 5.8 Surface roughness after planar compression (30 % reduction)

5.3.6 Comparison of surface roughness before and after compression

Two kinds of surface roughness are used in the simulation:

(a) Arithmetic average of absolute values:

$$R_a = \frac{1}{n}\sum_{i=1}^{n}|y_i| \tag{5.4}$$

(b) Root mean square value:

$$R_q = \sqrt{\frac{1}{n}\sum_{i=1}^{n} y_i^2} \tag{5.5}$$

where y_i is the distance from the average value line, n is the calculation points. The simulation results of surface roughness are shown in Figure 5.9. It is shown that there is a linear relationship between the surface roughness (R_a and R_q) and reduction.

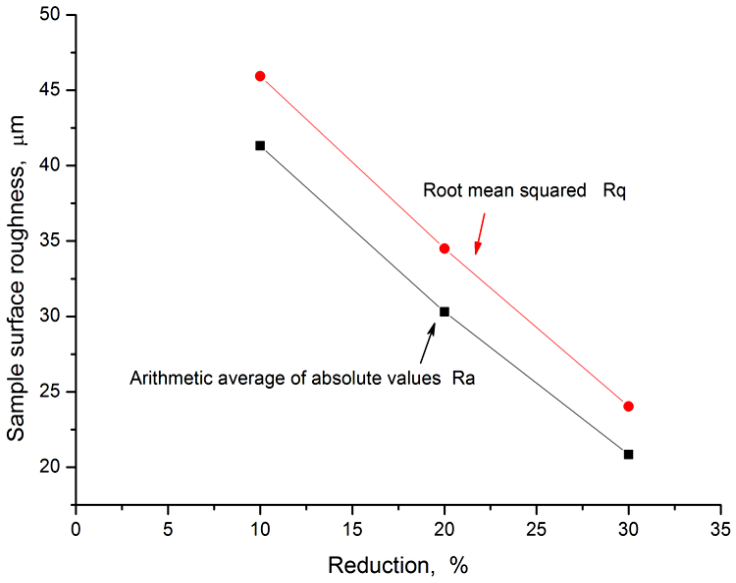

Figure 5.9 Surface roughness under different reductions

5.3.7 Conclusions

(1) With an increase in reduction, sample surface tends to become flattened under the uniaxial planar compression;
(2) In compression, grains with the largest stresses also have the largest rotation of Euler angles.
(3) With an increase in reduction, both the arithmetic average surface roughness R_a and root mean square surface roughness R_q decrease.

5.4 Influence of grain size on surface asperity flattening

5.4.1 Finite element averaging procedure

In this approach the finite element calculations are used to make a transition from the response of a single grain (or a region within a grain) to the response of a polycrystalline aggregate. It is assumed that each element represents one crystal, and is assigned an orientation as the initial texture [116]. So each grain is modelled to allow for non-uniform deformation between the grains and within the grains, and both the equilibrium and compatibility are satisfied in the weak finite element sense. In this study, we varied the number of elements and grains in each element, and the

distribution of grain orientations in the mesh.

5.4.2 Mesh and two dimensional polycrystal models

This study aims to analyse the relationship between reduction, grain size, and surface roughness during uniaxial plane strain compression. The sample material is 6061T5 aluminium alloy. There are three two-dimensional samples with different grain sizes (8, 25 and 50 μm). The sizes of the three samples are all 500 μm ×100 μm. Original surface roughness of the three samples is 1.35 μm. Reductions range from 5 to 15 %. Contact friction between the sample and compression tool is 0.01. A reduction is applied on the top of the sample by the elastic-plastic compression tool. Due to symmetry, all the nodes on the edge ab, a_1b_2, and a_2b_2 (Figures 5.10, 5.11 and 5.12) have no displacement in direction 1. A fully finite element polycrystal model has been used in this study. The simulation conditions include: a two dimensional model with 8 μm grain size with 741 CPE4R reduced integration elements, and one grain set with one element (total 741 grains in the model); a two dimensional model with 25 μm grain size has 320 CPE4R reduced integration elements, one grain set with 4 elements (total 80 grains in the model); a two dimensional model with 50 μm grain size also has 320 CPE4R reduced integration elements, one grain set with 16 elements (total 20 grains in the model).

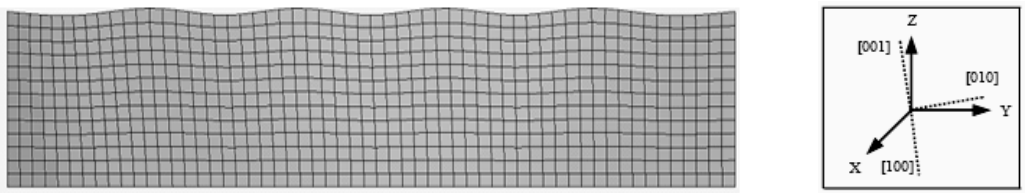

Figure 5.10 Two dimensional model with 8 μm grain size

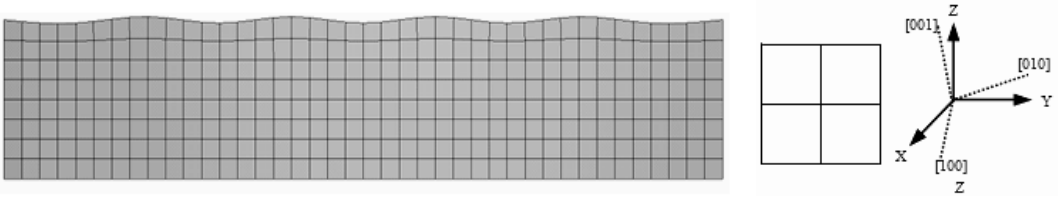

Figure 5.11 Two dimensional model with 25 μm grain size

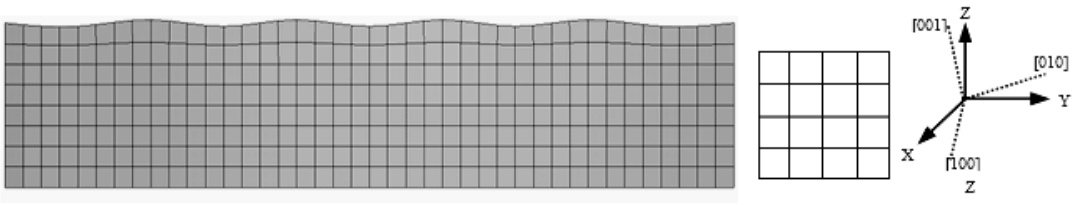

Figure 5.12 Two dimensional model with 50 μm grain size

5.4.3 Texture development during compression

In Figure 5.13, when deformation takes place in FCC metal, 12 slip systems with <110> slip directions and {111} slip planes will be activated and put into action (Figure 5.12). As usual the {111}<110> slip systems are the slip systems with a low slip resistance that the slip can take place easily. Sometimes it can be called “soft orientations”. Other slip systems where slip could not take place easily are “hard orientations”. In the deformation of different materials, the soft and hard orientations are very different.

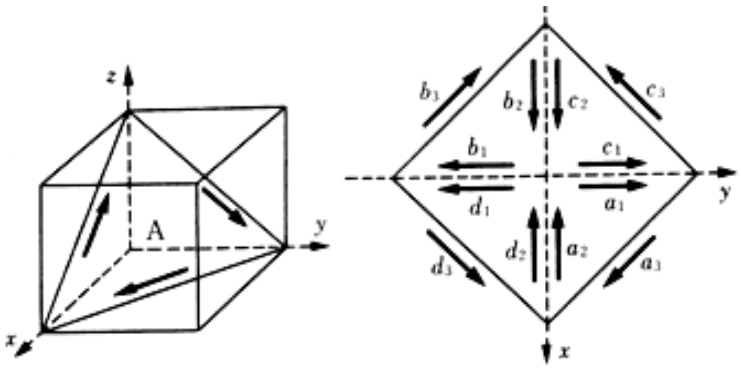

Figure 5.13 {111}<110> slip systems of pure FCC aluminium

Pole figure / Reduction		{100}	{101}	{111}
Original orientation		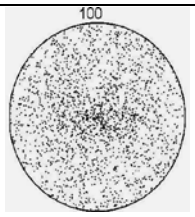	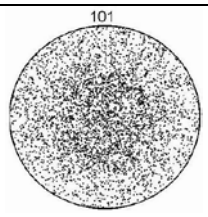	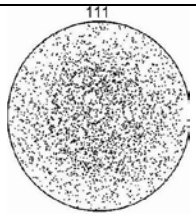
Friction coefficient	Reduction			
0.01	5 %	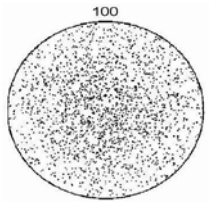	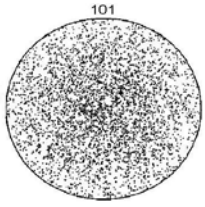	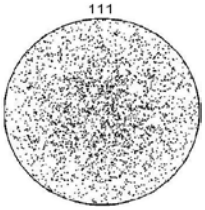
	10 %	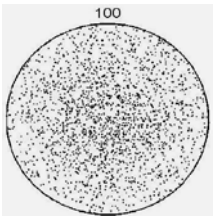	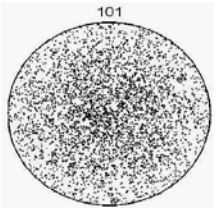	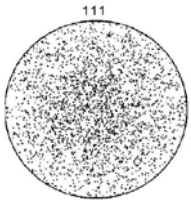
	20 %	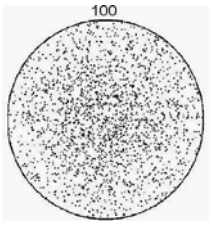	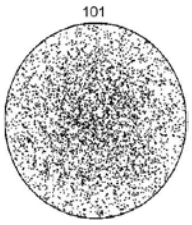	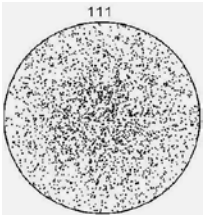
	50 %	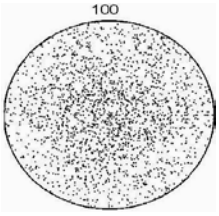	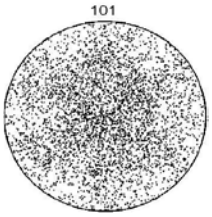	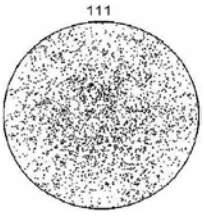
	70 %	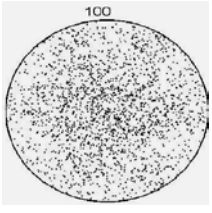	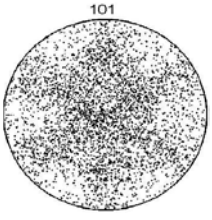	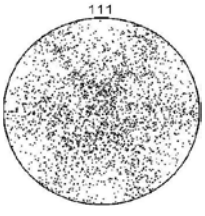

Figure 5.14 Pole figure of sample with 8 μm grain size

It is shown in Figure 5.14 that with an increase in reduction, the development of texture shows a certain tendency. At first, when reduction is low (less than 0.05), there is no obvious tendency in the pole figure. In this stage the main deformation is

elastic and the energy resulting from this plastic deformation could not support many slip systems to slip. So only a few slip systems will be activated to slip, and the grain rotation and stretch is insignificant. When reduction exceeds a certain value (10 %), an obvious tendency appears in the pole figure; all the grains tend to rotate along a certain direction and axis. In this stage, with an increase in plastic deformation, the elastic deformation will decrease and disappear quickly. The energy of cold deformation will activate many slip systems to slip, so many grains will rotate and stretch along the "soft orientations" (<110> slip directions and {111} slip planes). Furthermore, with an increase in reduction, the cubic texture becomes more and more obvious. In Figure 5.14, when reduction is 70 %, the texture is the most obvious and strongest. Therefore, in the deformed sample a stabilised cubic texture will be formed. The sample will obtain a new balance of grain distribution and arrangement. On the other hand, with an increase in reduction, there is no obvious tendency in the hard orientations (Pole figure {100}, etc.)

5.4.4 Influence of reduction on surface roughness during compression

With an increase in reduction, the surface roughness tends to decrease with three stages in this process (Figure 5.15). The first stage is the "main elastic deformation stage" where reduction is less than 5 % and the surface roughness decreases greatly. The decreasing rate here is the largest of the three stages. In this stage most of the deformation is elastic, with only a little plastic deformation taking place. The second stage is "plastic deformation stage" (reduction exceeds 5 %) where the decrease in surface roughness is also significant. However, the decreasing rate of surface roughness will be lower than that of the first stage. In this stage some slip systems will be activated and many grains will be arranged along the "soft orientations" (<110> slip directions and {111} slip plane). This stage is a fully "work hardening process". If reduction exceeds 10 %, compression will enter the third stage, the "orientation distribution balance stage" where there is an increase of reduction and the surface roughness will decrease slowly. Although plastic deformation continues, the rearrangement and rotation of the grains will almost finish, and the majority of grains and texture fibres will be arranged along a certain direction. A new "balance" and stabilised cubic texture is formed. During the first and second stages, it is

obvious that the increment of surface roughness in the rolling direction is proportional to the applied strain.

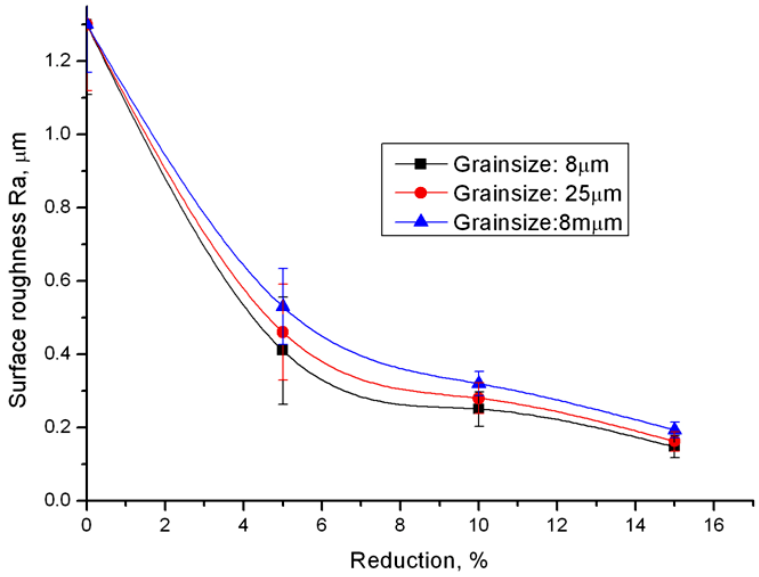

Figure 5.15 Relationship between surface roughness and reduction under different grain sizes

5.4.5 Influence of grain size on stress-strain curve during compression

From Figures 5.16 and 5.17, it can be seen consistently that with an increase of grain size, all the compression stresses of the samples increase accordingly. In the two figures, the compression stress for the samples with a large grain size increases much quicker than the sample with small grains, and the saturated values of compression stress reach 220 or 260 MPa. Samples with the small grain size have the lowest compression stress with the same strain, and it is only about 160 MPa.

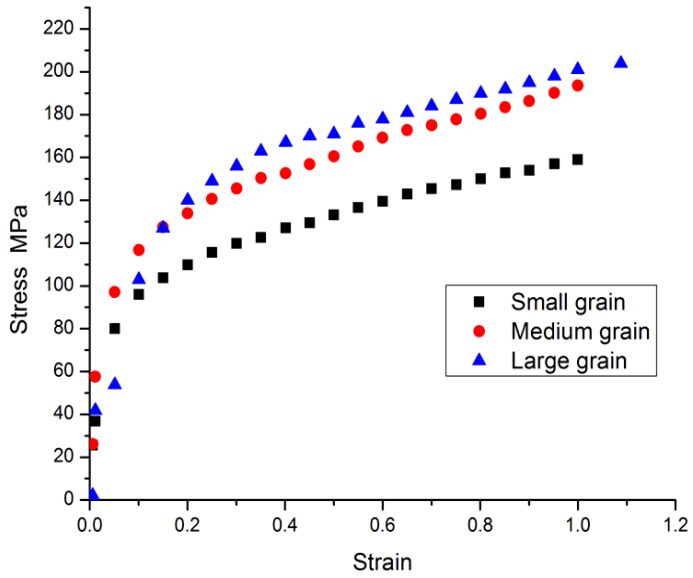

Figure 5.16 Stress- strain curve of different grain sizes with the strain rate 0.001 s^{-1}

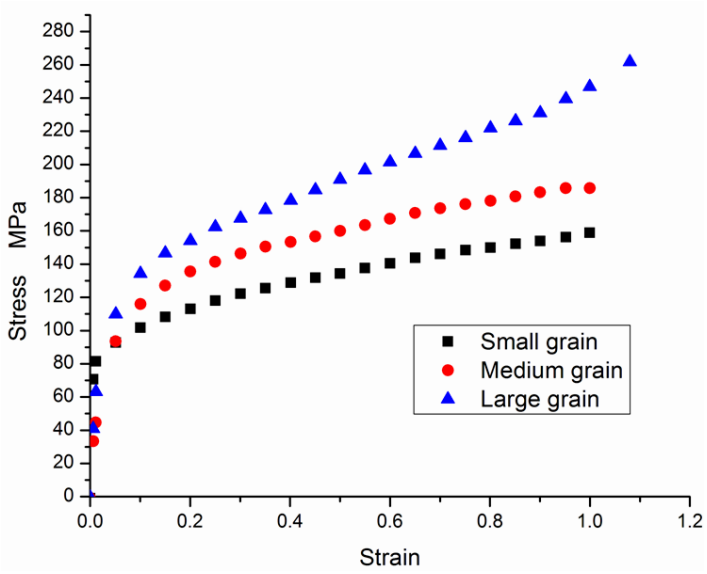

Figure 5.17 Stress-strain curve of different grain size with the strain rate 0.01 s^{-1}

5.4.6 Influence of grain size on surface roughness during compression

(a) Relationship between grain size and surface roughness

It is known from Figure 5.18 that when reduction is 5 %, deformation is in the first, “mainly elastic deformation stage”. During this stage, elastic deformation is mainly deformation of the sample. Plastic deformation only accounts for a small portion of

total deformation, so in this stage the surface roughness is greatly reduced and any residual stress can be followed by inhomogeneous deformation where only a few slip systems may be activated. The grain size has a significant influence on the change of surface roughness. With an increase in grain size, the surface roughness of the sample with a larger grain size (50 μm) decreases slower than the one with a smaller grain size (8 μm). The reason is that deformation in this stage is mainly elastic, and the sample with a large grain size has more elasticity than the one with a small grain size under the same reduction of compression. So the sample with a large grain size can maintain a relatively larger surface roughness than the sample with small grain size during the same compression process.

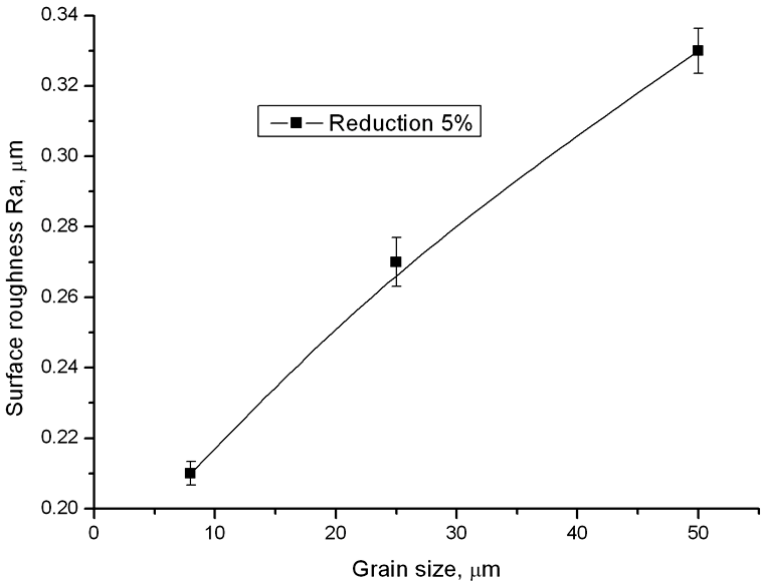

Figure 5.18 Relationship between surface roughness and grain size (low reduction)

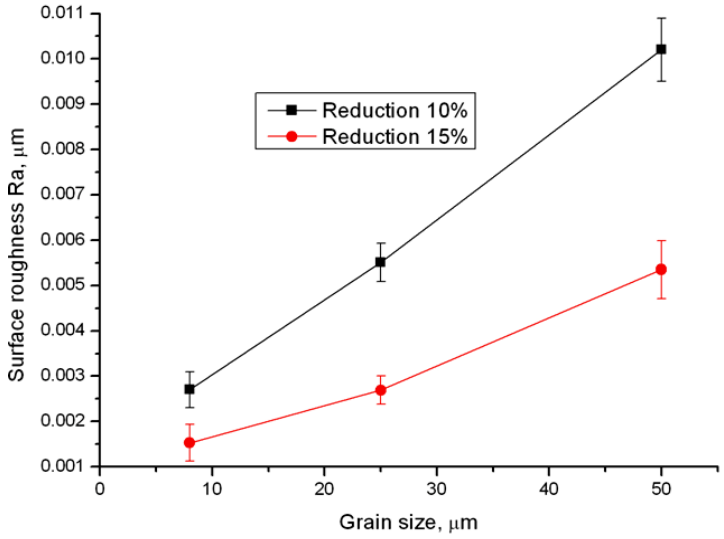

Figure 5.19 Relationship between surface roughness and grain size (larger reduction)

The changes in surface roughness are different in Figures 5.18 and 5.19: with an increase in grain size, the surface roughness increases from 0.21 to 0.33 μm, while in Figure 5.19 the surface roughness only increases from 0.0025 to 0.0105 μm with an increase in grain size. For this reason, Figures 5.18 and 5.19 describe the influences of grain size on surface roughness.

When reduction exceeds 10 %, deformation is in the second, "plastic deformation stage" (Figure 5.19) where elastic deformation will be completely finished and almost all the deformation is plastic deformation. In this stage, the grain size has an obvious influence on the surface roughness of the sample, indeed the tendency is almost the same as the curve in Figure 5.18. With an increase in grain size, the surface roughness of the sample obviously decreases, but with a lower rate than that in the first stage (Figure 5.18). The reason for this phenomenon is that in this stage, many slip systems will be activated by the deformation work. In FCC metal, a majority of grains slip generates along the soft orientation (<110> slip directions and {111} slip plane). If the sample has a small grain size, it has more slip systems to carry out plastic deformation with a large density of dislocation lines, so plastic deformation of the sample with a small grain size can occur much easier than that with a large grain size. On the other hand, compared with elastic deformation, plastic deformation in this stage can only give less space for any variation in surface roughness. This is why the decreasing speed of the surface roughness of the sample

is much lower in the second stage than that in the first stage. When reduction exceeds 15 %, deformation begins the third, "orientation distribution balance stage" where grain distribution will reach a new balance by slip, and a new balance will be established. In this stage only a few grains can slip along a certain orientation, so the influence of the grain size on surface roughness will be slight and the surface roughness of the sample will remain in a certain range.

(b) Regression analysis

All the results have been analysed by regression of Origin Pro 8. The result of this regression is obtained as

$$y_1 = A_1 * \exp(-x/t_1) + y_0 \quad (5.6)$$

where, x is the average grain size, y_1 is the average arithmetic surface roughness R_a, A_1 is a constant, and t_1 is a constant.

Table 5.6 Relationship between surface roughnesss and average grain under a reduction of 15 % (grain size are 8 μm, 25 μm and 50 μm respectively)

Reduction (%)	A_1	t_1	y_0
5	-0.24205	50.50442	0.41441
0	0.00225	-47.74407	-0.00114
15	0.02481	-167.55458	-0.02333

From Equation (5.6), it is obvious that the relationship between the grain size and surface roughness is an exponent function. In Section 2.5.4, Wang et al. [60] proposed a revised equation for the surface roughness R_α in the tensile test. They expressed the relationship between the surface roughness and average grain boundary with a power exponent function (Equations (2.29) and (2.30)). Both tensile and compression tests show the grain size has a significant influence on the surface

roughness. With an increase in grain size, the surface roughness tends to increase while the samples have been compressed under the same experimental conditions. It can be obtained from Table 5.6, surface roughness R_a is a power exponent function of the grain size.

5.4.7 Relationship between surface roughness and reduction

It can be known from previous results, when reduction is less than 10 %, the relationship between the surface roughness and reduction is linear. When the reduction is between 10-40 %, deformation is a combination of elastic and plastic deformation. With an increase in reduction, elastic deformation becomes less and less, but on the other hand, plastic deformation increases. So in this stage, the relationship between the surface roughness and reduction is complicated, and it has been studied by Origin and Matlab (Figure 5.20). When reduction exceeds 40 %, the influence of the reduction on surface roughness is not obvious.

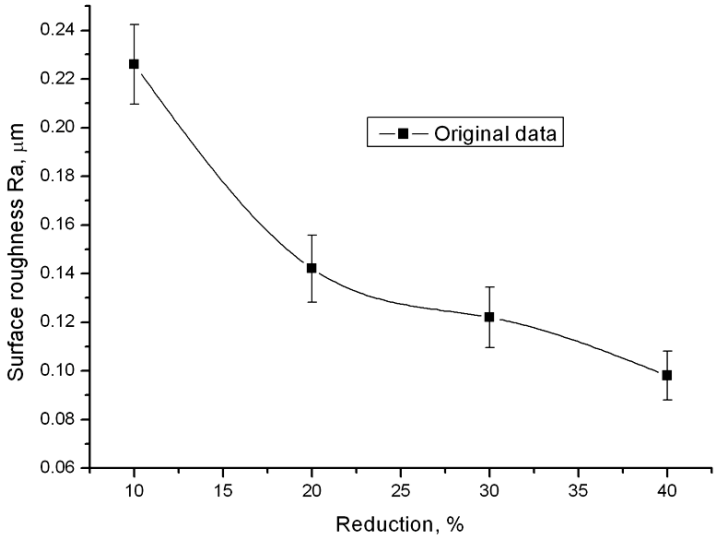

Figure 5.20 Relationship between surface roughness and reduction (plastic deformation stage)

When the reduction is between 10 % and 40 %, the relationship between the surface roughness of the sample and the reduction is obtained as

$$Y = A + B_1 * X + B_2 * X^2 \quad (5.7)$$

where Y is the average surface roughness, A is a constant, B_1 and B_2 are the coefficients of surface roughness X.

Table 5.7 Parameters of Equation (5.7)

Parameter	Value	Error
A	0.32955	0.03361
B_1	-0.01225	0.00307
B_2	1.6025E-4	6.03738E-5

In Section 2.5.2, it has been shown from the research that the surface roughness is linearly dependent on the plastic strain of tensile tests [41, 45-46], and it shows an empirical equation of the relationship between the surface roughness and plastic strain ε.

In uniaxial planar compression, the relationship between surface roughness and strain is different from that of the tensile test because of the evolution of the deformed surface. In the tensile test, the sample surface is an unconstraint surface that can develop freely, but in uniaxial planar compression the sample is constrained by the compression tool. The evolution of the sample surface will be affected by the surface roughness of the tool and the friction between the tool and the sample. This is why Equation (5.7) has a second order parameter $B_2 * X^2$.

5.4.8 Relationship between reduction and Euler angles

(a) Euler angle 1

From Figure 5.21 it can be seen that when reduction is between 20 % and 30 %, the Euler angle 1 has the largest variation. In this stage, many slip systems will be activated and plastic deformation will become the main deformation of the sample. The relationship between the surface roughness and reduction is non-linear.

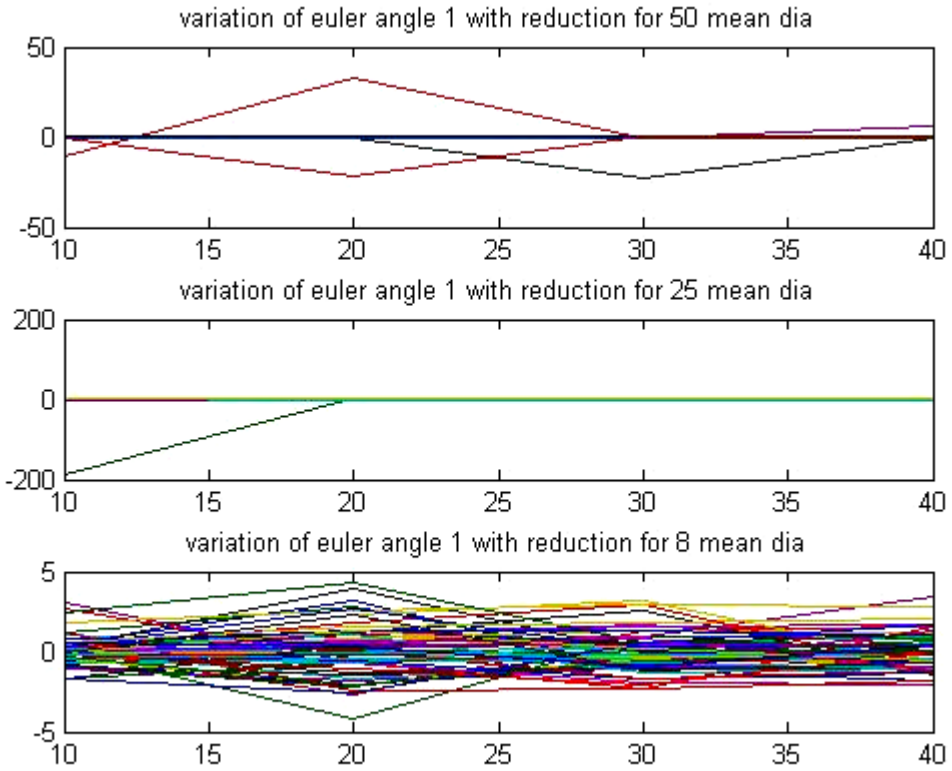

Figure 5.21 Relationship between Euler angle 1 and reduction

For 50 μm average grain

$$R_a = 0.017x^2 + 0.63x + 4.9 \quad (5.8)$$

For 20 μm average grain

$$R_a = 0.0081x^2 + 0.31x - 2.7 \quad (5.9)$$

For 8 μm average grain

$$R_a = -0.0075x^2 - 0.47x + 6.5 \quad (5.10)$$

(b) Euler angle 2

It is shown from Figure 5.22 that when reduction is between 20-30 %, the Euler angle 2 has a large variation. But when reduction exceeds 30 %, the Euler angle will change greatly. In this stage, elastic deformation will disappear and plastic

deformation will play a main role in the deformation and some new slip systems may be activated.

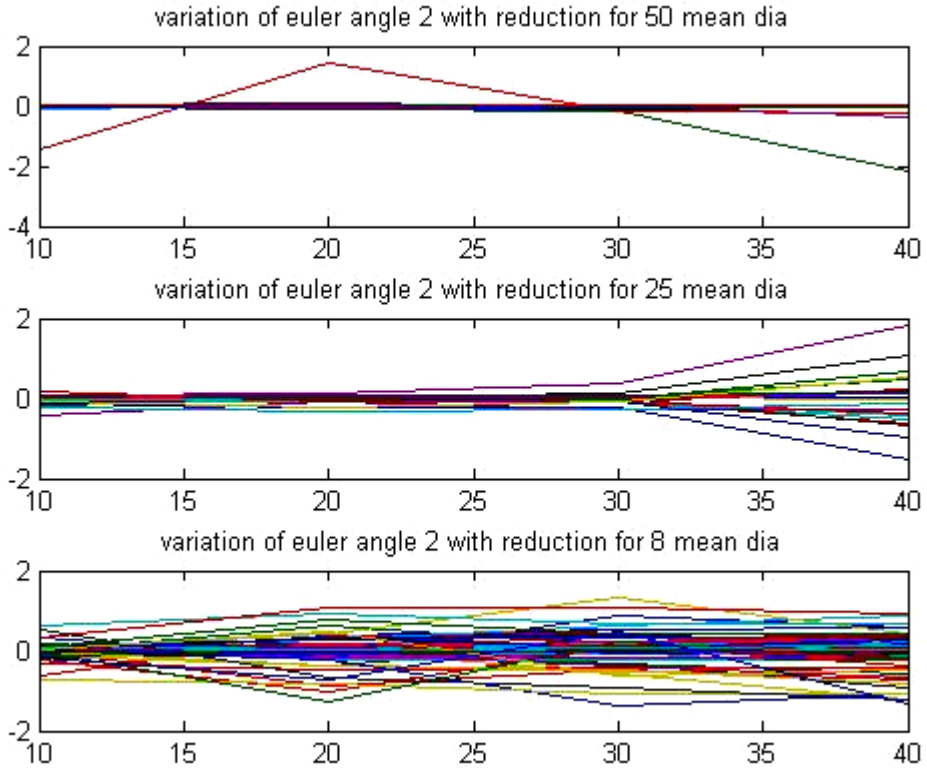

Figure 5.22 Relationship between Euler angle 2 and reduction**.**

For 50 μm average grain

$$R_a = -0.0012x^2 + 0.048x - 0.44 \quad (5.11)$$

For 20 μm average grain

$$R_a = 0.0077x^2 + 0.031x - 0.19 \quad (5.12)$$

For 8 μm average grain

$$R_a = -0.0028x^2 + 0.17x - 2 \quad (5.13)$$

(c) Euler angle 3

The variation of Euler angle 3 in Figure 5.23 shows a similar tendency to the Euler angle 2 shown in Figure 5.22.

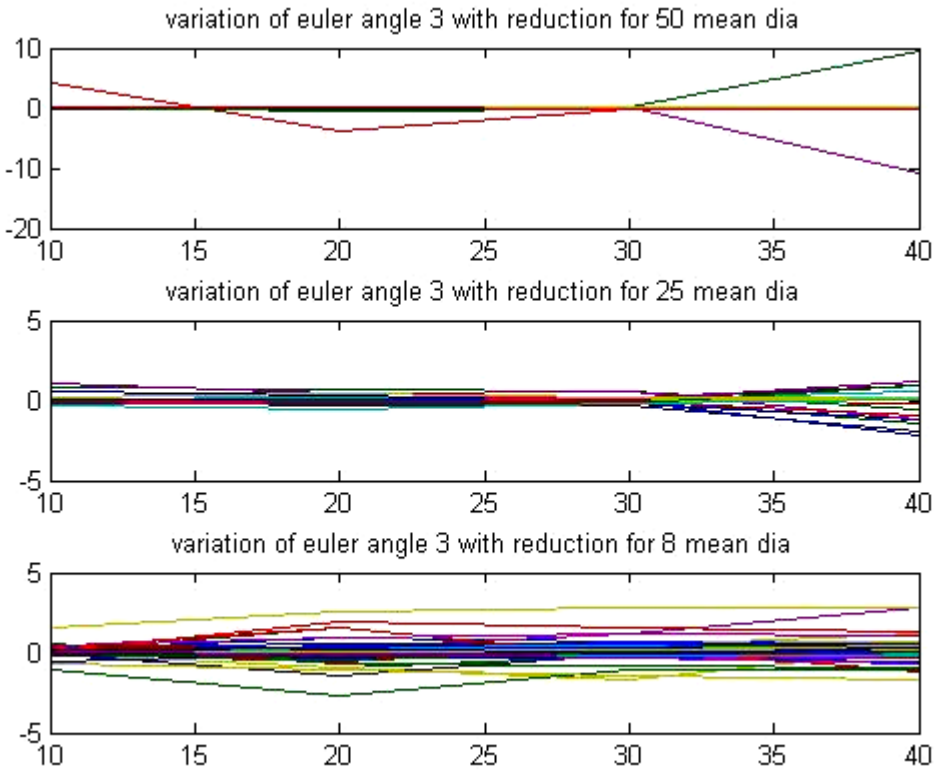

Figure 5.23 Relationship between Euler angle 3 and reduction.

For 50 μm average grain

$$R_a = -0.028x^2 + 1.1x - 8.5 \quad (5.14)$$

For 20 μm average grain

$$R_a = -0.00013925x^2 + 0.01x - 0.031 \quad (5.15)$$

For 8 μm average grain

$$R_a = -0.00098x^2 + 0.059x - 0.68 \quad (5.16)$$

It can be obtained from the above three cases (a), (b), and (c) that the relationship bet ween the surface roughness R_a and grain orientation (Euler angles) is non-linear.

5.4.9 Conclusions

This study aimed at understanding the influence of the grain size and reduction on surface roughness during uniaxial planar compression. From an analysis of the simulation results, the following conclusion can be obtained:

(1) With an increase in reduction, the texture tends to be stronger and much more obvious. In the compression, all the grains of the sample will slip along the certain slip directions and slip planes (<110> slip directions and {111} slip planes). Finally, the cubic texture will be formed, and the sample will obtain a new balance with stabilised microstructures.

(2) Under a certain reduction, reduction plays an important role on the surface roughness. Surface roughness shows a certain relationship with the reduction (strain), and with an increase in reduction (strain), the surface roughness decreases accordingly. In the tensile test the variation of surface roughness R_a is proportional to the applied strain. However, in a uniaxial compression test the relationship between the surface roughness and strain is non-linear according to the influence of the compression tool and friction between the sample and the tool.

(3) The grain size also has a significant influence on surface roughness. Under the same reduction, the surface roughness of the sample with a large grain size tends to decrease slowly, but after compression the sample with the maximal grain size has a maximal surface roughness. Both the tensile and compression tests show that the relationship between the surface roughness and average grain size is non-linear. The surface roughness R_a is a power exponent function of the grain size.

(4) Grain size also has an obvious influence on the sample stress: with an increase in grain size, stress in the sample increases accordingly.

(5) In the uniaxial compression test, grain orientation also plays an important role in the evolution of surface asperity. The relationship between the surface roughness and grain orientations (Euler angles) is non-linear.

5.5 Influence of friction and wave length on surface asperity flattening

Surface asperity is an important parameter of surface quality and is also an interesting topic in cold metal manufacturing. In general, there are many factors which result in variations of surface roughness, such as the original surface roughness of the product, grain size, crystal structure, crystal orientation, texture distribution, loading path, stress-strain state (deformation mode) and surface of the tool, etc [4]. There are some reports in terms of surface asperity flattening. Wilson et al. [10, 11] have investigated the effect of bulk plasticity on asperity flattening when the lay of the roughness was parallel to the direction of bulk straining (longitudinal roughness). They found that the rate of asperity flattening with bulk straining was related to the spacing and pressure of asperities. Makinouchi et al. [12] presented elastic-plastic finite element solutions for the case of transverse roughness. Wilson and Sheu [10] also found that a large increase of contact area with bulk strain and a reduction in the load was needed for bulk yielding. Sutcliffe [13] tested and developed Wilson and Sheu's theories and discovered that the high pressure between contacting asperities and the deformation of bulk material affects asperity deformation. However, there are only a few reports on the interaction between surface asperity flattening, reduction, and friction by the crystal plasticity theory. In order to figure out the relationship between the sample surface asperity flattening, reduction and friction by the crystal plasticity theory, a finite element model has been used in the commercial finite element software ABAQUS to simulate the surface asperity flattening of Al plate along the rolling direction during uniaxial planar compression. A finite element polycrystal model with a sub-grain scale is used in this study.

5.5.1 Experimental

(a) Sample preparation

The sample was polished by an auto-polishing machine along the transverse direction. All the samples were ground in a transverse direction with the same grinding time, pressure, and sand papers (grade P220). A 2D profile meter was used to measure the surface roughness of the sample, and before compression, a central

line was drawn on the top surface and the surface roughness was measured along this line. After compression, the surface roughness was measured along the same line. This line can be drawn in any position along a transverse direction, and therefore the surface roughness at any position (or line) can be determined. The errors in roughness between the different samples were below a certain range (less than 0.05 μm). After grinding, the roughness of all the samples was about 0.72 μm (R_a). When under compression the sample is constrained in a transverse direction, while roughness develops along the rolling direction. The compression test has been carried out by the INSTRON MTS. The samples are 10×10×6 mm^3 in size.

(b) Sample parameters

After mechanical polishing the heights of the samples were measured with a micrometer. All the parameters of samples for the compression are shown in Tables 5.8 (with lubrication) and 5.9 (without lubrication).

Table 5.8 Parameters for compression (with lubrication)

Number	Cross section (mm×mm)	Height (mm)	Displacement rate (mm/min)	Strain rate (s^{-1})	Reduction (%)	Reduction (mm)	Height (mm)
1	10.04×10.18	6.10	0.36	0.001	5	0.31	5.80
2	10.04×10.04	6.13	0.35	0.001	10	0.61	5.52
3	9.99×10.03	6.14	0.33	0.001	20	1.23	4.91
4	10.11×10.03	6.11	0.31	0.001	30	1.83	4.28
5	10.48×10.04	6.13	0.29	0.001	40	2.45	3.68

Table 5.9 Parameters for compression (without lubrication)

Number	Cross section (mm×mm)	Height (mm)	Displacement rate (mm/min)	Strain rate (s^{-1})	Reduction (%)	Reduction (mm)	Height (mm)
1	9.53×9.60	6.12	0.36	0.001	5	0.31	5.82
2	9.58×9.40	6.11	0.35	0.001	10	0.61	5.50
3	9.60×9.54	6.10	0.33	0.001	20	1.22	4.88
4	9.67×9.41	6.13	0.24	0.001	30	1.84	4.29
5	9.58×9.50	6.09	0.29	0.001	40	2.44	3.66

The strain rate for the compression is 0.001 s^{-1} but controlling the strain rate with the INSTRON MTS is difficult so it has been replaced by the displacement rate. The relationship between the strain rate and the displacement rate is as

$$H_0 = H + \Delta H, \varepsilon = \ln \frac{H}{H_0}, \ \Delta t = \varepsilon / \dot{\varepsilon}, \ \dot{U} = \Delta H / \Delta t \tag{5.17}$$

where H_0, H, ΔH are the original height, the height after compression and the height increment respectively. ε is the true strain, Δt is the time of deformation, and $\dot{U}$ is the displacement rate of the sample under compression.

(c) Development of surface roughness of the sample during uniaxial planar compression

It can be obtained from the experimental results (Table 5.10) that with an increase in reduction, the surface roughness of both samples (compression with and without lubrication) decreases significantly. When reduction is less than 5 %, the two samples retain the same surface roughness, but when reduction exceeds 10 % there is an obvious difference in the surface roughness. The samples without lubrication during the compression have a higher decreasing rate of surface roughness. Finally, the samples with lubrication during compression have a comparatively rougher surface than those without lubrication. The experimental results show that lubrication can constrain the surface asperity flattening process, that is, friction can increase the process of surface asperity flattening.

Table 5.10 Development of surface roughness under uniaxial planar compression:

(a) with lubrication

Reduction (%)	Roughness (with lubrication)
0	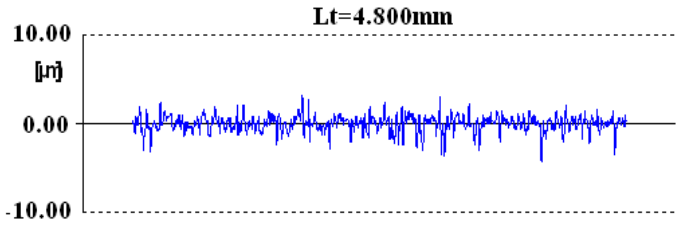
5	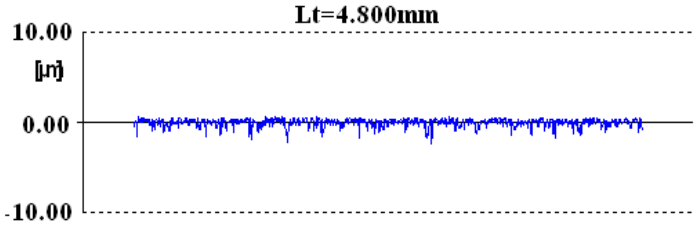
10	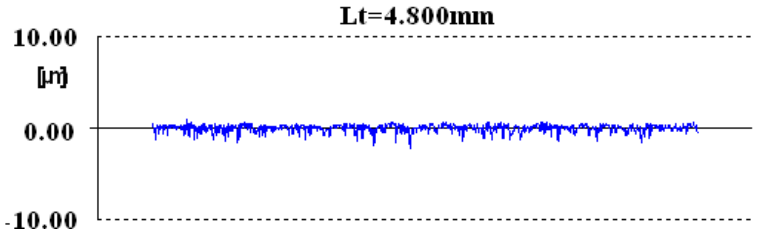
20	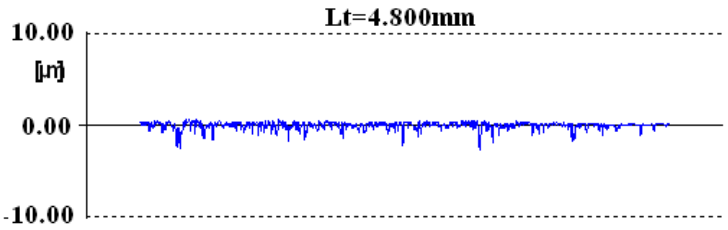
30	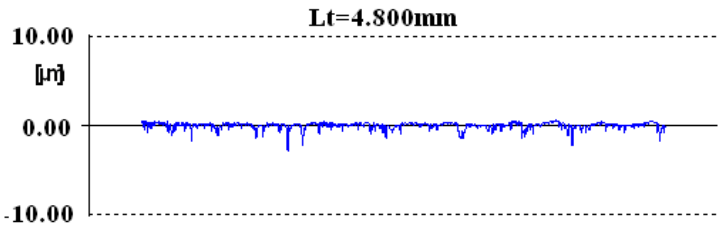
40	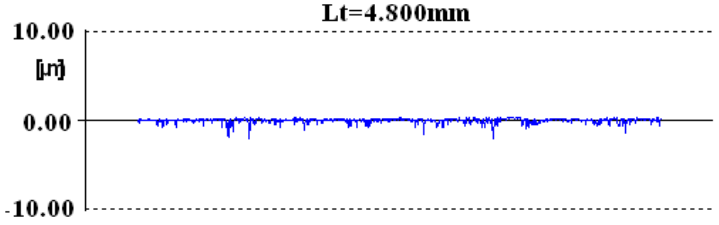

(b) without lubrication

Reduction (%)	Roughness (without lubrication)
0	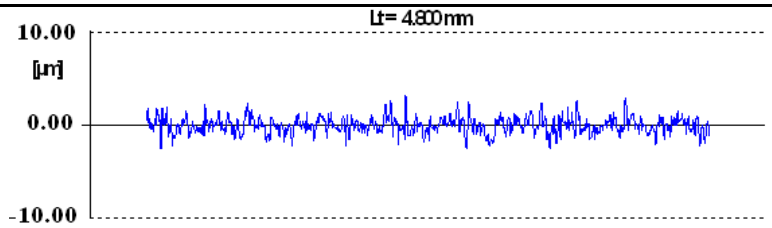
5	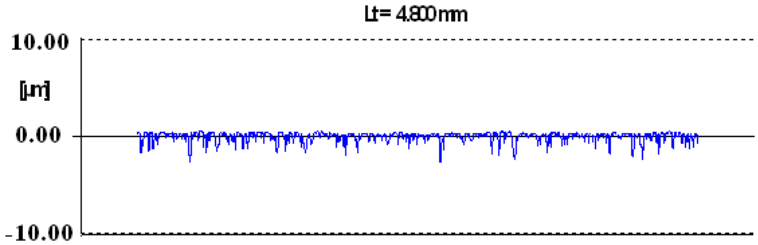
10	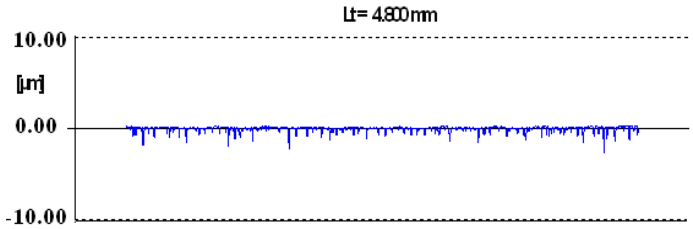
20	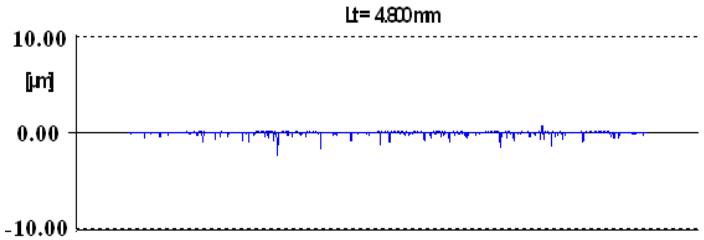
30	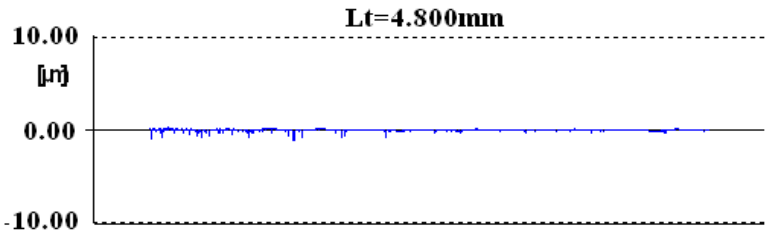
40	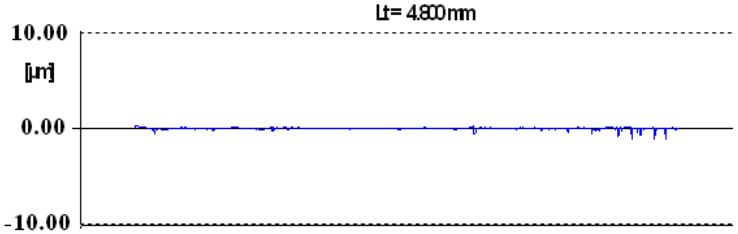

5.5.2 Relationship between surface roughness and friction

Firstly, during compression, when reduction is less than 5 %, the surface roughness of sample decreased greatly from 0.7 μm to 0.4 μm (Figure 5.24). In this stage the rough asperity does not make complete contact with the compression tool, which means that at this stage, lubrication has no obvious influence on the surface asperity flattening. Secondly, if reduction is between 5-30 %, the surface roughness of the sample will continue to decrease, but the decreasing rate of surface roughness is much lower than that in the first stage. In this stage, a stable layer of lubrication formed will limit the surface asperity flattening process. Therefore, the surface roughness of the sample will decrease slowly. In this stage, the lubrication layer plays an important role on surface asperity flattening. Thirdly, if the reduction exceeds 30 %, the surface roughness of the sample decreases quickly (from about 0.3 to 0.15 μm), and in this stage, with an increase in reduction, the layer of lubrication is destroyed by the large compression, but it will not affect the compression of the rough surface. Surface asperity flattening will thus quickly proceed again. Finally, if reduction exceeds 40 %, the two samples will keep a certain surface roughness, although the sample with lubrication has a much rougher surface than the sample without lubrication. The reason is that with lubrication, a layer of lubricant will be formed between the tool and the sample so the sample will receive less constraint from the tool, and therefore can be deformed easily. Furthermore, the slip system in the sample can also be easily activated. When reduction exceeds a certain value (about 40 %), the layer of lubrication will be destroyed, and the compression tool will make contact with the sample directly. However, because of the layer of lubrication, the sample with lubrication has a rougher surface than the one without lubrication.

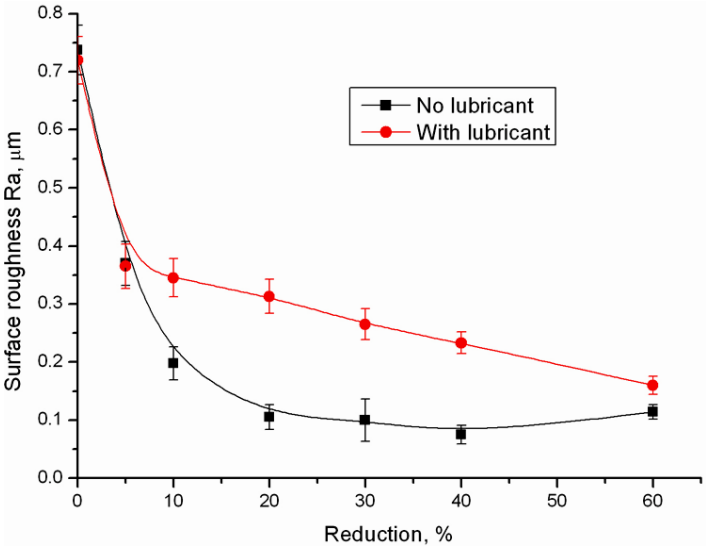

(a)

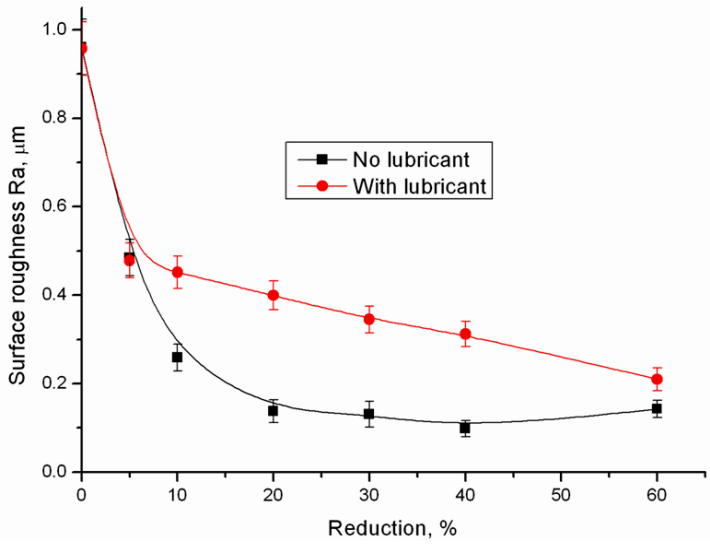

(b)

Figure 5.24 Relationship between the surface roughness and friction: (a) R_a, (b) R_q

On the other hand, an abnormal phenomenon has been observed from the experimental results. When reduction exceeded 60 % in the sample without lubrication, there was a slight increase in surface roughness (about 0.03 μm). There are three factors which may cause this phenomenon: firstly, a measuring error, second, friction and the surface of the tool, and third when reduction reaches 60 %, the aluminium sample cannot easily be deformed any more.

5.5.3 Crystal plasticity model

The relationship between a single crystal and polycrystal is too complicated to be expressed directly, although there are some assumptions given to simplify this relationship. The most widely used approach to obtain the response of a polycrystal from the response of individual crystals is to use the extended Taylor's assumption of iso-deformation gradient in all the crystals composing the polycrystal. Furthermore, if all the grains are assumed to be of the same size, the Cauchy stress in the polycrystal can be taken as a simple number average of Cauchy stresses in the various crystals [128].

On the basis of finite element theory, the averaging procedure has used the micro-macro link of the Taylor model to acquire the polycrystal plasticity response [186]. In these calculations of finite element averaging procedures, each grain is modelled by one or more finite elements to allow for no-uniform deformation between the grains and within the grains, and both equilibrium and compatibility are satisfied in the weak finite element sense. Following previous research, Kalidindi developed an implicit time-integration procedure [160, 117]. In this study, Kalidindi's implicit time-integration procedure [117] is used in the finite element calculation to make a transition from the response of a single crystal (or a region within a grain) to the response of a polycrystalline aggregate. Simultaneously, a group of relevant experiments has been carried out to test the simulation results.

5.5.4 Modelling

This study aimed to analyse the relationship between reduction, friction, and surface roughness during uniaxial plane strain compression. The model geometry is two dimensional. Although a 2D finite element analysis has the advantage of less computational time, the main reason for not using a 3D finite element analysis in this study is that during the compression test, the transverse direction is constrained by the mould (Figure 5.23), therefore, there is almost no deformation of the sample in this direction. On the other hand, the available generalised plane strain elements in ABAQUS make it possible to impose a uniform strain on the body in an out-of-plane

direction. Furthermore, as mentioned by Becker [8] and Wu [187], the 2D FE model still allows us to simulate both uniaxial and biaxial deformation.

For all the simulations, the 1-direction (Figure 5.25) corresponds to the previous rolling direction, the 2-direction to the normal sample, and the 3-direction to the transverse direction of the samples. The sample material is 6061T5 aluminium alloy. The two-dimensional model is 500×500 μm^2 in size. The initial length is denoted by L_0 and the initial height by H_0. Original roughness parameters of the samples are R_a 0.72 μm and R_q 0.98 μm. Longer and shorter wavelengths have been used to form the surface roughness. A longer wavelength (R_q 1.06 μm, R_a 0.79 μm) contributes about 60 % to the initial surface roughness, and a shorter wavelength (R_q 0.82 μm, R_a 0.61 μm) only accounts for about 40 % of the initial surface roughness. Becker's method [8] is used to calculate the average roughness obtained from the finite element results and the experimental ones. Surface roughness of the model is determined by the experimental results. A line is drawn through the surface nodal coordinate data, therefore, the distance from this line to the surface nodes is δ [8] and

$$\int_0^L \delta dx = 0 \tag{5.18}$$

Although there are not many differences between the surface profiles of the 2D model and the sample, they all have the same initial roughness R_a. The surface roughness of the model is determined by the surface roughness of the sample. The average roughness R_a is determined from

$$R_a = \frac{1}{L}\int_0^l |\delta| dx \tag{5.19}$$

Reduction of the sample ranges from 5 to 40 %. The contact coefficient of friction between the sample and the rigid compression tool and mould ranges from 0.001 to 0.35. Reduction was applied onto the top of the sample by the rigid compression tool. Due to symmetry, all the nodes on the edge ab (Figure 5.25) have no displacements in direction 1. In order to understand the relationship between surface roughness, friction, and reduction, by the crystal plasticity theory, a finite element polycrystal model has been used in this study. The two dimensional model has 902 CPE4R

reduced integration elements, and one grain set with one element. The rigid tool and mould both have 20 discrete rigid elements. Kalidindi's method [188] has been employed to incorporate crystal plasticity into FEM. The constitutive model and time-integration procedures are implemented into the implicit finite element code ABAQUS by applying the user material subroutine UMAT. The combinations of slip systems are taken into account during modelling, including 12 {110}<111>. It is assumed that the shearing rate is equal on each slip system. 902 random Euler angle triplets are input into ABAQUS as the initial crystallographic condition of the model. All the taken parameters are listed in Table 5.1. The components of the elasticity tensor are taken as C_{11}=106750 MPa, C_{12}=60410 MPa, C_{44}=28340 MPa [184]. As hardening matrix parameters, $q_{\alpha\beta}$=1.0 for co-planar systems and $q_{\alpha\beta}$=1.4 for non co-planar slip systems were used [99]. The other material parameters are according to reference [133].

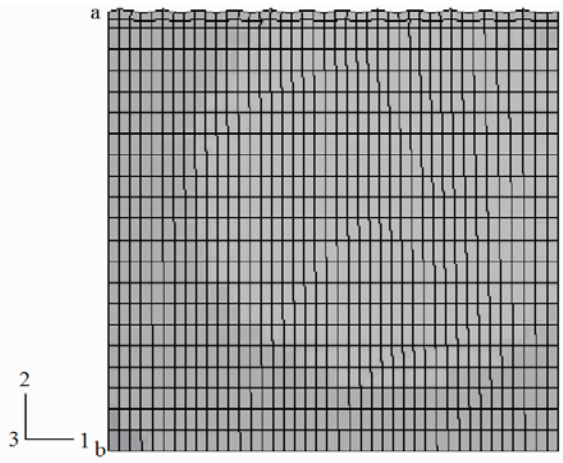

Figure 5.25 Two dimensional model and mesh

5.5.5 Relationship between surface roughness, friction, and reduction

It is shown in the modelling results, with an increase in reduction the surface roughness of the sample decreases quickly (Figure 5.26). In other words, surface asperity flattening takes place quickly, and compression with lubrication has an obvious difference from that without lubrication. With an increase in the coefficient of friction, the rate of surface asperity flattening of sample increases significantly.

Under the condition of increased friction, the sample will obtain a lower surface roughness due to compression. The reason for this phenomenon is that the friction between the sample and the compression tool is expressed by the penalty function as a constraint to the sample. Therefore, during compression the friction will prevent the sample from being deformed and restrain the slip system from activation and action. On the other hand, the practical layer of lubricant that lies between the sample and the tool acts as a transfer layer to block the surface asperity flattening process. It can obviously reduce the surface asperity flattening process. Here in this simulation, friction is only set as a coefficient but the sample will definitely come into direct contact with the tool. Therefore, it is also directly affected by the tool. Because the compression tool in this study is smooth, the surface of the sample will be flattened quickly. With an increase in the coefficient of friction, the influence of the tool on the sample accelerates the surface asperity flattening process.

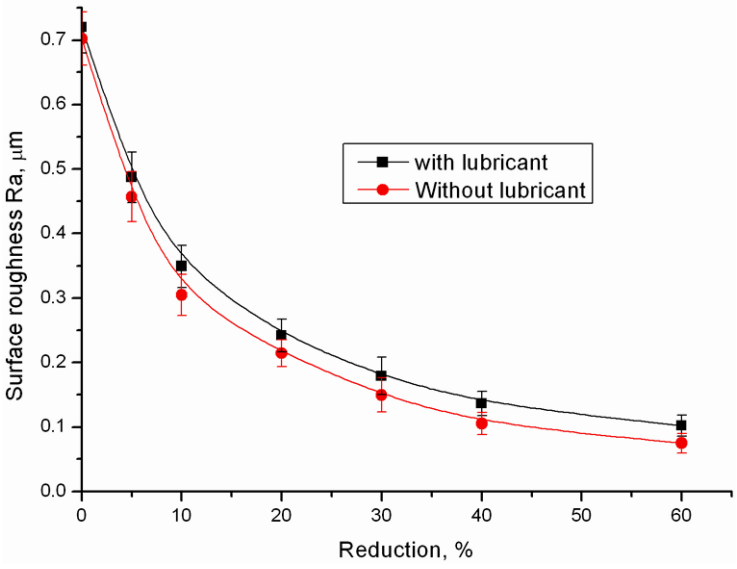

(a)

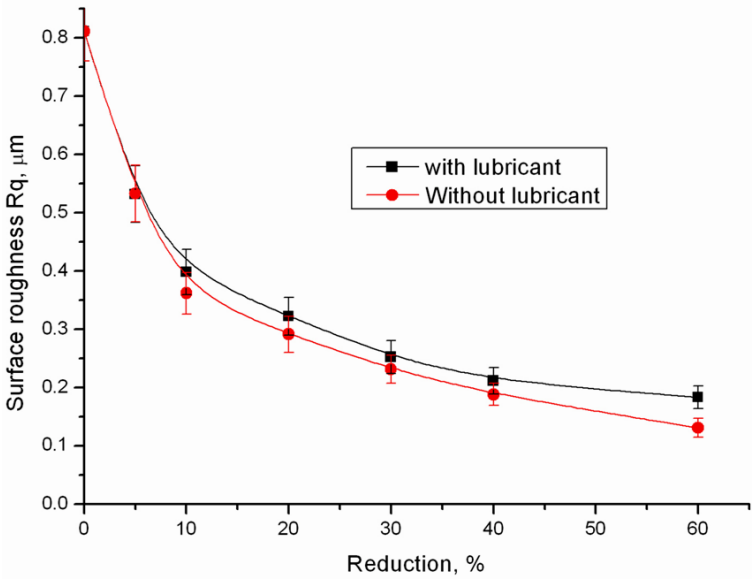

(b)

Figure 5.26 Relationship between surface roughness, friction, and reduction: (a) R_a, (b) R_q

After compression, an area of localised strain appears on the surface of the sample, which will also result in a transfer layer on this surface. This transfer layer will play a direct role in changing the surface roughness. Other neighbouring layers will affect the surface roughness by this transfer layer. From the simulation, we observed the obvious change of crystals' orientations in this layer. This will be further focused on in this study.

5.5.6 Comparison of experimental and modelling results

It is shown from Figure 5.27 that the experimental results are close to the simulated results. Both results reveal that with an increase in reduction, the surface roughness of the sample decreases quickly, and lubrication can delay the process of surface asperity flattening. On the other hand, there is a difference between the experimental and simulated results. The developing tendency of surface roughness in the two results is different: the simulated result has a higher decreasing rate of surface roughness than the experimental results. In Figure 5.27(a), when reduction is less than 10 %, the two results maintain the same tendency of surface asperity flattening.

On the other hand, when reduction exceeds 10 %, the decreasing rate of surface roughness from simulation is a slightly more than that from the experiment. In the experiment, when reduction exceeds 10 %, the layer of lubrication can play a remarkable role in delaying surface asperity flattening.

However, in the simulation, the penalty coefficient of friction is used to replace the layer of lubrication. There is an obvious difference between the simulation results and experimental ones. This error may result from a computational error and a frictional model error. From the calculation, the maximum error between the experimental and simulation results is about 0.08 μm. When the maximum error appears, the sample roughness is more than 0.25 μm (Figure 5.27(a) and (b)). This error is about 25 % of sample roughness. In the finite element simulation this error may be acceptable. When reduction is between 10 and 40 %, the lubrication can perform properly. The difference between the simulated and experimental results is obvious. When reduction exceeds 40 %, the layer of lubrication is damaged and cannot continue to constrain the surface asperity flattening. In Figure 5.27(b), if reduction exceeds 60 %, the roughness of experimental results increases by about 0.03 μm. The reasons for this phenomenon are the same as those in Figure 5.24.

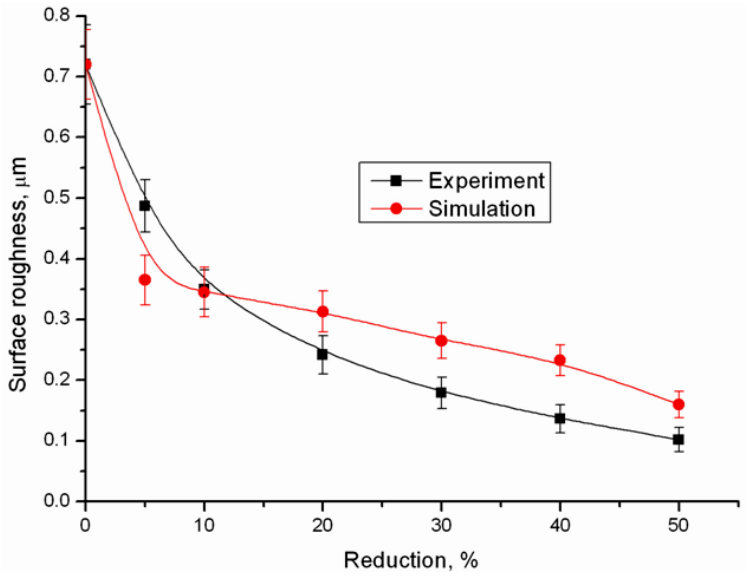

(a)

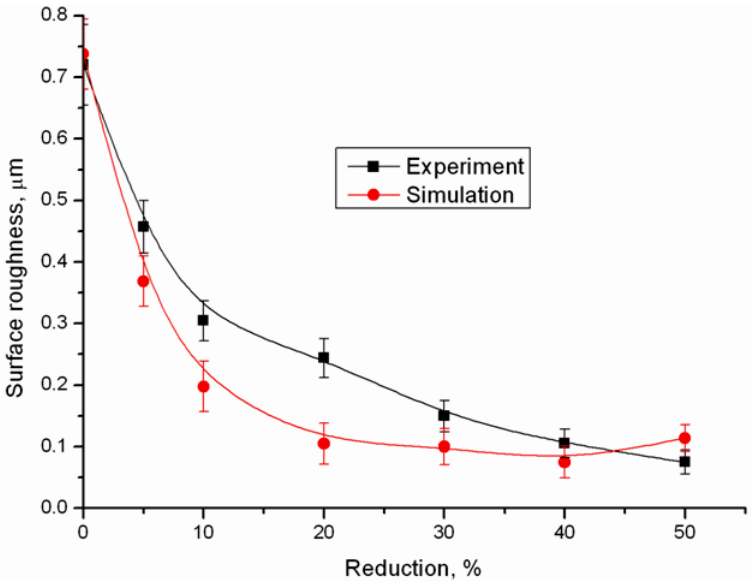

(b)

Figure 5.27 Relationship between surface roughness, friction, and reduction: (a) with lubrication, (b) without lubrication

5.5.7 Influence of longer wavelength and shorter wavelength on surface roughness

Figure 5.28 shows with an increase in reduction, the influence of the shorter wavelength on sample roughness (R_a, R_q) increases during compression, and the influence of the longer wavelength on sample roughness (R_a, R_q) decreases. In this model the longer wavelength has a larger initial roughness (R_a, R_q), and the shorter wavelength has a smaller initial roughness (R_a, R_q). During compression, the compression tool will contact the longer wavelength first, and the roughness of the longer wavelength will decrease quickly. Furthermore, at the beginning, under very small reduction (less than 5 %), the longer wavelength is the main factor which affects the sample roughness while the shorter wavelength has no obvious influence on sample roughness. With an increase in reduction, the compression tool will contact with the shorter wavelength subsequently. The shorter wavelength will thus play a primary role on sample roughness while the influence of the longer wavelength on the sample can be omitted.

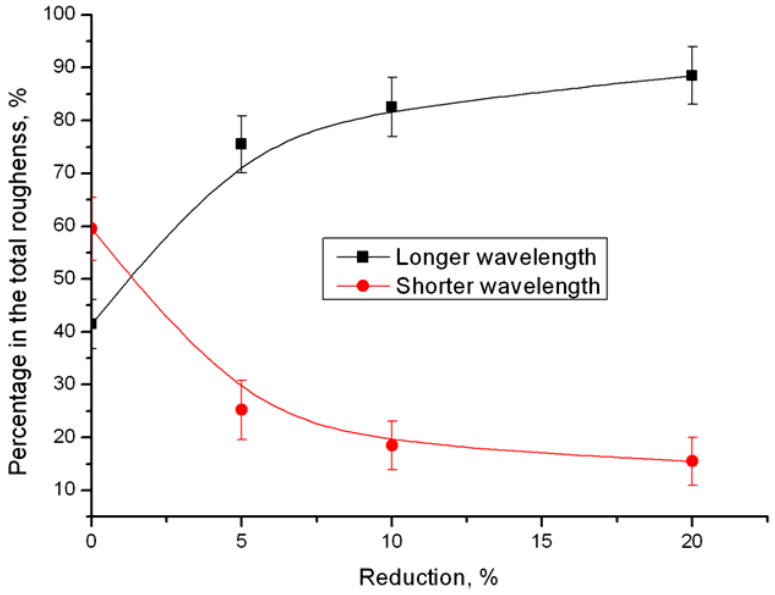

Figure 5.28 Influence of longer wavelength and shorter wavelength on sample roughness

5.5.8 Texture development

If the coefficient of friction is low (0.001), the development of texture has a certain relationship with reduction. At first, when reduction is low (less than 5 %), there is no obvious tendency in the pole figure. At this stage the majority of elements occur elastic deformation, and the energy resulting from plastic deformation cannot support many slip systems to slip. So only few slip systems will be activated and grain rotation and stretch are not significant. When reduction exceeds a certain value (10 %), an obvious tendency appears in the pole figure. All the grains tend to rotate along a certain direction and axis. At this stage, with an increase of elements in plastic deformation, the elements in elastic deformation decreases quickly. The energy of cold deformation will activate many slip systems. So many grains will rotate and stretch along the “soft orientations” (<110> slip directions and {111} slip plane). Furthermore, with an increase in reduction, the cubic texture becomes more and more obvious.

Reduction (%)	With lubrication {100}	With lubrication {101}	With lubrication {111}	Without lubrication {100}	Without lubrication {101}	Without lubrication {111}
0	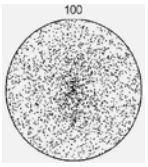	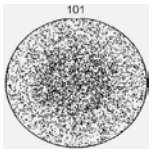	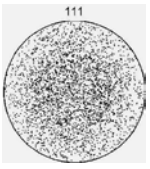	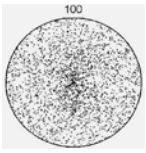	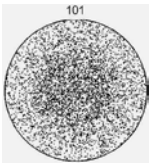	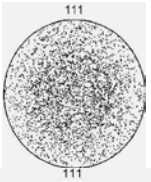
5	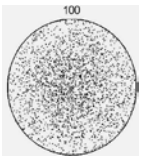	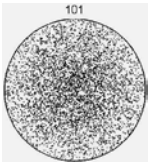	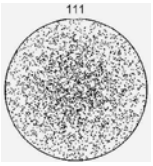	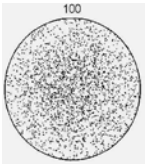	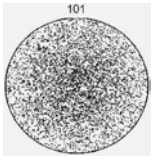	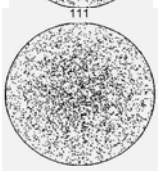
10	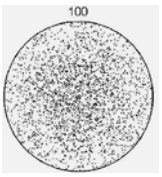	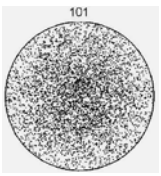	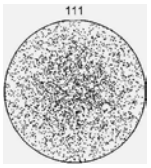	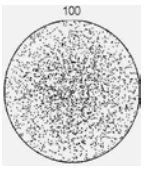	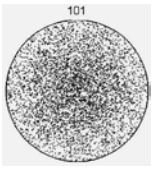	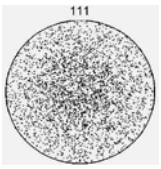
20	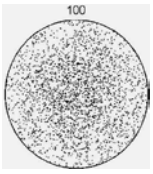	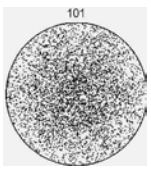	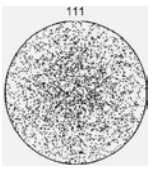	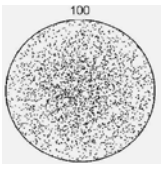	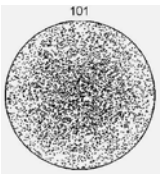	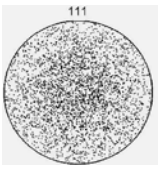
30	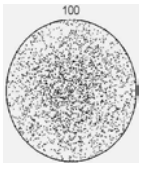	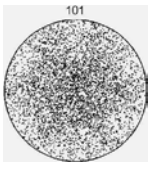	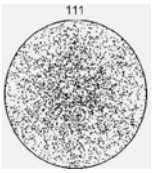	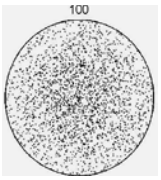	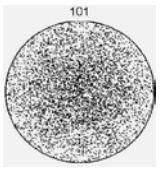	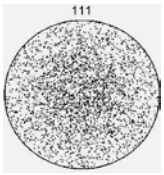
40	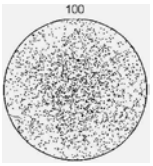	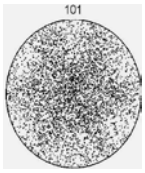	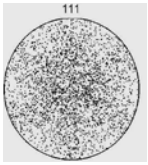	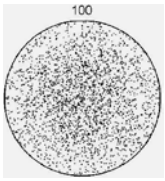	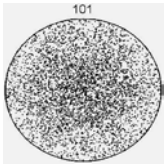	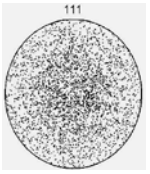
50	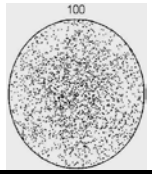	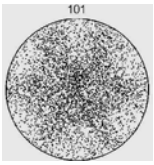	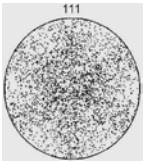	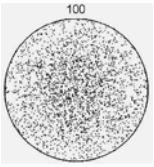	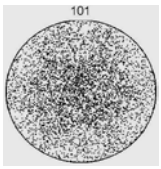	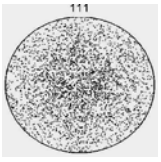

Figure 5.29 Development of texture in uniaxial planar compression

In Figure 5.29, when reduction is 40 % the texture is very obvious and stronger. In the deformed sample a stabilised cubic texture will be formed. The sample will obtain a new balance of grain distribution and arrangement. On the other hand, with

an increase in reduction, there is no obvious tendency in the hard orientations (Pole figure {100}, etc.). However, when the coefficient of friction is large (0.35), there is no obvious cubic texture formed. Therefore, friction between the sample and the tool has a significant influence on the development of cubic texture. It can hinder the form of cubic texture. In the process of grain slip and deformation, the contact friction sometimes becomes a barrier to restrain the activation of the <110> {111} slip systems. So with an increase in reduction, the shear stress of some slip systems cannot reach the saturated stress of the slip system. Furthermore, the slip system cannot meet the energy requirement for activating the slip systems. Therefore, the cubic texture in the sample without lubrication is not stronger and sharper than the one with lubrication.

5.5.9 Conclusions

(1) In uniaxial planar compression, the evolution of surface asperity has three obvious stages: when reduction is less than a certain value, the surface roughness decreases greatly with a decrease in reduction (reduction less than 10 %). Elastic deformation plays an important role in the evolution of surface asperity. When reduction exceeds 10 % the decreasing rate of surface roughness is less than that in the first stage. The influence of plastic deformation on the surface asperity evolution increases while the influence of elastic deformation decreases significantly. When reduction is greater than 40 % the surface asperity changes slowly. Plastic deformation is the main deformation in this stage, and a certain texture will also be formed.

(2) The influence of lubrication on the evolution of surface asperity is also very complicated. Within a certain reduction range (in this case between 10 and 40 %), lubrication can significantly limit surface asperity flattening, but if reduction is less than 10 %, lubrication has no obvious influence on the surface roughness of the sample. When reduction exceeds 40 %, the layer of lubrication will be damaged during uniaxial planar compression.

(3) Both the experimental and simulation results show the same tendency: with an increase in reduction, the surface roughness of the sample decreases greatly and the lubrication can constrain the surface asperity flattening process.

(4) In the simulation, with an increase in reduction, the influence of a longer wavelength on the sample roughness decreases quickly, while the effect of the shorter wavelength of surface asperity on sample roughness increases significantly.

5.6 New findings

Through the analysis of simulation and experiments, surface roughness in uniaxial planar compression was investigated and the following new results were obtained:

(1) In uniaxial planar compression, the rough surface of the sample tends to be flattened as reduction increases, and the evolution of surface asperity has three obvious stages.

(2) Lubrication can constrain the surface asperity flattening process. However, relationship between the lubrication (friction) and surface roughness is very complicated. Within a certain range of reduction, lubrication can significantly limit surface asperity flattening. However, when reduction exceeds 40 %, the layer of lubrication will be damaged during uniaxial planar compression.

(3) With an increase in reduction, the certain texture tends to be stronger and obvious. All the grains of the sample slip along the certain slip directions and slip planes (<110> slip directions and {111} slip planes). Finally, the cubic texture is formed and the sample obtains a new balance with a stabilised microstructure. Friction can also constrain the forming of cubic texture.

(4) Compared to the tensile test, the relationship between surface roughness and strain in uniaxial planar compression is different and more complicated than the tensile test. In a tensile test the variation of surface roughness R_a is

proportional to the applied strain. But in a uniaxial planar compression test, the relationship between the surface roughness and strain is non-linear.

(5) Grain size and grain orientation both have a significant influence on the surface asperity flattening. Under the same reduction an increasing grain size can constrain surface asperity flattening, and the relationship between surface roughness and grain orientation is also non-linear.

(6) Different wavelength components can also affect the surface roughness. With an increase in reduction, the influence of longer wavelengths on surface roughness of the sample decreases quickly, but the surface roughness increases significantly with a shorter wavelength.

CHAPTER 6

CRYSTAL PLASTICITY FINITE ELEMENT MODELLING OF 3D SURFACE ASPERITY FLATTENING IN UNIAXIAL PLANAR COMPRESSION

In this chapter two case studies are introduced. Firstly, 3D surface asperity flattening in uniaxial planar compression has been investigated by crystal plasticity finite element method (CPFEM), and then the influence of the strain rate on 3D surface asperity flattening in uniaxial planar compression is discussed.

6.1 3D surface asperity flattening in uniaxial planar compression

6.1.1 Introduction

Surface quality is always a key issue in manufacturing industries. As an important parameter, the surface roughness of cold metal manufactured products is an interesting topic in the metal forming process. There are many factors related to variations in surface roughness such as the original surface roughness, grain size, crystal structure and orientation, texture distribution, loading path, stress-strain state (deformation mode) and tool surface, etc [2]. During plastic deformation, unconstrained metal surfaces tend to become rough. Osakada and Oyane [5] found that surface roughening increases with strain and it is greater in coarser grain materials or metals with a small number of slip systems. Therefore, CPH (close packed hexagonal) metals roughen most, FCC (face centred cubic) material less, and

BCC (body centred cubic) materials the least. Tokizawa and Yosikawa [6] further discussed the influence of two material phases on the roughening process. Chen et al. [7] found that grain rotation is the most important factor. Becker [8] established a model to address the influence of inhomogeneities in deformation by suggesting that unconstrained deformation at the surface causes grain displacement in a direction normal to the surface, and thereby increases the overall surface area. Stoudt and Ricker [56] carried out a tensile experiment with AA5052 alloy. They demonstrated that the roughening rate ($dR_a/d\varepsilon_{pl}$) is dependent on the grain size, and pointed out that the surface roughening of a polycrystalline material is a highly complex process related to multiple deformation mechanisms.

On the other hand, most metal forming are strain constraint processes such as rolling and compression. A surface asperity flattening process exists when the tool contacts the workpiece. Wilson et al. [11, 69] have investigated the effect of bulk plasticity on asperity flattening when the lay of the roughness is parallel to the direction of bulk straining (longitudinal roughness). They found that the rate of asperity flattening with bulk straining was related to the spacing and pressure of asperities. Makinouchi et al. [12] used elastic-plastic finite element solutions for the case of transverse roughness. Wilson and Sheu [69] also found out that a large increase in the contact area, with bulk strain and a reduction in the load, are needed for bulk yielding. Sutcliffe [13] tested and developed Wilson and Sheu's theories and pointed out that the high pressure between contacting asperities and the deformation body of bulk material affects the asperity deformation. Dieter [14] found that the inhomogeneous deformation mechanisms that generate surface roughening also initiate localised strains which induce necking, tearing, or wrinkling in the component during the forming process. Wilson [15] also points out that inhomogeneous deformation can accelerate die wear by increasing the friction and abrasion between the metal sheet and the die. Groche [16, 17] analysed the surface evolution caused by contact loading in a 2D-plane strain finite element (FEA) model and established a correlation between the surface topology, grain size, and surface evolution.

However, there are few studies on the interaction between surface asperity flattening, and texture and reduction by crystal plasticity theory. In previous work we analysed

the relationship between surface asperity flattening, friction [189] and grain size [190] by establishing a 2D crystal plasticity finite element model. In order to work out the relationship between the surface asperity flattening, reduction, and grain orientation of the sample, a 3D surface roughness model has been established to analyse the development of surface roughness and grain orientation by using the crystal plasticity finite element method. Compared to the 2D surface roughness model, the 3D model is able to show the development of surface asperity and texture in the third dimension. Because its ductility is highly multiaxial, a thin sheet of 6061 aluminium alloy has been selected as the experimental material in this study. The simulation results show a good agreement with the measured parameters. The development of surface asperity shows a certain dependence on the gauged reduction. Certain crystallographic orientation ([111]) of near surface grains also plays a significant role in the development of surface roughness.

6.1.2 Material and experimental procedure

The material is Al 6061alloy. All the samples were annealed before compression by being heated to 450 °C for 2 hours in a furnace and then allowed to cool in the furnace. The samples were manufactured by an automatic grinding/polishing machine (with ridge and valley) so that after grinding the surface roughness was approximately 0.70 μm (R_a). 2D and 3D profile meters were used to measure the surface roughness. The measured area is marked to ensure it can be tracked after compression. Any errors in surface roughness between the samples are less than 0.05 μm. When compression takes place, the sample is constrained in the transverse direction to ensure the surface roughness develops along the rolling direction. The compression equipment comprises a compression mould and tool. To help handle the samples, the compression mould also includes two separate parts which are assembled by a screw. The samples are approximately 10 mm×10 mm×6 mm, as shown in Figure 6.1c. The compression test was carried out by INSTRON 8033 Material Testing Machine. The compressing equipment is shown in Figure 6.1. The contact surface of the compression tool has been polished to a surface roughness of approximately 10-20 nm. The parameters are shown in Table 6.1.

The strain rate is 0.001 s^{-1}, but controlling the strain rate on the MTS is difficult so a displacement rate is used instead [189]. The relationship between the strain rate and displacement rate can be obtained by Equation (5.17) of Section 5.5.1.

Table 6.1 Compression schedule

Sample	Height (mm)	Reduction (%)	Strain rate (s^{-1})	Displacement rate (mm/min)	Displacement (mm)	Height after deformation (mm)
1	6.3	10	0.001	-0.359	0.63	5.67
2	6.3	20	0.001	-0.339	1.26	5.04
3	6.3	40	0.001	-0.296	2.52	3.78
4	6.3	60	0.001	-0.248	3.78	2.52

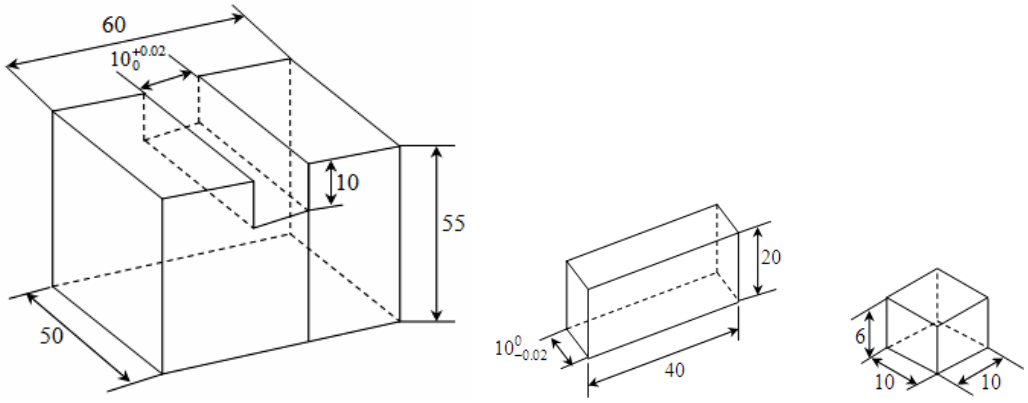

(a) (b) (c)

Figure 6.1 Compressing equipment and sample: (a) compression mold, (b) compression tool, and (c) sample. Unit: mm

The microstructure and grain orientation were examined by JOEL 7100F FEG SEM (Field Emission Gun Scanning Electron Microscope). The scanning area on the sample is at the centre of the TD (Transverse Direction) plane of the sample. The microstructures of the annealed sample are shown in Figure 6.2. The hardness is measured by an M-400-H1 Hardness Testing Machine. In the hardness test, hardness in the ridges and valleys were measured. The valley and ridge were identified by the sequence of focus in the experiment. First focus area is the ridge and the following area is the valley.

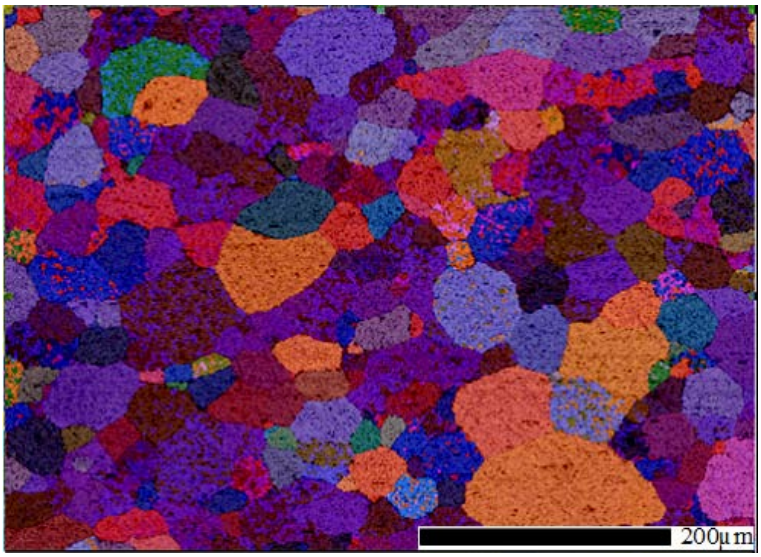

Figure 6.2 Microstructure before compression (450 °C, 2 h)

6.1.3 Crystal plasticity finite element model

The relationship between a single crystal and polycrystal is too complicated to be directly expressed so some assumptions have been given to simplify the relationship between the single crystal and polycrystal. The most widely used approach to obtain the response of a polycrystal aggregate from that of an individual crystal (or a region within a grain) is to use the extended Taylor's assumption of iso-deformation gradient in all of the crystals composing the polycrystal. Furthermore, if all grains are assumed to be the same size, the Cauchy stress in the polycrystal can be taken as a simple average number of the Cauchy stresses in the various crystals [99, 190].

In order to understand the relationship between the surface roughness, reduction and grain orientation (texture), a 3D crystal plasticity finite element polycrystal model has been developed. The 3D model has 840 C3D8R reduced integration elements. Some elements on the top surface are small. So to keep the weight function of orientation in the modelling, every four neighbouring elements at the top surface have one orientation. There are 280 elements in total, with 70 Euler angle triplets. The other 560 elements follow the rule of fully finite element model: one element with one orientation. A spatial distribution of orientations has been assigned on a

basis of the EBSD experimental results. The rigid tool and mould both have 460 discrete rigid elements. The same method shown in Section 5.5.3 is used in this study: Kalidindi's method [188] is used to incorporate crystal plasticity into FEM. The constitutive model and time integration procedures were implemented into the implicit finite element code ABAQUS by using the user material subroutine UMAT. The combination of slip systems were taken into account during modelling, including 12 {110}<111>. It is assumed that the shearing rate is equal on each slip system [187]. 630 Euler angle triplets from the experimental results are input into ABAQUS as the initial crystallographic condition of the model. All the parameters are taken as in Table 5.1. Elasticity tensors are taken as C_{11}=106750 MPa, C_{22}=60410 MPa, C_{44}=28340 MPa [184]. The $q_{\alpha\beta}$=1.0 for co-planar systems and $q_{\alpha\beta}$=1.4 for non co-planar slip systems [99, 191]. The other material parameters are set according to reference [133, 192].

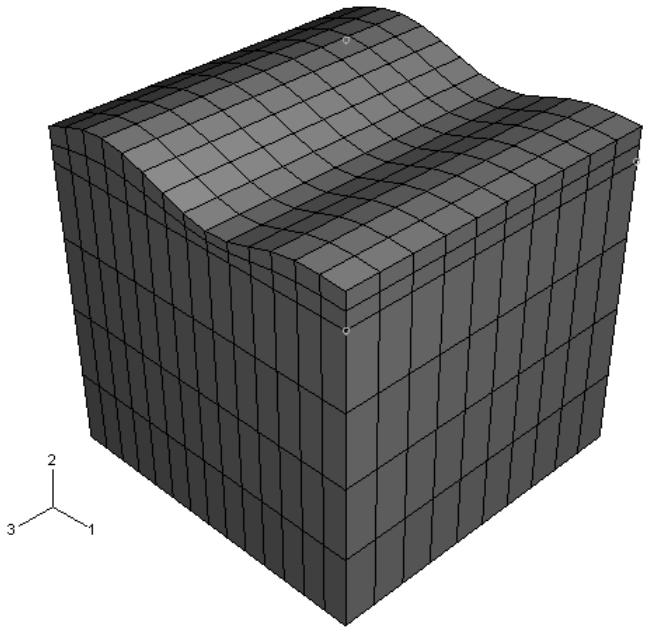

Figure 6.3 3D finite element model and mesh

In the simulation, direction 1 (Figure 6.3) corresponds to the rolling direction, direction 2 to the normal, and direction 3 to the transverse direction. The three dimensional model is 100 μm×100 μm×100 μm in size. The initial length of the surface asperity along the rolling direction is denoted by L_0 and the initial height by H_0. The original average roughness R_a of the samples is 0.72 μm. Becker's method

[8] was used to calculate the average roughness obtained from the simulation and experimental results. The surface roughness of the model is determined by the experimental results, which is the same as Section 5.54. A line is drawn through the surface nodal coordinates. Therefore, the distance from this line to the surface nodes is δ [8], and Equation (5.18) is the requirement for the line. Although a few differences exist between the 3D surface model and the practical sample profiles, they both have the same initial roughness R_a. The average roughness R_a, is calculated by Equation (5.19)

6.1.4 Results and discussion

6.1.4.1 Surface roughness

Due to the consistently contact, it is almost impossible to track the distribution of surface roughness during compressing process. Without any lubrication, the development of surface roughness shows that the surface asperity becomes flattened with an increase in reduction. It can be seen from Figures 6.4 and 6.5 that when reduction is less than 10 %, surface roughness decreases from 0.72 to 0.47 μm. The relationship between the surface roughness and reduction is linear. At the same time the average grain size (in this session, grain size refers to average grain diameter) also decreases from 45.7 to 43.5 μm. In this stage, the compression tool mainly makes contact with the ridges. Owing to the elasticity of the tool and workpiece, elastic deformation of the ridge area contributes significantly to the surface asperity flattening process, while the influence of plastic deformation on surface roughness of the ridge area is not significant. When reduction is 20 % the flattening rate of surface asperity obviously reduces, and the relationship between the surface roughness and reduction is nonlinear. The average diameter of the grain decreases from 43.5 to 37.6 μm, and the influence of plastic deformation on surface asperity flattening increases. However, the surface asperity flattening increases quickly when reduction is greater than 40 %, and some ridges disappear and some valleys become much shallower. The average grain size decreases significantly from 37.6 to 22 μm. Plastic deformation of ridge is the main reason for surface asperity flattening in this stage. Both results show a good agreement with the results from the previous 2D simulation [189, 194].

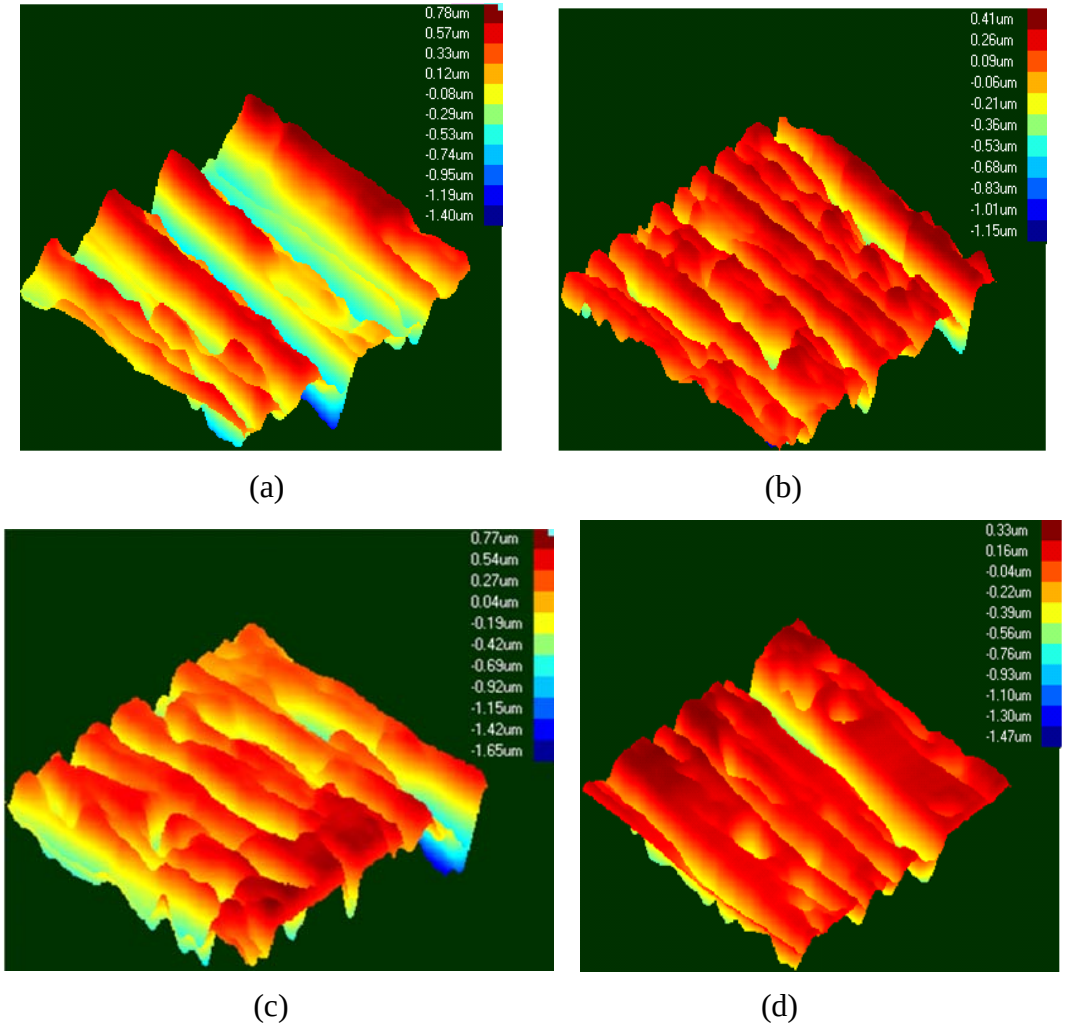

Figure 6.4 Surface asperity development under different reductions: (a) 0 %, (b) 10 %, (c) 20 %, and (d) 40 %

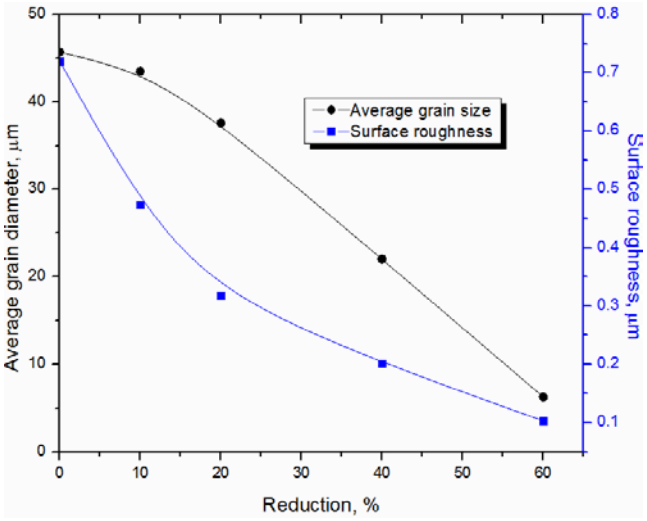

Figure 6.5 Effects of reduction on surface roughness and grain size

The experimental results have also been compared with the simulation results; they have a good agreement, and the surface roughness decreases with an increase in reduction (Figure 6.6). Moreover, when reduction is less than 10 %, the decrease in surface roughness is proportional to the gauged reduction, but when reduction exceeds 10 %, the relationship between the surface roughness and gauged reduction is non-linear. Surface asperity flattening is obviously influenced by the increasing plastic deformation, but when reduction exceeds 40 %, the rate of surface asperity flattening decreases. As mentioned above, plastic deformation is the main source of deformation in the surface area.

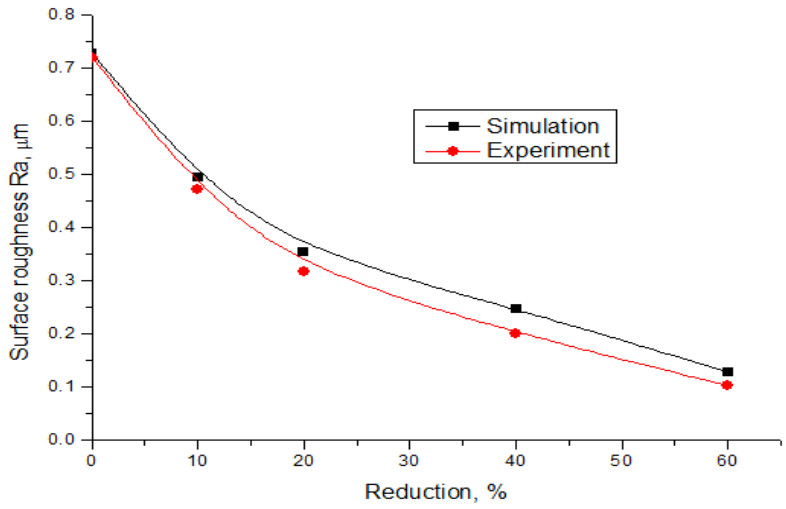

Figure 6.6 Comparison of simulation and experimental results

6.1.4.2 Analysis of grain size (grain diameter)

All the samples were annealed before being compressed, and therefore the grains are equiaxed and the distribution of grain orientation is random. With an increase in reduction the grain diameter tends to decrease, but there are two obvious stages in this deformation (Figure 6.7). When reduction is less than 10 %, the distribution of grain diameter shown in Figure 6.7b is similar to that in Figure 6.7a. In this stage the distribution of grain diameter shows certain randomness from the annealing heat treatment. When reduction exceeds 20 % (Figure 6.7c), plastic deformation has an increasing influence on the microstructure, while the effect of annealing heat treatment on the sample becomes weaker. When reduction exceeds 40 %, the distribution of grain diameter loses its randomness (it obviously has a preferred

orientation). Grain diameter is distributed by a certain rule: majority of grain has a smaller grain diameter. A grain diameter of 3.64 μm has the highest relative frequency of about 60 %, as shown in Figure 6.7d. The average grain diameter decreases significantly from 37.6 to 22 μm. Plastic deformation that resulted from a larger gauged reduction has a significant influence on the distribution of grain diameter. When reduction is over 60 %, the average grain size of the sample is about 6.25 μm. The relative frequency of grain diameter of 3.64 μm increases from 60 to 82 % (Figure 6.7e), and plastic deformation becomes the main source which influences the distribution of grain sizes.

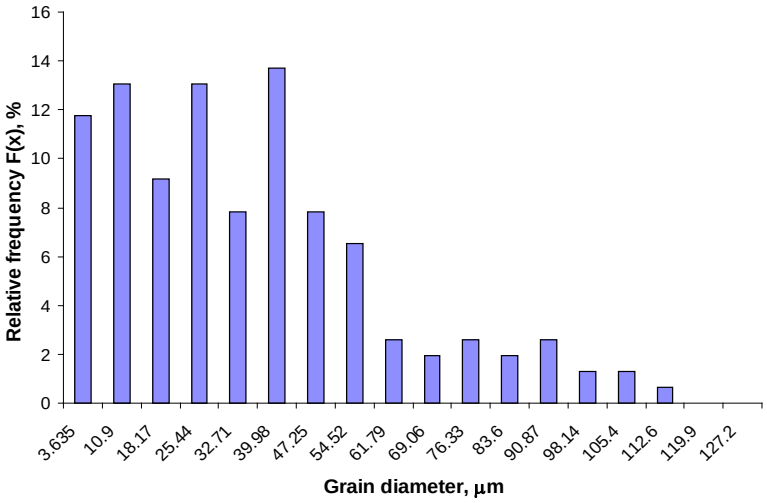

(a)

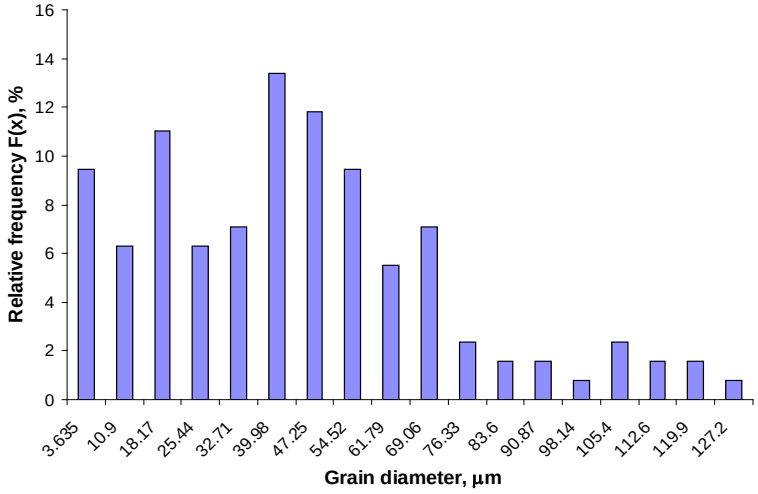

(b)

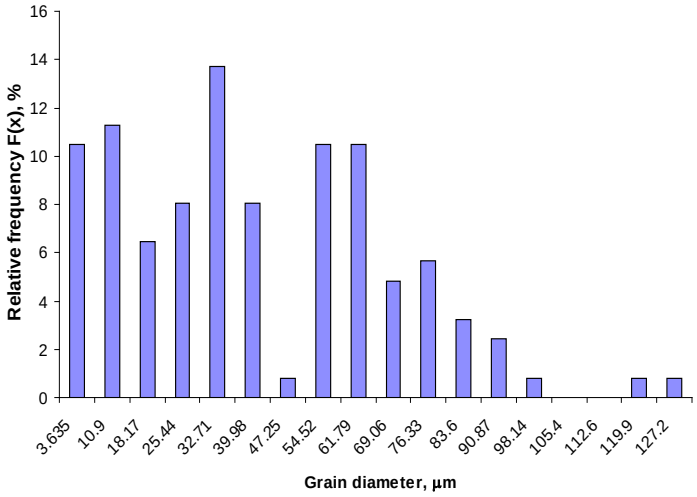

(c)

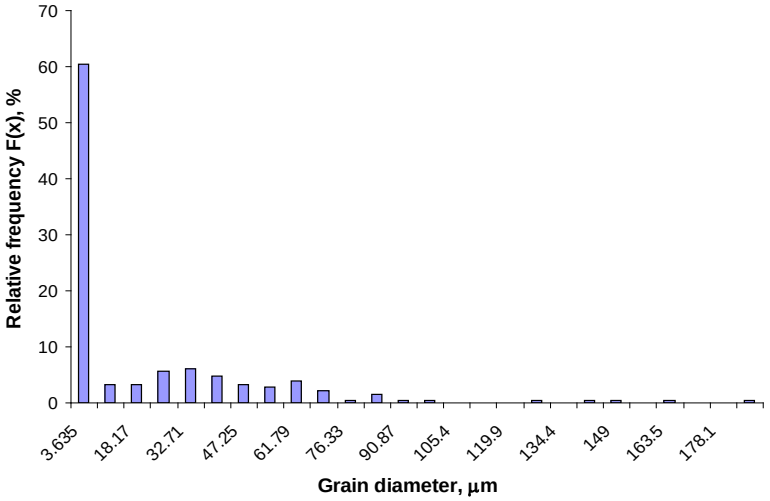

(d)

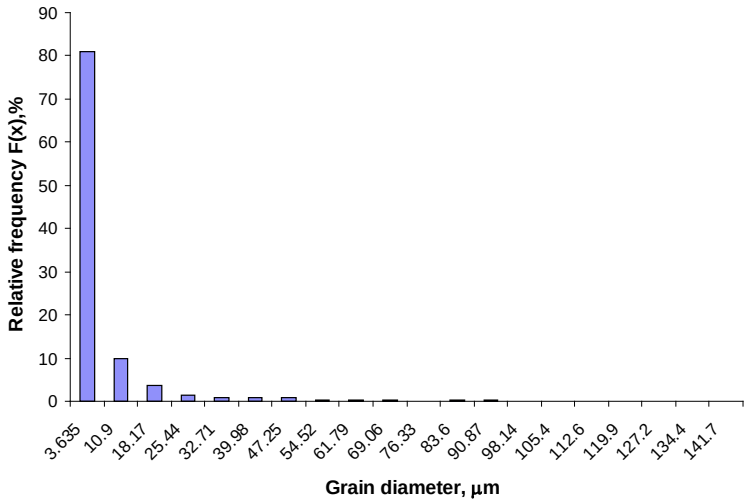

(e)

Figure 6.7 Grain size (diameter) of sample under different reductions: (a) 0 %, (b) 10 %, (c) 20 %, (d) 40 %, and (e) 60 %

6.1.4.3 Analysis of hardness

The hardness of both ridges and valleys increases with reduction (Figure 6.8). When reduction is less than 20 %, the increase in Vickers hardness is not remarkable in both areas of ridges and valleys. This is because at this stage, work hardening occurs but its influence on surface asperity flattening is not very significant. This result is consistent with the distribution of grain sizes and Schmid factor. When reduction is greater than 20 %, the contribution of plastic deformation to surface asperity flattening increases, but when reduction is greater than 40 % the hardness of sample increases significantly, as does the work hardening, although the ridge area is harder than the valley area under all reductions. During compression the ridge makes contact with the tool first, and then the valley. So when the valley area of the workpiece makes contacts with the tool, work hardening has already occurred in the neighbouring area of the ridge, and therefore deformation in the ridge area needs higher stress.

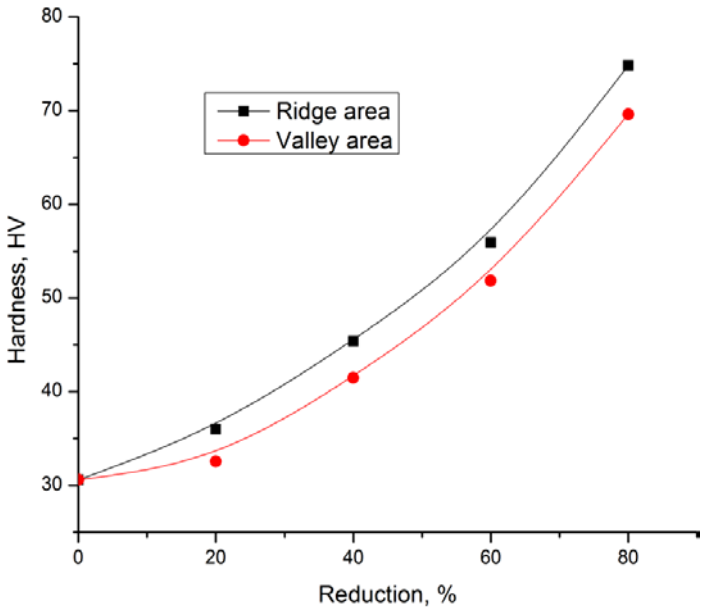

Figure 6.8 Relationship between hardness and reduction (without lubrication)

6.1.4.4 Influence of the Schmid factor

When a load is applied onto the workpiece (Figure 6.9), the shear stress which acts on the slip system along the slip direction can be expressed as [195].

$$\tau_{\mathrm{nd}} = \sigma_y = \frac{\mathrm{P}}{\mathrm{A}} \cos\phi \cos\lambda \tag{6.1}$$

where P is the load, A is the loaded section, ϕ is the angle between the loading axis and normal to slip plane, λ is the angle between the loading axis and slip direction, τ_{nd} is the shear stress of slip system.

$$\tau_{nd} = \tau^{(\alpha)} \tag{6.2}$$

where $\tau^{(\alpha)}$ represents the critical resolved shear stress. The Schmid factor is defined as

$$M = \cos\phi \cos\lambda \tag{6.3}$$

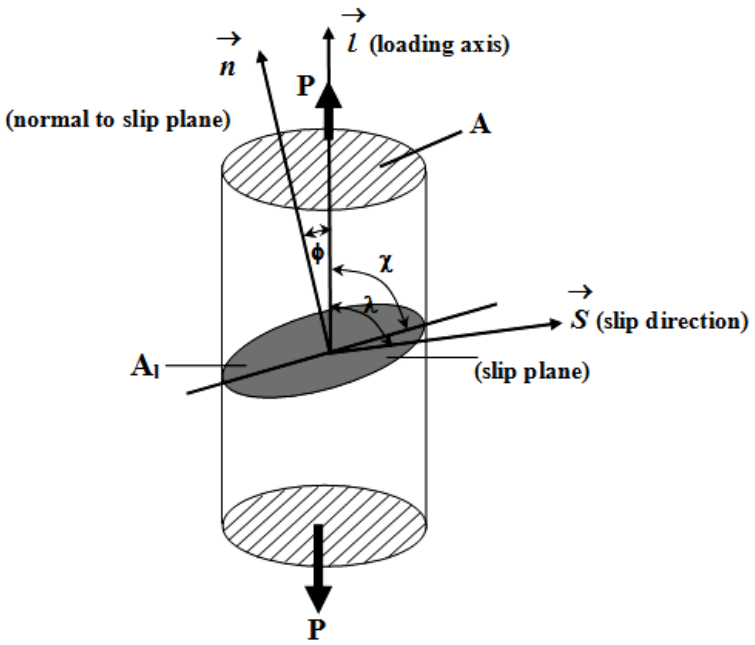

Figure 6.9 Relationship between the stress axis and slip plane and direction [195]

The Schmid factor M is also called the orientation factor or orientation hardness. It gives an indication of how easy a slip occurs for a particular slip system. When the Schmid factor equals 0.5, slip occurs easily. This orientation is called “soft orientation”. If the Schmid factor is 0 the orientation is called “hard orientation”.

It is shown that there is a difference in the distribution of Schmid factor in the edge area with an increase in reduction (Figure 6.10). In Figure 6.10a most Schmid factors of grains range between 0.41 and 0.46, which means that before reduction every orientation of FCC metal in the edge area is in the same conditions (annealed microstructure). With an increase in reduction some grains obtain higher values of Schmid factor, which is close to the "soft orientation area" (The Schmid factor is about 0.5). The reason for this is that the slip pushes some grains rotation from "hard orientation" to "soft orientation", and the slip in some grains does not take place. When reduction reaches 40 %, dislocation accumulates in grains, and owing to this influence, many orientations will shift to "soft orientation" (Figure 6.10d). In some darker areas grains have a higher dislocation density in which in-grain shear bands appear (Figure 6.11a). A shear band appears in the area which is 4-5 grain sizes away from the edge, and strain localisation starts. This result shows a consistency with Becker's results [8]. When reduction is about 60 %, the in-grain shear bands that resulted from the slip of grains are very common in the microstructure (Figure 6.11b), and most grains are obviously deformed. A few transgranular shear bands appear in the area with a high dislocation density but when the transgranular shear band is formed, some new grains will generate from the broken grains. In other words, the slip overcomes the barrier of grain boundary and crosses the grain boundary in this area. Obviously, it is true that the surface asperity and texture will be location dependently, which is going into my future research project.

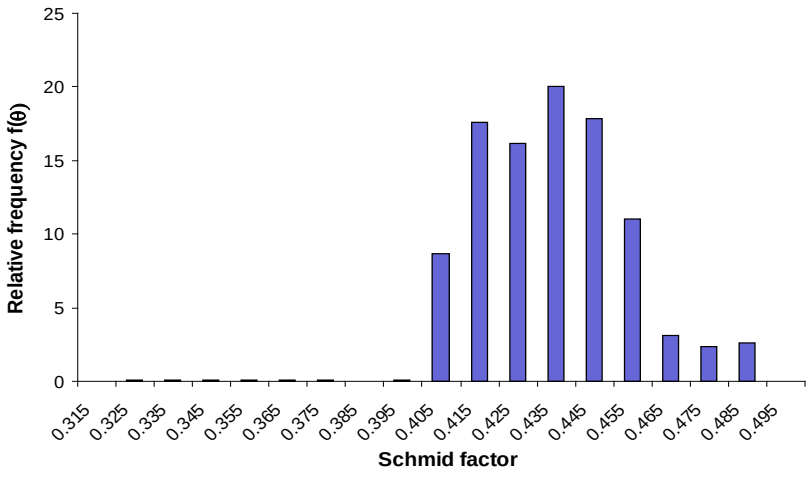

(a)

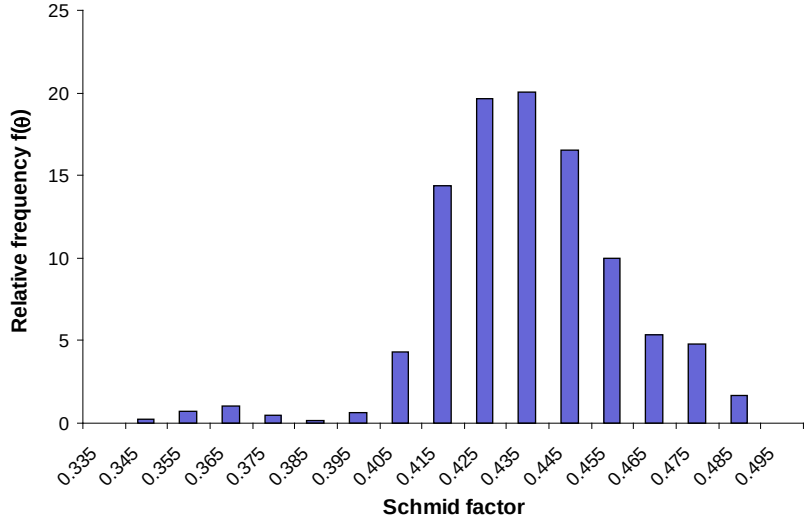
Relative frequency f(θ)
25
20
15
10
5
0
0.335 0.345 0.355 0.365 0.375 0.385 0.395 0.405 0.415 0.425 0.435 0.445 0.455 0.465 0.475 0.485 0.495
Schmid factor

(b)

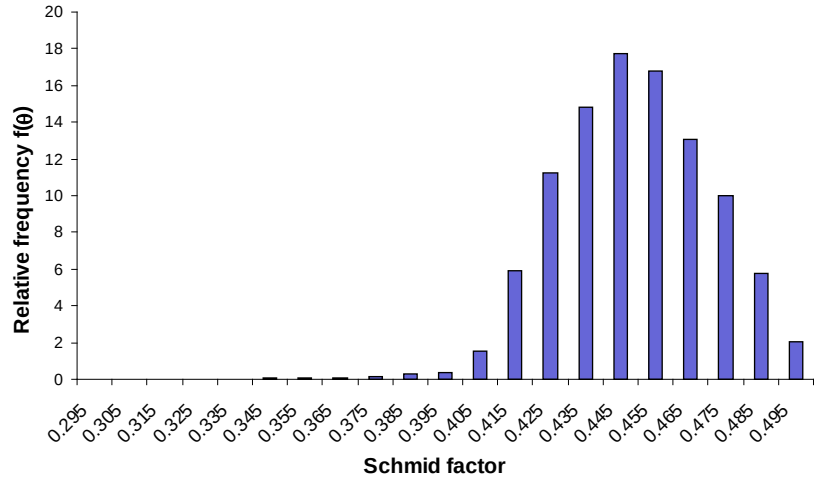
Relative frequency f(θ)
20
18
16
14
12
10
8
6
4
2
0
0.295 0.305 0.315 0.325 0.335 0.345 0.355 0.365 0.375 0.385 0.395 0.405 0.415 0.425 0.435 0.445 0.455 0.465 0.475 0.485 0.495
Schmid factor

(c)

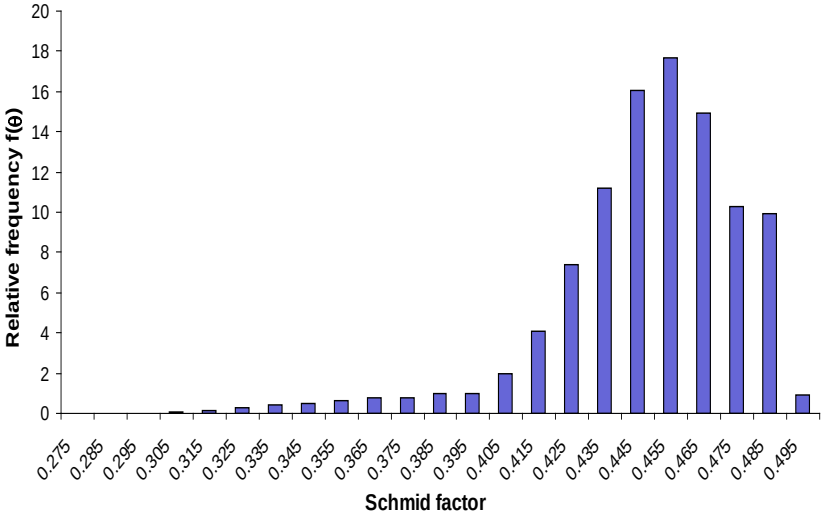
Relative frequency f(θ)
20
18
16
14
12
10
8
6
4
2
0
0.275 0.285 0.295 0.305 0.315 0.325 0.335 0.345 0.355 0.365 0.375 0.385 0.395 0.405 0.415 0.425 0.435 0.445 0.455 0.465 0.475 0.485 0.495
Schmid factor

(d)

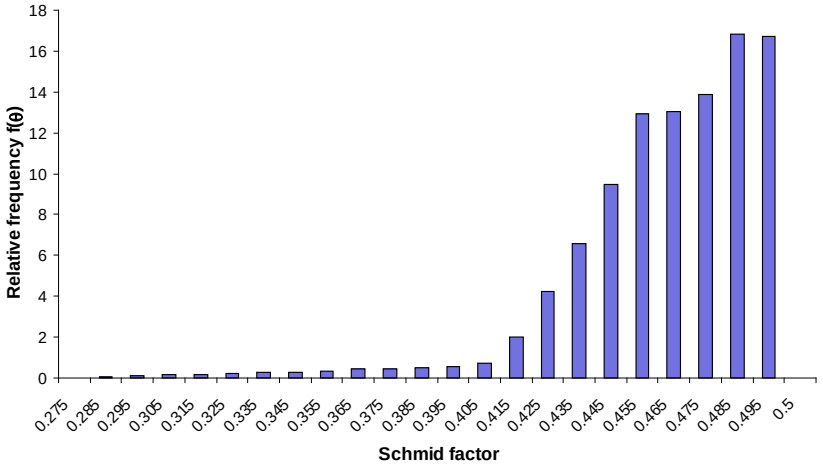

(e)

Figure 6.10 Distribution of Schmid factor under different reductions: (a) 0 %, (b) 10 %, (c) 20 %, (d) 40 %, and (e) 60 %

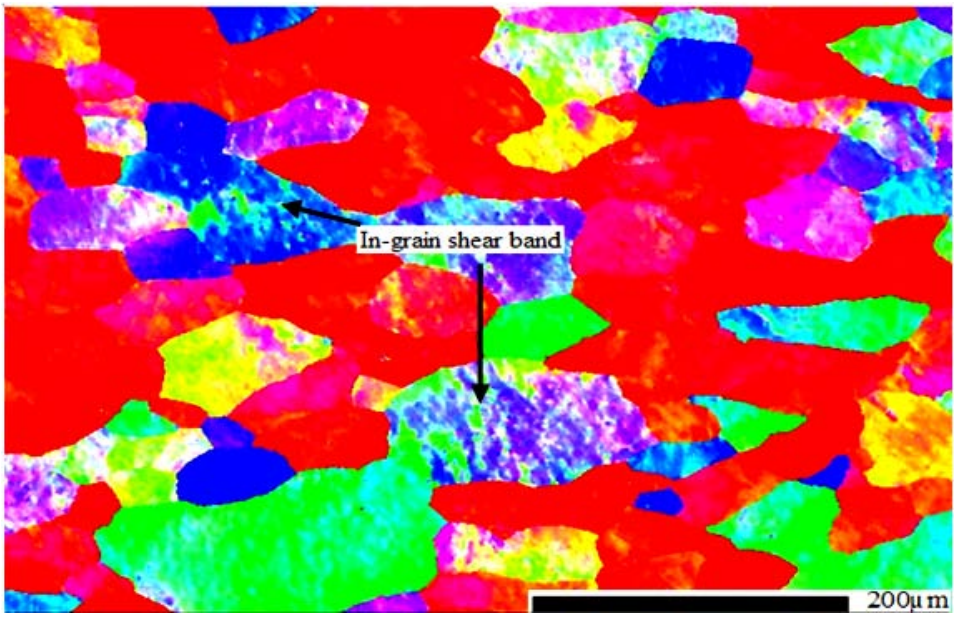

(a)

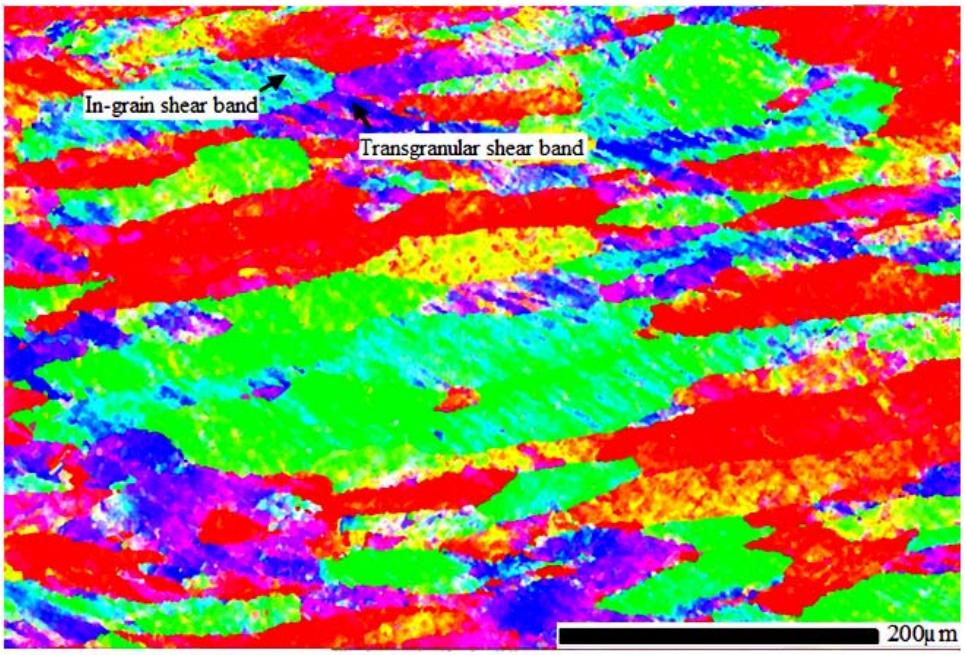

(b)

Figure 6.11 Shear bands and deformed grains: (a) 40 % reduction, and (b) 60 % reduction

6.1.4.5 Stress-strain analysis

With an increase of true strain, the experimental and simulated stresses show the same tendency (Figure 6.12), and there are two obvious stages in the stress-strain curves. When reduction is less than 10 %, the relationship between the stress and strain is linear but if reduction exceeds 20 %, plastic deformation takes place in the sample. In this experiment the strain rate is about 0.001 s^{-1}. The simulation result is higher than the experimental result because the model applied in the simulation has been modified from Taylor's model [88], and the minimum energy dissipation is used to analyse the deformation [88, 194]. In one grain, only five independent slip systems were considered, and there are twelve potential {111}<110> slip systems in one grain. The simulation result also shows a good agreement with Kalidindi [117] and Pi's [164] research results.

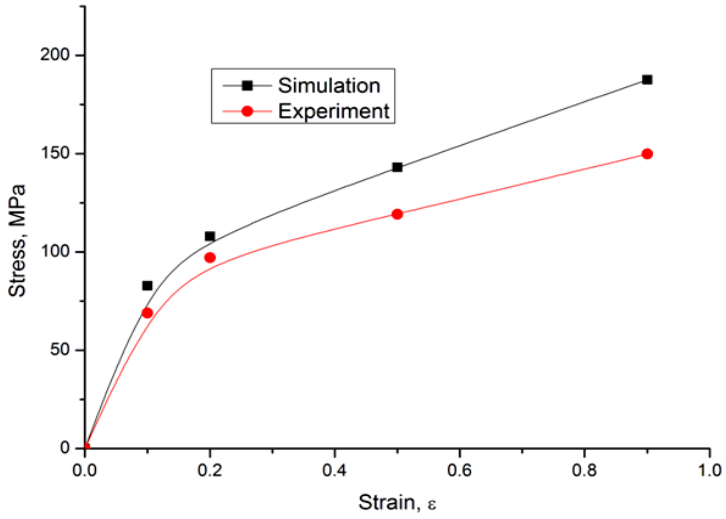

Figure 6.12 Stress-strain analysis of experiment and simulation

6.1.4.6 Analysis of pole figure

Normally, the close packed plane in FCC metal is {111}. In this study the pole figure {111} is used for analysis. Before compression the sample has a cubic texture {100}<001> (Figure 6.13, reduction 0 %). The predicted result has been compared to the experimental result, both of which show the same texture development. In the pole figure {111}, with an increased reduction, the brass orientation {110}<112> of silk texture becomes obvious while the cubic texture {001}<100> becomes weaker. When reduction is about 60 % (true strain is about 0.91), the brass orientation {110}<112> of silk texture is very strong in areas a and d of Figure 6.13. Meanwhile, a few S orientations {123}<634> appear in areas b and c. The results basically agree with the Sarma and Dawson's results [118], which show a consistent development in hardness and grain size.

Reduction, %	Experimental	Simulation
0	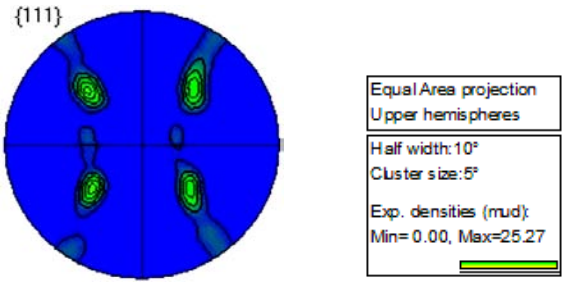	
10	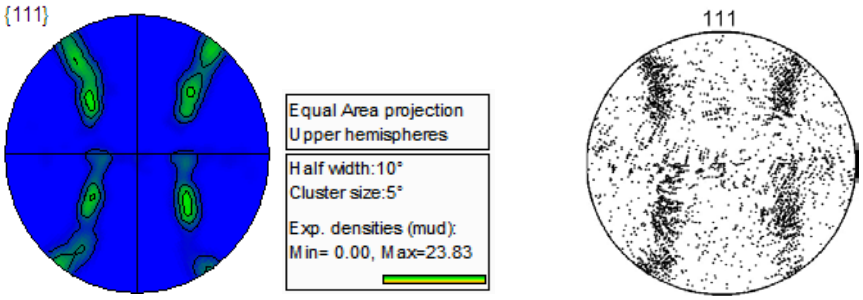	
20	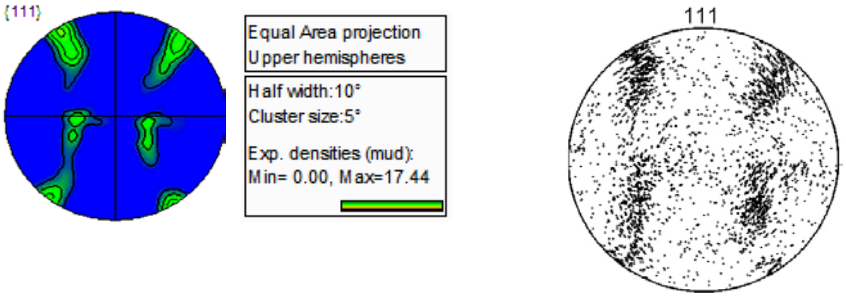	
40	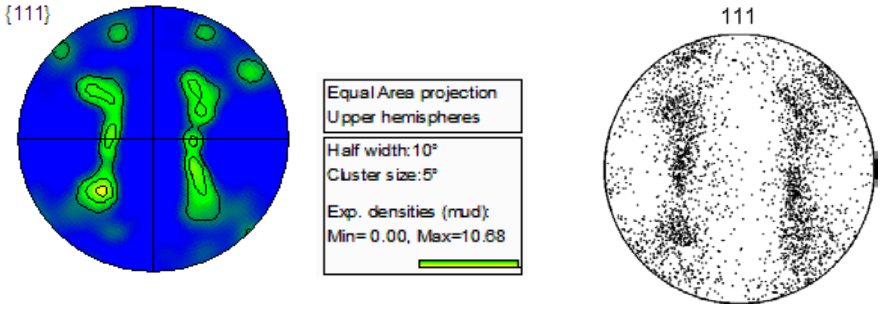	
60	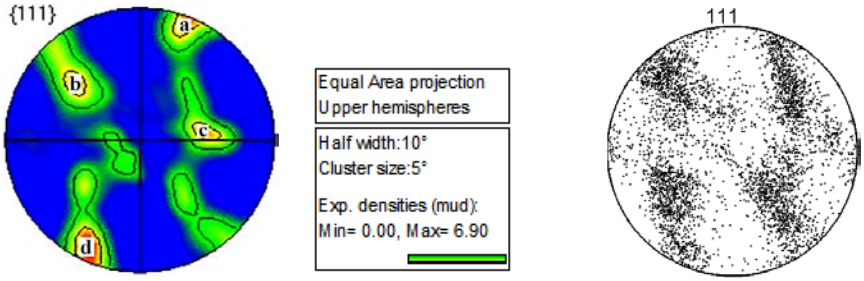	

Figure 6.13 Comparison of the experimental pole figures with the simulation results

6.1.4.7 Orientation sensitivity of surface feature

Figure 6.14a shows the orientation of grain at the centre of the top surface on Al workpiece by the FEG-SEM (Field Emission Gun-Scanning Electron Microscope). The workpiece has experienced a uniaxial planar compression of 60 % reduction without lubrication. Scale of FEG-SEM figure is 200 μm, and the scan step is 0.5 μm. Shear bands that resulted from localised strains are obvious in the grains of [101] and [111] orientations. The grains of [101] and [111] orientations have a high intensity at the centre of the top surface. Grains with orientation [100] are in an area that is several diameters of grains away from the centre of the top surface. Compared to those orientated in [100], in the top surface area of the workpiece, grains orientated in [111] show a much stronger tendency of evolution. Aicheler et al [196] found that regions of [111] orientation have highly developed surface features at the top surface of RFF (Radio-Frequency-heating fatigue) FCC copper, while regions of [100] have no significantly developed surface features, as shown in Figure 6.14b. Despite the different FCC materials and deformation modes (Copper and Aluminium are all FCC material but different metals, and the deformation mode of Aicheler et al is different from ours), both results show a good agreement. Different orientated grain has various evolvements in the plane stress state. The order of this inhomogeneity was calculated by Wikstroem et al. [197] and Baker et al [198]. Moenig [199] who also confirmed that the ratio between the plane stresses in [111] and [100] is about 2.3 ($\sigma_{111}/\sigma_{100}$). For aluminium, the stresses in different orientations are also different. The practical ratio of stresses in different orientations will be investigated further.

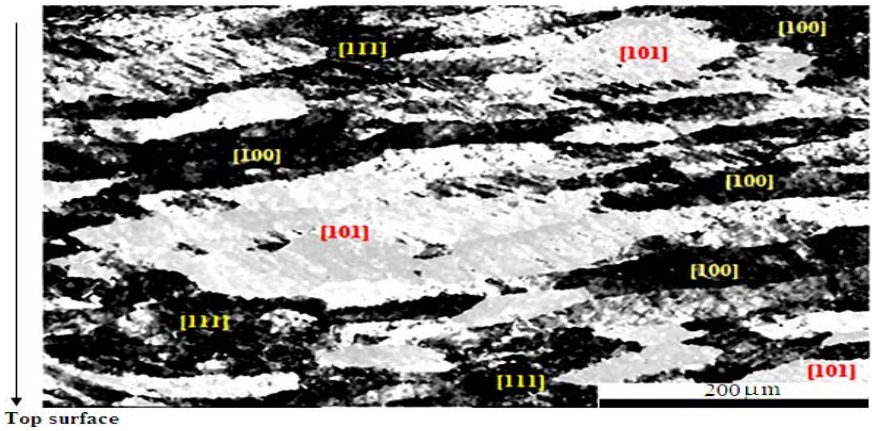

(a)

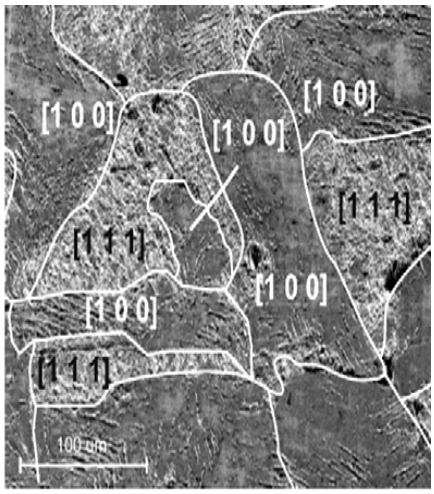

(b)

Figure 6.14 Orientation distribution of SEM picture (a) aluminium SPC, and (b) copper RFF [196]

6.1.5 Conclusions

There are three obvious stages in the surface asperity flattening of a rough surface in uniaxial planar compression. When reduction is 10 % or less, the elastic deformation of asperities on the workpiece plays an important role in the surface asperity flattening of the workpiece, while the influence of plastic deformation on the surface roughness is insignificant. When reduction is less than 20 %, plastic deformation of asperities takes place on an elastic substrate at the centre of the top surface. If reduction exceeds 40 %, the in-grain shear band appears in some grains which are 4-5 grains distance away from the edge, and localised strain starts in this area. When reduction exceeds 60 %, most grains have plastic slips. The material in the centre of the sample's top surface is inhomogeneous.

With an increase in reduction, both the grain size and surface roughness decrease while the stress increases. The simulation result agrees with the experimental one. The simulation results also show that with an increase in reduction, the cubic texture {001}<100> is weak, while the brass orientation {110}<112> becomes strong. From the experimental results, the surface roughness shows obvious grain orientation sensitivity to the orientations of near-surface grains. In this study, the oriented {111} grains are the main source of localised strains.

6.2 Influence of strain rate on 3D surface asperity flattening in uniaxial planar compression

6.2.1 Introduction

In Section 6.1, 3D surface asperity flattening in planar compression has been carried out by the CPFEM method, and some related parameters (for example surface roughness, hardness, stress, texture etc.) were investigated. In this Section the effect of the strain rate on 3D surface asperity flattening has been studied.

In metal forming process, the strain rate is an important parameter. Practically, most metal materials are rate dependent, and therefore the strain rate can influence many properties of metal forming products such as the strength, stress, facture, microstructure, work hardening, plasticity, and so on. There are many reports that mentioned the effects of the strain rate. Liu et al. [200] developed a combined finite element (FE) simulation and discrete dislocation dynamics (DD) approach to investigate the dynamic deformation of single-crystal copper at mesoscale. They found that with an increase in the strain rate, the yield stress of single-crystal copper increases rapidly, the formed shear band width also increases. Travis et al. [201] studied the interactive effects of strain, strain rate, and temperature in the severe plastic deformation of copper. They pointed out that nano-twinning was demonstrated at strain rates as small as 1000 s^{-1} at -196 °C, and at strain rates of ≥ 10000 s^{-1} even when the deformation temperature was well above room temperature. Serebrinsky et al. [202] investigated the effect of the strain rate on the stress corrosion crack propagation rate for strain rates covering a range of values from 10^{-6}-20 s^{-1}. They found that the accelerating effect of the strain rate was always higher for intergranular stress corrosion cracking than for transgranular stress corrosion cracking. Serebrinsky and Galvele [203] also pointed that increasing the SR (strain rate) causes a monotonic increase of the log CPR (crack propagation rate) to take place. Wu et al [204] analysed the inverse effect of strain rate on the mechanical behaviour and phase transformation of super-austenitic stainless steel, and pointed out that the ductility of super-austenitic stainless steel increases significantly with an

increase in the strain rate. Papakaliatakis [205] analysed the strain rate on crack growth in aluminium alloy 1100-0 and found that compared to plasticity theory, the strain rate dependent model would predict a lower load for crack initiation. Urcola and Sellars [206] investigated the effect of changing the strain rate on stress-strain behaviour during high temperature deformation and found that in both the ferritic stainless steel and Al-l % Mg alloy, the flow stress is only dependent on the instantaneous strain rate and not on how this strain rate is reached. Vaynman et al [207] studied the effect of the strain rate and temperature on the mechanical properties and the fracture mode of high strength precipitation hardened ferritic steels. They concluded that the effect of the strain rate on the flow stress of a low carbon high strength ferritic steel containing nanometer size Cu-Ni-Al precipitates is much less than HSLA 65 without these precipitates. Takuda et al [208] investigated the effect of the strain rate on the deformation of an Mg-8.5Li-1Zn alloy sheet at room temperature and reported that at room temperature, the ductility decreases with an increase of strain rate, and the stress is also sensitive to the strain rate. Bhattacharyya et al. [209] analysed the effect of the strain rate on the deformed texture in OFHC (Oxygen-free high thermal conductivity) copper and found that an increase in the strain rate causes an increase in strain hardening which thereby influences the texture. Wu and Lin [210] investigated the effect of the strain rate on high temperature low-cycle fatigue 17-4 PH stainless steels and pointed out that for various heat treated 17-4 PH stainless steels tested at a given temperature, the number of cycles to failure consistently decreased with a reduction in strain rate due to an enhanced dynamic strain aging effect. Zhang and Shim [211] studied the effect of the strain rate on the microstructure of polycrystalline oxygen free high conductivity copper that had been severely deformed by liquid nitrogen. They pointed out that a difference in the strain rate leads to a change in the density, character, and arrangement of dislocations, as well as the size and configuration of the dislocated cells/(sub)grains in the deformed sample. They also identified that a strain rate of 10^3 s^{-1} is the threshold for the formation of local deformation bands which characterise the heterogeneity of deformation at high strain rates. Kodeeswaran and Gnanamoorthy [212] analysed the effect of the strain rate on the formation of a nanocrystalline surface of AISI 304 SS (American Iron and Steel Institute 304 stainless steel) as a result of a controlled ball impact process. They

pointed out that the surface roughness of these treated samples depends on the strain rate exerted and the velocity at which the samples were travelling. Eghbali [213] analysed the effect of the strain rate on the microstructural development of microalloyed steel using torsion equipment and found that at a lower strain rate, the continuous dynamic recrystallised grains enlarge under a high strain rate deformation, when the time for grain growth is diminished and the coalescence of continuous dynamically recrystallised grains is inhibited. Percy [214] analysed the influence of the strain rate on the forming limit diagram of sheet metal in tensile test and pointed out that the strain hardening exponent falls as the strain increases. Qin et al. [215] analysed the mechanism of the strain rate based on dislocation theory and then proposed that the strain rate criteria rather than stress criteria should be satisfied when a metal is fully yielded at a given strain rate.

However, there are no reports about the effect of the strain rate on the surface asperity flattening (surface roughness change) process. On the basis of our experimental results, we investigated the relationship between surface asperity, friction [189], and grain size [190] by applying a 2D crystal plasticity finite element model. In Section 6.1 we analysed the relationship between surface asperity flattening, reduction and texture, and grain orientation with a 3D surface roughness model [216]. In this study, on the basis of Section 6.1, the influence of the strain rate on the surface asperity flattening process has been analysed. Both the simulation and experimental results agreed under the same reduction, the sample deformed with a higher strain rate has a much flatter surface (lower surface roughness R_a) than the one with a low strain rate. Increasing the strain rate generally increases the rate of work hardening at smaller strains, while at larger strains, the work hardening rate decreases with an increasing strain rate due to adiabatic heating. The strain rate also plays an important role in the development of texture.

6.2.2 Material and experimental procedure

The material used here was also Al 6061alloy samples annealed before compression in a furnace heated to 450 °C for 2 hours, and then cooled in the furnace. The samples are ground by automatic grinding/polishing machine (with ridges and

valleys). Surface roughness of the samples after grinding was kept at about 0.70 μm (R_a). 2D and 3D profile meters were used to measure the surface roughness. The same method as Section 6.1.2 was used to trace the samples before and after compression. Any errors in surface roughness between different samples were less than 0.05 μm. When compression takes place, the sample is constrained in a transverse direction and the surface roughness develops along the rolling direction. The same compression equipment was used in this study (Figure 6.1) and the samples were also about 10 mm×10 mm×6 mm in size, as shown in Figure 6.1c. The compression test was carried out by applying the compression tool in the INSTRON 8033 Material Testing Machine. The contact surface of the compression tool was polished to about 10-20 nm. The parameters are shown in Table 6.1.

Table 6.2 Compression schedule for different strain rates

Sample	Height (mm)	Reduction (%)	Strain rate (s^{-1})	Displacement rate (mm/min)	Displacement (mm)	Height after deformation (mm)
1	6.3	10	0.001/0.01	-0.359	0.63	5.67
2	6.3	20	0.001/0.01	-0.339	1.26	5.04
3	6.3	40	0.001/0.01	-0.296	2.52	3.78
4	6.3	60	0.001/0.01	-0.248	3.78	2.52

Two strain rates have been applied in this study: 0.001 and 0.01 s^{-1}. However, it is difficult to control the strain rate on the INSTRON equipment so the displacement rate was used instead [189]. The method for controlling the strain rate is the same as in Section 6.1.2. The relationship between the strain rate and displacement can be obtained from Equation (6.1).

The hardness was measured with an M-400-H1 Micro-hardness Testing Machine using the same method in Section 6.1.1, and during this test, hardness under different strain rates was measured. The ridges and valleys on the top surface of the same sample were also measured and identified by the sequence of focus in the experiment. The first area of focus was the ridge and the second area was the valley.

6.2.3 Crystal plasticity finite element model

The same crystal plasticity finite element model has been used to analyse the strain rate effect on surface asperity flattening, and the 5 assumptions used for a single crystal were still used in this simulation.

6.2.3.1 Slip systems of FCC crystals

The key point with plastic deformation is how to ensure which slip system is activated and how many slip systems are deformed. The Taylor model is the main answer to this problem. It is assumed that 5 independent slip systems in a grain will take the function of slip deformation [88].

We all know that different crystals have different slip systems, but in FCC crystals there are 12 {111}<110> slip systems (Figure 6.15).

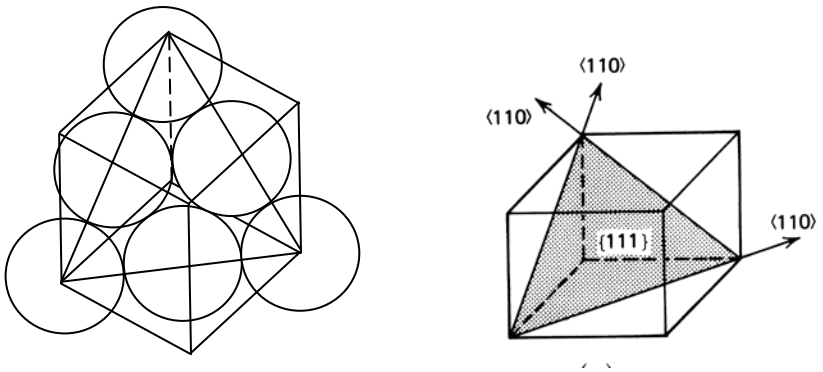

Figure 6.15 Slip systems of FCC crystal: slip planes {111}, slip directions <101> [88]

On the basis of the Taylor model the imposed strain rate can be obtained from the following equation.

$$\dot{\boldsymbol{\varepsilon}} = \begin{pmatrix} \dot{\varepsilon}_{11} & \frac{\dot{\varepsilon}_{12}}{2} & \frac{\dot{\varepsilon}_{13}}{2} \\ \frac{\dot{\varepsilon}_{12}}{2} & \dot{\varepsilon}_{22} & \frac{\dot{\varepsilon}_{23}}{2} \\ \frac{\dot{\varepsilon}_{13}}{2} & \frac{\dot{\varepsilon}_{23}}{2} & -\dot{\varepsilon}_{11} - \dot{\varepsilon}_{22} \end{pmatrix} \tag{6.4}$$

In Section 3.3, the slip law can be obtained by Equations (3.19) - (3.23). On the basis of these equations, the strain rate tensor $\dot{\boldsymbol{\varepsilon}}$ and rotation tensor $\boldsymbol{\omega}$ can be written as a combination of all the slip systems. They are shown as

$$\dot{\boldsymbol{\varepsilon}} = D^p = \sum_{\alpha=1}^{n} P^{(\alpha)} \dot{\gamma}^{(\alpha)} = \sum_{\alpha=1}^{n} \frac{\dot{\gamma}^{\alpha}}{2} \left(s^{*(\alpha)} m^{*(\alpha)T} + m^{*(\alpha)} s^{*(\alpha)T} \right) \tag{6.5}$$

$$\mathbf{W} = \Omega^p = \sum_{\alpha=1}^{n} W^{(\alpha)} \dot{\gamma}^{(\alpha)} = \sum_{\alpha=1}^{n} \frac{\dot{\gamma}^{\alpha}}{2} \left(s^{*(\alpha)} m^{*(\alpha)T} - m^{*(\alpha)} s^{*(\alpha)T} \right) \tag{6.6}$$

6.2.3.2 Set of five independent slip systems

Following the Taylor assumption, the set of five independent slip systems can be determined by the minimum dissipation of energy. It is shown in Equation (6.7).

$$W^q = \sum_{\alpha} \tau^{\alpha} \left| \dot{\gamma}^{\alpha} \right| \tag{6.7}$$

For non hardening material:

$$\tau^{\alpha} = \tau_s \tag{6.8}$$

The minimum dissipation of energy can be obtained by the following equation.

$$W^q = \tau_s \sum_{\alpha} \left| \dot{\gamma}^{\alpha} \right| \tag{6.9}$$

6.2.3.3 Slip law

In plastic deformation all the slip systems obey the following equations. Based on Equations (6.5) and (6.6), the strain rate tensor and rotation tensor can be expressed bellow:

The strain rate tensor is

$$\dot{\boldsymbol{\varepsilon}} = \sum_{\alpha=1}^{n} \frac{\dot{\gamma}^{\alpha}}{2}\left(s^{*(\alpha)} m^{*(\alpha)T} + m^{*(\alpha)} s^{*(\alpha)T}\right) \tag{6.10}$$

The rotation tensor is

$$\mathbf{W} = \sum_{\alpha=1}^{n} \frac{\dot{\gamma}^{\alpha}}{2}\left(s^{*(\alpha)} m^{*(\alpha)T} - m^{*(\alpha)} s^{*(\alpha)T}\right) \tag{6.11}$$

The power law of strain hardening can be expressed by Equation (3.65). On the basis of Equation (3.66), the stress tensor can be expressed as

$$\boldsymbol{\tau} \approx \mathbf{T}^{(1)} \cdot \mathbf{s}_{(\alpha)} \otimes \mathbf{m}_{(\alpha)} = \boldsymbol{\sigma} \bullet \frac{1}{2}\left(s^{*(\alpha)} m^{*(\alpha)T} + m^{*(\alpha)} s^{*(\alpha)T}\right) \tag{6.12}$$

6.2.3.4 Strain rate tensor in a uniaxial stress state

In a FCC crystal the uniaxial stress (without friction) is shown in Figure 6.16.

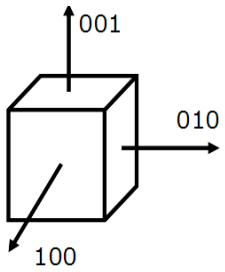

Figure 6.16 Schematic uniaxial stress in a FCC crystal

a) Applied stress

The applied stress for uniaxial stress is

$$\begin{pmatrix} \sigma & 0 & 0 \\ 0 & 0 & 0 \\ 0 & 0 & 0 \end{pmatrix} \tag{6.13}$$

b) Slip systems

In a FCC crystal, there are 12 potential slip systems in total shown in Table 6.3.

Table 6.3 12 potential slip systems of a FCC crystal

System	$\mathbf{s}^{(a)}$	$\mathbf{m}^{(a)}$
1	$\frac{1}{\sqrt{3}}[111]$	$\frac{1}{\sqrt{2}}[0\bar{1}1]$
2	$\frac{1}{\sqrt{3}}[111]$	$\frac{1}{\sqrt{2}}[10\bar{1}]$
3	$\frac{1}{\sqrt{3}}[111]$	$\frac{1}{\sqrt{2}}[\bar{1}10]$
4	$\frac{1}{\sqrt{3}}[\bar{1}11]$	$\frac{1}{\sqrt{2}}[101]$
5	$\frac{1}{\sqrt{3}}[\bar{1}11]$	$\frac{1}{\sqrt{2}}[0\bar{1}1]$
6	$\frac{1}{\sqrt{3}}[\bar{1}11]$	$\frac{1}{\sqrt{2}}[110]$
7	$\frac{1}{\sqrt{3}}[\bar{1}\bar{1}1]$	$\frac{1}{\sqrt{2}}[011]$
8	$\frac{1}{\sqrt{3}}[\bar{1}\bar{1}1]$	$\frac{1}{\sqrt{2}}[101]$
9	$\frac{1}{\sqrt{3}}[\bar{1}\bar{1}1]$	$\frac{1}{\sqrt{2}}[\bar{1}10]$
10	$\frac{1}{\sqrt{3}}[\bar{1}1\bar{1}]$	$\frac{1}{\sqrt{2}}[011]$
11	$\frac{1}{\sqrt{3}}[\bar{1}1\bar{1}]$	$\frac{1}{\sqrt{2}}[10\bar{1}]$
12	$\frac{1}{\sqrt{3}}[\bar{1}1\bar{1}]$	$\frac{1}{\sqrt{2}}[110]$

c) P_α matrices

In Section 3.21, P_α matrices can be obtained by Equation (3.20). In a uniaxial strain state the P_α matrices are calculated as

Table 6.4 P_α Matrices

$\frac{1}{2\sqrt{6}}\begin{pmatrix}0 & -1 & 1\\ -1 & -2 & 0\\ 1 & 0 & 2\end{pmatrix}$	$\frac{1}{2\sqrt{6}}\begin{pmatrix}2 & 1 & 0\\ 1 & 0 & -1\\ 0 & -1 & -2\end{pmatrix}$	$\frac{1}{2\sqrt{6}}\begin{pmatrix}-2 & 0 & -1\\ 0 & 2 & 1\\ -1 & 1 & 0\end{pmatrix}$	$\frac{1}{2\sqrt{6}}\begin{pmatrix}-2 & 1 & 0\\ 1 & 0 & 1\\ 0 & 1 & 2\end{pmatrix}$
$\frac{1}{2\sqrt{6}}\begin{pmatrix}0 & 1 & -1\\ 1 & -2 & 0\\ -1 & 0 & 2\end{pmatrix}$	$\frac{1}{2\sqrt{6}}\begin{pmatrix}-2 & 0 & 1\\ 0 & 2 & 1\\ 1 & 1 & 0\end{pmatrix}$	$\frac{1}{2\sqrt{6}}\begin{pmatrix}0 & -1 & -1\\ -1 & -2 & 0\\ -1 & 0 & 2\end{pmatrix}$	$\frac{1}{2\sqrt{6}}\begin{pmatrix}-2 & -1 & 0\\ -1 & 0 & -1\\ 0 & -1 & 2\end{pmatrix}$
$\frac{1}{2\sqrt{6}}\begin{pmatrix}2 & 0 & -1\\ 0 & -2 & 1\\ -1 & 1 & 0\end{pmatrix}$	$\frac{1}{2\sqrt{6}}\begin{pmatrix}0 & -1 & -1\\ -1 & 2 & 0\\ -1 & 0 & -2\end{pmatrix}$	$\frac{1}{2\sqrt{6}}\begin{pmatrix}-2 & 1 & 0\\ 1 & 0 & -1\\ 0 & -1 & 2\end{pmatrix}$	$\frac{1}{2\sqrt{6}}\begin{pmatrix}-2 & 0 & -1\\ 0 & 2 & -1\\ -1 & -1 & 0\end{pmatrix}$

d) Stress of different slip systems

In any slip system, if the stress meets Equations (6.8) and (6.12), this slip system will be activated. The calculated stress of different slip systems li listed in Table 6.5.

Table 6.5 Calculated stress of different slip systems

Slip system	1	2	3	4	5	6
τ	0	$\frac{\sigma}{\sqrt{6}}$	$\frac{-\sigma}{\sqrt{6}}$	$\frac{-\sigma}{\sqrt{6}}$	0	$\frac{-\sigma}{\sqrt{6}}$
Slip system	7	8	9	10	11	12
τ	0	$\frac{-\sigma}{\sqrt{6}}$	$\frac{\sigma}{\sqrt{6}}$	0	$\frac{-\sigma}{\sqrt{6}}$	$\frac{-\sigma}{\sqrt{6}}$

e) Total strain rate

The total strain rate in a grain can be obtained as

$$\dot{\varepsilon} = \frac{\dot{\gamma}}{2\sqrt{6}} \begin{pmatrix} 16 & 0 & 0 \\ 0 & -8 & 0 \\ 0 & 0 & -8 \end{pmatrix} \tag{6.14}$$

6.2.3.5 3D model and mesh

The model and its mesh is the same as in Section 6.1.3.3 (Figure 6.3). The 3D model has 840 C3D8R reduced integration elements. Some elements on the top surface are small. To maintain the weight of orientation in modelling, every four neighbouring elements at the top surface have one orientation. There are 280 elements in total, with 70 Euler angle triplets. The other 560 elements follow the rule of a fully finite element model: one element with one orientation. The spatial distribution of orientations is assigned on the basis of the EBSD experimental results. The rigid tool and mould both have 460 discrete rigid elements. Kalidindi's method [188] was used to incorporate crystal plasticity into FEM. The constitutive model and time-integration procedures were implemented into the implicit finite element code ABAQUS using the user material subroutine UMAT. It is considered that during the modelling, the combined slip systems include 12 {110}<111> slip systems (slip planes and slip directions). The shearing rate on each slip system [186] is assumed to be identical. 630 Euler angle triplets from the experimental results were input into ABAQUS as the initial crystallographic condition of the 3D model. All the parameters of simulation are taken from Table 5.1 as a reference. Elasticity tensors were taken as C_{11}=106750 MPa, C_{22}=60410 MPa, C_{44}=28340 MPa [184]. The $q_{\alpha\beta}$=1.0 for co-planar systems and $q_{\alpha\beta}$=1.4 for non co-planar slip systems [99, 191]. The other material parameters were set according to reference [133,192].

6.2.4 Results and discussion

6.2.4.1 Surface roughness

From Figures 6.17 and 6.18, it can be seen that with an increase of reduction, the surface asperity of the samples tends to be flattened. In the evolution of surface asperity, the strain rate plays an important role: under the same reduction, the sample

deformed with a higher strain rate has a much flatter surface (with a lower surface roughness R_a) than the sample deformed at a lower strain rate. In other words, with an increase in reduction the sample with a higher strain rate has a higher flattened rate of surface asperity than the sample with a lower strain rate. Equations (6.5) and (6.10) show the relationship between the applied macroscopic strain rate $\dot{\boldsymbol{\varepsilon}}$ and the shear rate $\dot{\gamma}$ of the slip system. The shear rate $\dot{\gamma}$ is proportional to the applied macro strain rate $\dot{\boldsymbol{\varepsilon}}$. Therefore, increasing the applied macroscopic strain rate $\dot{\boldsymbol{\varepsilon}}$ will increase the shear rate $\dot{\gamma}$ of slip systems in the surface area. Then, under the same reduction the sample deformed at a higher strain rate will activate more slip systems in the surface area. Furthermore, the sample with the higher strain rate will have more surface deformation than the sample with the lower strain rate. So under the same reduction, the sample with a higher strain rate will have a much flatter surface than the sample with a lower strain rate. When reduction is 40 %, the surface roughness R_a of the sample with a higher strain rate is 0.16 μm, while the sample with a lower strain rate is only 0.09 μm.

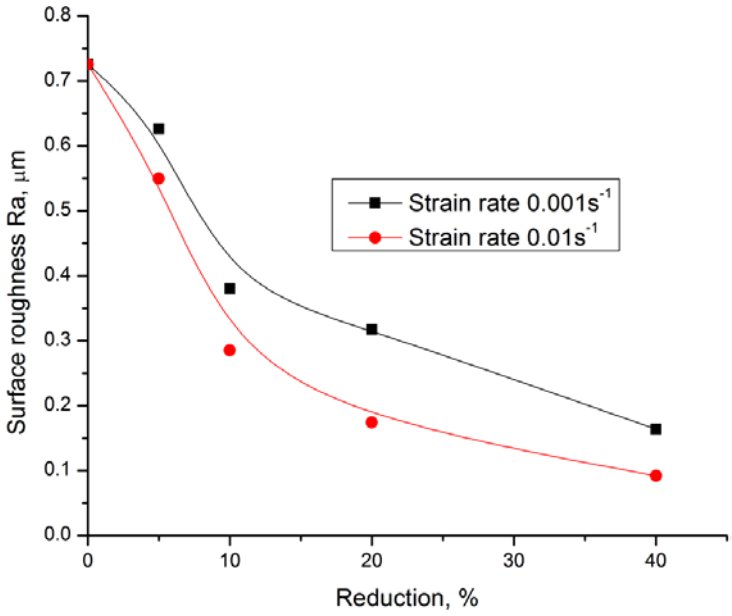

Figure 6.17 Influence of strain rate on surface roughness

Reduction (%)	Strain rate 0.001 s^{-1}	Strain rate 0.01 s^{-1}
0	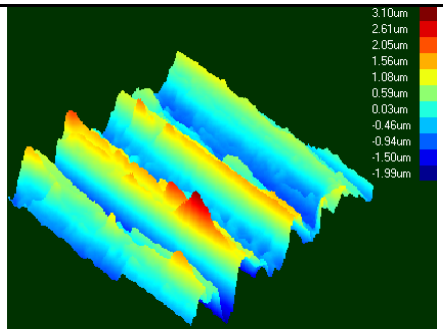	
5	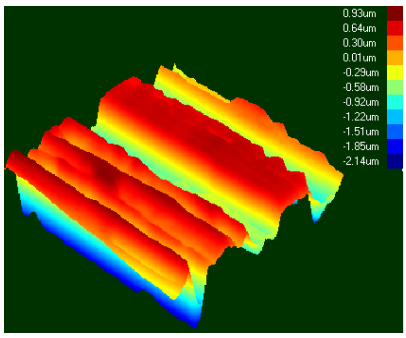	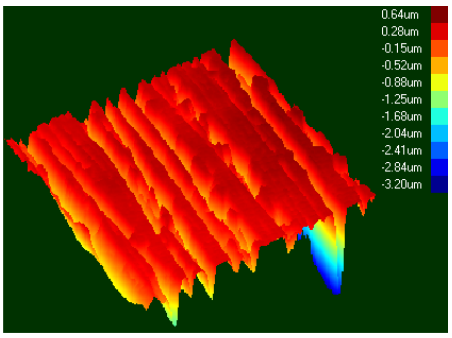
10	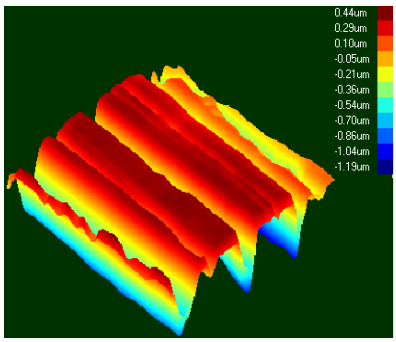	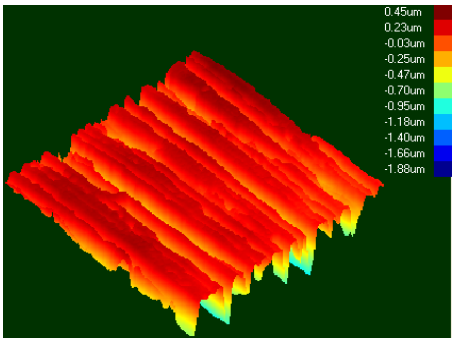
20	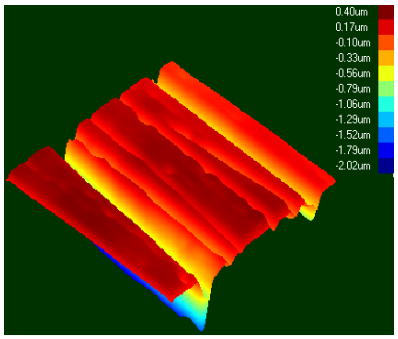	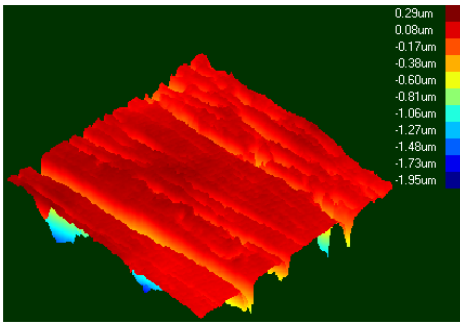
40	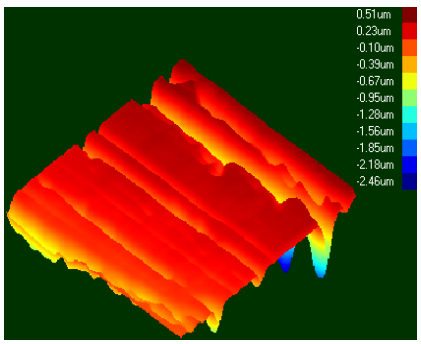	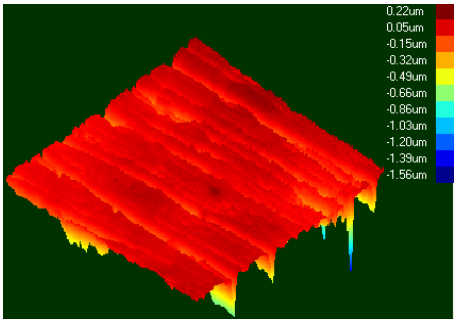

Figure 6.18 Evolution of surface asperity under different strain rates

6.2.4.2 Flow stress

Figure 6.19 shows the influence of the strain rate on flow stress; when samples experience the same plastic strain, the sample with higher strain rate will have higher flow stress. When the strain exceeds a certain value (in this study about 0.4), the influence of the strain rate on flow stress is more significant. This result agrees with that of Qin et al. [215]. They used the stress dependence of dislocation velocity equation to analyse the relationship between the stress and strain rate. The equation is shown as

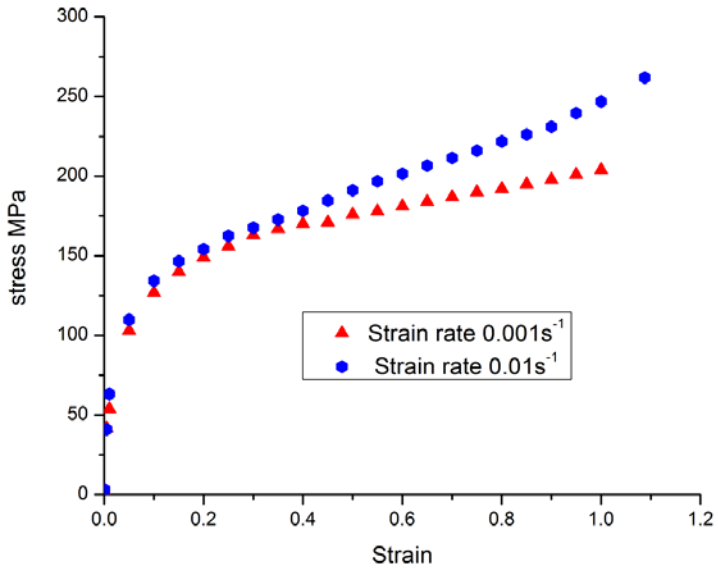

(a)

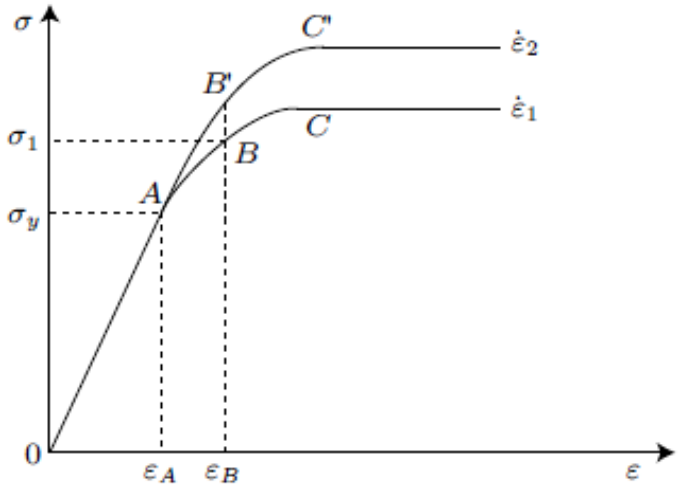

(b)

Figure 6.19 Influence of the strain rate on flow stress

$$\bar{v} = A_q T^{m_q} \tag{6.15}$$

where A_q and m_q are the material constant, $\bar{v}$ is the dislocation velocity, and T is the stress. In our study, the power law of strain hardening has been applied, as mentioned in Equation (3.65), and it includes information on resistance to slip shear and saturated deformation. It is much accurate than Equation (6.15).

With an increase in the strain rate, the shear rate of the slip system will also increase, and in some areas the dislocation density will increase. Therefore, the flow stress increases with an increase in the strain rate.

6.2.4.3 Hardness

a) Difference between valley and ridge

Figure 6.20 shows the evolution of the ridge and valley areas of the sample in the surface asperity flattening process respectively. Figures 6.20a and b both show the same tendency as in Section 6.1.4.3; with an increase of reduction, the sample becomes harder as well. Under the same reduction, the ridge area is more likely to be harder than that of the valley. During deformation the compression tool makes contact with the ridge first, and then the valley, when the compression tool makes contact with the ridge, deformation has already occurred in this area.

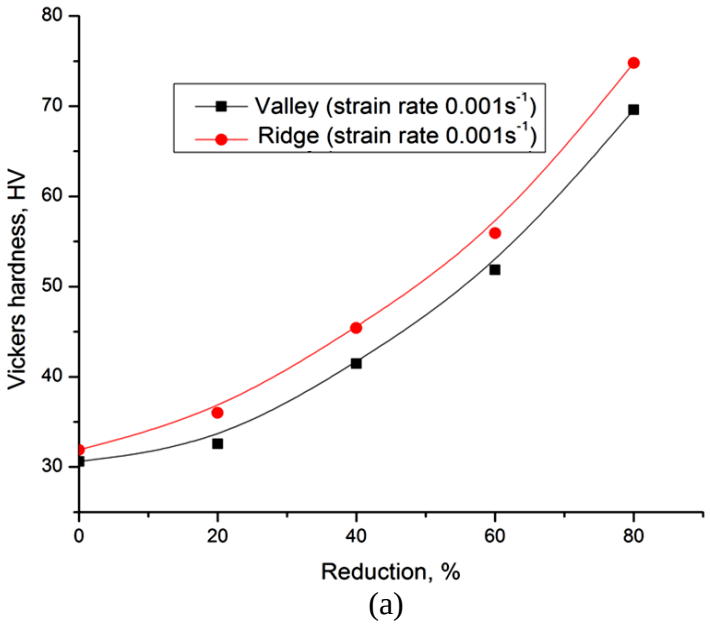

(a)

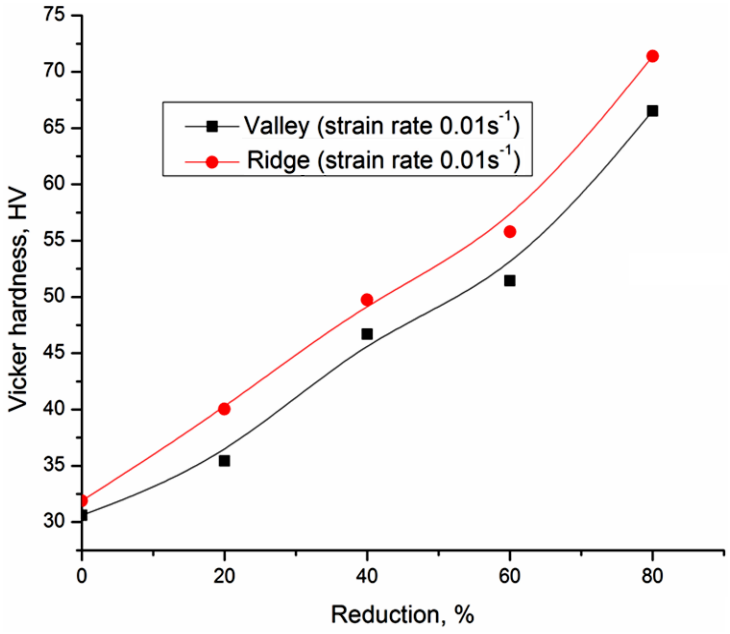

(b)

Figure 6.20 Difference in hardness between the ridge and valley areas

b) Influence of the strain rate

Figure 6.21 shows the influence of the strain rate on the hardness of the sample, it can be seen that the influence is non-linear. There are different stages in the evolution of hardness because when the reduction is lower (in this study less than 60 %), increasing the strain rate generally increases the hardness (work hardening rate). At a larger reduction (in this study it exceeds 60 %), the hardness of the sample with a higher strain rate is lower than the sample with a lower strain rate. Increasing the strain rate decreases the hardness under the same reduction. This result agrees with the results of Link et al. [217]. When reduction is low, increasing the strain rate can increase the shearing rate of slip systems, and also increase the density of dislocation. When reduction exceeds a certain value, the dislocation motion will overcome the barrier of grain boundary. In some areas, the density of dislocation decreases.

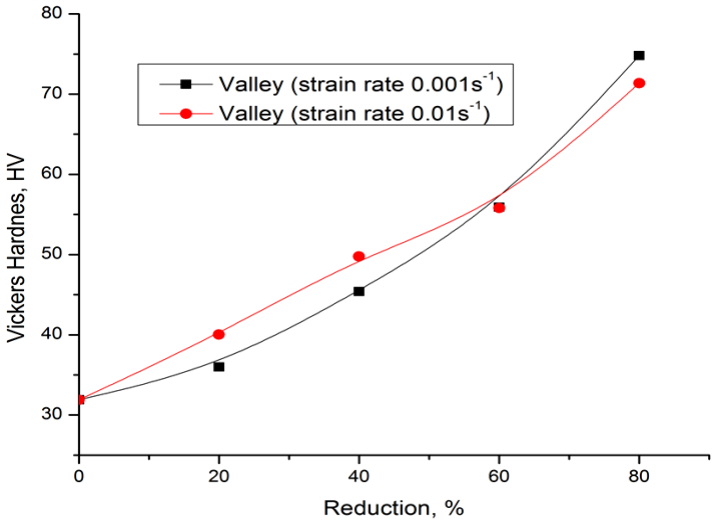

(a)

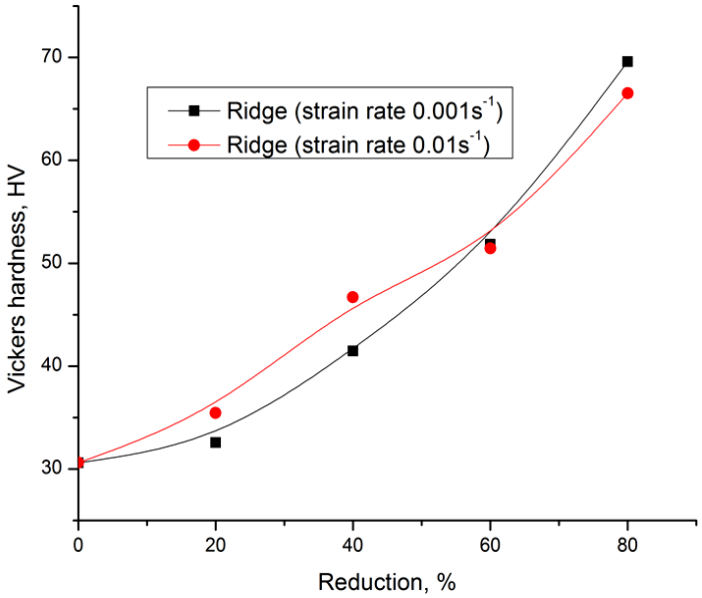

(b)

Figure 6.21 Influence of the strain rate on hardness

6.2.4.4 Comparison of simulation and experimental results

(a) Effect of the strain rate on flow stress

Figure 6.22 shows the experimental and simulation results considering the effect of strain rate on stress. Both the experimental and simulation results agree that at room temperature the strain rate plays an important role in the stress in uniaxial planar

compression. At a smaller strain (0.3 in the experiment and 0.2 in the simulation), the influence of the strain rate on stress is not significant. In this stage, any elastic deformation in the surface area is perhaps the main source of deformation. For elastic deformation, the relationship between the stress and the strain is linear because the stress depends only on the elastic modulus, so increasing the strain rate has no significant influence on stress. At a larger strain, stress increases by the rise of strain rate. In the larger strain case, the main deformation is plastic deformation. It can be obtained from Equations (6.5) and (6.10) that the shear rate strain rate $\dot{\gamma}$ is proportional to the applied macro strain $\dot{\varepsilon}$. With an increase of the shear rate $\dot{\gamma}$, more slip systems will be activated and the density of dislocation will also increase. As a result of strengthening dislocation, the stress increases.

Due to an assumption by the model, a simplification of the calculation and the difference between the experimental and simulation conditions, there is a difference between the simulated and experimental results. Generally, the calculated stress is lower than the experimental one. When the strain is about 1.0 and the strain rate is 0.01 s^{-1}, the experimental stress is about 230 MPa, while the calculated stress is only 200 MPa. In the experiment, when the strain is about 1.0, the stress with a strain rate of 0.001 s^{-1} is much lower than with a strain rate of 0.01 s^{-1}. On the other hand, the influence of the varied strain rate is not significant.

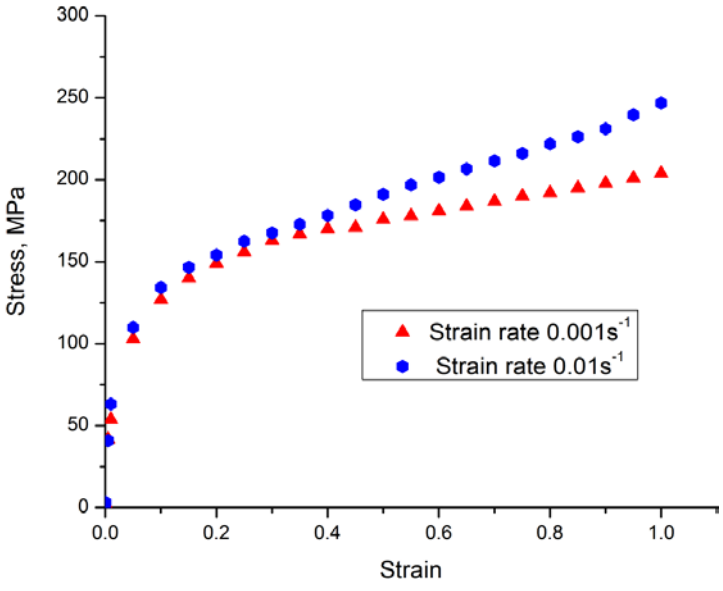

(a)

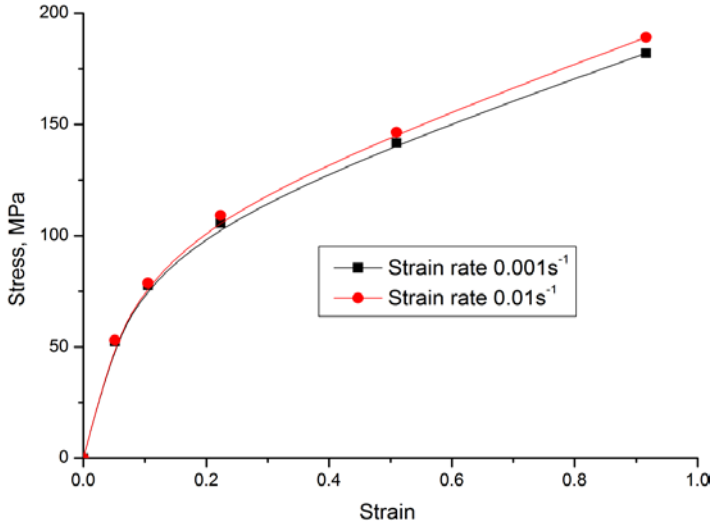

(b)

Figure 6.22 Strain rate effect on stress: (a) experimental, and (b) simulation

(b) Effect of strain on surface roughness (R_a)

In Figure 6.23 the experimental and simulation results both show the same tendency; increasing the strain rate can lead to a decrease in surface roughness under the same reduction. When reduction is less than 10 %, the effect of the strain rate on surface roughness is insignificant. At this stage elastic deformation plays an important role in the surface asperity flattening process. Because the strain rate has no obvious effect on elastic deformation, increasing the strain rate shows no significant influence on surface roughness. When the gauged reduction exceeds 10 % the effect of plastic deformation on surface area increases. Assumed slip is the only deformation mode, so increasing the strain rate can lead to an increase in slip by increasing the slip shear rate. This will increase the surface deformation even under the same reduction state. Therefore, the surface roughness will decrease greatly according to an increase in the strain rate.

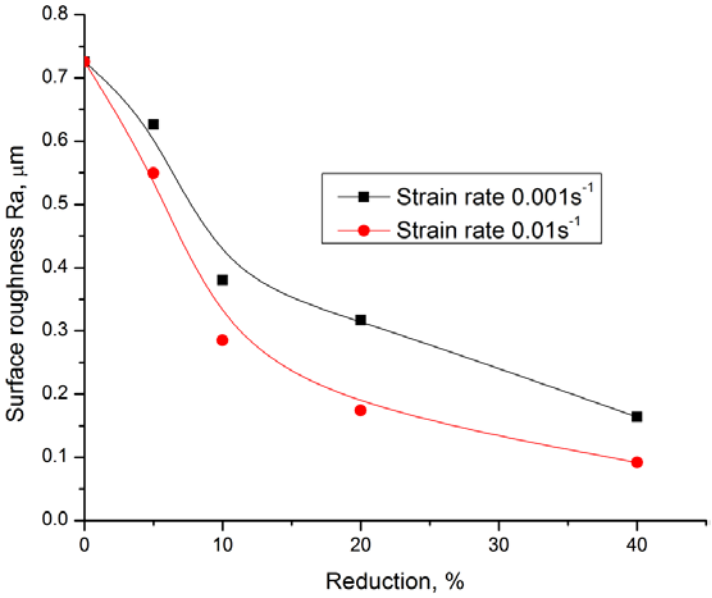

(a)

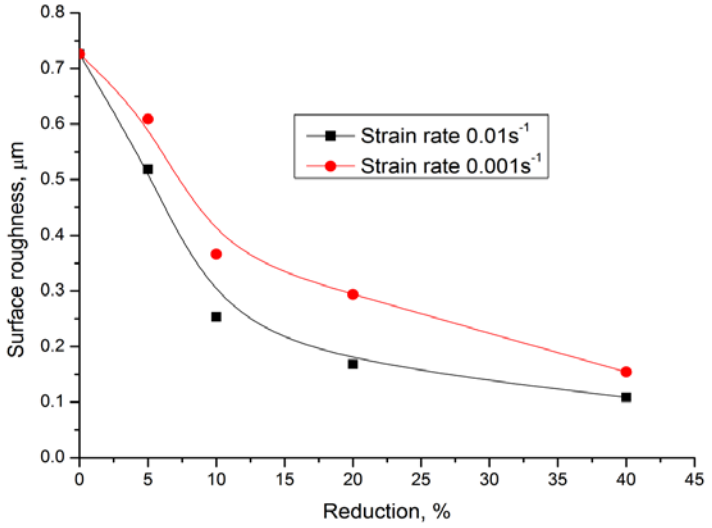

(b)

Figure 6.23 Effect of the strain rate on surface roughness R_a: (a) experimental, and (b) simulation

(c) Effect of the strain rate on texture

Figure 6.24 shows the influence of the strain rate on the pole figures of the sample under 60 % reduction. Compared to pole figures with a strain rate of 0.001 s^{-1}, pole figures with strain rate of 0.01 s^{-1} have no obvious difference. In this study, every experiment has been carried out at room temperature, and the two applied strain rates are quite small. Deformation under the two strain rates belongs to the quasi-static

deformation, and compared to the other dynamic deformation, the difference between the two applied strain rates are small. The above two reasons may contribute to the results shown in Figure 6.24. The results agreed with those of Bhattacharyya et al. [209].

Pole figure type	Strain rate 0.001 s^{-1}	Strain rate 0.01 s^{-1}
100	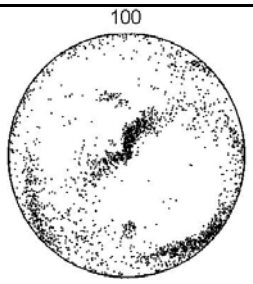	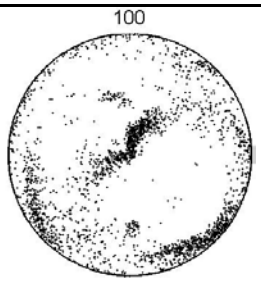
101		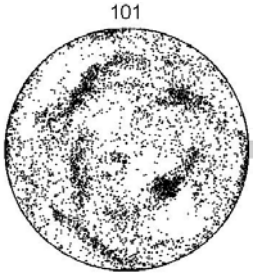
111	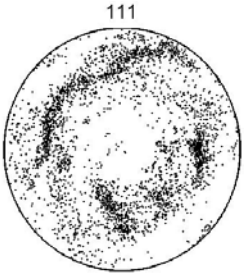	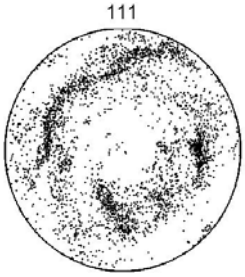

Figure 6.24 Effect of the strain rate on texture (reduction 60 % without lubrication)

6.2.5 Conclusions

The influence of the strain rate on surface asperity flattening has been divided into two stages: in elastic deformation, due to the linear relationship between the stress and the strain, the influence of the strain rate on surface asperity flattening is insignificant. In plastic deformation the role of the strain rate on surface asperity flattening is shown in Figure 6.25.

During plastic deformation, with an increase of strain rate, the shear rate of the slip systems in the surface area will also increase. This will lead to more slip systems being activated and an increase in dislocation density of the surface areas, and the work hardening increases as well. Flow stress in the surface areas will increase following the rise of strain rate. The above phenomenon means that under the same reduction, the rate of surface deformation increases with a rise of strain rate. So at larger strain rates surface asperity flattening will be accelerated. In other words, the surface roughness decreases greatly.

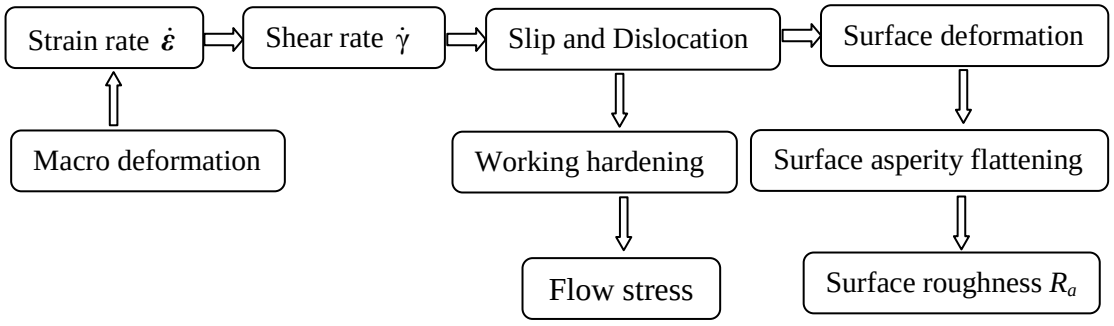

Figure 6.25 Influence of the strain rate on surface asperity flattening (in plastic deformation)

In plastic deformation the influence of the strain rate on parameters can be obtained as

(1) The strain rate plays a significant role in surface asperity flattening by changing the slip shear rate. In uniaxial planar compression, the relationship between the macroscopic strain rate and the shear rate is linear.

(2) Under the same reduction, the surface roughness with a higher strain rate (0.01 s^{-1}) has a larger flattening rate (lower roughness R_a) than a surface with a lower strain rate (0.001 s^{-1}).

(3) The influence of the strain rate on flow stress can be divided into two stages: in elastic deformation stage where the strain rate has no obvious influence

on the flow stress, while in the plastic deformation stage the flow stress increases according to a rise in the strain rate.

(4) At a lower strain the Vickers hardness of both ridge and valley increases with an increase in the strain rate, but at a larger strain (60 % in this study), the Vickers hardness decreases with an increase of strain rate, and the ridges are normally harder than the valleys.

(5) The simulated results agreed with those from the experimental ones, such that an increase in the strain rate leads to a decrease in surface roughness while the flow stress increases, even under the same deformation condition.

(6) There is still a difference between the simulated and experimental results where under the same deformation conditions, the simulated stress is much lower than the experimental one. At a larger strain, the influence of the strain rate on stress is not significant as the experimental one.

(7) In this study, the strain rate does not show an obvious influence on the development of texture.

6.3 New findings

(1) When the reduction is about 40 %, an in-grain shear band appears in some grains which are 4-5 grains distance away from the edge, and localised strain commences in this area. When reduction exceeds 60 % most grains have plastic slips. With an increase in reduction, both the grain size and surface roughness decrease while the flow stress increases.

(2) With an increase in reduction, the hardness of ridges and valleys increases. Normally, the ridge area is much harder than the valley area. With an increase in reduction the Schimid factor (orientation hardness) of the slip system in the surface area will shift from “hard” to “soft”.

(3) In uniaxial planar compression, the mechanism of the macroscopic strain rate on surface asperity flattening has been built up by establishing a linear relationship between the macroscopic strain rate and the slip shear rate (especially for plastic deformation). The influence of the strain rate on surface asperity flattening is divided into two stages: elastic deformation and plastic deformation. In the elastic stage, the strain rate has no significant influence on surface asperity flattening. However, in

plastic deformation, the strain rate plays a significant role in surface asperity flattening, and the strain rate does not show an obvious influence on the development of texture.

(4) Under the same experimental conditions (temperature, reduction, and friction), the surface with a higher strain rate has a lower surface roughness value of R_a than the one with a lower strain rate. Flow stress in the plastic deformation stage increases due to a rise in the strain rate. At a lower strain, the hardness of ridges and valleys both increase with an increase in the strain rate, while at a larger strain the tendency is reversed: an increasing strain rate can lead to a decrease in hardness.

CHAPTER 7

MICROTEXTURE BASED ANALYSIS OF THE SURFACE ASPERITY FLATTENING OF ANNEALED ALUMINIUM ALLOY IN UNIAXIAL PLANAR COMPRESSION

7.1 Introduction

During metal forming processes, surface roughness has a significant influence on products quality. The final surface quality of metal products depends on the development of surface topology. Numerous research papers show that surface evolution is a function of plastic strain, and grain size and orientation [4, 8, 46, 218, 219]. In practical metal forming processes, the development of surface topology includes two types of surfaces: an unconstraint surface and a constraint surface. During plastic deformation, unconstrained metal surface tends to become rougher. Osakada and Oyane [5] found that surface roughening increases with strain, and it is greater for coarser grain materials and for metals with a small number of slip systems. Therefore, CPH (close-packed hexagonal) metals roughen the most, FCC (face-centred cubic) material less, and BCC (body-centred cubic) materials the least. Tokizawa and Yosikawa [6] further discussed the influence of two material phases on the roughening process. Chen et al. [7] found that grain rotation is the most important factor determining surface roughening. Becker [8] established a model to address the influence of inhomogeneities on deformation by suggesting that unconstrained deformation at the surface causes grains to displace in a direction normal to the surface, which increases the overall surface area. Stoudt and Ricker

[56] carried out a tensile experiment with AA5052 alloy and showed that the roughening rate ($dR_a/d\varepsilon_{pl}$) is dependent on grain size, and pointed out that the surface roughening of a polycrystalline material is a highly complex process resulting from multiple deformation mechanisms. On the other hand, most metal forming processes are strain constraint processes such as rolling and compression. In these processes, when the tool makes contact with the workpiece, it is practically a process of surface asperity flattening. Wilson et al. [11, 69,] investigated the effect of bulk plasticity on asperity flattening when the lay of the roughness is parallel to the bulk straining direction (longitudinal roughness). They found that the rate of asperity flattening with bulk straining was related to the spacing and pressure of asperities. Makinouchi et al. [12] used elastic-plastic finite element solutions for the case of transverse roughness. Wilson and Sheu [69] also found a large increase in the contact area with bulk strain and a reduction in the load needed for bulk yielding. Sutcliffe [13] tested and developed Wilson and Sheu's theories and pointed out that the high pressure between contacting asperities and deformation of bulk material affects asperity deformation. Dieter [14] found that inhomogeneous deformation mechanisms that generate surface roughening also initiate localised strains that induce necking, tearing, or wrinkling in the component during the forming process. Wilson [15] also points out that inhomogeneous deformation can accelerate die wear by increasing the friction and abrasion between the metal sheet and die faces. Groche et al. [16, 17] analysed the surface evolution caused by contact loading in a 2D-plane strain finite element (FEA) model and established a correlation between the surface topology, grain size, and surface evolution.

However, there are few reports of the interaction between surface asperity flattening (roughness), texture, and grain orientation. In the previous work we analysed the relationship between surface asperity flattening, friction [189] and grain size [190] by 2D and 3D crystal plasticity finite element simulation [216]. In order to figure out the relationship between surface asperity flattening, texture and grain orientation of the sample, uniaxial planar compression has been carried out with a INSTRON 8033 Material Testing Machine with different deformation conditions (reduction) and friction conditions (with and without lubricant). Because aluminium has a high

multiaxial ductility, a light aluminium 6061 alloy was selected as the experimental material in the study. After compression, surfaces of the samples were measured by AFM and the microstructure along the transverse direction was measured by FEG-SEM 7100F. The experimental results show that the surface asperity of the workpiece tends to decrease and strain hardening increases with an increase in the gauged reduction. Lubrication can constrain the surface asperity flattening process. It was also obtained from an analysis of the microstructure that certain crystallographic orientation ([111]) of near surface grains plays a significant role in the development of surface roughness. In-grain slip plays a main role in the development of surface microstructure. A few transgranular slips occurred under a gauged reduction of 60 %.

7.2 Experimental

7.2.1. Equipment and sample preparations

Samples of 6061 aluminium (10 mm×10 mm×6.3 mm, as shown in Figure 4.7) were fully annealed (450 °C for 2 hours) and then, all the samples were constrained in a transverse direction in a channel die. To reduce the influence of tool surface and shape, the compression tool was smoothly polished (average arithmetic roughness R_a is about 10-20 nm) and flat. The rough surface was generated according to the same method in Chapter 6. Before compression, all the samples were ground and polished to about 0.7 μm by an automatic grinding and polishing machine. Before compression, the measured area was marked to ensure it could be tracked after compression. The surface roughness errors for different samples were less than 0.05 μm. The compression schedule is shown in Table 7.1. The deformation ranges are from 0 to 60 %. The compression equipment of channel die includes a compression mould and tool (Figures 4.7). The compression test was carried out by INSTRON 8033 MTS. Strain rate is about 0.001 s^{-1}. Lubrication applied in this study is molly bond, a solid lubricant which is a black cream-like lubricant.

Table 7.1 Parameters for compression

Samples	Height (mm)	Reduction (%)	Strain rate (s^{-1})	Displacement rate (mm/min)	Displacement (mm)	Height after compression (mm)
1	6.3	10	0.001	-0.359	0.63	5.67
2	6.3	20	0.001	-0.339	1.26	5.04
3	6.3	40	0.001	-0.296	2.52	3.78
4	6.3	60	0.001	-0.248	3.78	2.52

7.2.2. Testing of AFM (Atomic Force Microscope) and Vickers hardness

a) AFM test (Atomic Force Microscope)

3D surface topology was measured by a Dimension 3100 Scanning Probe Microscope (SPM). Surface asperity maps were scanned by contact mode with the following parameter setting: scan size of 60.00 μm, scan rate of 1.00 HZ, Data type of height, data scale of 5.716 μm and resolution of 512.

b) Vickers hardness test

The Vickers hardness of samples under different reductions has been carried out by the LECO M-400-H1 Microhardness Tester. The hardness tester is shown in Figures 4.13 and 4.15. The hardness can be calculated by Equation (4.10) [179].

7.2.3. Testing of EBSD

Atomic Force Microscope (AFM) and Electron Back-Scattering Diffraction (EBSD) are applied to analyse the relationship between the surface asperity feature and surface texture. The measuring map of cold-planar compressed sample was analysed by the method shown in Ref [220]. Low-angle grain boundary (LAGB) is defined as $2°\leq\theta<15°$ where θ is the angle of grain orientation spread. High-angle grain boundary (HAGB) is defined as $15°\leq\theta\leq62.8°$. The threshold of subgrain is 2°. Before and after compression, the surface morphology and roughness of the sample

were measured in the same area by AFM. The measuring map has a range of 60 μm ×60 μm and data resolution of 512. EBSD was conducted at the mid-section of the normal direction (ND)-rolling direction (RD) samples (as shown in Figure 7.1), step sizes of 0.5 and 0.25 μm were used for the different reduction samples. The EBSD acquisition of mapping is detailed in Ref. [220].

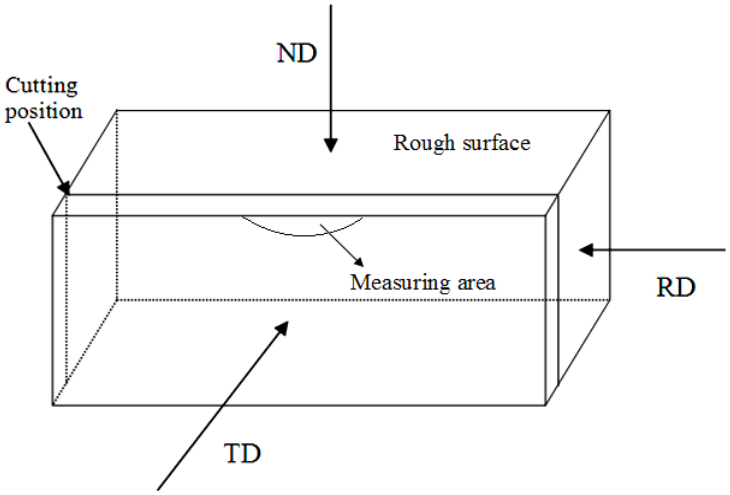

Figure 7.1 Schematic of EBSD sample

7.3 Results and discussion

7.3.1 Analysis of surface roughness and hardness

A blue line was drawn through the surface nodal coordinates (Figure 7.2) [177] and assumed to be the smooth surface after compression, therefore, the average roughness R_a, is determined from Equations (5.18) and (5.19). The development of surface morphology under different reductions is shown in Figure 7.3. There is an obvious tendency that, with an increase of gauged reduction, the surface asperity (surface roughness) tends to be flattened. Deformation of surface asperity flattening includes deformation of the contact zone of surface asperity and the no contact area of the sample. At first, when an external load is applied onto the surface, deformation (including elastic deformation and relatively low plastic deformation) occurs at the contact zone of surface asperity. When deformation takes place, the contact zone of surface asperity decreases from a previous $d+\delta$ to δ. At the same time, deformation

will occur at the non contact area of the sample. If the reduction is small (20 %), deformation of the surface asperity contact zone is shown in Figure 7.3. Under the same reduction there was no significant increase of average Vickers hardness, but after annealing heat treatment, the average Vickers hardness was about 30 HV. Under a reduction of 20 %, the average Vickers hardness was about 34 HV (Figure 7.4). Strain hardening is not obvious, and the deformation mainly concentrates on the contact area of surface asperity (ridge and valley areas) [189]. With an increase in reduction (30 and 40 %), surface asperity flattening will become obvious, as shown in Figure 7.3, and fundamentally, the tool will flatten the surface, although friction between the tool and the sample. Surface slip leads to surface scratches in the area where the contact stress is large and metal flow in different areas is very different. The strain hardening is also significant. As shown in Figure 7.4, the average Vickers hardness increases from 34 to 45 HV (reduction 40 %) and 57 HV (reduction 60 %). Lubrication can constrain the surface asperity flattening [189], as shown in Figure 7.3. Under the same reduction, the sample compressed with lubrication (molly bond) was rougher than the sample compressed without lubrication.

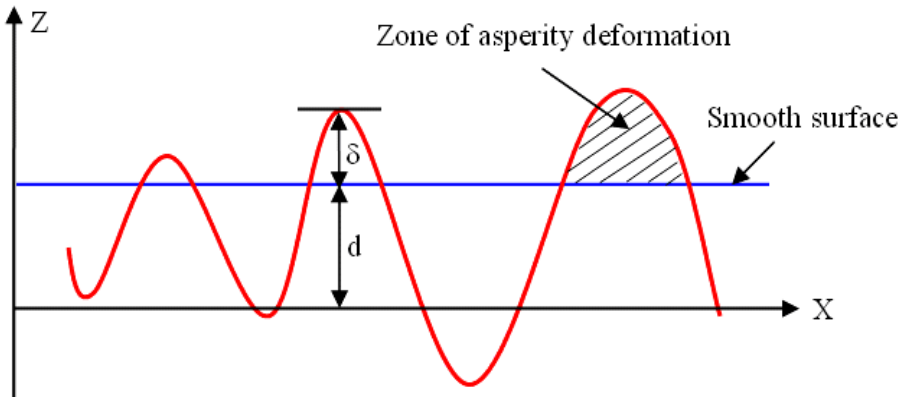

Figure 7.2 Schematic of surface asperity deformation [177]

Reduction	Without lubrication	With lubrication
Original surface	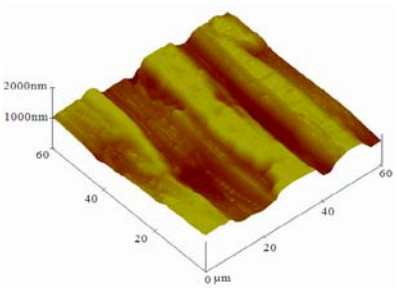	
10 %	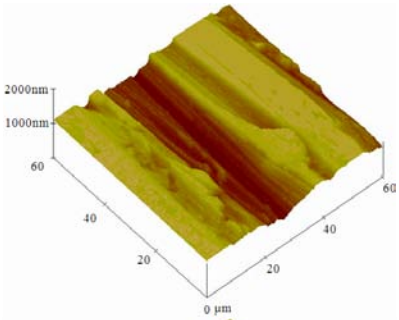	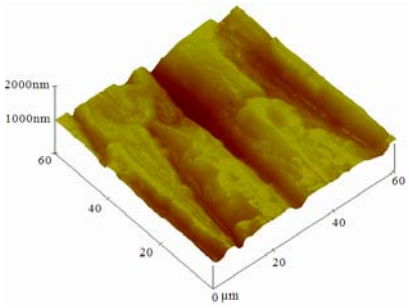
20 %	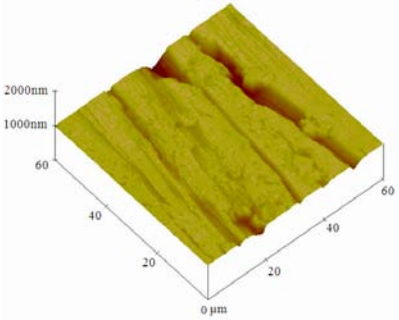	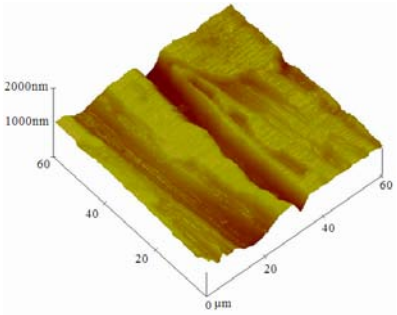
30 %	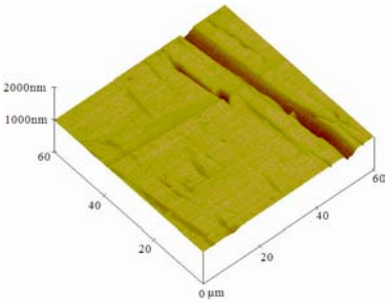	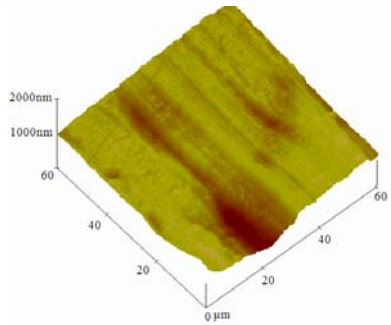
40 %	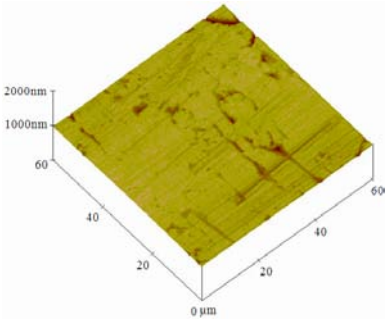	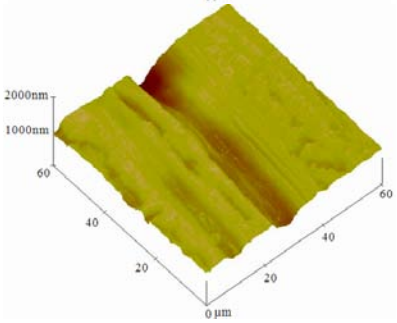

Figure 7.3 Development of surface asperity under different reductions, with and without lubrication

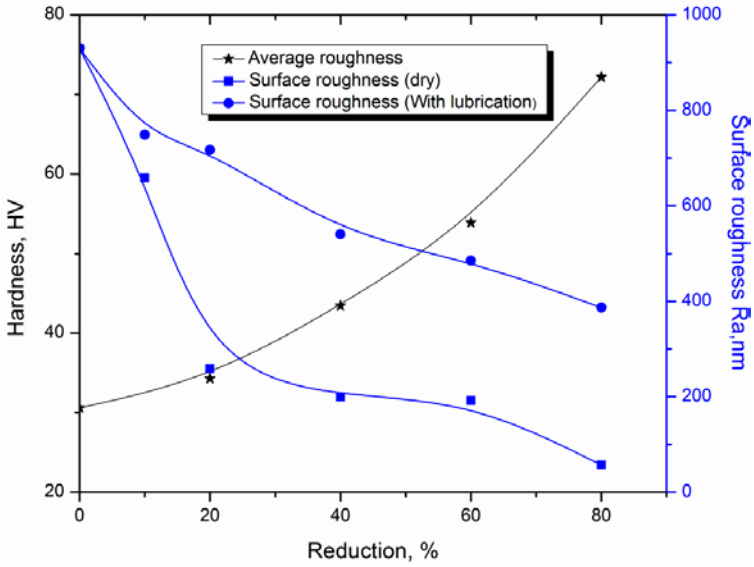

Figure 7.4 Hardness development and influence of lubrication on roughness

7.3.2. Analysis of microstructure

Figure 7.5(a) and (b) depict the inverse pole figure (IPF) and colour mapping of microstructures measured by EBSD of FEG-SEM (scale 200 μm). After annealing heat treatment, the microstructures of samples are the equiaxed grains with a grain size of about 26 μm (Figure 7.5(a)). Most grains orientate in the orientation of [001], which is shown in red, while other grains orientate in the orientation of [101] as shown in green. The lamellar grain shapes which are thinner due to an extra reduction (60 %) having a grain size smaller than 3.6 μm (Figure 7.5(b) and (c)). The density of deep blue area increases significantly, in which grain has [111] orientation. These areas also have a high intensity of dislocation. In-grain shear bands are present and typically inclined at 15-35° to the RD [220]. As a result of higher total dislocation densities, the cold-uniaxial-planar-compressed sample contained a higher area fraction of in-grain shear bands. On the other hand, a few transgranular shear bands also appear in area A, as shown in Figure 7.5(b), which is about 4-5 grains distance away from the ND (Normal Direction) surface. Dislocation in this area was the most intense, which prompted an increase of internal energy of accumulated dislocation, and can thus overcome the obstacle of a grain boundary. Therefore, dislocation can spread across the grain boundaries. The original grains are broken into new grains. Practically, some HAGBs form in area B (Figure 7.5(c)).

This confirms the result that the shear banding is preceded by the formation of obstacles to the homogeneous dislocation glide in the grain [221]. Under a reduction of 60 %, the surface roughness of the sample decreased from an original 930 to 192 nm, and hardness increased from 30 to 57 HV. Furthermore, localised surface strains commenced at this hardening area. This observation confirms the prediction of Hill [222] and Asaro [223] that the shear banding develops according to instability in the macroscopic constitutive description of the inelastic deformation of hardening material. By using a different experimental method, Aicheler et al. [196] also found that on the top surface of RFF (Radio-Frequency-heating Fatigue) FCC (face-centred cubic) copper, regions of [111] orientation have highly developed surface features), while regions of [100] do not have significantly developed surface features. Figure 7.5(c) shows a few twinned areas (60°<111> Σ3 twin) of the same sample under a reduction of 60 %. Area B is an obvious twinned area. Area B (Figure 7.5(c)) and Area A (Figure 7.5(b)) are almost similar. Therefore, the twinned area is not from annealed heat treatment (annealed twins), but generated from compression deformation (deformation twins). However, as the deformation twins have a small volume fraction, they will not have a volume effect on texture evolution [224]. The influence of deformation twins on the development of surface asperity is also not significant. On the other hand, the hardening resulting from the transgranular shear banding of deformation twins is also not very large. It only increased from 30 HV (0 %) to 57 HV (60 %).

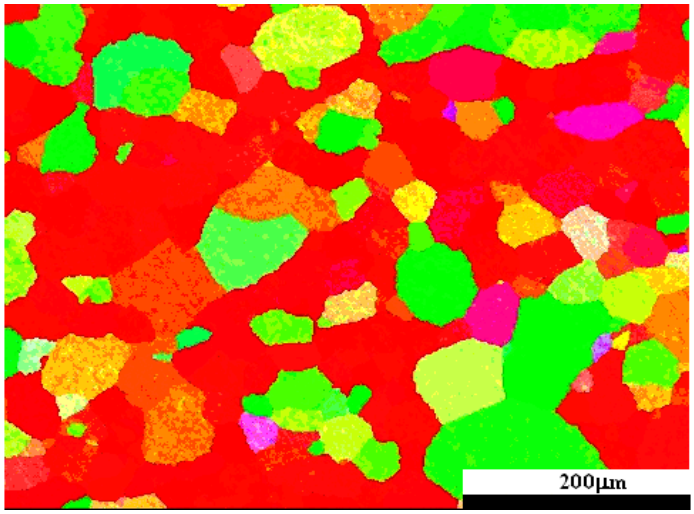

(a)

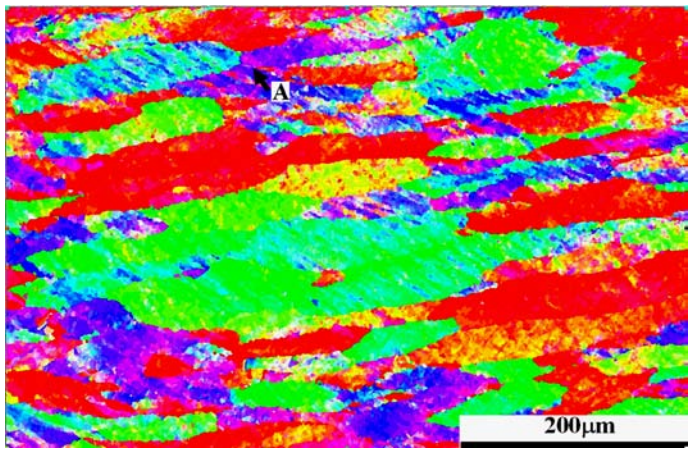

(b)

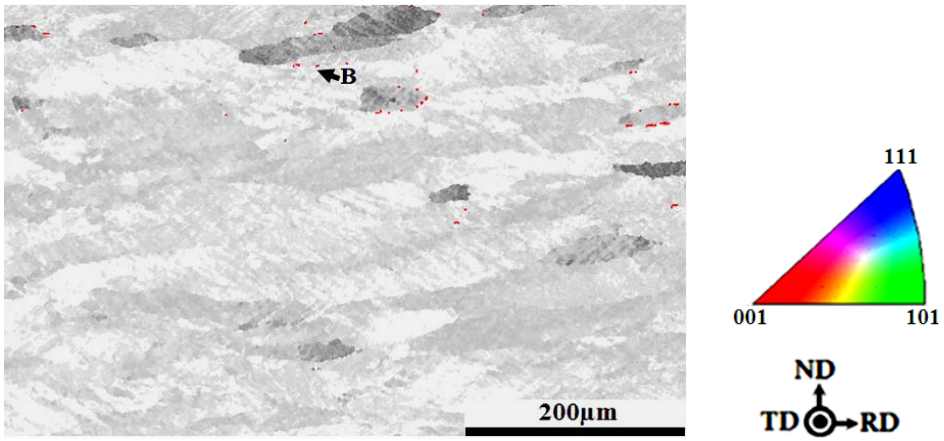

(c)

Figure 7.5 Microstructures of FEG-SEM micrograph (a) annealed microstructure IFP, (b) aluminium IFP (cold reduction 60 %), and (c) slip (Schmid factor) and <111> 60° twin (cold reduction 60 %), LAGBs ($2° \leq \theta < 15°$)=grey, HAGBs ($15° \leq \theta \leq 57.5°$) =black and 60°<111> Σ3=red lines. Contour level: 0.5×.

7.3.3 Analysis of ODF figure

Orientation Distribution Function figures under different reductions in $\phi_2 = 0$ and 45° sections describe the developing tendency of the deformed texture (Figure 7.6). Figure 7.6(a) shows the texture component after annealed heat treatment. Orientation C (cubic orientation {001}<100>) has a high intensity in the fully annealed sample. With an increase in reduction (at room temperature), the intensity of orientation C decreases while the texture component, orientation G (Goss orientation {001}<110>)

becomes obvious (Figure 7.6(b)). When reduction is about 40 %, the intensity of Goss orientation {001}<110> tends to be much stronger. Simultaneously, a few new texture component B (brass orientation {110}<112>) appears (Figure 7.6(c)). As shown in Figure 7.6(d), Goss orientation has the highest intensity which is opposed to that of cubic orientation, while brass orientation {110}<112> becomes much stronger and obvious. This observation agrees with the cold rolling deformation of aluminium [167, 225]. Under a reduction of 60 %, a few transgranular shear bands appear that are resulted from deformation twins (Figure 7.6(a) and (c)). Therefore, the formation of a shear band can be ascribed to the twinning of brass (B, {110}<112>) [224]. Under a reduction of 60 %, samples have their lowest roughness R_a. Thus, Goss orientation plays a major role in the development of surface feature (roughness R_a). Due to the small volume, the influence of brass orientation on the development of surface asperity is not significant.

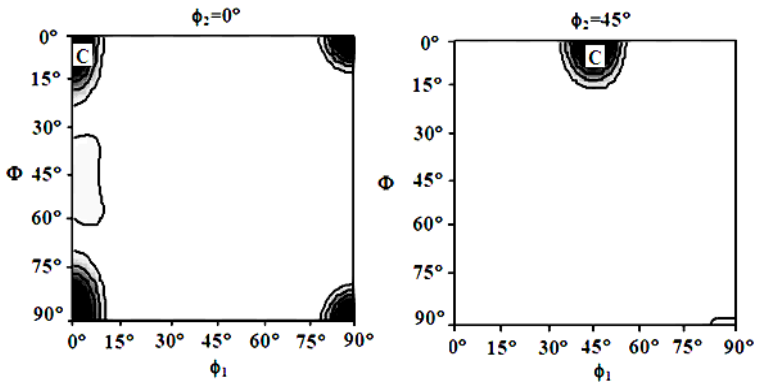

(a)

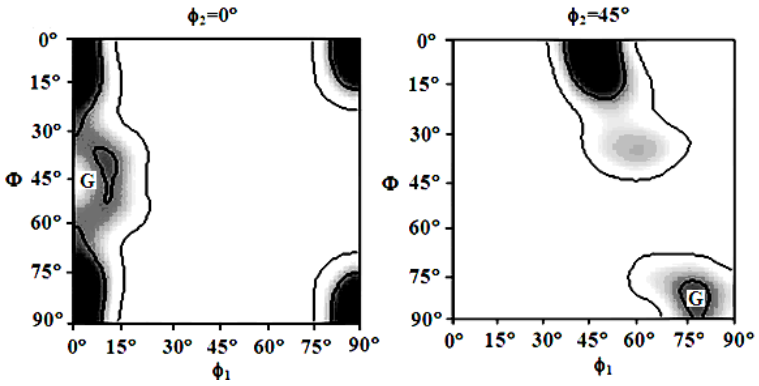

(b)

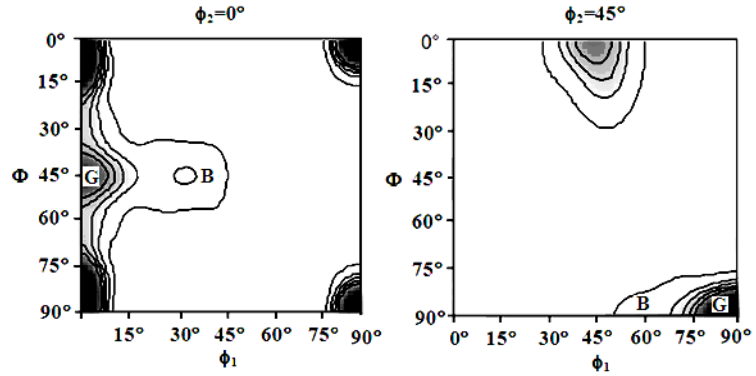

(c)

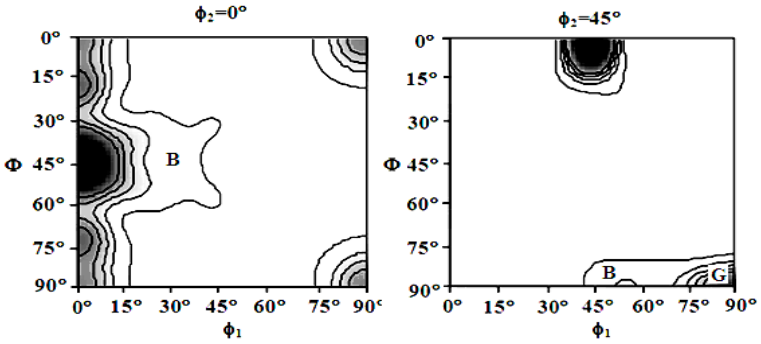

(d)

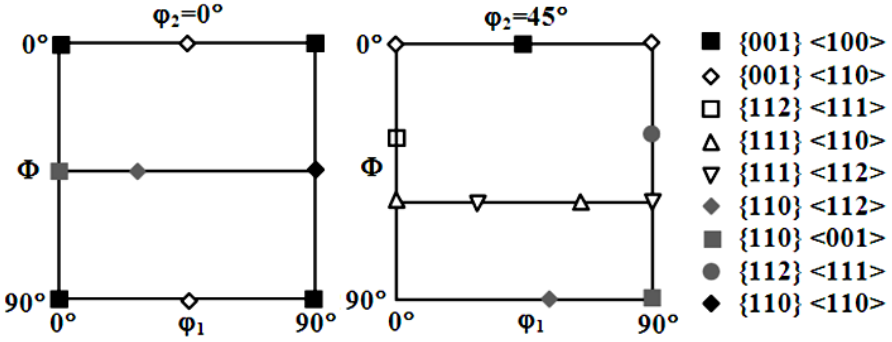

(e)

Figure 7.6 ϕ_2=0° and 45° sections of (a) annealed sample (450 °C, 2 h), (b) 20 % cold planar compression, (c) 40 % cold planar compression, (d) 60 % cold planar compression, and (e) main orientation representations. Contour levels: 0.5×.

7.3.4. Analysis of Misorientation and CSL (Coincidence Site Lattice) boundary

Misorientation of different reductions is shown in Figure 7.7(a). Deformed grains possess lower internal misorientation and stored energy. Furthermore, deformation

grains have large low-angle grain boundary (LAGB) populations and small deformation twin fractions (Σ3) [226]. Owing to the low deformation temperature (room temperature), the influence of recovery is not significant. Figure 7.7(b) shows the development of microstructure under different reductions. Due to the influence of an external load, a fraction of the deformed structure tends to reduce, while the sub-structured (θ<2°) fraction increases significantly from 1.3 to 18. With the increase in reduction, a fraction of the recrystallised structure almost keeps the same value. This observation indicates that at room temperature, there is no obvious dynamic recovery taking place in the deformed Al sample. Under small reductions, dislocation accumulates and tangles in grains. As a result, more substructures are formed in the deformed sample. Σ3 (60°{111}) and Σ7 (38°{111}) populations of newly nucleated and growing grains are shown in Figure 7.7(c). Populations of the lower twin boundaries are opposed to the growth of reduction. Here, twinning contributes insignificantly to the overall reduction in stored energy during deformation [227]. In-grain dislocation mobility and accumulation are the main sources of stored energy in deformation. During the surface asperity flattening process, Goss orientation has the highest intensity on the top surface of ND. Therefore, Goss orientation contributes significantly to the surface asperity flattening (surface roughness).

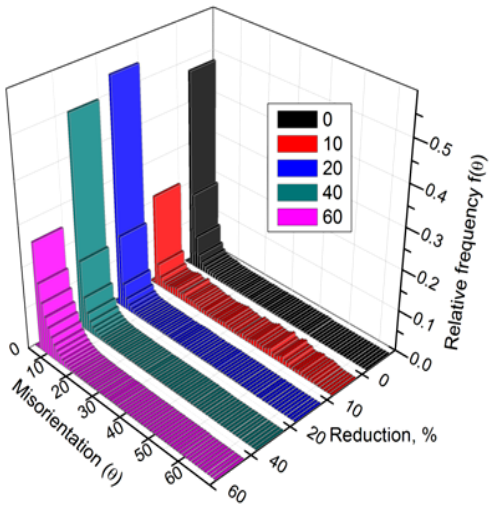

(a)

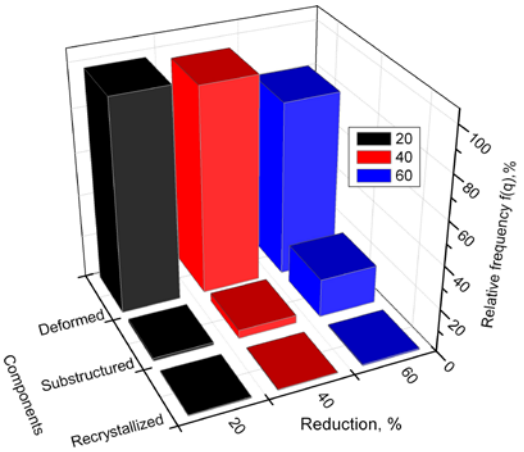

(b)

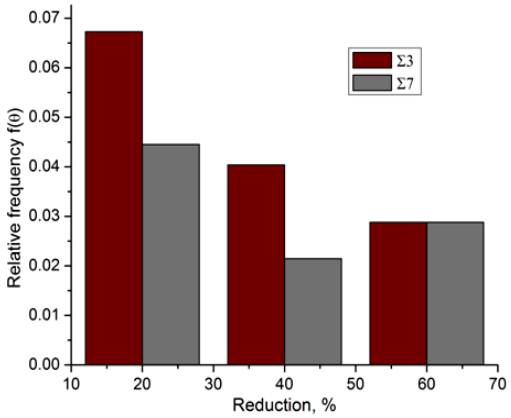

(c)

Figure 7.7 Development of related parameters of ND surface: (a) misorientation, (b) microstructure components, and (c) CSL (Coincidence Site Lattice) boundary of Σ3 and Σ7.

7.4. Conclusions

In summary, the surface asperity of a sample tends to decrease, while strain hardening increases with an increase of reduction. Lubrication can constrain the surface asperity flattening process. The dependency of a surface asperity feature on the development of surface (ND) microtexture was also analysed, while accumulated dislocation and mobility contributed significantly to the misorientation by investigating the AFM and EBSD maps of cold uniaxial planar compressed (CUPC) sample. The results show that the orientated [111] grains play an important role in the development of surface asperity. In-grain slip (local stored energy) existed under

overall reduction. However, its influence on surface asperity increases according to the increase of gauged reduction. The recovery and recrystallisation under deformation are not significant. A few transgranular shear bands that resulted from the deformation twins of brass orientation were observed.

7.5 New findings

(1) Lubrication can constrain the surface asperity flattening process: under the same reduction, a sample compressed with current solid lubricant, a molly bond that has been applied in this study has a rougher surface (higher value of R_a) than a sample without lubricant.

(2) Dislocation accumulation and mobility contribute significantly to the misorientation of an EBSD map of cold uniaxial planar compressed (CUPC) sample. Orientated [111] grains play an important role in the development of surface asperity. Recovery and recrystallisation under deformation are not significant in the CUPC process of aluminium.

(3) In-grain slip (local stored energy) exists under overall reduction. Its influence on surface asperity increases according to an increase in reduction. A few transgranular shear bands that resulted from the deformation twins of brass orientation were observed in this study.

CHAPTER 8

CONCLUSIONS AND RECOMMENDATIONS FOR FUTURE WORK

8.1 Introduction

In this present study both experimental methods and crystal plasticity finite element methods have been applied to investigate surface asperity flattening process in uniaxial planar compression. The cold compressing parameters and friction have been studied to identify their effects on the evolution of surface asperity (surface roughness). Some parameters related to the microstructures such as grain size, and grain orientation and texture, have also been considered and their influences on the evolution of surface asperity have been analysed. With this understanding of the evolution of surface asperity in uniaxial planar compression, a controlled procedure for cold uniaxial planar compression is expected to improve the surface quality of final products.

8.2 General conclusions

8.2.1 Evolution of surface asperity

Through experiments and simulation, the evolution of rough surface topology in uniaxial planar compression has been shown as a surface asperity flattening process with three obvious stages. They are:

1) In first stage plastic deformation takes place in the elastic aggregate (reduction is less than 10 %). Elastic deformation plays an important role in the evolution of surface asperity. Plastic deformation takes place in an aggregate of elastic deformation. Surface roughness decreases greatly according to the increase in reduction.
2) In the second stage, when reduction exceeds 10 %, the influence of plastic deformation on surface asperity will obviously increase while the influence of elastic deformation will significantly decrease. With an increase in reduction, surface roughness will continue to decrease, but compared to the first stage, the rate of surface asperity flattening decreases. The relationship between the surface roughness and reduction is non-linear.
3) In the third stage, when the reduction exceeds 40 %, the rate of surface asperity flattening will decrease significantly, but in comparison to the former two stages, this stage has the lowest rate of flattening. With an increase in reduction the surface roughness (R_a) has no significant decrease, but plastic deformation occurs in this stage, and a certain texture will be formed, and a balance of surface roughness and texture will be obtained.

8.2.2 Effects of deformation parameters on the evolution of surface asperity

Effects of some deformation parameters on surface asperities (surface roughness) were investigated and the following results were obtained:

1) The effect of lubrication (friction) on the evolution of surface asperity is very complicated, but like the evolution of surface asperity, it also has three similar stages. When reduction is less than 10 %, the lubrication has no obvious influence on surface roughness. In the first stage, elastic deformation plays a major role on surface asperity, but when the reduction is at a certain range (in this study between 10 and 40 %), lubrication can significantly limit surface asperity flattening. In the second stage, the layer of lubrication between the sample and tool continues to play its role very well, but when reduction exceeds 40 %, the lubrication will be dissipated during uniaxial planar compression and play no obvious role in the

evolution of surface asperity. In a word, lubrication can constrain the surface asperity flattening process.

2) Compared to the tensile test, the relationship between the surface roughness and strain in uniaxial planar compression is different and more complicated. In a tensile test, the variation of surface roughness R_a is proportional to the applied strain. However, in the uniaxial planar compression test the relationship between the surface roughness and strain is non-linear according to the influence of the compression tool and friction between the sample and tool. Both tests agreed with the same rule: with an increase in reduction, both the arithmetic average surface roughness R_a and root mean squared surface roughness R_q decrease.
3) Different wavelength components also affect the surface roughness. In the simulation, with an increase in reduction, the influence of longer wavelengths on the sample roughness decreased quickly, whereas the shorter wavelength increased the surface asperity significantly.
4) In uniaxial planar compression the influence of the strain rate on surface asperity flattening can be divided into two stages: elastic deformation and plastic deformation. In elastic deformation, the strain rate has no significant influence on the evolution of surface asperity, but in plastic deformation, the influence of the strain rate on surface asperity flattening is significant.
5) The mechanism of the effect of strain rate on surface asperity flattening in uniaxial planar compression has been analysed, and the relationship between the macroscopic strain rate and shear rate of a slip system has been investigated. In uniaxial planar compression, it is linear, and the strain rate plays its role by the shear rate of the slip system. Therefore, the strain rate increases, and the surface roughness also increases.
6) Flow stress of samples increased significantly according to an increase in the gauged reduction,
7) With an increase in reduction, the Vickers hardness tends to increase. During compression, the ridge areas make contact with the tool first, and then the valleys, which means the ridges were harder than the valleys under the same reduction.

8) Influence of the strain rate on Vickers hardness included two stages. At a lower strain, an increasing strain rate can result in a higher hardness, while at a larger strain (60 %) this tendency is reversed: an increasing strain rate leads to a lower hardness. Under the same reduction, an increasing strain rate can lead to a higher flow stress in uniaxial planar compression.

8.2.3 Relationship between microstructures and surface asperity

In uniaxial planar compression, the relationship between microstructures (grain size, texture and grain orientation) and surface asperity were studied by experiment and simulation. The following results were obtained:

1) Grain stress is related to grain rotation, i.e., grains with higher stresses also have larger rotations of Euler angles in compression.
2) With an increase in reduction the grain size tends to decrease and the texture tends to be strong and obvious. All the grains of the sample will slip along a certain direction and slip plane (<110> slip directions and {111} slip plane). The simulation shows that with an increase of reduction the cubic texture {001}<100> is weak while the brass orientation {110}<112> becomes strong. With an increase of reduction, the Schmid factor (also called “orientation hardness”) of surface area will shift from “hard” to “soft”.
3) When reduction exceeds 40 %, the in-grain shear band appears in some grains, which are 4-5 grains away from the edge, and the localised strain begins in this area. When reduction exceeds 60 %, most grains have plastic slips. A few transgranular shear bands resulting from the deformation twins of brass orientation were observed in the surface area.
4) The grain size also has a significant influence on surface roughness. Under the same reduction, the surface roughness of the sample with a large grain size tends to decrease more slowly, but after compression the sample with the maximum size grain had the maximum surface roughness. Both tensile and compression tests show that the relationship between the surface roughness and average grain size is non-linear. The surface roughness R_a is a power exponent function of grain size.

5) Grain size also has a significant influence on the sample's stress: with an increase in grain size, the sample's stress increases accordingly. In the uniaxial compression test, the grain orientation also plays an important role in the evolution of surface asperity. The relationship between the surface roughness and grain orientations (Euler angles) has been obtained from the simulation, and is a non-linear relationship.
6) Surface roughness shows obvious sensitivity to the orientations of grains near the surface. In this study, the oriented {111} grains are the main source of localised strain. Dislocation accumulation and mobility contribute significantly to the misorientation of the EBSD map of the cold uniaxial planar compressed (CUPC) sample.
7) Recovery and recrystallisation under deformation are not significant in the CUPC process of aluminium. In this study, the results show that the strain rate has no obvious influence on evolution of texture.

8.2.4 Crystal plasticity finite element analysis

The initial data of the sample's surface roughness, friction and microstructures (texture, grain orientation) have been included in the 2D and 3D crystal finite element models, and after a numerical simulation, the following results have been obtained:

1) Three stages in the evolution of surface asperity have been successfully predicted, and the relationship between the surface roughness and reduction has also been identified.
2) The tendency for texture from simulation result is the same as that from the experimental one. Brass orientation has also been successfully predicted. The influence of the strain rate on the evolution of surface asperity from the simulation is the same as from the experimental results.
3) Influence of lubrication (friction) on surface asperity has been simulated successfully, and the influence of grain size on the evolution of surface asperity has also been simulated well.

4) The relationship between the reduction and stress was predicted, and the influence of the strain rate on the flow stress has also been determined.
5) The influences of different wavelengths on the evolution of surface asperity have been successfully discussed, and the influence of the strain rate on the evolution of surface asperity as well.

8.3 Future work

The evolution of surface asperity plays an important role in the quality of metal forming products. Understanding how they evolve and what factors affect them can provide substantial information for controlling their evolution in cold uniaxial planar compression and also improve the surface quality. In this present study, the relationships between deformation parameters (reduction and strain rate), initial surface roughness (different wavelength components), friction state, microstructures (grain size, texture and grain orientation), and evolution of surface asperity have been studied in the FCC (face centred crystal) metal. On the basis of these experimental results, crystal plasticity finite element modelling was conducted. Based on this current research, the author suggests that future work may include the following:

- BCC (body centred crystal) metals and Hexagonal close-packed (HCP) metals such as magnesium (Mg) will the investigated in uniaxial compression with different deformation parameters, friction state and microstructures.
- The rolling process will be the focus of the evolution of surface asperity.
- Effect of the compression tool on the surface asperity evolution of the sample initial surface roughness should be discussed, although there may be some difficulties with simulation.
- Other lubricants should be used to study the effect of lubrication on the evolution of surface asperity.
- High temperature deformation processes are also needed to analyse the influences of temperature and oxidation on surface asperity transfer.
- Crystal plasticity constitutive model will be revised and modified for high

temperature deformation processes.

- 3D EBSD mapping by the FIB (Focus Ion Beam) technique will be a good method to show the practical development of surface microstructure in three dimensions.
- Practical microstructures should be incorporated into the 2D and 3D crystal plasticity finite element models to accurately simulate the surface deformation process.
- Further discussion on size effect of the workpieces should be carried out.

REFERENCES

[1] http://en.wikipedia.org/wiki/Surface_roughness/Amplitude_parameters [Accessed 8 June 2011].

[2] E.P. Degarmo, J.T. Black, and R.A. Kohser, Materials and Processes in Manufacturing (9th ed.), Wiley, (2003).

[3] O.A. Den, J.F. Kaashoek, and H.R.G.K. Hack, Difficulties of using continuous fractal theory for discontinuity surfaces, International Journal of Rock Mechanics and Mining Science & Geomechanics Abstracts, Vol. 32 (1) (1995). pp. 3-9.

[4] D. Raabe, M. Sachtleber, H. Weiland, G. Scheele, and Z.S Zhao, Grain-scale micromechanics of polycrystal surfaces during plastic straining, Acta Mater., Vol. 51 (2003), pp. 1539-1560.

[5] K. Osakada, and M. Oyane, On the roughing of free surface in deformation process, Bulletin of J.S.M.E., Vol. 14 (1971), pp. 171-177.

[6] M. Tokizawa, and Y. Yosikawa, The mechanism of lubricant trapping under the cold compression of metals, J.Jpn. Inst. Met., Vol. 37 (1973), pp. 19-25.

[7] G. Chen, H. Shen, S. Hu, and B. Baudelet, Roughening of the free surfaces of metalic sheets during stretching forming, Mat. Sci. Eng A., Vol. 128 (1990), pp. 33-38.

[8] R. Becker, Effect of strain localization on surface roughening during sheet forming, Acta Mater., Vol. 46 (1998), pp. 1385-1401.

[9] M.R. Stoudt, and R.E. Ricker, The Relationship between grain size and the surface roughening behaviour of Al-Mg alloys, Metallurgical and Materials Transactions A, Vol. 33 (2002), pp. 2883-2889.

[10] S. Sheu, and W.R.D. Wilson., Flattening of workpiece surface asperities in metal forming, Proc. 11. N.A.M.R.C., (1983), 172-178.

[11] W.R.D. Wilson, and W.M. Lee, Mechanics of surface roughening in metal forming process, J. Manuf. Sci. Eng., Vol. 123 (2001), pp. 279-283.

[12] A. Makinouchi, H. Ike, M. Murakawa, and N. Koga, A finite element analysis of flattening of surface asperities by perfectly lubricated rigid dies in metal working processes, Wear, Vol. 128 (1988), pp. 109-122.

[13] M.P.F. Sutcliffe, Surface asperity deformation in metal forming processes, Int. J. Mech. Sci., Vol. 11 (1988), pp. 847-868.

[14] G.E. Dieter, Mech. Metall. 3rd McGraw-Hill, New York, NY (1986).

[15] W.R.D. Wilson, Tribology in Cold Metal Forming, J. Manu. Sci. Eng., Vol.119 (1997), pp. 695-698.

[16] P. Groche, R. Schafer, H. Justinger, and M. Ludwig, On the correlation between crystallographic grain size and surface evolution in metal forming processes, Int. J. Mech. Sci., Vol. 52 (2010), pp. 523-530.

[17] P. Groche, R. Schafer, and M. Henning, Finite element calculation of surface Evolution considering grain size and crystallographic texture effects, Proc. ICTMP2007.Yokohama: Yokohama National University, (2007) pp. 219-226.

[18] O. Kienzle, and K. Mietzner, Grundlagen einer Typologie umgeformter metallischer Oberflachen mittels Verfahrensanalyse, Springer, Berlin, (1965).

[19] K. Osakada, and M. Oyane, On the roughing of free surface in deformation process, Bulletin of JSME., Vol. 14 (1971), pp. 172-176.

[20] E. Dannenmann, Techn. Mitt., Vol. 73 (1980), pp. 893-901 (German).

[21] J.A. Schey, Lubric. Eng., Vol. 39 (1983), pp. 376-382.

[22] O. Kienzle, and K. Mietzner, Atlas umgeformter metallischer Oberflachen, Springer, Berlin, 1967.

[23] http://en.wikipedia.org/wiki/Friction [Accessed 14 February 2011].

[24] J.A. Schey, Tribology in Metalworking, American Society for Metals (1983).

[25] M.C. Shaw, in Fundamentals of Deformation Processing, Syracuse University Press (1964).

[26] J. Halling, Principles of Tribology, Macmillan, London (1975).

[27] P.P. Bowden, and D. Tabor, The Friction and Lubrication of Solids, Clarendon Press, Oxford, Pt. I, 1950, and Pt, II 1964.

[28] T. Wanheim, and N. Bay, Model for friction in metal forming processes Ann. CIRP., Vol. 27 (1978), pp. 189-194.

[29] I.F. Collins, Geometrically self-similar deformations of a plastic wedge under combined shear and compression loading by a rough flat die, Int. J. Mech. Sci., Vol. 22 (1980), pp. 735-742.

[30] S. Ishizuka, J. JSLE (Int. Ed), Vol. 1 (1980), pp. 33-38.

[31] P.K. Gupta, and N.H. Cook, Junction deformation models for asperities in sliding interaction, Wear, Vol. 20 (1972), pp. 73-87.

[32] J.E. Williams, An asperity interaction machining theory of friction, Wear, Vol. 56 (1979), pp. 363-375.

[33] J.M. Challen, and P.L.B Oxley, An explanation of the different regimes of friction and wear using asperity deformation models, Wear, Vol. 53 (1979), pp. 229-243.

[34] P.L.B. Oxley, Metallic friction under near-seizure conditions, Wear, Vol. 65 (1980), pp. 227-241.

[35] J.A. Schey, in Proc. 4th NAMRC, SME, Dearborn, 1976, pp. 108-114.

[36] J.A. Schey, in Metal forming Plasticity, H. Lippmann (ed.), Springer, Berlin, 1979, pp. 336-348

[37] M.B. Peterson, and F.F. Ling, Frictional behavior in metalworking processes, Trans. ASME, Ser.F, J. Lub. Tech., Vol. 92 (1970), pp. 535-542.

[38] T. Kayaba, and K. Kato, Experimental analysis of junction growth with a junction model, Wear, Vol. 51 (1978), pp. 105-116.

[39] R. Bartram, M. lung, and O. Mahrenholz, arch. Eisenhuttenw., Vol. 41 (1970), pp. 969-973.

[40] D.V. Wilson, W.T. Roberts, and P.M.B. Rodrigues, Effect of Grain anisotropy on limit strains in biaxial stretching: part i. influence of sheet thickness and grain size in weakly textured sheets, Metall Trans A., Vol.12 (1981), pp. 1603.

[41] G.J. Baczynski, and R. Guzzo, Development of roping in an aluminium automotive alloy AA6111, Acta Mater., Vol. 48 (2000), pp. 3361-3376.

[42] C. Messner , C. Oberndorfer, E.A. Werner, Surface roughness of duplex steels: role of the microstructure, Computational Materials Science, Vol. 32 (2005), pp. 455-462.

[43] J. Grum, M. Kisin, Influence of microstructure on surface integrity in turning-part I: the influence of the size of the soft phase in a microstructure

on surface-roughness formation, International Journal of Machine Tools & Manufacture, Vol. 43 (2003), pp. 1535-1543.

[44] A.I. Morosov, I.A. Morosov, A.S. Sigov, Magnetic structure inhomogeneites near the surface of uniaxial antiferromagnet: ‘‘Magnetic field–roughness’’ phase diagram, Journal of Magnetism and Magnetic Materials, Vol. 310 (2007), pp. 2170-2171.

[45] K. Yamaguchi, N. Takakura, and S. Imatani, Increase in forming limit of sheet metals by removal of surface roughening with plastic Strain. J. Mater. Process. Technol., 1995, Vol. 48 (1995), pp. 27-34.

[46] M. Jain, D.J. Lloyd, and S.R. Macewen, Surface roughness and biaxial tensile limit strains of sheet aluminium alloys, Int. J. Mech. Sci., 1996, Vol. 38 (1996), pp. 219-232.

[47] N. Kawai, T. Nakamura, and Y. Ukai, Surface roughing mechanism of polycrystalline metal sheet during plastic deformation, Bulletin of JSME, Vol. 29 (1986), pp. 1337-1343.

[48] Y.Z. Dai, and F.P. Chiang, On the mechanism of plastic deformation induced surface roughness, Trans. of the ASME, Vol. 114 (1992), pp. 432-438.

[49] P.F. Thomson, and P.U. Nayak, The effect of plastic deformation on the roughing of free surfaces of sheet metal, Int. J. Mech. Sci., Vol. 20(1980), pp. 73-86.

[50] R. Mahmudi, and M. Mehdizadeh, Surface roughening during uniaxial and equibiaxial stretching of 70-30 brass sheets, J. Mater. Process. Technol., Vol. 80-81 (1998), pp. 707-712.

[51] D.V. Wilson, W.T. Roberts, and P.M.B. Rodrigues, Effects of grain anisotropy on limit strains in biaxial stretching: Part 1. Influence of sheet thickness and grain size in weakly textured sheets, Metall. Trans A., Vol. 12 (1981A), pp. 1595-1602.

[52] D.V. Wilson, W.T. Roberts, and P.M.B. Rodrigues, Effects of grain anisotropy on limit strains in biaxial stretching: Part 2. Sheets of cubic metals and alloys with well-developed preferred orientations, Metall. Trans A., Vol. 12 (1981B), pp. 1603-1611.

[53] M.Y. Huh, and O. Engler, Effect of intermediate annealing on texture, formability and ridging of 17%Cr ferritic stainless steel sheet, Mater. Sci. Eng., A Vol. 308 (2001), pp. 74-87.

[54] O. Engler, and J. Hirsch, Texture control by thermomechanical processing of AA6xxx Al-Mg-Si sheet alloy for automotive applications-a review, Mater. Sci. Eng., A Vol. 336 (2002), pp. 249-262.

[55] H. Ji, and G.S. Was, Linkage between crystallographic texture and surface roughness in niobium films synthesized by ion beam assisted deposition, Instr. and Meth. in Phys. Res. B., Vol. 148 (1999), pp. 880-888.

[56] M.R. Stoudt, and R.E. Ricker. The Relationship between Grain Size and the Surface Roughening Behaviour of Al-Mg Alloys, Mater. Trans. A., Vol. 33 (2002), pp. 2883-2889.

[57] M.R. Stoudt, and R.E. Ricker. in Innovations in Processing and Manufacturing of Sheet Materials, M. Demeri, ed., TMS, Warrendale, PA, (2001).

[58] Aluminium Standards and Data 1988, 9th ed., The Aluminium Association, Washington, DC, 1988.

[59] Properties and Selection, Nonferrous Alloys and Pure Metals, 9th ed. ASM INTERNATIONAL, Metals Park, OH (1979).

[60] X.Q. Wang, A.B.E Takeji, T. Naoya, and S. Ichiro, Microscopic surface Change of Polycrystalline Aluminium during Tensile Plastic Deformation, Memoirs of the Faculty of Engineering, Okayama University., Vol. 39 (2005), pp. 7-15.

[61] G.N. Chen, S.G. Hu, and B. Baudelet, Roughening of the Free Surface of Metallic Sheets during Stretching Forming, Mater. Sci. Eng., A Vol. 128 (1990), pp. 33-38.

[62] H. Wiegand, and K.H. Kloos, Stahl u. Eisen., Vol. 83 (1963), pp. 406-415.

[63] M. Tokizawa, and K. Yoshikawa, Bull, Jpn. Soc. Prec. Eng., Vol. 4 (1970), pp. 105-106.

[64] J.A. Schey, and A.H. Lonn, Durability of Graphite Films in Plastic Deformation, Trans. ASME, Ser.F, J.Lub. Tech., Vol. 97 (1975), pp. 289-295.

[65] J.A. Schey, and R.E. Myslivy, J. Mater. Process. Technol, Vol. 47 (1967), pp. 67.

[66] T. Mizuno, and K. Hasegawa, Trans. ASME, Ser.F, Effects of die surface roughness on lubricating conditions in the sheet metal compression-friction test, J. Lub. Tech., Vol. 104 (1982), pp. 23-28.

[67] P.S. Lee, H.R Piehler, B.L. Adams, G. Jarvis, H. Hampel, A.D. Rollett, Influence of surface texture on orange peel in aluminium, J. of Mater. Proc. Tech., Vol. 80-81 (1998), pp. 315-319.

[68] N.J. Wittridge, and R.D. Knutsen, A microtexture based analysis of the surface roughening behaviour of an aluminium alloy during tensile deformation, Materials Sci. Eng., A Vol. 269 (1999), pp. 205-216.

[69] S. Sheu, and W.R.D. Wilson, Flattening of workpiece surface asperities in Metal forming Proc. NAMRC XI, (1983), pp. 172-178.

[70] W.R.D. Wilson, and S. Sheu, Real area of contact and boundary friction in metal forming, Int. J. Mech. Sci., Vol. 30 (1988), pp. 475-489.

[71] A.J. Beaudoin, and J.D. Bryant, Analysis of ridging in aluminium auto body sheet metal, Mater. Trans. A., Vol. 29 (1998), pp. 2323-2332.

[72] H.J. Shin, J.K. An, S.H. Park, and D.N. Lee, The effect of texture on ridging of ferritic stainless steel, Acta Mater., Vol. 51 (2003), pp. 4693-4706.

[73] P.D. Wu, and D.J. Lloyd, A. Bosland, H. Jin, and S.R. MacEwen, Analysis of roping in AA6111 automotive sheet, Acta Mater., Vol. 51 (2003) pp. 1945-1957.

[74] P.D. Wu, and D.J. Lloyd, Analysis of surface roughing in AA6111 automotive sheet, Acta Mater., Vol. 52 (2004), pp. 1785-1798.

[75] H. Oktem, T. Erzurumlu, and F. Erzincanli, Prediction of minimum surface roughness in end milling mold parts using neural network and genetic algorithm, Mater. Des., Vol. 27 (2006), pp. 735-744.

[76] A.M. Zain, H. Haron, and S. Sharif, Prediction of surface roughness in the end milling machining using Artificial Neural Network, Expert Systems with Applications., Vol. 37 (2010), pp. 1755-1768.

[77] I.A. El-Sonbaty, U.A. Khashab, A.I. Selmy, and A.I. Ali, Prediction of surface roughness profiles for milled surfaces using an artificial neural network and fractal geometry approach. J. Mater. Process. Technol., Vol. 200 (2008), pp. 271-278.

[78] E. Susic, and I. GRABEC. Application of a neural network to the estimation of surface roughness from ae signals generated by friction process, Int. J. Mach. Tools Manufact., Vol. 35 (1995), pp, 1077-1086.

[79] H.K. Durmus, E. Ozkaya, and C. Meric, The use of neural networks for the prediction of wear loss and surface roughness of AA 6351 aluminium alloy, Mater. Des., Vol. 27 (2006), pp. 156-159.

[80] R. Courant, Variational methods for the solution of problems of equilibrium and vibrations, Bull Am Math Soc., Vol. 49 (1943), pp. 1-23.

[81] O.C. Zienkiewicz, The finite element method in structural and continuum mechanics. 1st ed. New York: McGraw-Hill (1967).

[82] P.R. Dawson, Computational crystal plasticity, Int. J. Solids Struct., Vol. 37 (2000), pp. 115-130.

[83] G.I. Taylor, The mechanism of plastic deformation of crystals. Part I-theoretical, Proc Roy Soc Lond A., Vol. 145 (1934), pp. 362-87.

[84] G.I. Taylor, The mechanism of plastic deformation of crystals. Part II-comparison with observations, Proc Roy Soc Lond A., Vol. 145 (1934), pp. 388-404.

[85] E. Orowan, and Z. Kristallplastizitat, Z Phys., Vol. 89 (1934), pp. 605-659.

[86] M. Polanyi, U ber eine Art Gitterstorung, die einen Kristall plastisch machen ko nnte. Z Phys., Vol. 89 (1934) pp. 660-664.

[87] G. Sachs. Zur Ableitung einer Fliessbedingung, Z. VDI., Vol. 72 (1928), pp. 734-736.

[88] G.I. Taylor, Plastic strain in metals, J Inst Met., Vol. 62 (1938), pp. 307-324.

[89] J.F.W. Bishop, and R. Hill, A theory of the plastic distortion of a polycrystalline aggregate under combined stresses, Philos Mag., Vol. 42 (1951), pp. 414-427.

[90] J.F.W. Bishop, and R. Hill, A theory of the plastic distortion of a polycrystalline aggregate under combined stresses, Philos Mag., Vol. 42 (1951), pp. 1298-1307.

[91] E. Kroner, On the plastic deformation of polycrystals, Acta Mater., Vol. 9 (1961), pp. 155-161.

[92] E. Orowan, in: Dislocations in Metals, American Institute of Mining and Metallurgy Engineering, New York, (1954).

[93] E. Schmid, and W.Boas, Kristallplastizitat, Springer-Verlag, Berlin, (1935).

[94] J.C. Polanyi, and N. Sathyamurthy, Location of energy barriers. VIII. Reagent →product energy conversion on surfaces with sudden or gradual late-barriers, Chemical Physics., Vol. 37 (2) (1979), pp. 259-264.

[95] D.S. Perry, J.C. Polanyi, and C. Woodrow, Location of energy barriers. VI. The dynamics of endothermic reactions, Chemical Physics., Vol. 3 (3) (1974), pp. 317-331.

[96] J.C. Polanyi, and N. Sathyamurthy. Location of energy barriers. VII. Sudden and gradual late-energy-barriers, Chemical Physics., Vol. 33 (2) (1978), pp. 287-303.

[97] R. Hill, and J.R. Rice, Constitutive analysis of elastic-plastic crystals at arbitrary strain, J. Mech. Phys. Solids., Vol. 20 (1972), pp. 401-413.

[98] D. Pierce, R.J. Asaro, and A. Needleman, An analysis of nonuniform and localized deformation in ductile single crystals, Acta Mater., Vol. 30 (1982), pp. 1087-1119.

[99] R.J. Asaro, and A. Needleman, Texture development and strain hardening in rate dependent polycrystals, Acta Mater., Vol. 33 (1985), pp. 923-953.

[100] E. Kroner, Kontinuumstheorie der Versetzungen und Eigenspannungen. Berlin: Springer, (1958) (in German).

[101] E. Kroner, In: Physics of defects. Amsterdam, Netherlands: North-Holland Publishing Company. (1981).

[102] E. Kroner, Allgemeine Kontinuumstheorie der Versetzungen und Eigenspannungen, Arch Ration Mech Anal., Vol. 4 (1959), pp. 273-334.

[103] E.H. Lee, and D.T. Liu, Finite-strain elastic-plastic theory with application to plane-wave analysis, J Appl Phys., Vol. 38 (1967), pp. 19-27.

[104] D. Pierce, R.J. Asaro, and A. Needleman, Material rate dependence and localized deformation in crystalline solids, Acta Mater., Vol. 31 (1983), pp. 1951-1976.

[105] R.J. Asaro, Crystal plasticity, J. Appl. Mech., Vol. 50 (1983), pp. 921-934.

[106] D. Raabe, Computaional Materials Science., WILEY-VCH Verlag GmbH, Weinheim (1998).

[107] J.F. Bishop, and R. Hill, A theoretical derivation of the plastic properties of a polycrystalline face-centred metal, Philos. Mag., Vol. 5 (1951), pp. 1298-1307.

[108] T.H. Lin, Analysis of elastic and plastic strains of a face-centred cubic crystal, J. Mech. Phys., Vol. 5 (1957), pp. 143.

[109] H. Honneff, and H. Mecking, Proceeding of the Sixth International Conference on Texture of Materials (ICOTOM-6) (1981).

[110] B. Budiansky, and T.T Wu, Theoretical prediction of plastic strains of polycrystals, Proceeding of the 4th U.S. National Congress on Applied Mechanics (1962).

[111] R. Hill, A self-consistent Mechanics of Composite Materials, J. Mech. Phys. Solids., Vol. 13 (1965), pp. 213-222.

[112] M. Berveiller, A. Zaoui, An extension of the self-consistent scheme to plastically-flowing polycrystals, J. Mech. Phys. Solids., Vol. 29 (1979), pp. 325-344.

[113] T. Iwakuma, and S. Nemat-Nasser, Finite elastic plastic deformation of polycrystalline metals, Proc. Roy. Soc. London., A Vol. 394 (1984), pp. 87-119.

[114] K.K. Mathur, P.R. Dawson, and U.F. Kocks, On modelling anisotropy in deformation process involving textured polycrystals with distorted grain shape, Mech. Mater., Vol. 10 (1990), pp. 183-202.

[115] K.K. Mathur, and P.R. Dawson, On modelling the development of crystallographic texture in bulk forming process, Int. J. Plast., Vol. 5 (1989), pp. 191-232.

[116] S.R. Kalidindi, C.A. Bronkhorst, and L. Anand, Crystallographic texture evolution in bulk deformation processing of FCC metals, J. Mech. Phys. Solids., Vol. 40 (1992), pp. 537-569.

[117] S.R. Kalidindi, and L. Anand, An approximate procedure for predicting the evolution of crystallographic texture in bulk deformation processing of fcc metals, Int. J. Mech. Sci., Vol. 34(4) (1992), pp. 309-332.

[118] G.B. Sarma, and P.R. Dawson, Texture predictions using a polycrystal plasticity model incorporating neighbor interactions, Int. J. Plast., Vol. 12 (1996), pp. 1023-1054.

[119] A. Kumar, and P.R. Dawson, The simulation of texture evolution with finite elements over orientation space, Computer methods in applied mechanics and engineering, Vol. 130 (1996a), pp. 227-246.

[120] A. Kumar, and P.R. Dawson, The simulation of texture evolution with finite elements over orientation space II, Application to planar crystals, Computer methods in applied mechanics and engineering, Vol. 130 (1996b), pp. 247-261.

[121] A. Kumar, and P.R. Dawson, Modelling crystallographic texture evolution with finite elements over neo-Eulerian orientation spaces, Computer methods in applied mechanics and engineering, Vol. 153 (1998), pp. 259-302.

[122] A. Kumar, and P.R. Dawson. Computational modelling of F.C.C. deformation textures over Rodrigues' space, Acta Mater., Vol. 48 (2000), pp. 2719-2736.

[123] V. Bachu, and S.R. Kalidindi, . On the accuracy of the predictions of texture evolution by the finite element technique for fcc polycrystals, Mater. Sci. Eng., A Vol. 257 (1998), pp. 108-117.

[124] S.H. Choi, Texture evolution of FCC sheet metals during deep drawing process, Int. J. Mech. Sci., Vol. 42 (2000), pp. 1571-1592.

[125] L. Delannay, S.R. Kalidindi, and P.V. Houtte, Quantitative prediction of textures in aluminium cold rolled to moderate strains, Mater. Sci. Eng., A Vol. 336 (2002), pp. 233-244.

[126] D. Raabe, and F. Roters, Using texture components in crystal plasticity finite element simulations, Int. J. Plast., Vol. 20 (2004), pp. 339-361.

[127] A.J. Beaudoin, P.R. Dawson, K.K. Mathur, U.F. Kocks, and D.A. Korzekwa, Application of polycrystal to sheet forming, Computer methods in applied mechanics and engineering, Vol. 117 (1994), pp. 49-70.

[128] S.R. Kalidindi, and S.E. Schoenfeld, On the prediction of yield surfaces by the crystal plasticity models for fcc polycrystals, Mater. Sci. Eng., A Vol. 293 (2000), pp. 120-129.

[129] K. Kowalczyk, and W. Gambin, Model of plastic anisotropy evolution with texture-dependent yield surface, Int. J. Plast., Vol. 20 (2004), pp. 19-54.

[130] S. Balasubramanian, and L. Anand, Single crystal and polycrystal elasto-viscoplasticity: application to earring in cup drawing of FCC materials, Comput. Mech., Vol. 17 (1996), pp. 209-225.

[131] Y. Zhou, J.J. Jonas, J. Savoie, A. Makinde, and S.R. MacEwen, Effect of texture on earring in FCC metals: finite element simulations, Int. J. Plast., Vol. 14 (1998), pp. 117-138.

[132] K. Inal, P.D. Wu, and K.W. Neale, Simulation of earrings in textured aluminium sheets, Int. J. Plast., Vol. 16 (2000), pp. 635-648.

[133] D. Raabe, Y. Wang, and F. Roters, Crystal plasticity simulation study on the influence of texture on earing in steel, Comput Mater Sci., Vol. 34 (2005), pp. 221-234.

[134] L. Delannay, M. Beringhier, Y. Chastel, and R.E. Loge, Simulation of cup drawing based on crystal plasticity applied to reduced grain samplings, Mater. Sci. Forum., Vol. 495-497 (2005), pp. 1639-1644.

[135] Y. Zhou, and K.W. Neale, Prediction of forming limit diagrams using a rate-sensitive crystal plasticity model, Int. J. Mech. Sci., Vol. 37 (1995), pp. 1-20.

[136] P.D. Wu, K.W. Neale, E. Giessen, M. Jain, A. Makinde, and S.R MacEwen, Crystal plasticity forming limit diagram analysis of rolled aluminium sheets, Mater. Trans. A, Vol. 29 (1998), pp. 527-535.

[137] J. Savoie, M. Jain, A.R. Carr, P.D. Wu, K.W. Neale, Y. Zhou, and J.J. Jonas, Predictions of forming diagrams using crystal plasticity models, Mat. Sci. Eng. Ser. A, Vol. 257 (1998), pp. 128-133.

[138] E. Nakamachi, C.L. Xie, H. Morimoto, K. Morita, and N. Yokoyama, Formability assessment of FCC aluminium alloy sheet by using elastic/crystalline viscoplastic finite element analysis, Int. J. Plast., Vol. 18 (2002), pp. 617-632.

[139] C.L. Xie, and E. Nakamachi, Investigations of the formability of BCC steel sheets by using crystalline plasticity finite element analysis, Mater. Des., Vol. 23(2002), pp. 59-68.

[140] S. He, V.A. Bael, S.Y. Li, P.V. Houtte, F. Mei, and A. Sarban, Residual stress determination in cold drawn steel wire by FEM simulation and X-ray diffraction, Mater. Sci. Eng., A, Vol. 346 (2003), pp. 101-107.

[141] H.J. Li, Z.Y. Jiang, J.T. Han, D.B. Wei, H.C. Pi, and A.K. Tieu, Crystal plasticity finite element modelling of necking of pure aluminium during uniaxial tensile deformation, Steel Res., Vol. 2 (2008), pp. 655-662.

[142] F. Rotersa, P. Eisenlohr, L. Hantcherli, D.D. Tjahjanto, T.R. Bieler, and D. Raabe, Overview of constitutive laws, kinematics, homogenization and

multiscale methods in crystal plasticity finite-element modelling: Theory, experiments, applications, Acta Mater., Vol. 58 (2010), pp. 1152-1211.

[143] C.H. Goh, J.M. Wallace, R.W. Neu, and D.L. McDowell, Polycrystal plasticity simulations of fretting fatigue, Int. J. Fatigue., Vol. 23 (2001), pp. S423-S435.

[144] H.S. Turkmen, P.R. Dawson, and M.P. Miller, The evolution of crystalline stresses of a polycrystalline metal during cyclic loading. Int. J. Plast., Vol. 18 (2002), pp. 941-969.

[145] H.S. Turkmen, R.E. Loge, P.R. Dawson, and M.P. Miller, On the mechanical behaviour of AA 7075-t6 during cyclic loading, Int. J. Fatigue., Vol. 25 (2003), pp. 267-281.

[146] S. Sinha, and S. Ghosh, Modelling cyclic ratcheting based fatigue life of HSLA steels using crystal plasticity FEM simulations and experiments, Int. J. Fatigue., Vol. 28 (2006), pp. 1690-1704.

[147] M. Zhang, J. Zhang, and D.L. McDowell. Microstructure-based crystal plasticity modelling of cyclic deformation of Ti–6Al–4V. Int. J. Plast., Vol. 23 (2007), pp. 1328-1348.

[148] K.S. Cheong, M.J. Smillie, and D.M. Knowles, Predicting fatigue crack initiation through image-based micromechanical modelling, Acta Mater., Vol. 55 (2007), pp. 1757-1768.

[149] F.P.E. Dunne, A. Walker, and D. Rugg. A systematic study of hcp crystal orientation and morphology effects in polycrystal deformation and fatigue, Proc. Roy. Soc. Lond. A, Vol. 463 (2007), pp. 1467-1489.

[150] T.R. Bieler, P. Eisenlohr, F. Roters, D. Kumar, D.E. Mason, M.A. Crimp, D. Raabe, The role of heterogeneous deformation on damage nucleation at grain boundaries in single phase metals, Int. J. Plast., Vol. 25 (2009), pp. 1655-1683.

[151] D. Kumar, T.R. Bieler, P. Eisenlohr, D.E. Mason, M.A. Crimp, F. Roters, D. Raabe, On predicting nucleation of microcracks due to slip-twin interactions at grain boundaries in duplex c-TiAl, J. Eng. Mater. Technol., Vol. 130 (2008), pp. 021012-1-021012-12.

[152] S.D. Patil, R. Narasimhan, P. Biswas, and R.K. Mishra, Crack tip fields in a single edge notched aluminium single crystal specimen, J. Eng. Mater. Technol., Vol. 130 (2008), pp. 021013.

[153] C.H. Goh, R.W. Neu, and D.L. McDowell, Crystallographic plasticity in fretting of Ti–6AL–4V, Int. J. Plast., Vol. 19 (2003), pp. 1627-1650.

[154] S. Nemat-Nasser, Plasticity: a treatise on finite deformation of heterogeneous inelastic materials. Cambridge: Cambridge University Press (2004).

[155] S.C. Hunters, Mechanics of continuous media (2nd edition). Ellis Horwood Limited (1983).

[156] P. Haupt, Continuum Mechanics and theory of Materials. Springer-Verlag Berlin Heidelberg (2000).

[157] J.R. Rice, Inelastic constitutive relations for solids: an internal variable theory and its application to metal plasticity, J. Mech. Phys. Solids., Vol. 19 (1971), pp. 433-455.

[158] J.W. Hutchinson, Bounds and self-consistent estimates for creep of polycrystalline materials, Proc. Roy. Soc. Lond. A, Vol. 348 (1976), pp. 1001-1127.

[159] J. Hirsch, K. Lucke, and M. Hatherly, Overview no. 76: Mechanism of deformation and development of rolling textures in polycrystalline f.c.c. metals-I. Description of rolling texture development in homogeneous CuZn alloys, Acta Mater., Vol. 36 (1988), pp. 2863-2882.

[160] S.R. Kalidindi, and L. Anand, Macroscopic shape change and evolution of crystallographic texture in pre-textured FCC metals, J. Mech. Phys. Solids., Vol. 42 (1994), pp. 459-490.

[161] U.F. Kocks, The Relation between Polycrystal Deformation and Single Crystal Deformation, Metall. Trans. A, Vol. 1 (1970), pp. 1121-1143.

[162] R.J. Asaro, and J.R. Rice, Strain localization in ductile single crystals, J. Mech. Phys. Solids., Vol. 25 (1977), pp. 309-338.

[163] J.W. Hutchinson, Elastic-Plastic Behaviour of Polycrystalline Metals and Composites, Proc. R. Soc. A, Vol. 319 (1970), pp. 247-272.

[164] H.C. Pi, Modelling Deformation of Cubic Metals by Crystal Plasticity Finite Element Method, PhD. Thesis, USTB Beijing (2006).

[165] W.M. Mao, and X.M. Zhang, Quantitative analysis of crystal texture. Beijing: Metallurgical Industry Press (1993).

[166] W.M. Mao, Crystallographic texture and anisotropy of metal material. Beijing: Science Press (2002).

[167] W.M. Mao, P. Yang, and L. Cheng, Analyzing principle and testing technique of material texture. Beijing: Metallurgical Industry Press (2008).

[168] V. Randle, and O. Engler, Introduction to texture analysis: macrotexture, microtexture and orientation mapping. Amsterdam, The Netherlands: Gordon & Breach c (2000).

[169] H.J. Bunge, Texture analysis in materials science: mathematical methods. London: Butterworth (1982).

[170] U.F. Kocks. Texture and anisotropy: preferred orientations in polycrystals and their effect on materials properties Cambridge, U.K.; New York: Cambridge University Press (1998).

[171] G.J. Davies, Texture and the properties of materials. London: Metals Society, (1976).

[172] ABAQUS/Standard user's manual. Hibbitt, Karlsson& Sorensen, Inc, (2002).

[173] SIMULINK, ABAQUS GUI Toolkit Reference Manual, USA, (2008).

[174] Z. Zhuang, F. Zhang, and S. Cen. Analysis and examples of ABAQUS Nonlinear Finite Element. Beijing: Science Press (2004).

[175] http://www.vacaero.com/Metallography-with-George-Vander-Voort/Metallography-with-George-Vander-Voort/metallography-and-microstructure-of-aluminum-and-alloys.html [Accessed 11 September 2010].

[176] J.F. Cao, and Y.P. Shi, Analysis of common problems in ABAQUS finite element modeling. Bejing: China Machine Press, (2009).

[177] H.B. Xie, The Research on the Edge Crack of Cold Rolled Thin Strip, PhD. Thesis, University of Wollongong, (2011).

[178] http://en.wikipedia.org/wiki/Vickers_hardness_test [Accessed 11 November 2011].

[179] R.L. Smith, and G.E. Sandland, An Accurate Method of Determining the Hardness of Metals, with Particular Reference to Those of a High Degree of Hardness, Proceedings of the Institution of Mechanical Engineers, Vol. I (1922), pp. 623-641.

[180] http://www.ukcalibrations.co.uk/vickers_htm.html [Accessed 18 October 2011].

[181] Smithells Metals Reference Book, 8th Edition, ch. 22.

[182] K. Shinohara, Sci. Pap. Inst. Phys. Chem. Res., 20 (1932/1933) pp. 39.

[183] A.P. Day, Channel 5 User Manual, HKL Technology A/S, Hobro, Denmark, (2001).

[184] E.A. Brandes, and G.B. Brook, Smithells Metals Reference Book. Bath: The Bath Press, (1999).

[185] F. Roters, Y.W. Wang, J.C. Kuo, D. Raabe, Comparison of single crystal simple shear deformation experiments with crystal plasticity finite element simulations, Adv. Eng. Mater., Vol. 6(8) (2004), pp. 653-656.

[186] A.J. Beaudoin, P.R. Dawson, K.K. Mathur, and U.F. Kocks, A hybrid finite element formulation for polycrystal plasticity with consideration of macrostructural and microstructural linking, Int. J. Plast., Vol. 11 (1995), pp. 501-521.

[187] P.D. Wu, and D.J. Lloyd, Modelling surface roughening with crystal plasticity, Proc. 1st I.S.M.M.A.A, (2003), pp. 15-20.

[188] S.R. Kalidindi, C.A. Bronkhorst, and L. Anand, Crystallographic texture evolution in bulk deformation processing of FCC metals, J. Mech. Phys. Solids., Vol. 40 (1992), pp. 552-555.

[189] H.J. Li, Z.Y. Jiang, D.B. Wei, J.T. Han, and A.K. Tieu, Study on surface asperity flattening during uniaxial planar compression, Wear, Vol. 271 (2011), pp. 1778-1784.

[190] H.J. Li, Z.Y. Jiang, D.B. Wei, P.J. Yan, A.K. Tieu, and J.T. Han, Crystal plasticity finite element modelling of surface asperity flattening during uniaxial planar compression, International Conference on Tribology in Manufacturing Processes, (2010), pp. 397-406.

[191] Z.Y. Chen, Modeling of intergrowth deformation of twin and slip in the FCC metal. PhD. Thesis, CSU Changsha (2002).

[192] R.J. Asaro, and A. Needleman, Flow localization in strain hardening crystalline solids, Scr. Mater., Vol. 18(5) (1984), pp. 429-435.

[193] H.C. Pi, J.T. Han, C.G. Zhang, A.K. Tieu, and Z.Y. Jiang, Modelling uniaxial tensile deformation of polycrystalline Al using CPFEM, Journal of University of Science and Technology Beijing, Mineral, Metallurgy, Material. Vol. 15(1) (2008), pp. 43-47.

[194] H.J. Li, Z.Y. Jiang, D.B. Wei, J.T. Han, and A.K. Tieu, Crystal plasticity finite element modelling of the influence of friction on surface roughening

during uniaxial planar compression, Mater. Sci. Forum., Vol. 654-656 (2010), pp. 1606-1609.

[195] W.F. Hosford, The mechanics of crystals and textured polycrystals. Oxford University Press, Oxford, 29, (1993).

[196] M. Aicheler, S. Sgobba, G. Arnau-Izquierdo, M. Taborelli, S. Calatroni, H. Neupert, and W. Wuensch, Evolution of surface topography in dependence on the grain orientation during surface thermal fatigue of polycrystalline copper, Int. J. Fatigue., Vol. 33 (2011), pp. 396-402.

[197] A. Wikstroem, and M. Nygards, Anisotropy and texture in thin copper films-anelasto-plastic analysis, Acta Mater., Vol. 50 (2002), pp. 857-870.

[198] S.P. Baker, A. Kretschmann, and E. Arzt, Thermo mechanical behaviour of different texture components in Cu thin films, Acta Mater., Vol. 49 (2001), pp. 2145-2160.

[199] R. Moeing, Y.B. Park, C.A. Volkert, Thermal fatigue in copper interconnects, In: Proceedings of the 8th int. workshop on stress-induced phenomena in metallization, (2005) pp. 147-156.

[200] Z.L. Liu, X.C. You, and Z. Zhuang, A mesoscale investigation of strain rate effect on dynamic deformation of single-crystal copper, Int. J. Solids Struct., Vol. 45 (2008), pp. 3674-3687.

[201] L. Travis, A. Brown, S.A. Christopher, G. Tejas, A. Murthy et tal., A study of the interactive effects of strain, strain rate and temperature in severe plastic deformation of copper, Acta Mater., Vol. 57 (2009), pp. 5491-5500.

[202] S.A. Serebrinsky, G.S. Duffo, and J.R. Galvele, Effect of strain rate on stress corrosion crack velocity difference between intergranular and transgranular cracking, Corros. Sci., Vol. 41 (1999) pp. 191-195.

[203] S.A. Serebrinsky, and J.R. Galvele, Effect of the strain rate on stress corrosion crack velocities in face-centred cubic alloys. A mechanistic interpretation, Corros. Sci., Vol. 46 (2004), pp. 591-612.

[204] C.C Wu, S.H. Wang, C.Y. Chen, J.R. Yang, P.K. Chiu and J. Fang, Inverse effect of strain rate on mechanical behaviour and phase transformation of super-austenitic stainless steel, Scr. Mater., Vol. 56 (2007), pp. 717-720.

[205] G.E. Papakaliatakis, Effect of strain rate on crack growth in aluminium alloy 1100-0, Theor. Appl. Fract. Mech., Vol. 31 (1999), pp. 131-139.

[206] J.J. Urcola, and C.M. Sellars, Effect of changing strain rate on stress-strain behaviour during high temperature deformation, Acta Mater., Vol. 35 (11) (1987), pp. 2631-2647.

[207] S. Vaynman, M.E. Fine, S. Leeb and H.D. Espinosa, Effect of strain rate and temperature on mechanical properties and fracture mode of high strength precipitation hardened ferritic steels, Scr. Mater., Vol. 55 (2006), pp. 351-354.

[208] H. Takuda, S. Kikuchi, T. Tsukada, K. Kubota, N. Hatta, Effect of strain rate on deformation behaviour of a Mg–8.5Li–1Zn alloy sheet at room temperature, Mater. Sci. Eng., A, Vol. 271 (1999), pp. 251-256.

[209] A. Bhattacharyya, D. Rittel, and G. Ravichandran, Effect of strain rate on deformation texture in OFHC copper, Scr Mater., Vol. 52 (2005), pp. 657-661.

[210] J.H. Wu, and C.K. Lin, Effect of strain rate on high-temperature low-cycle fatigue of 17-4 PH stainless steels, Mater. Sci. Eng., A, Vol. 390 (2005), pp. 291-298.

[211] B. Zhang, and V.P.W. Shim, Effect of strain rate on microstructure of polycrystalline oxygen-free high conductivity copper severely deformed at liquid nitrogen temperature, Acta Mater., Vol. 58 (2010), pp. 6810-6827.

[212] M. Kodeeswaran, and R. Gnanamoorthy, Effect of strain rate on nanocrystalline surface formation in controlled ball impact process in AISI 304 SS, Mater. Lett., Vol. 62 (2008), pp. 4516-4518.

[213] B. Eghbali, Effect of strain rate on the microstructural development through continuous dynamic recrystallization in a microalloyed steel, Mater. Sci. Eng., A, Vol. 527 (2010), pp. 3402-3406.

[214] J. H. Percy, The Effect of Strain Rate on the Forming Limit Diagram for Sheet Metal, Annals of the CRIP., Vol. 29(1) (1980), pp. 151-152.

[215] K. Qin, L.M. Yang, and S.S. Hu, Mechanism of strain rate effect based on dislocation theory, CHIN. PHYS. LETT., Vol. 26(3) (2009) pp. 036103 1-4.

[216] H.J. Li, Z.Y. Jiang, and D.B. Wei, Crystal plasticity finite modelling of 3D surface asperity flattening in uniaxial planar compression, Tribol. Lett., Vol. 46 (2) 2012, pp. 101-112.

[217] T.M. Link, and B.M. Hance, Effects of Strain Rate and Temperature on the Work Hardening Behaviour of High Strength Sheet Steels, SAE Technical Paper, Vol. 1 (2003), pp. 516.

[218] Z. Zhao, M. Ramesh, D. Raabe, A.M. Cuitino, and R. Radovitzky, Investigation of three-dimensional aspects of grain-scale plastic surface deformation of an aluminium oligocrystal, Int. J. Plast., Vol. 24 (2008), pp. 2278-2297.

[219] Z. Zhao, R. Radovitzky, and A. Cuitino, A study of surface roughening in fcc metals using direct numerical simulation, Acta Mater., Vol. 52 (2004), pp. 5791-5804.

[220] A. Gazder, M. Sanchez-Araiza, J. Johnas, and E. Pereloma, Evolution of recrystallization texture in a 0.78 wt.% Cr extra-low-carbon steel after warm and cold rolling, Acta Mater., Vol. 59 (2011), pp. 4847-4865.

[221] S. Kulkarni, E. Starke, and D. Kuhlmann-Wilsdorf, Some observations on deformation banding and correlated microstructures of two aluminium alloys compressed at different temperatures and strain rates, Acta Mater., Vol. 46 (1998), pp. 5283-5301.

[222] R. Hill, Constitutive laws and waves in rigid/plastic solids, J. Mech. Phys. Solids., Vol. 10 (1962), pp. 89-98.

[223] R.J. Asaro, Geometrical effects in the inhomogeneous deformation of ductile single crystals, Acta Mater., Vol. 27 (1979), pp. 445-453.

[224] A.A. Gazder, A.A. Saleh, and E.V. Pereloma, Microtexture analysis of cold-rolled and annealed twinning-induced plasticity steel, Scripta Mater., Vol. 65 (2011), pp. 561.

[225] P. Yang, Application of Electron backscatter diffraction technique, Beijing, (2007).

[226] J.C. Huang, I.C. Hsiao, T.D. Wang, and B.Y. Lou, Ebsd study on grain boundary characteristics in fine-grained Al alloys, Scripta Mater., Vol. 43 (2000), pp. 213-220.

[227] G. Gindraux, and W. Form, New concepts of annealing-twin formation in face-centered cubic metals, J. Inst. Met., London, Vol. 101 (1973), pp. 85-92.

APPENDIX I

TENSOR OPERATIONS

Tensors are geometric objects that describe the linear relationships between vectors, scalars, and other tensors. Vectors and scalars themselves are also tensors. A tensor can be represented as a multi-dimensional array of numerical values. Tensor operation can be described as

(1) Equal

If a tensor $\boldsymbol{T} = T_{ij}\boldsymbol{e}_i\boldsymbol{e}_j$ equals the tensor $\boldsymbol{S} = S_{ij}\boldsymbol{e}_i\boldsymbol{e}_j$, then the related components will also be equal.

$$T_{ij} = S_{ij} \tag{A1.1}$$

(2) Addition and subtraction

If two tensors $\boldsymbol{A} = A_{ij}\boldsymbol{e}_i\boldsymbol{e}_j$ and $\boldsymbol{B} = B_{ij}\boldsymbol{e}_i\boldsymbol{e}_j$ are the same rank, and tensor $\boldsymbol{T} = T_{ij}\boldsymbol{e}_i\boldsymbol{e}_j$ meets the equation $\boldsymbol{T} = \boldsymbol{A} \pm \boldsymbol{B}$, then the following equation will be:

$$T_{ij} = A_{ij} \pm B_{ij} \tag{A1.2}$$

(3) Multiplication by a scalar

If the tensor $\mathbf{A}$ is multiplied by a number λ (or a scalar), then the result is:

$$\mathbf{T} = \lambda\mathbf{A}\,,\ T_{ij} = \lambda A_{ij} \tag{A1.3}$$

(4) Tensor product

The product of any two tensors A (rank is m) and B (rank is n) is a tensor T with the rank of m+n. That can be expressed as

$$\mathbf{T} = \mathbf{A} \otimes \mathbf{B} \tag{A1.4}$$

For components they are:

$$T_{ijklm} = A_{ijk} B_{lm} \tag{A1.5}$$

(5) Dot product of two tensors

The inner product of two tensors **a** and **b** is commutative and produces a scalar s where:

$$s=a_i b_i=a_1 b_1+ a_2 b_2+ a_3 b_3 \tag{A1.6}$$

(6) Double dot product of two tensors

The double dot product of two second rank tensors $\mathbf{T}$ and $\mathbf{S}$ produces a scalar s=**T:S**, which can be evaluated as the sum of the 9 products of the tensor components.

$$s = T_{ij} S_{ij} = T_{11}S_{11} + T_{12}S_{12} + T_{13}S_{13} + T_{21}S_{21} + T_{22}S_{22} + T_{23}S_{23} + T_{31}S_{31} + T_{32}S_{32} + T_{33}S_{33} \tag{A1.7}$$

APPENDIX II

VOIGT NOTATION

In mathematics, the Voigt notation or Voigt form in multi-linear algebra is a way to represent a symmetric tensor by reducing its order. It is very popular in the programming of tensor operations.

1. Voigt Notation of low rank tensor

(a) Stress tensor

If the stress tensor $\boldsymbol{\sigma}$ is a symmetric tensor, it can be expressed in Voigt notation as

$$\text{Stress tensor} \rightarrow \text{Voigt}$$

$$\boldsymbol{\sigma} = \begin{bmatrix} \sigma_{11} & \sigma_{12} & \sigma_{13} \\ \sigma_{21} & \sigma_{22} & \sigma_{23} \\ \sigma_{31} & \sigma_{32} & \sigma_{33} \end{bmatrix} \rightarrow \begin{Bmatrix} \sigma_{11} \\ \sigma_{22} \\ \sigma_{33} \\ \sigma_{23} \\ \sigma_{13} \\ \sigma_{12} \end{Bmatrix} = \begin{Bmatrix} \sigma_1 \\ \sigma_2 \\ \sigma_3 \\ \sigma_4 \\ \sigma_5 \\ \sigma_6 \end{Bmatrix} \equiv \{\boldsymbol{\sigma}\} \qquad \text{(A2.1)}$$

(b) Strain tensor

When the symmetric strain tensor $\boldsymbol{\varepsilon}$ is expressed in Voigt notation, the coefficients of shear strains should be two.

$$\text{Strain tensor} \rightarrow \text{Voigt}$$

$$\boldsymbol{\varepsilon} = \begin{bmatrix} \varepsilon_{11} & \varepsilon_{12} & \varepsilon_{13} \\ & \varepsilon_{22} & \varepsilon_{23} \\ \text{Symmetry} & & \varepsilon_{33} \end{bmatrix} \rightarrow \begin{Bmatrix} \varepsilon_{11} \\ \varepsilon_{22} \\ \varepsilon_{33} \\ 2\varepsilon_{23} \\ 2\varepsilon_{13} \\ 2\varepsilon_{12} \end{Bmatrix} \equiv \{\boldsymbol{\varepsilon}\} \tag{A2.2}$$

On the basis of energy expression, the coefficients of shear strains refer to 2. Right components of Equation (A2.2) equal to left right components of Equation (A2.2).

2. Voigt Notation of low rank tensor

It is very useful to apply the Voigt notation in the high rank tensor, especially for the tetradics. For example, the elastic law of tetradics can be expressed as

$$\sigma_{ij} = C_{ijkl}\varepsilon_{kl}, \boldsymbol{\sigma} = \mathbf{C} : \boldsymbol{\varepsilon} \tag{A2.3}$$

Equation (A2.3) can be expressed in the mode of Voigt matrix.

$$\{\boldsymbol{\sigma}\} = [\mathbf{C}]\{\boldsymbol{\varepsilon}\}, \text{ or } \sigma_a = C_{ab}\varepsilon_b \tag{A2.4}$$

where $a \leftarrow ij$ and $b \leftarrow kl$.